Università degli Studi di Cagliari

DOTTORATO DI RICERCA

Ingegneria Elettronica e Informatica

Ciclo XXIX

TITOLO TESI

LASER DIODES AND THEIR RELIABILITY. PHYSICAL MODELS AND EXPERIMENTAL VALIDATION.

Settore scientifico disciplinare di afferenza

ING-INF/01 ELETTRONICA

Presentata da:	Giulia Marcello
Coordinatore Dottorato	Professor Fabio Roli
Tutor	Professor Massimo Vanzi

Esame finale anno accademico 2015 – 2016
Tesi discussa nella sessione d'esame marzo – aprile 2017

Contents

Related papers

Mura G, M. Vanzi, G. Marcello, R. Cao
"The role of the optical trans-characteristics in laser diode analysis."
Microelectronics Reliability, vol. 53, pp 1538-1542 (2013)

Vanzi M., Mura G., Marcello G.
"Ideality factor and threshold voltage in laser diodes"
Photonics Conference, 2014 Third Mediterranean (pp. 1-3). IEEE.

Giovanna Mura, Massimo Vanzi, Giulia Marcello
"FIB-induced electro-optical alterations in a DFB InP laser diode."
Microelectronics Reliability 54(9-10): 2151-2153 (2014)

G.Marcello, G.Mura, M. Vanzi, M. Bagatin, S. Gerardin, A. Paccagnella,
"Proton Irradiation Effects on Commercial Laser Diodes"
2015 15th European Conference on Radiation and Its Effects on Components and Systems (RADECS), Moscow, 2015, pp. 1-4.

M. Vanzi, G. Mura, G. Marcello, G. Martines
"Clamp voltage and ideality factor in laser diodes"
Microelectronics Reliability 55 (2015) 1736–1740

Massimo Vanzi, K. Xiao, Giulia Marcello, and Giovanna Mura
"Side-Mode Excitation in Single-Mode Laser Diodes"
IEEE Transactions on Device and Materials Reliability, Vol. 16, No. 2, June 2016

M. Vanzi, G. Mura, G. Marcello, K. Xiao
"ESD tests on 850nm GaAs-based VCSELs"
Microelectronics Reliability, 64 (2016), 617-622

M. Vanzi, G.Marcello, G. Mura, L. Bechou, D. Yannick, G. Le Gales, S. Joly
"Extended modal gain measurement in DFB laser diodes."
IEEE Photonics Technology Letters, Vol. PP, Issue. 99, pp 1-1

G. Le Galès, S. Joly, G. Marcello, G. Pedroza, A. Morisset, F. Laruelle, L. Bechou
"Seed laser diodes in pulsed operation: limitations and reliability investigations."
Proc. SPIE 10098, Physics and Simulation of Optoelectronic Devices XXV, 100980S (February 22, 2017)

Conference proceedings

Marcello G., Vanzi M., Mura G.
"Experimental gain in single mode laser diodes"
2014 International Symposium on Reliability of Optoelectronics for Systems.

M.Vanzi, G. Marcello, G. Mura, G. Le Galès, S. Joly, Y. Deshayes, L. Bechou
"An extended model for optical gin calculations in single-mode laser diodes."
2016 International Symposium on Reliability of Optoelectronics for Systems.

G. Le Galès, G. Marcello, S. Joly, G. Pedroza, A. Morriset, F. Laurelle, F. Darracq, L. Bechou
"1060nm Seed laser diodes: performances and safe operating area."
2016 International Symposium on Reliability of Optoelectronics for Systems.

G.Marcello, G.Mura, M. Vanzi
"Reliability-oriented characterization protocols for low-power laser diodes."
2016 Pharos Event (Bordeaux).

Introduction

This PhD thesis focuses on laser diodes, and reports on three years spent within the Optoelectronic Reliability team of prof. Massimo Vanzi and prof. Giovanna Mura, at the Department of Electric and Electronic Engineering (DIEE) of the University of Cagliari.

The relevance of laser diodes in several technological fields increases progressively with the evolution of their technology, and then of their performances. A summary of such history will be given in detail at the beginning of Ch.1.

Telecommunications in particular have been both the most intense prompt and the hardest challenge to solid state semiconductor light emitters. Faster and faster, and more and more powerful devices have been progressively developed, with the conflicting constraints of single-mode operation combined with tenability, and the continuous request for integrated optical functions.

The team at DIEE is historically involved, since decades, in studying the survival of laser diodes, that is, their Reliability.

Reliability is in itself a manifold activity, that involves statistics, failure physics, modeling, microscopic analysis, strategy.

This work witnesses three years of intense evolution of a new physical model for describing laser diodes, that was initially developed for giving account of the measured degradation of electric and optic parameters of failed devices. The model became progressively more and more inclusive, and also caused several deep revisions of the widespread approaches to laser diode physics and reliability.

At the beginning of this period, the model was existing, and had been yet applied to several studies of specific failure cases. Anyway, it left some open questions, that limited its application to the totality of real cases.

Along the three years of this PhD course, I had the chance to cooperate in first refining the fundamental model, and then in solving one by one all the unresolved issues, and in signing as an Author all the relevant papers published by the DIEE team in this field.

The Thesis is accordingly organized in three parts and some appendices.

The first resumes the general model, including a quite new formulation of optical gain that has been only partially published, at the date of the presentation of this work. Also the most relevant non-idealities are here discussed and solved.

The second part collects the several experimental studies that have been carried out and published on real devices, looking for physical validation of the theoretical predictions, or, conversely, measuring the magnitude of some relevant quantities requested for calibrating the model.

The third part faces the issue of failures. Experimental cases, with the interpretation of the most puzzling ones, are complemented with a sort of dictionary

of failure modes, that is the systematic prediction of the measurable electric and optic degradations, to be compared with the real world for sorting and classifying effects and then addressing the physical analysis to discover their root causes.

The final appendices resume some more theoretical details, or report on still incomplete studies that require further refinement and calibration.

It has been a choice to keep the thesis quite close to the papers which it refers to: all those parts have been deeply discussed, distilled and organized, word by word, with my Tutors, before each publication. No better form could be found for them. On the other hand, no paper is here reported, from paragraph 1.2 to the end of the thesis, where my name is not included in the list of Authors of the published version. On the contrary, some points are here reported anticipating their publication, as for the gain-current $g(I)$ formulas and the paragraph on the dV/dI curves. It is the kind permission of prof. M.Vanzi to use this material for my thesis that allows its presence here.

Chapter 1

An extended model for Laser Diodes

Introduction

The first chapter summarizes and extends a new model for laser diodes developed at the University of Cagliari in the last decade [1–3], that embraces the whole injection range, below and beyond threshold and embeds the threshold itself. Quantities are referred to the measurable applied voltage, and include radiative and non-radiative currents as well as relevant functions as gain and quantum efficiency. Several popular formulas for the laser regime are shown to be the limiting cases of a new and wider treatment. Comparison with literature is continuously carried on.

On the past few years, a model has been proposed and developed for laser diodes [1–3] based on a new version of the Rate Equations for photons and charges.

The prompt for going back and revise the foundations themselves of laser diode modelling has been the difficulty to apply the available Rate Equations in a coherent way when analyzing DC electro-optical characteristics evolving in time, that is when dealing with degradations. The point is exactly the plural form "Rate Equations", because a unique form does not exist. Gain, optical power, threshold, efficiency, and in general all quantities that are relevant for characterizing and monitoring such devices are referred to different representations of injection: separation of the quasi-Fermi levels, carrier density, current. It is difficult to harmonize them and look, for instance, for a self-consistent treatment able to correlate gain saturation with current injection, or to continuously describe the transition between the ranges where spontaneous or stimulated emission dominate. An illuminating example is the search for a relationship between the clamp value of the quasi-Fermi levels and the threshold current; despite they are different representations of the same phenomenon: the achievement of lasing.

The opinion is that this situation is a consequence of the historical evolution of laser equations in general and of laser diodes in particular. Then, some history may help.

After the seminal Einstein's papers [4,5] that in 1916-17 first proposed the idea of stimulated radiation, for decades the studies focused on amplification of radiation in the microwave domain [6–8] up to the definition of a fundamental Rate

Equation for Maser given by Statz and De Mars [9] in 1960. The translation to the optical domain, moving from Maser to Laser, was theoretically investigated by Lamb [10] in 1964. The peculiarity of this phase was the consideration of physical systems where the probability of upward or downward energetic transitions were separately defined by the population of, respectively, the non-excited end the excited states. No mass-action laws have ever been invoked, taking into account for a same transition the populations of both the initial and the final states. This is an important point, to be considered when the laser history approaches the world of Solid State Physics, whose milestones appeared after the Einstein's works: Pauli's Exclusion principle [11] on 1925, Fermi-Dirac statistics [12, 13] on 1926, the Bloch Theorem [14] on 1928. This prepared the playground for the capital book by Shockley [15] on electrons and holes on 1950.

The two lines (maser/laser and solid state electronics) run nearly independently, and when they merged [16–23] the laser diode rate equations on one side looked at the formalism of the semiconductor collective states, and on the other tried to harmonize with the assessed heritage of maser/laser physics, developed for systems of local wave functions. It resulted a dual description of photon-charge interactions: one, keeping the concepts of quasi-Fermi levels and of band population, was mostly used for spectral properties and in particular for gain (including the transparency condition); the other, counting the rate of change of the number of particles, with a set of two lumped equations for charges and photons, mainly applied to current and optical power. If the former approach still shows its clear foundation on Quantum Mechanics, the latter generally faces the computational challenges for many quantities introducing phenomenological considerations.

The first fundamental books summarizing the state of the art [24–26], including the evolving technology that rapidly brought to Double Heterostructure laser diodes, certified that dual approach, and even when further studies widened the field of application of laser diodes, studying their modulation [27–29], they did not change this original dichotomy.

When one opens the currently available most popular textbooks [30–33], he still finds spectral gain and transparency condition in different chapters than current-power relationship. This makes difficult to correlate any observed kinetics, as for degradations, with Physics.

If we want to point out the kernel of the problem, the difference between the Solid State world and the historical Rate Equations for lasers is dramatically simple: the latter, neglecting the mass-action law for the non-equilibrium transitions, renounces to refer any relevant quantity to the voltage V. This, for a device that is built, is named and largely behaves as a diode, is a serious handicap.

The new model, presented in this chapter, aims to rewrite the Rate Equations for a laser diode focusing on the voltage V as the main reference parameter. Nothing of laser physics is modified, but the choice is proven to greatly unify the study of the many different quantities that characterize such kind of devices.

The approach is to start with an ideal Double Heterostructure Quantum Well diode, whose inner part, the active region, is responsible for all recombination, and recombination is completely radiative (unit internal efficiency). Here the quantum size of the active layer is invoked to justify the transversal uniformity of densities (usually assumed for infinitely extended regions), based on the loss of significance

of locality on a quantum scale. Also the detailed band structure will be packed into the effective masses and density of states, so that the simple (and widely used) parabolic band model will be employed. A specific appendix A will be dedicated to the more refined picture that includes light and heavy hole subbands.

The k-selection rule is preserved, which implies to neglect the non-collective states in band tails. It will be shown that the basic characteristics of a real device are not affected by such approximation. The Rate Equation for the ideal active region will then be derived by first considering and then modifying the equilibrium state. The separation of the quasi-Fermi levels is here identified with the energy equivalent qV of the applied voltage V.

Several results come from the solution of the Rate Equation, including spectral and modal gain, the ideal *I(V)* current-voltage characteristics and the initial form of the $P_{OUT}(I)$ power-current relationship. Threshold will appear as an asymptotic value for voltage, and a fast but non abrupt transition will continuously connect the regions under and above threshold. This bunch of results follows the simple strategy inversion in the proposed approach, when compared with the previous treatments: instead of computing the total number of electron-hole transitions and then look for the fraction that creates light, the sole radiative ones are first considered, finding a harmonic, self-consistent and quite peculiar relationship between V, I and $P_{OUT}(I)$, that describe the ideal diode as a device.

It is only after this step that comparison with real world will force to include non radiative recombination inside the active layer itself, and to model it as an additive Shockley current sharing the same voltage of the radiative one.

This non radiative current at threshold voltage will be shown to rule over the measurable threshold current. Its formulation will display the most striking difference with literature, but it will also be shown to be, surprisingly, numerically undistinguishable from the previous results, validated by experiments along decades.

Being $P_{OUT}(V)$ available, the expression of the total (radiative and non-radiative) current I as a function of the same V will lead to the continuous *L-I* curve [21, 22, 30–32], whose asymptotic limits exactly recover the well-known expression for the LED and the laser regimes.

Other currents are then considered, dominant at very low injection, in a region usually neglected in standard current-driven measurements. They will be identified and weighted for their relevance, that is null in regular devices, but can become important under degradation.

Optical gain equations are revised on the basis of this recent new model. Explicit relationships with total current and voltage are shown, able to include proper gain saturation limits with experimental estimate of gain on the basis of the DC characteristics s proposed.

A list of further non-idealities and open points will be given and discussed. Among them, the harmonization of the new modal gain relationships with the existing ones, the puzzle of the ideality factor, the sharpness of the threshold transition, the effects of longitudinal and transversal non-uniform pumping.

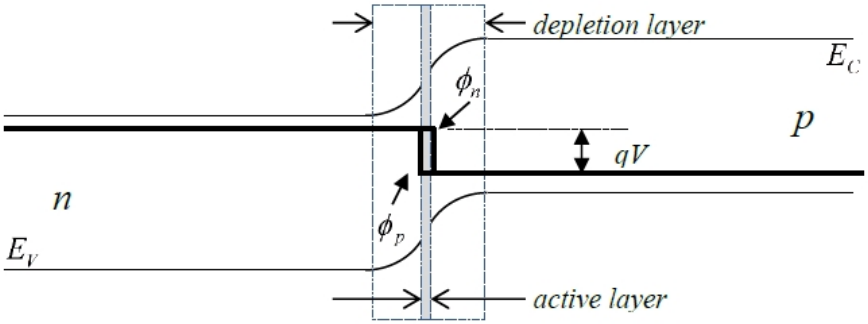

Figure 1.1: Quasi-Fermi levels in the ideal laser diode

1.1 The basic model

1.1.1 Energies and densities

Let us consider an ideal laser diode fig.1.1, where

(a) all recombination is radiative and

(b) it occurs inside the very thin QW undoped active layer of a Double Heterostructure.

The quantum size of the active layer makes any concept of density gradient meaningless, allowing electrons, holes and photons to interact irrespective of their position along the whole thickness of the layer itself.

This is the same as saying that the quasi-Fermi levels for electrons and holes, as well as the existing photon density, are uniform inside the active layer.

Dealing with optical transitions in a semiconductor, the usual concepts [33] that define tab.1.1 and fig.1.2 electron and hole energy and density, as well as their complementary density are introduced:

$$\begin{cases} E_e = E_C + \dfrac{\hbar^2 K_e^2}{2m_e^*} \\ \\ E_h = E_V - \dfrac{\hbar^2 K_h^2}{2m_h^*} \end{cases} \tag{1.1}$$

$$\begin{cases} n(E_e) = \dfrac{g_e(E_e)}{1 + \exp\left(\dfrac{E_e - \phi_n}{kT}\right)} \\ \\ p(E_h) = \dfrac{g_h(E_h)}{1 + \exp\left(\dfrac{\phi_p - E_h}{kT}\right)} \end{cases} \tag{1.2}$$

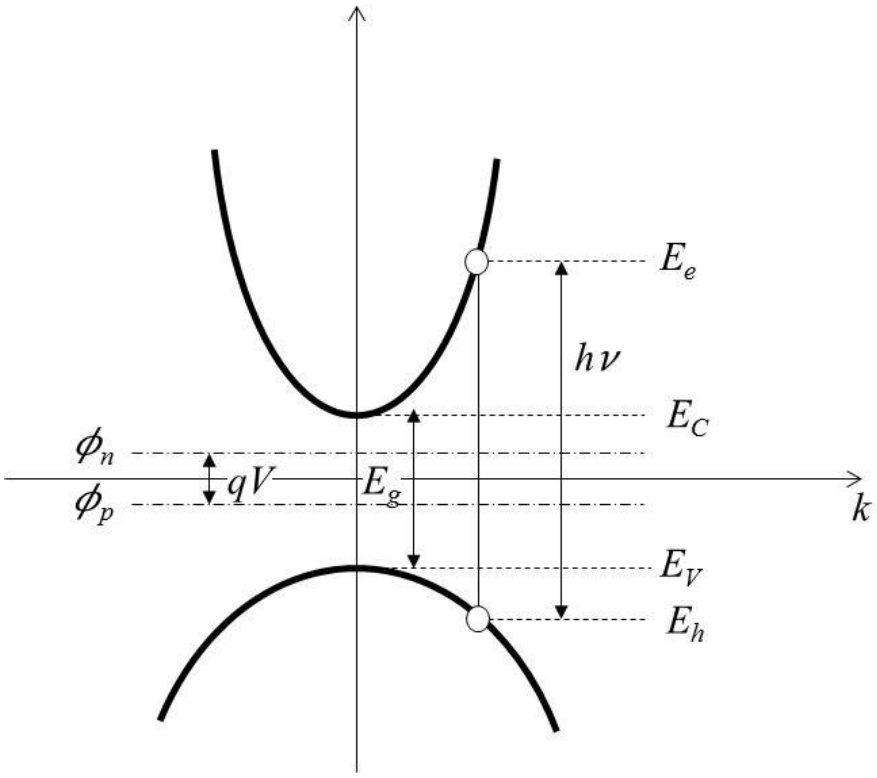

Figure 1.2: Definition of energy levels.

$$\begin{cases} \bar{n}(E_e) = n(E_e) \exp\left(\dfrac{E_e - \phi_n}{kT}\right) \\ \\ \bar{p}(E_h) = p(E_h) \exp\left(\dfrac{\phi_p - E_h}{kT}\right) \end{cases} \tag{1.3}$$

These elements are complemented with the quantum-mechanical selection rules on momentum and energy:

$$\begin{cases} \hbar k_e = \hbar k_h \\ E_e - E_h = h\nu \end{cases} \tag{1.4}$$

The only not common definition that will be here also introduced relates the difference in the quasi-Fermi levels to the electrostatic potential V.

$$\phi_n - \phi_p = qV \tag{1.5}$$

This clearly recalls the similar definition that enters the Shockley's theory [15] of an ideal *pn* junction, where V is the final voltage applied to the classic semiconductor diode. Here it is proposed for the ideal laser diode. Physics of the two ideal devices are nearly opposite: recombination occurs totally outside the depletion region in the Shockley diode, while it is concentrated inside the active layer, fully embedded inside the depleted volume, for the ideal laser diode, that in this way resembles the deeply non-ideal device considered by Shockley when traps

Symbols	**Definitions**
E_e	Conduction band edge
E_h	Valence band gap
$E_e = E_C + \frac{h^2 K_e^2}{2m_e^*}$	Electron energy in conduction band
$E_h = E_V - \frac{h^2 K_h^2}{2m_h^*}$	Hole energy in valence band
$\hbar k_e$	Electron momentum in conduction band
$\hbar k_h$	Hole momentum in valence band
m_e^*	Electron effective mass
m_h^*	Hole effective mass
$g_e(E_e)[cm^{-3}eV^{-1}]$	Electron density of state at energy E_e
$g_h(E_h)[cm^{-3}eV^{-1}]$	Hole density of state at energy E_h
$n(E_e) = \frac{g_e(E_e)}{1 + e^{\frac{E_e - \phi_n}{kT}}}[cm^{-3}eV^{-1}]$	Electron density at energy E_e
$p(E_h) = \frac{g_h(E_h)}{1 + e^{\frac{\phi_p - E_h}{kT}}}[cm^{-3}eV^{-1}]$	Hole density at energy E_h
$\bar{n}(E_e) = n(E_e) \exp\left(\frac{E_e - \phi_n}{kT}\right)[cm^{-3}eV^{-1}]$	Complementary electron density at energy E_e
$\bar{p}(E_h) = p(E_h) \exp\left(\frac{\phi_p - E_h}{kT}\right)[cm^{-3}eV^{-1}]$	Complementary hole density at energy E_h
ϕ_n	Quasi-Fermi level for electrons
ϕ_p	Quasi-Fermi level for holes
$T[K]$	Absolute temperature
k	Boltzmann's constant
h	Planck's constant
$\hbar$	Reduced Planck's constant
q	Electron charge
ν	Photon frequency

Table 1.1: Definition of relevant parameters.

cause high recombination in the transition region. It is interesting to observe that Shockley predicts for this case the dependence of current I on half the applied voltage V. This will not happen for the laser diode. The reason is the quantum size of the recombination layer that makes the concept of charge density gradients meaningless.

The listed relations allow to write the joint densities that enter all processes of light emission and absorption as

$$\begin{cases} p_\nu n_\nu = \dfrac{N_\nu^2}{f_\nu^2} \\ \\ \bar{p}_\nu \bar{n}_\nu = p_\nu n_\nu \exp\left(\dfrac{h\nu - qV}{kT}\right) \end{cases} \tag{1.6}$$

Where

$$N_\nu^2 = g_e(E_e) g_h(E_h)\big|_{E_e - E_h = h\nu} \tag{1.7}$$

is the joint density of states for an optical transition at frequency ν, when the k-selection rule holds, and

$$\begin{aligned} f_\nu^2 = \left[\exp\left(\frac{h\nu - qV}{kT}\right) + 2\exp\left(\frac{h\nu - qV}{2kT}\right) cosh(\epsilon) + 1\right] \rightarrow \\ \xrightarrow[\epsilon \approx 0]{} \left[\exp\left(\frac{h\nu - qV}{2kT}\right) + 1\right]^2 \end{aligned} \tag{1.8}$$

with

$$\epsilon = \frac{(E_e + E_h) - (\phi_n + \phi_p)}{2kT} \tag{1.9}$$

The limit in (1.8), calculated for vanishing values of ϵ, links the current version of the model to the previous ones, and should be discussed. Referring to fig.1.2, it should be clear that the term $(E_e + E_h)/2$ represents the energy level midway between the electron and hole energies in the given transition, while $(\phi_n + \phi_p)/2$ is the mean value of the quasi-Fermi levels. Their difference is strictly null only for symmetrical bands (not necessarily parabolic), in which case both mean values are separately null. For asymmetric bands this is no more true, although it is difficult to estimate the difference at a glance.

Anyway, the approximation of symmetric bands makes many of the next results intuitively evident, while the exact formulation renders them physically sound. For this reason, most of the following part of the chapter will show both versions whenever possible and advisable.

The role of a non-null ϵ will be discussed in Appendix A, to point out the effects of the band asymmetry, and also of valence sub-bands, on the several results that are going to be shown.

Another point that needs to be clarified deals with dimensions of the joint densities. This is the goal of Appendix B.

1.1.2 Rate and Balance

1.1.2.1 Equilibrium

The most convenient starting point is the equilibrium state, when *qV=0*. Here the century-old Einstein's treatment of the black-body spectrum still holds as a roadmap [4, 5].

Let us add the suffix 0 to the densities of electrons and holes and introduce the photon density $\phi_{0\nu}$ at equilibrium, at frequency ν.

When one specializes the Einstein approach to the black-body to the case of a semiconductor at equilibrium, the upward and downward transitions from the conduction to the valence band and the reverse process (photon absorption) give rise to rates that balance according with

$$A_{CV} p_{0\nu} n_{0\nu} + B_{CV} p_{0\nu} n_{0\nu} \phi_{0\nu} - B_{VC} \bar{p}_{0\nu} \bar{n}_{0\nu} \phi_{0\nu} = 0 \tag{1.10}$$

where A_{CV},B_{CV} and B_{VC} are coefficients, not depending on temperature, referring respectively to photon spontaneous emission, stimulated emission, and absorption. Because of (1.6), at equilibrium

$$\bar{p}_{o\nu} \bar{n}_{0\nu} = p_{0\nu} n_{0\nu} \exp\left(\frac{h\nu}{kT}\right) \tag{1.11}$$

and then one has

$$A_{CV} + B_{CV} \phi_{0\nu} - B_{VC} \phi_{0\nu} \exp\left(\frac{h\nu}{kT}\right) = 0 \tag{1.12}$$

Exactly as in the Einstein's treatment, for increasing temperatures the exponential approaches unity, the photonic density increases (Stefan's law), but the coefficients remain unchanged. This leads to identify $B_{CV} = B_{VC}$ and then to rename

$$\begin{cases} B \equiv B_{CV} = B_{VC} \\ A \equiv A_{CV} \end{cases} \tag{1.13}$$

and then

$$\phi_{0\nu} = \frac{A}{B} \frac{1}{\exp\left(\frac{h\nu}{kT}\right) - 1} \tag{1.14}$$

The usual way to proceed in the treatment of the black-body radiation will allow to identify the ratio

$$\frac{A}{B} = \frac{8\pi\nu^2}{c^3} \tag{1.15}$$

which gives back the Planck's formula for the power density u_ν per unit frequency

$$u_\nu \equiv \phi_{0\nu} h\nu = \frac{8\pi\nu^2}{c^3} \frac{h\nu}{\exp\left(\frac{h\nu}{kT}\right) - 1} \tag{1.16}$$

For the scopes of the current study it will be sufficient to recognize that

$$\frac{A}{B} = \phi_{0\nu} \exp\left(\frac{h\nu}{kT}\right) - 1 \tag{1.17}$$

1.1.2.2 The rate equation

Moving to the non-equilibrium steady state, the balance must introduce the possibility that a net flux of photons enters or leaves the system. A net incoming flux will be here neglected, while an escape term is introduced. This term must be a rate, proportional to the photon density through a factor with the dimensions of the reciprocal of a time, that assumes the meaning of the mean permanence time τ_c. This net escape rate must vanish at equilibrium, and then the balance equation for the steady state reads as

$$Ap_\nu n_\nu + Bp_\nu n_\nu \phi_\nu - Bp_\nu n_\nu \exp\left(\frac{h\nu - qV}{kT}\right)\phi_\nu - \frac{\phi_\nu - \phi_{0\nu}}{\tau_c} \tag{1.18}$$

The solution of this rate equation is a function $\phi_\nu(V)$ that will be explicitly calculated in the next subparagraph. Anyway, some general considerations can be done since now:

a)The last term, when multiplied by the photon energy $h\nu$ and the volume V_{ol} of the cavity, and integrated over frequencies, represents the total emitted optical power P_{TOT}, proportional to the measured optical power P_{OUT}, one of the measurable quantities for a real laser diode.

b)The sum of the first three terms (equated, because of the balance, again by the last term) is the net number of radiative recombination events, and then, once multiplied by the electron charge q and the volume V_{ol} of the cavity, and summed over frequencies, gives the net light-producing current I_{ph}.

c)Any other current that will be introduced for considering non-radiative phenomena *inside the active layer* will share the same voltage V.

It follows that the solution of the rate equation will supply the link between the voltage V, the total current I and the emitted optical power P of the ideal laser diode, as the next subparagraphs will demonstrate.

The solution itself will show, as obviously expected, that the photon density ϕ_ν increases with increasing bias qV. It follows that the ratio between the stimulated and the spontaneous emission

$$\frac{R_{st}}{R_{sp}} = \frac{\phi_\nu}{A/B} = \frac{\phi_\nu}{\phi_{0\nu}\left[\exp\left(\frac{h\nu}{kT}\right)\right]} \tag{1.19}$$

will rapidly increase with bias, which legitimates neglecting the spontaneous term at high injection in many textbooks. Anyway, it is the spontaneous emission that provides the stimulus for the stimulated one, and also mathematically that term will be crucial for achieving the solution. Also the transparency condition $R_{st} = R_{abs}$, that is by definition the injection level that exactly balances stimulated emission and absorption, is immediately identified with:

$$qV = h\nu \tag{1.20}$$

Before proceeding with its solution, some further handling of the equation itself will lighten other important features.

1.1.3 Gain and losses

Dividing all terms in the rate equation by the group velocity of light ν_g and the photon density ϕ_ν, one transforms a balance of rates $\frac{\partial \phi_\nu}{\partial t} = 0$ into a balance of gain and loss terms

$$\frac{1}{\partial \phi_\nu} \frac{\partial \phi_\nu}{\partial (\nu_g t)} \equiv \frac{1}{\partial \phi_\nu} \frac{\partial \phi_\nu}{\partial x} = 0 \tag{1.21}$$

It is convenient here to partially explicit the joint densities and write

$$\left[\frac{A}{B}\frac{B}{\nu_g}\frac{N_\nu^2}{f_\nu^2}\frac{1}{\phi_\nu}\right] + \left[\frac{B}{\nu_g}\frac{N_\nu^2}{f_\nu^2}\right] - \left[\frac{B}{\nu_g}\frac{N_\nu^2}{f_\nu^2}\exp\left(\frac{h\nu - qV}{kT}\right)\right] - \left[\frac{1}{\nu_g \tau_c}\left(1 - \frac{\phi_{0\nu}}{\phi_\nu}\right)\right] = 0 \tag{1.22}$$

where the function f_ν^2 represents the denominator of the equation of the joint density of charge, as given by (1.8).

The unessential square brackets in the modified balance equation (1.22) have the cosmetic role to put into evidence the two gain terms (positive sign) and the two loss terms (negative sign).

Starting with the second term in (1.22), it is possible to represent the *pure* gain (*net* gain will be defined, later on, as the difference between the second and third term) and introduce the "gain coefficient":

$$g_m = \frac{B N_\nu^2}{\nu_g} \tag{1.23}$$

This term is obviously a function of the frequency ν, and embeds all information about the density of states, and then vanishes for any transition involving forbidden states in the band-gap. It also appears in the first and third term of (1.22), and is then a good candidate for a more compact and physically clear formulation of the balance equation itself. Moreover, considering the last term in (1.22)

$$\left[\frac{1}{\nu_g \tau_c}\left(1 - \frac{\phi_{0\nu}}{\phi_\nu}\right)\right] \tag{1.24}$$

It gives account for escape phenomena, and even for very low injection levels is practically a constant at a given frequency ν, that we will here define as the total loss coefficient

$$\alpha_T = \frac{1}{\nu_g \tau_c} \tag{1.25}$$

We can now rewrite the gain-loss equation (1.22) as

$$\left[\frac{A}{B}\frac{g_m}{f_\nu^2}\frac{1}{\phi_\nu}\right] + \left[\frac{g_m}{f_\nu^2}\right] - \left[\frac{g_m}{f_\nu^2}\exp\left(\frac{h\nu - qV}{kT}\right)\right] - \left[\alpha_T\left(1 - \frac{\phi_{0\nu}}{\phi_\nu}\right)\right] = 0 \tag{1.26}$$

and proceed with

a) the first term, that is a rather unusual gain term, being related to those spontaneous transitions that can indeed add photons, but without any coherence with the laser radiation that is under investigation. It is then usually omitted, but this hides the balance between creation and destruction of photons, that is simple in itself. It is interesting to observe that neglecting the first term, as usual in many textbooks, simply inhibits the solution of the equation.

b) The algebraic sum of the two central terms represents all light-induced transitions: spontaneous emission and optical absorption, and is the definition of the gain g.

c) The last term, that represents escape losses, has the important role to link the solution to measurable parameters as current and optical power, as pointed out in comments a) and b) to (1.18). The issue of practical integration over frequencies will be considered in more detail in the following.

Finally, considering (1.23) and (1.25), this allows to rewrite the steady-state rate equation (1.18) as:

$$g_m \frac{\exp\left(\frac{h\nu}{kT}\right) - 1}{\left[1 + \exp\left(\frac{h\nu - qV}{2kT}\right)\right]^2} \phi_{0\nu} + g_m \frac{1 - \exp\left(\frac{h\nu - qV}{kT}\right)}{\left[1 + \exp\left(\frac{h\nu - qV}{2kT}\right)\right]^2} \phi_\nu = \alpha_T \left(\phi_\nu - \phi_{0\nu}\right) \tag{1.27}$$

Before proceeding with the solution of the rate equation, some comments should be given about gain, its saturation and the way to take account for vertical losses, which means what is known as vertical confinement.

1.1.3.1 Gain limits

The explicit form for the gain function, following the previous comments, is given by (1.28)

$$\begin{aligned} g &= \frac{g_m}{f_\nu^2} \left[1 - \exp\left(\frac{h\nu - qV}{kT}\right)\right] = \\ &= g_m \frac{1 - \exp\left(\frac{h\nu - qV}{kT}\right)}{\left[\exp\left(\frac{h\nu - qV}{kT}\right) + 2\exp\left(\frac{h\nu - qV}{2kT}\right)\cosh(\epsilon) + 1\right]} \xrightarrow[\epsilon \approx 0]{} g_m \tanh\left(\frac{qV - h\nu}{4kT}\right) \end{aligned} \tag{1.28}$$

At any given voltage V, the spectral gain combines the high-pass filter of the joint density of states embedded in g_m and the *tanh* function that monotonically decreases for increasing frequencies. Positive gain is then restricted to a frequency range $E_g < h\nu < qV$, which obviously implies $qV > E_g$.

When one assumes a stepwise density of states, corresponding to an ideal Quantum Well, without broadening, and compares with one that includes broadening by means of a suitable Lorentzian lineshape, fig.1.3 is obtained, whose parameters (bandgap, bias and vertical scale) have been adjusted in order to compare with fig.4.8 in ref. [31].

This result in (1.28) agrees with ref. [33], Ch.11.4.1, once one recalls the relationship between the voltage V and the quasi-Fermi levels and recalls (1.6) for describing the joint charge densities. Anyway, this formally allows bias to increase unlimitedly, which is not the case, as the next sub-subparagraph will show and experience tells. This leads to the conclusion, also given in the previous reference,

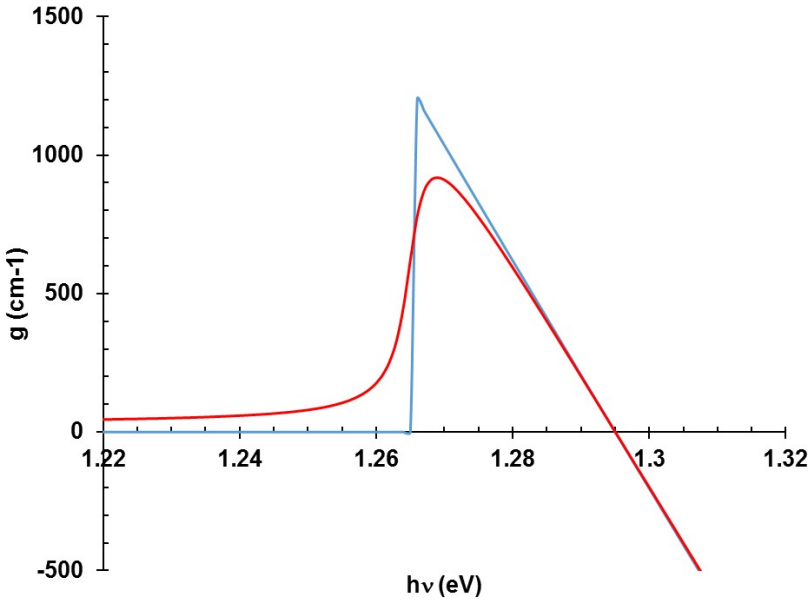

Figure 1.3: The gain curves from (1.34). Blue line: ideal QW. Red line: Lorentzian-broadened

that the upper limit for gain is its own lower limit with a positive sign. This is mathematically correct but physically wrong.

This last point is made clear when going back to modal gain, that is specifying a single frequency. Gain g, represented by the second and third term of (1.34), balances with the first and fourth ones.

$$g = \left[\alpha_T \left(1 - \frac{\phi_{0\nu}}{\phi_\nu}\right)\right] - \left[\frac{A}{B}\frac{g_m}{f_\nu^2}\frac{1}{\phi_\nu}\right] \tag{1.29}$$

This expression hides the transparency condition that just leads g to vanish, but allows to find the upper and lower limit for the gain itself, when the photon density ϕ_ν respectively approaches ∞ or $\phi_{0\nu}$. It should be evident that f_ν^2 will always remain finite for any positive bias qV, and that, at $qV = 0$, for any permitted photon energy

$$\frac{A}{B}\frac{1}{\phi_{0\nu}}\frac{1}{f_{\nu,qV=0}^2} = \frac{\exp\left(\frac{h\nu}{kT}\right) - 1}{\exp\left(\frac{h\nu}{kT}\right) + 2\exp\left(\frac{h\nu}{2kT}\right)\cosh(\epsilon) + 1} \approx 1 \tag{1.30}$$

it then follows:

$$\begin{cases} g \xrightarrow[\phi_\nu \to \phi_{0\nu}]{} -g_m \\ g \xrightarrow[qV \to 0]{} 0 \\ g \xrightarrow[\phi_\nu \to \infty]{} \alpha_T \end{cases} \tag{1.31}$$

The lower, negative, limit of gain $-g_m$ results then strictly related to the sole material properties, while the upper limit α_T is mostly due to device-specific issues.

This upper limit, on the other hand, indicates that gain saturates at a level g_{th} exactly balancing the total losses α_T, as expected by the self-sustentation condition of a laser cavity after a round trip of the radiation.

Would an expression of gain be available as a function of the injection current I, (1.31) would implicitly define the threshold current I_{th} below which gain changes with injection, and above which remains clamped at its threshold value

$$g(I_{th}) = \alpha_T \tag{1.32}$$

The search for such $g(I)$ equation has been concluded only very recently, and the whole next paragraph will be spent on it.

1.1.3.2 Total losses and confinement factor

Usually it is not always clearly reminded that "losses" means anything loosing photons, but NOT including absorption due to generation of electron-hole pairs, that is embedded in the concept itself of gain, and leads it to be negative below threshold. On the other hand, any other kind of absorption, as the one caused for instance by free electrons, must merge into a separate loss term, that will then give account of such internal losses in conjunction with any photon escaping mechanism.

A private discussion with the Authors of the main reference papers [1–3], not yet published, focused on the unsatisfying use of a confinement factor Γ as a multiplying term of the gain at threshold g_{th}, to give account of the lateral and transversal losses. They could be well taken into account in the same additive way that leads to sum the mirror loss term.

On the contrary, the use of Γ as a multiplier comes from a first-order approximation of the effective-index method [Appendix A5 of [31]] and perturbs the simplicity of the gain-loss balance. Would losses α_T be defined as the addictive contribution of a purely internal mechanism (whatever could be) α_i, a vertical escape α_V, a lateral escape α_L and mirror escape α_m

$$\alpha_T = \alpha_i + \alpha_V + \alpha_L + \alpha_m \tag{1.33}$$

The simple definition

$$\Gamma = 1 - \frac{\alpha_V + \alpha_L}{g_{th}} = 1 - \frac{\alpha_V + \alpha_L}{\alpha_T} \tag{1.34}$$

would make the standard (1.32) formula

$$\Gamma g_{th} = \alpha_i + \alpha_m \tag{1.35}$$

consistent with the balance $g_{th} = \alpha_T$, provided one reminds that $\alpha_i + \alpha_m \neq \alpha_T$ defines another set of "total losses". Anyway, such definition of Γ safely holds at and beyond threshold, but remains questionable at lower injection, when spontaneous emission should not be neglected. Being one of the result discuss in this chapter the continuous definition of measurable DC characteristics along the full below/above threshold ranges, the additive form (1.33) for losses, that excludes the use of Γ, will be used.

1.1.4 Solving the rate equation

The rate equation, after the introduction of the ratio:

$$R = \frac{\alpha_T}{g_m} \tag{1.36}$$

reads as

$$\frac{A}{B} + \left[1 - \exp\left(\frac{h\nu - qV}{kT}\right)\right]\phi_\nu - Rf_\nu^2(\phi_\nu - \phi_{0\nu}) = 0 \tag{1.37}$$

Some further manipulation (putting $\phi_\nu = (\phi_\nu - \phi_{0\nu}) + \phi_{0\nu}$ in the second term), and the recall of the explicit expressions for A/B (1.17) and f_ν^2 (1.8), lead to

$$\begin{aligned}
\phi_\nu - \phi_{0\nu} &= \phi_{0\nu}\frac{\exp\left(\frac{qV}{kT}\right) - 1}{Rf_\nu^2 \exp\left(\frac{qV - h\nu}{kT}\right) + \left[1 - \exp\left(\frac{qV - h\nu}{kT}\right)\right]} = \\
&= \phi_{0\nu}\frac{\exp\left(\frac{qV}{kT}\right) - 1}{R\left[\exp\left(\frac{qV - h\nu}{kT}\right) + 2\exp\left(\frac{qV - h\nu}{2kT}\right)\cosh(\epsilon) + 1\right] + \left[1 - \exp\left(\frac{qV - h\nu}{kT}\right)\right]} \approx \\
&\approx \phi_{0\nu}\frac{\exp\left(\frac{qV}{kT}\right) - 1}{R\left[\exp\left(\frac{qV - h\nu}{2kT}\right) + 1\right]^2 + \left[1 - \exp\left(\frac{qV - h\nu}{kT}\right)\right]}
\end{aligned} \tag{1.38}$$

It predicts that

1. for any bias lower of, and not too close to, the transparency condition $qV = h\nu$, all exponentials in the denominator are negligible when compared with unity

$$\phi_\nu - \phi_{0\nu}\big|_{qV<h\nu} \approx \phi_{0\nu}\frac{\exp\left(\frac{qV}{kT}\right) - 1}{R + 1} \tag{1.39}$$

2. At the transparency

$$\phi_\nu - \phi_{0\nu}|_{tr} = \phi_{0\nu}\frac{\exp\left(\frac{qV}{kT}\right) - 1}{4R\cosh^2\left(\frac{\epsilon}{2}\right)} = \frac{8\pi\nu^2}{c^3}\frac{1}{4R\cosh^2\left(\frac{\epsilon}{2}\right)} \xrightarrow[\epsilon\approx 0]{} \frac{8\pi\nu^2}{c^3}\frac{1}{4R} \tag{1.40}$$

3. The denominator vanishes, leading to infinite density and infinite energy at a threshold voltage

$$qV_{th} = h\nu + kT\ln\left(\frac{\sqrt{1 + R^2\sinh^2(\epsilon)} + R\cosh(\epsilon)}{1 - R}\right)^2 \xrightarrow[\epsilon\approx 0]{} h\nu + kT\ln\left(\frac{1 + R}{1 - R}\right)^2 \tag{1.41}$$

The considerations above look at the photon density at a given frequency as a function of the applied voltage qV.

The same result can be conversely considered as the spectral distribution at a given voltage. Of course, parameters as the actual densities of states (included in the g_m coefficient) must be specified. They give account for the forbidden states inside the band gap, and then for the minimum allowable frequency $h\nu \geq E_g$. In the same way, the escape coefficient must be defined as a function of frequency, to take into account for instance the resonant modes of a Fabry-Perot cavity.

In any case, among the many possible frequencies, only one leads to the lowest value of qV_{th}: it will be the ultimate threshold condition for the whole device, because any further voltage increase would require infinite energy. At the same time, that specific frequency will first reach positive net gain and will soon stimulate and drain all new recombination events: it will be the peak frequency for the laser diode.

1.1.5 Current and power

Two quantities are related to the escape rate given by the last term in (1.18), as pointed out commenting that equation: the radiative current I_{ph}, responsible for all and sole the photon emission, and the total emitted optical power P_{TOT}.

$$\begin{cases} I_{ph} = qVol \displaystyle\int_0^\infty \frac{\phi_\nu - \phi_{0\nu}}{\tau_c} d\nu \\ \\ P_{TOT} = Vol \displaystyle\int_0^\infty h\nu \frac{\phi_\nu - \phi_{0\nu}}{\tau_c} d\nu \end{cases} \tag{1.42}$$

Both receive contributions from all frequencies in the emitted spectrum, and then the problem arises of integrating over frequencies. Many factors should be taken into account, all of which should be embedded into the frequency dependence of τ_c:

1. The intrinsic (homogeneous and inhomogeneous [30–32] lineshape broadening. This changes the ideal step function for the 2D size of the Quantum Well into a smooth function that is usually considered by convolving the ideal function with some suitable peaked function, as a Gaussian, a Lorentzian or other.

2. The frequency selection introduced in single mode devices by DFB (Distributed Feedback) gratings, DBR (Distributed Bragg Reflector) structures at the side of the cavity, or external devices, as adjustable sets of Etalon filters in tunable lasers.

3. In multi-mode devices, the resonant function introduced by the Fabry-Perot cavity.

Anyway, in practical measurements of real devices, both current and power are measured with an accuracy not exceeding the percent. This is, roughly, the inaccuracy that one could obtain when considering any of the possible frequencies,

allowed by the spontaneous emission spectrum, with respect to the peak frequency ν_0 at which the device will first reach threshold. This means that (1.42) can be evaluated as:

$$\begin{cases} I_{ph} = q \cdot Vol \cdot \hat{\nu} \cdot \dfrac{\phi_\nu - \phi_{0\nu_0}}{\tau_c} \\ \\ P_{TOT} = Vol \cdot \hat{\nu} \cdot h\nu \cdot \dfrac{\phi_\nu - \phi_{0\nu_0}}{\tau_c} \end{cases} \tag{1.43}$$

where $\hat{\nu}$ is an integration constant, with the dimensions of a frequency, that is determined by the actual line-shape of the spectrum peaked at ν_0.

Would I_{ph} be the only current flowing in the device, when one defines the output power P_{OUT} as the fraction α_m/α_T of the total emitted power P_{OUT} (where α_m is the loss for the sole escapes from the laser side faced to the detector system ([31], Ch.2), one would obtain the simple relationship

$$P_{OUT} = \frac{h\nu}{q} I_{ph} \frac{\alpha_m}{\alpha_T} \tag{1.44}$$

This is obviously not the case, but (1.44) is the starting point for the final power-current characteristics, once I_{ph} is expressed in term of the total current I.

1.1.5.1 The current I_{ph}

Substituting the escape time τ_c in (1.43) with the loss coefficient α_T by means of (1.25):

$$I_{ph} \approx q \cdot Vol \cdot \nu_g \cdot \hat{\nu} \cdot \alpha_T [\phi_\nu - \phi_{0\nu}] \tag{1.45}$$

one can use the solution (1.38) of the rate equation to obtain:

$$I_{ph} = 4I_{ph0}R \frac{\exp\left(\dfrac{qV}{kT}\right) - 1}{R\left[\exp\left(\dfrac{qV - h\nu}{kT}\right) + 2\exp\left(\dfrac{qV - h\nu}{2kT}\right)\cosh(\epsilon) + 1\right] + \left[1 - \exp\left(\dfrac{qV - h\nu}{kT}\right)\right]} \rightarrow$$
$$\xrightarrow[\epsilon \approx 0]{} 4I_{ph0}R \frac{\exp\left(\dfrac{qV}{kT}\right) - 1}{R\left[\exp\left(\dfrac{qV - h\nu}{2kT}\right) + 1\right]^2 + \left[1 - \exp\left(\dfrac{qV - h\nu}{kT}\right)\right]} \tag{1.46}$$

where the frequency ν must now be considered the peak frequency $\nu = \nu_0$ and I_{ph0} is a constant with the dimensions of a current that is not dependent on α_T:

$$I_{ph0} = [q \cdot Vol \cdot \nu_g \cdot \hat{\nu} \cdot g_m] \tag{1.47}$$

In the sub-threshold range one has $qV \ll h\nu$, which makes both exponential in the denominator much smaller than unity, and then:

$$I_{ph} \approx \left(I_{ph0} \frac{R}{R+1}\right)\left[\exp\left(\frac{qV}{kT}\right) - 1\right] \tag{1.48}$$

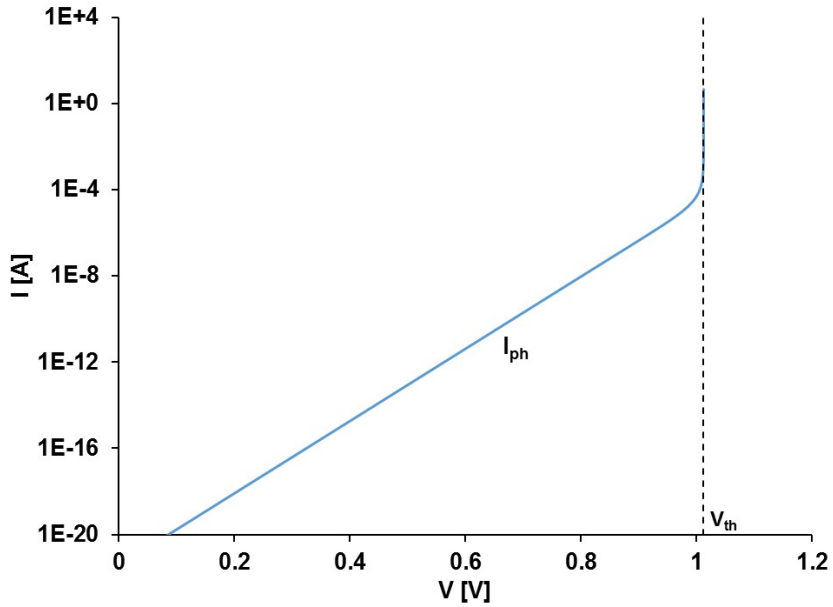

Figure 1.4: The bimodal behavior of the purely radiative current I_{ph}

It is a perfect Shockley-like behavior, where

$$I_{sh0} = I_{ph0}\frac{R}{R+1} \tag{1.49}$$

plays the role of the saturation current.

The dependence on R has been kept into evidence, instead of embedding it in a simpler definition of I_{ph0}, because of the relevance of the optical losses in general.

The vanishing limit of such "saturation current" for very low losses should be not surprising: no loss means infinite time for photon escape from the cavity, that, in turn, needs no current to sustain the steady state.

On the opposite side, high losses lead this term to saturate at I_{ph0}, but also, for $R > 1$, they cause the disappearance of the threshold voltage, (1.41): the device never achieves the transition to the laser regime, and only is allowed to operate as a LED.

In summary, it is possible now to plot (fig.1.4) the forward DC electrical characteristics of the ideal laser diode and also graphically appreciate the sub-threshold Shockley-like behavior, the voltage clamp at V_{th} at increasing current and the transition between the two regimes.

It is interesting to check that if one neglects the sole stimulated emission in the original balance equation, one gets the very same Shockley-like $I_{ph}(V)$ characteristics, but no voltage clamp at any current. This means that any other recombination mechanism, not stimulated by photons, will not be able to create the voltage clamp displayed in fig.1.4.

1.1.5.2 The non-radiative current I_{nr}

The peculiar behavior of I_{ph}, with its striking bimodal characteristics, that strictly follow the ideal Shockley equation for $V < V_{th}$ and then sharply clamps at

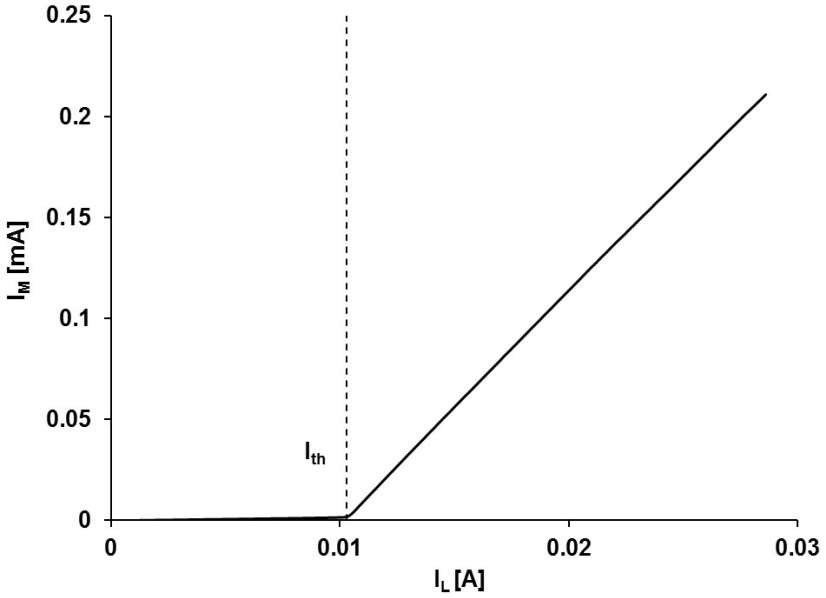

Figure 1.5: Experimental $I_M(I)$ curve on an InP-based edge emitter at 1310 nm

$V = V_{th}$ at higher injection, should be compared with the experimental measurements.

Two currents are available: the total current I and the monitor current I_M, that is usually represented as a measurement of the externally collected optical power P_{OUT}. It should be evident that the experimental I_M is also proportional to the theoretical I_{ph}.

At the same time, it is evident form experiments (fig.1.5) that the two currents are not proportional, otherwise the plot of $I_M(I)$ would be a straight line starting from the origin, as predicted by (1.44). A well-defined threshold value I_{th} separates two regions that look mostly linear, with largely different slopes. The conclusion is that an extra current, non-radiative (all optical emission is collected into I_{ph}), and here indicated as I_{nr}, does exist.

Besides such evident and well known conclusion, a second important one can be drawn when one plots (fig.1.6) both I and $I_M(I)$, versus the reduced voltage, that is using $V - R_s I$ at the abscissa, where V and I are the externally applied and measured voltage and current of the laser diode, and R_s is its overall series resistance, easily obtained by the dV/dI curve ([31], Ch.2.8.5).

The many details of this figure will be considered in the following. A first comment must be given for the area A in fig.1.6. It includes all the I, I_M pairs that led to fig.1.5. The area on the left of region A belongs to the sub-mA range, where current still spreads laterally outside the active area and also small shunting currents are often detected. This current can be easily modeled [2] for a ridge structure, up to achieve the perfect fit of the experimental data by introducing a distributed structure made of infinitesimal diodes and resistors, parallel to the active region. A short description of such currents is given in the next sub-subparagraph 1.1.5.5. What is important is the conclusion that all currents dominating the sub-mA range become negligible entering the area A of fig.1.6: in that plot area, all the measured currents belong to the active region of the laser diode.

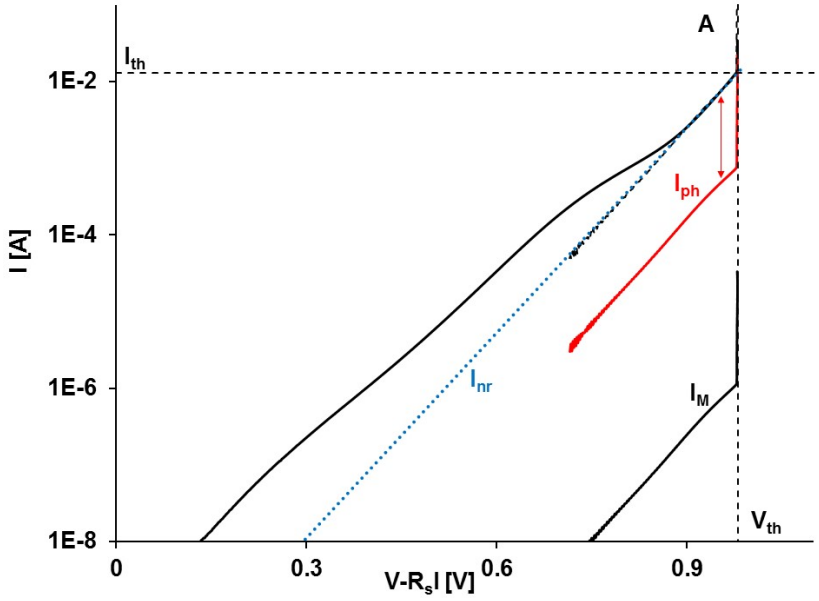

Figure 1.6: Experimental current-voltage characteristics plotted vs. the reduced voltage $V - R_s I$ for the same device of fig.1.5.

Focusing then on the sole area A of fig.1.6, the two experimental curves I and I_M, clearly display the same voltage clamp at some $V = V_{th}$, and also the same slope in the sub-threshold domain, where the logarithmic vertical scale reveals the perfect and identical exponential dependence of both currents on the same voltage V.

Now, such a kind of exponential I(V) is likely to be related to diffusion/recombination phenomena that are common in standard pn junctions. None of them is able to introduce the sharp threshold displayed by I_{ph}, that then must be considered the sole responsible for the observed voltage clamp. This means that the voltage clamp introduced by the sole I_{ph} forces also the voltage driving I_{nr} to clamp. In other words, any model attributing separately I_{ph} and I_{nr} to some equivalent circuital blocks must connect those blocks in *parallel*.

I_{nr}, it is then a Shockley-like current typical of general diodes and then monotonically increases with the same V that drives I_{ph}. Because of the experimental evidence, I_{nr} dominates over I_{ph} for $V < V_{th}$, and then clamps at $V = V_{th}$. This leads to estimate the threshold current I_{th} as that clamp value:

$$I(V_{th}) \approx I_{nr}(V_{th}) \tag{1.50}$$

The next sub-subparagraph 1.1.5.5 will demonstrate this conclusion to be not a simple estimation, but an exact rule.

But in fig.1.6 one discovers another intriguing feature: I and I_{ph} are parallel (that means, proportional) in the sub-threshold region A, up to the point that if one vertically shifts I_{ph} upwards (dashed line), it coincides with I.

This simply means that, for $V < V_{th}$, also I_{nr} behaves as I_{ph}, and then:

$$I_{nr} = I_{nr0}\left[\exp\left(\frac{qV}{kT}\right)\right] \tag{1.51}$$

Equation (1.51), assuming the same voltage dependence of I_{nr} and I_{ph} in the sub-threshold range, on one side obeys the indication of experiments, but on the other confirms what ref. [31] states when introducing its eq.2.41 (the threshold current equation), that is that bimolecular (electron-hole) recombination dominates for the sub-threshold range, up to threshold. In case, the novelty is that (1.48) tells the same for $V < V_{th}$.

It follows that the total current is:

$$I(V) = I_{nr}(V) + I_{ph}(V) = I_{nr0}\left[\exp\left(\frac{qV}{kT}\right) - 1\right] + \\ + I_{ph0} 4R \frac{\exp\left(\frac{qV}{kT}\right) - 1}{R\left[\exp\left(\frac{qV - h\nu}{kT}\right) + 2\exp\left(\frac{qV - h\nu}{2kT}\right)\cosh^2(\epsilon) + 1\right] + \left[\exp\left(\frac{qV - h\nu}{kT}\right)\right]} \tag{1.52}$$

Some relevant values can be considered: At transparency ($qV = h\nu$)

$$I_{nr,tr} = I_{nr0}\left[\exp\left(\frac{h\nu}{kT}\right) - 1\right] \approx I_{nr}\exp\left(\frac{h\nu}{kT}\right) \tag{1.53}$$

At threshold (1.41):

$$I_{th} = I_{nr}(V_{th}) = I_{nr0}\left[\exp\left(\frac{qV_{th}}{kT}\right) - 1\right] \approx I_{nr0}\exp\left(\frac{qV_{th}}{kT}\right) = \\ = I_{nr0}\exp\left(\frac{h\nu}{kT}\right)\left(\frac{\sqrt{1 + R^2\sinh^2(\epsilon)} + R\cosh(\epsilon)}{1 - R}\right)^2 \tag{1.54}$$

That can be written as:

$$I_{th} = I_{th0}\left(\frac{h\nu}{kT}\right)\left(\frac{\sqrt{1 + R^2\sinh^2(\epsilon)} + R\cosh(\epsilon)}{1 - R}\right)^2 \underset{\epsilon\approx 0}{\approx} I_{th0}\left(\frac{1 + R}{1 - R}\right)^2 \tag{1.55}$$

where the (ideal) zero-loss ($R = 0$) minimum threshold current I_{th0} is identified as the value of I_{nr} at transparency

$$I_{th0} = I_{nr0}\exp\left(\frac{h\nu}{kT}\right) = I_{nr,tr} \tag{1.56}$$

Also fig.1.5 is now easily obtained by calculating separately $I_{ph}(V)$, that is proportional to I_M, and $I(V)$ and then plotting $I_{ph}(V)$. The analytic expression for that last curve can also be obtained by eliminating qV from $I_{ph}(V)$ and $I(V)$ by means of (1.46) and (1.52), that is more easily obtained in closed form as $I(I_{ph})$. Being this calculation mostly the same that leads to the more familiar $P_{OUT}(I)$, because of the proportionality of the monitor current I_M to the measured optical power P_{OUT}, this will considered in detail in the next sub-subparagraph 1.1.5.5.

Anyway, the striking difference of (1.55) with any other formulas for I_{th} known from literature asks for a final consideration. It will be sufficient to refer to the approximation $\epsilon = 0$ to fully appreciate the main conclusion.

The dominance of the non-radiative current in the sub-threshold range makes (1.56), specific for that component, about, say, 1% different from the value I_{tr} of the total I at transparency, so that (1.55) could be written, within the available accuracy limits and making R explicit by means of (1.36), as

$$I_{th} = I_{tr}\left(\frac{1+\dfrac{\alpha_T}{g_m}}{1-\dfrac{\alpha_T}{g_m}}\right)^2 \tag{1.57}$$

This should be compared with the corresponding empirical formula, based on the logarithmic model for gain available in literature ([31], table 4.5, two-parameter gain-current curve fits)

$$g = g_0 \ln\left(\frac{J}{J_{tr}}\right) \equiv g_0 \ln\left(\frac{I}{I_{tr}}\right) \tag{1.58}$$

where the ratio of the current densities J has been transformed into the corresponding ratio of currents, and g_0 is an empirical constant. From the reference [34], the calculated current at threshold gives:

$$I_{th} = I_{tr} \exp\left(\frac{\alpha_T}{g_0}\right) \tag{1.59}$$

At zero-loss (1.57) and (1.59) coincide, which confirms for both model the prediction that the minimum (ideal) threshold current is the value of the total current (or of its dominating non-radiative component) at transparency.

But the surprising result is that if one assumes $g_m = 4g_0$, the power expansion of (1.57) and (1.59) near the value $\alpha_T/g_0 = 0$ coincide at the zero, first and second order. The difference achieves 1% for values of that ratio as high as about 0.7, which would correspond to a real threshold current I_{th} twice its value I_{tr} at zero losses, a case that never occurs in well-designed real devices.

What is even more interesting is that the empirical quantity g_0 now assumes a physical significance. When one goes back to (1.26) and considers separately the second and third term (pure gain and absorption) at transparency, within the approximation $\epsilon = 0$ here applied, their absolute values are not only equal, but each of them is exactly $g_m/4 = g_0$. The threshold is then completely related to the sole transparency condition and total optical losses.

The important novelty is that (1.57) tells that, beyond some loss level ($\alpha_T = g_m = 4g_0$), no current will be available to force the device to achieve threshold, which does not appear in (1.59).

1.1.5.3 Internal efficiency η_i

Fig.1.6 carries a last information: the explicit $I_{ph}(V - R_sI)$ curve, that up to now was only considered as proportional to the measurable monitor current $I_M(V - R_sI)$. This proportionality can be estimated as follows.

If the total current is $I = I_{nr} + I_{ph}$ and I_{nr} stops for for $I > I_{th}$, this means that the monitor current I_M, for $I > I_{th}$, must be $I_M = K(I - I_{th})$. Being I, I_{th} and I_M measurable, one gets the coupling constant K. This constant represents the total conversion efficiency that collects the transformation of I_{ph} into a photon flux, made of their partial loss traveling from the laser facet to the monitor diode and the back-conversion of light into current into the monitor diode. If one assumes negligible any focusing effect of the optical beam, K should be the same at any injection level, and then I_M directly measures I_{ph}:

$$I_{ph} = \frac{1}{K} I_M \tag{1.60}$$

This allows to draw $I_{ph}(V - R_s I)$, the so called *Trans-characteristic* [35] in fig.1.6 by upscaling $I_M(V - R_s I)$ by the factor $1/K$. Moreover, the difference $I - I_{ph}$ gives the non-radiative current I_{nr} that has such an important role in defining threshold.

Finally, the ratio between the photonic current I_{ph} and the total current I is, by definition, the internal efficiency η_i, that is then expected to be a constant only in the sub-threshold range, and then to approach unity for increasing current. This is confirmed by the previous results (it is here sufficient to apply the simplification $\epsilon = 0$):

$$\eta_i = \frac{I_{ph}}{I} = \frac{I_{ph0}}{I_{ph0} + I_{nr0} \dfrac{R\left[1 + \exp\left(\dfrac{qV - h\nu}{2kT}\right)\right]^2 + \left[1 - \exp\left(\dfrac{qV - h\nu}{kT}\right)\right]}{R}} \tag{1.61}$$

This is obviously not a constant. In the sub-threshold range $qV < h\nu$ it reduces (using also (1.49)) to

$$\eta_i\big|_{V<V_{th}} = \frac{I_{ph0}}{I_{ph0} + I_{nr0}\dfrac{R+1}{R}} = \frac{I_{ph0}}{I_{ph0} + I_{sh0}} \tag{1.62}$$

that is, as expected, the ratio between the "saturation currents" of the sole I_{ph} and of the total current I in their common Shockley regime. This result, that predicts a constant value of the internal efficiency for the sub-threshold range, agrees with the observation of the parallelism of I and I_{ph} in region A of fig.1.6. Anyway in laser regime, when the voltage clamps at its threshold value, it goes to unity

$$\eta_i\big|_{V=V_{th}} = 1 \tag{1.63}$$

Measuring efficiency as a function of the total current I, the value in (1.63) becomes an asymptotic limit smoothly approached by the experimental curve I_{ph}/I, because more and more current is required to slightly increase the (internal) voltage when the last approaches its threshold.

1.1.5.4 Optical power

The total emitted optical power P_{TOT} is proportional to the radiative current I_{ph}, as stated in (1.43).

If now α_m is the fraction of the total losses that exits the emitting mirror facet, and is the collection and conversion efficiency of the optical system, one has the measured optical power P_{OUT} as:

$$P_{OUT} = \frac{h\nu}{q}\eta_C I_{ph}\frac{\alpha_m}{\alpha_T} \tag{1.64}$$

The previous results on currents and voltage allow to find an analytic relationship between P_{OUT} and the total current I, possibly the most familiar tool in laser diode characterization. One can first express:

$$I_{ph} = [I - I_{nr}] = \left[I - I_{nr0}\exp\left(\frac{qV}{kT}\right)\right] \tag{1.65}$$

and then eliminate the voltage V by means of the previously found (1.58).

It is sufficient indeed to solve that equation for the voltage V to obtain a rather cumbersome analytic expression of $V(I_{ph})$

$$\begin{aligned}\exp\left(\frac{qV - h\nu}{2kT}\right) = \\ = \frac{I_{ph}R\cosh(\epsilon) + \sqrt{I_{ph}^2(1 + R^2\sinh^2(\epsilon)) + I_{ph}I_0R(1+R) + (I_0R)^2\exp\left(\frac{h\nu}{kT}\right)}}{I_0R + I_{ph}(1-R)}\end{aligned} \tag{1.66}$$

where we put for simplicity:

$$I_0 = I_{ph0}\exp\left(\frac{h\nu}{kT}\right) \tag{1.67}$$

Direct inspection shows that (1.66) correctly predicts that the voltage V vanishes for I_{ph} approaching 0, and that, on the contrary, it clamps at its threshold value, given by (1.41) for very large values of I_{ph}.

The expression (1.66) itself appears a little bit more friendly in the bias range where $\exp(qV/kT) \gg 1$:

$$\begin{aligned}qV = h\nu + kT\ln\left[\frac{\sqrt{1 + R^2\sinh^2(\epsilon) + \frac{I_0}{I_{ph}}R(1+R)} + R\cosh(\epsilon)}{1 - R + \frac{I_0}{I_{ph}}R}\right]^2 \underset{\epsilon\approx 0}{\approx} \\ \underset{\epsilon\approx 0}{\approx} h\nu + kT\ln\left[\frac{\sqrt{1 + \frac{I_0}{I_{ph}}R(1+R)} + R}{1 - R + \frac{I_0}{I_{ph}}R}\right]^2\end{aligned} \tag{1.68}$$

The proportionality between I_{ph} and P_{OUT} allows to replace the ratio I_0/I_{ph} with the ratio P_0/P_{OUT} by defining:

$$P_0 = \frac{h\nu}{q}\eta_C I_0 \frac{\alpha_m}{\alpha_T} \tag{1.69}$$

one has:

$$P_{OUT} = \frac{P_0}{I_0}\left\{ I - I_{th0}\left[\frac{\sqrt{1+R^2 sinh^2(\epsilon) + \frac{P_0}{P_{OUT}}R(1+R)} + R\cosh(\epsilon)}{1-R+\frac{P_0}{P_{OUT}}R}\right]^2\right\} \underset{\epsilon\approx 0}{\approx}$$
$$\underset{\epsilon\approx 0}{\approx} \frac{P_0}{I_0}\left\{ I - I_{th0}\left[\frac{\sqrt{1+\frac{P_0}{P_{OUT}}R(1+R)} + R}{1-R+dd\frac{P_0}{P_{OUT}}R}\right]^2\right\} \tag{1.70}$$

Where I_{th0} is defined according with the previous (1.56). It is, once again, a rather heavy formula.

Anyway, it deals with P_{OUT} and I in the full operative range of a laser diode, including the sub-threshold regime and the transition to the gain domain. It also embeds the threshold condition, and defines the threshold current that clearly appears when one lets P_{OUT} to increase in the right-hand side

$$P_{OUT} \xrightarrow[POUT\to\infty]{} \frac{P_0}{I_0}\{I - I_{th}\} = \frac{h\nu}{q}\eta_C(I - I_{th})\frac{\alpha_m}{\alpha_T} \tag{1.71}$$

with I_{th}, here calculated as the limit of the term in square brackets in (1.70) for large current and power, coincides with the expression given by (1.55). This was inferred in the previous subparagraph about currents, but here it finds its demonstration.

The full formula can be inverted, too, leading to an analytic form for $I(P_{OUT})$ that can be easily plotted, perfectly recovering the experimental fig.1.5. The explicit expression, here limited to the approximation $\epsilon = 0$, is

$$I = I_0\frac{P_{OUT}}{P_0} + \left[I_{th0}\left[\frac{\sqrt{1+\frac{P_0}{P_{OUT}}R(1+R)} + R}{1-R+\frac{P_0}{P_{OUT}}R}\right]^2\right] \tag{1.72}$$

This not only agrees, as natural, with (1.71) for high values of P_{OUT}, but also predicts the linearity of the $P_{OUT}(I)$ curve in the sub-threshold range:

$$I_{sub-th} = \frac{P_{OUT}}{P_0}I_0\left(1 + \frac{I_{th0}}{I_0}\frac{1+R}{R}\right) \equiv$$
$$\equiv \frac{P_{OUT}}{P_0}I_0\left(1 + \frac{I_{nr0}}{I_{ph0}}\frac{1+R}{R}\right) = \frac{P_{OUT}}{P_0}I_0\frac{1}{\eta_i} \equiv I_{ph}\eta_i \tag{1.73}$$

That means:

$$P_{OUT} \xrightarrow[POUT \to 0]{} \eta_i \frac{P_0}{I_0} I = \frac{h\nu}{q} \eta_C \eta_i I \frac{\alpha_m}{\alpha_T} \tag{1.74}$$

Equation (1.71) and (1.74) are then the asymptotic limits of (1.70) (or (1.72)), and coincide with the well-known relationships for, respectively, the laser and the LED range of a semiconductor optical emitter.

The novelty is that now the two ranges are connected in a self-consistent way that embeds the calculation of the threshold condition, usually introduced from outside (see, for instance, (1.29), or eq.2.39, and eq.2.34 in ref. [31]).

Just to conclude this sub-subparagraph, we can consider the apparently puzzling prediction that high efficiency seems to lead the threshold current to zero.

Indeed, the ideal case of a pure emitting diode, with total conversion of current into light, requires unit internal efficiency $\eta_i = 1$ even in the LED regime. This implies that the $P_{OUT}(I)$ has no kink ($I_{th} = 0$), and displays a uniform slope, increasing linearly with I irrespective of the LED or laser regime. Being that kink the fingerprint of the threshold current, one could conclude that the threshold current is null.

This is not true, and the solution is simple: the sole I_{ph} flows across the device, and the optical power is correctly proportional to it. Anyway, this does not mean that stimulated emission dominates over the full range of injected current: the voltage still requires to approach its threshold value in order to achieve the laser regime. One can simply say that for currents lower than the limit of the LED regime for V approaching its threshold (within the approximation $\epsilon = 0$)

$$I_{th} = \lim_{qV \to qV_{th}} \left[I_{ph0} \left(\exp\left(\frac{qV}{kT}\right) - 1 \right) \right] = I_{ph0} \exp\left(\frac{h\nu}{kT}\right) \left(\frac{1+R}{1-R}\right)^2 \tag{1.75}$$

the device is operating in the LED regime, and for higher currents it behaves as a laser. Intermediate cases can be considered, with high but not total efficiency.

1.1.5.5 Other currents

Fig.1.6 shows that at the left of the highlighted region A the total current deviates from the ideal behavior predicted by (1.52).

This is a region, confined in the sub-mA range, usually neglected in measurements performed by forcing a current into the laser diode and then measuring voltage and optical power. Anyway, it is worth of some consideration because of its capability to show early stages of degradation mechanism, well before their measurable effect on the relevant electro-optical characteristics.

First of all, some shunting path may be allowed to give account for surface conduction or other parasitic mechanisms. It is easily modeled as a parallel element with ohmic characteristics.

$$I_{sh} = \frac{V}{R_{sh}} \tag{1.76}$$

where R_{sh} is, in good devices, an extremely high resistance, whose effects are limited at the very low conduction range (fig.1.7).

The most interesting "other" current is that flowing in the side areas surrounding the active region. Here the specific technology for lateral current confinement

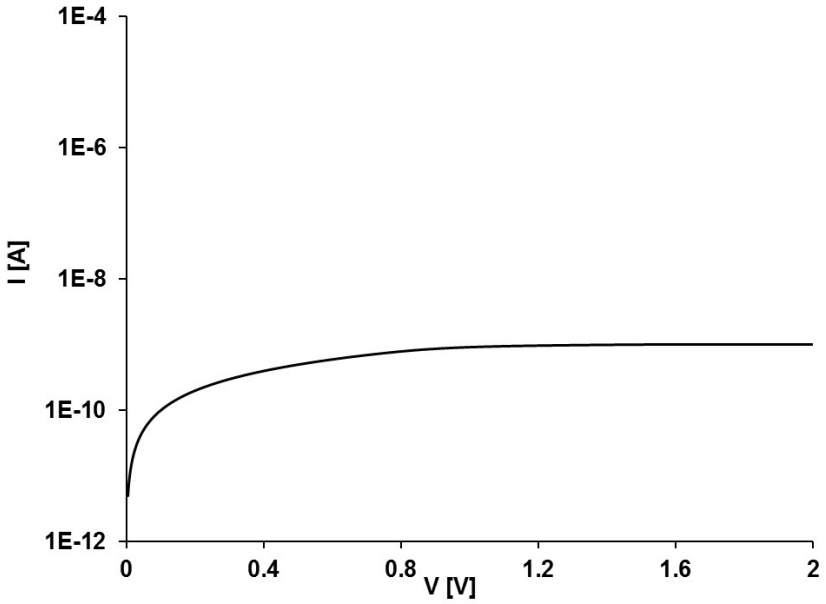

Figure 1.7: The shunt resistance effect.

should be called into play, leading to peculiar results. The simple case of a ridge structure in an edge-emitting device (fig.1.8) can qualitatively clarify the general situation, and even allow for accurate fitting when the device under test actually displays that technology. Ref. [2] proposes a model where the epitaxial stack is the same under the ridge and at its sides. This means that the conduction properties of each section of the stack are the same, but that the electrical connection is modified by some resistive path in the side areas (fig.1.8).

It is demonstrated [2] that the lateral current I_W is given by:

$$I_W = \frac{kT}{qR_W}\left[\sqrt{1+2\frac{R_W I_{W0}}{kT/q}\exp\left(\frac{qV}{kT}\right)}-1\right] \tag{1.77}$$

where R_W is the total resistance of the lateral path and I_{W0} is the saturation current of the whole area of the lateral diodes, the plot of this component as a function of the voltage V is reported in fig.1.9.

Such current displays a bimodal behavior, with an ideality factor of 1 at low conduction (when the square root can be approximated at the first order), and an ideality factor of 2 beyond some higher level (when both unities can be neglected), depending on the value of R_W. For a well - designed device, such current limitation takes place well before the mA range, and leaves the ideal current given by (1.52) to dominate.

Variants to such model of the side currents are introduced by specific technologies: for instance, Buried Heterostructures (BH), where the optical cavity is also laterally confined by higher band-gap material, may display different ideality factor in I_W with respect to I_{ph} and I_{nr}, while in VCSELS the circular lateral confinement of the active area modifies the model in fig.1.8 calling for radial 2D networking. In any case, at low conduction, when the side resistances are negligible, the lateral current displays its own ideality factor, that doubles, limiting the current itself, as soon as the ohmic effect enters into play.

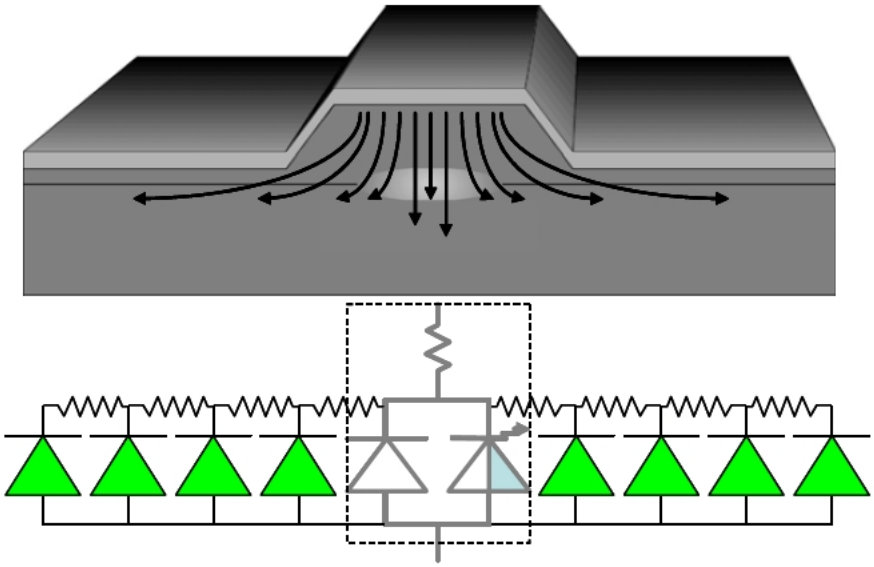

Figure 1.8: The model for lateral currents.

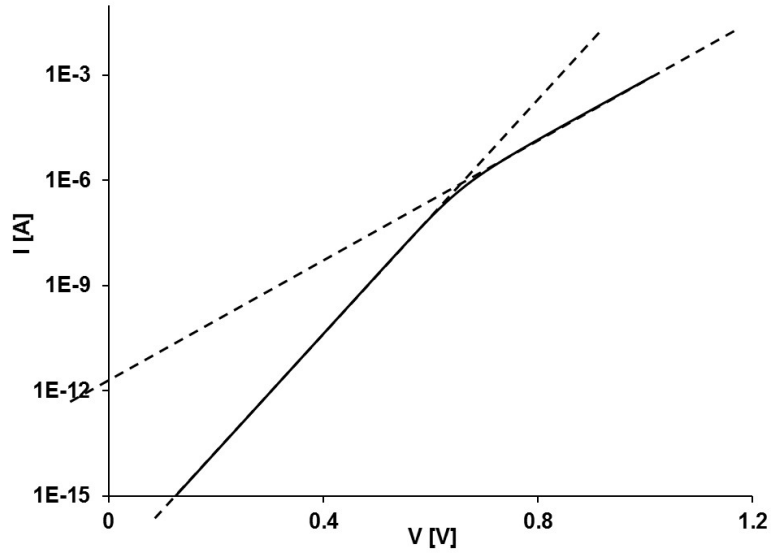

Figure 1.9: The lateral current component $I_W(V)$.

Fig.1.10 summarizes all currents in this model for a theoretical edge-emitting ridge-structure device emitting at $h\nu = 1eV$, with loss ratio (see (1.42)) $R = 0.12$. Here region A represents the same as in fig.1.6, that is the range where $I_{ph} + I_{nr}$ dominate. Region B, that is in the sub-mA range, the domain of I_W and region C the extremely low conduction limit, where the shunt current I_{sh} hides the correction of the pure exponential behavior in the dominating I_W that would be introduced by the "-1" term in the corresponding Shockley equation.

Also the threshold voltage V_{th} and current I_{th}, as well as the relevant values I_{th0} and I_0 at transparency qV_{tr} are shown in fig.1.10

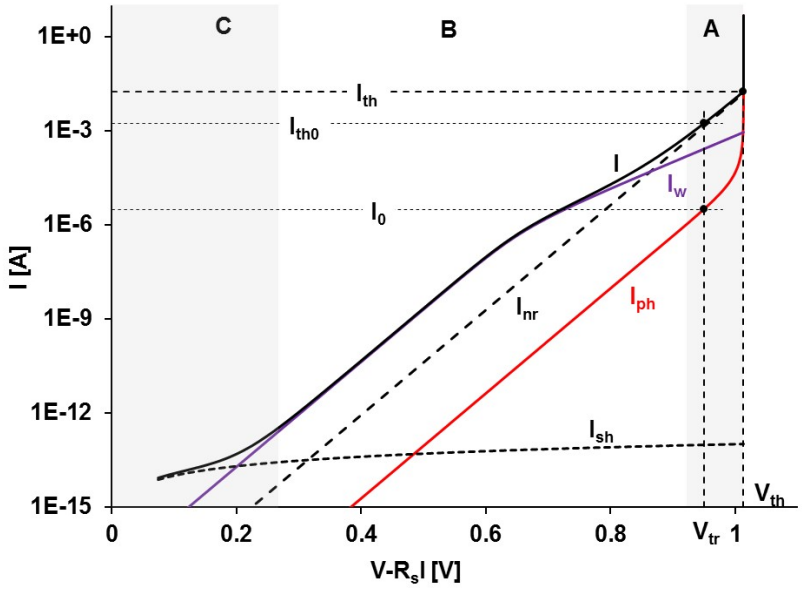

Figure 1.10: Prediction of the complete model in the $V - R_S I$ representation

1.1.6 Measurement and plot protocols

1.1.6.1 Electrical characteristics

As a practical remark, the illustrated results strongly recommends to slightly modify the standard protocols for DC characterization of laser diodes, in order to have the most clear representation of their performances [35,36]. The only practical variation, with respect to the assessed practice, is to perform DC measurements forcing voltage instead of current, and measuring I and I_M simultaneously. A practical rule, suitable for the most part of laser diodes, is

1. to apply a linear sweep of the forward voltage V_L at steps of, say, 5mV. A suitable compliance should be set to avoid excess current to flow at high bias. With this measurement three series of data are measured, the input voltage V, the laser current I and the induced current in the monitor diode I_M (fig.1.11).

2. The series resistance R_S of the device is easily obtained from the dV/dI_L plot, looking at the voltage ranges where the plot line flattens just at the R_S value (see fig.1.12).

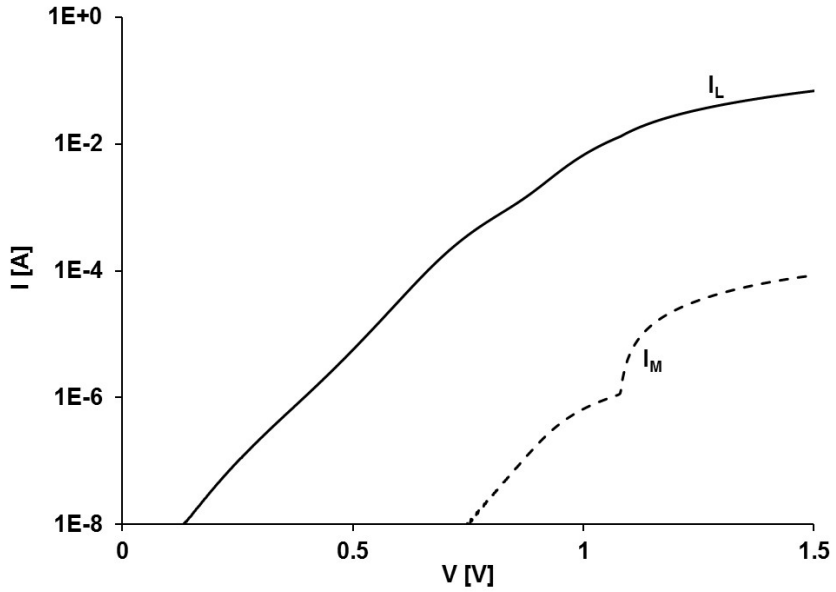

Figure 1.11: The total laser current and the monitor current in logarithmic scale vs. the voltage.

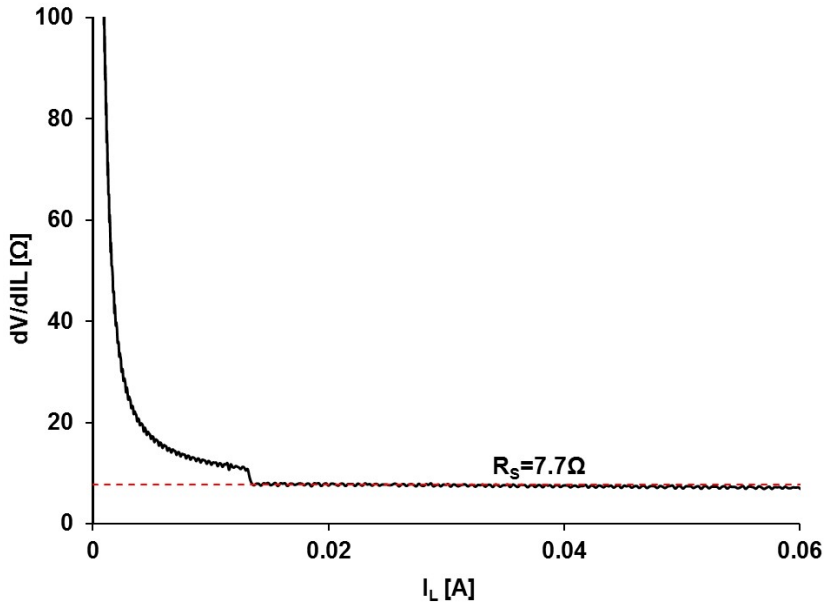

Figure 1.12: The first derivative dV/dI vs. the laser current

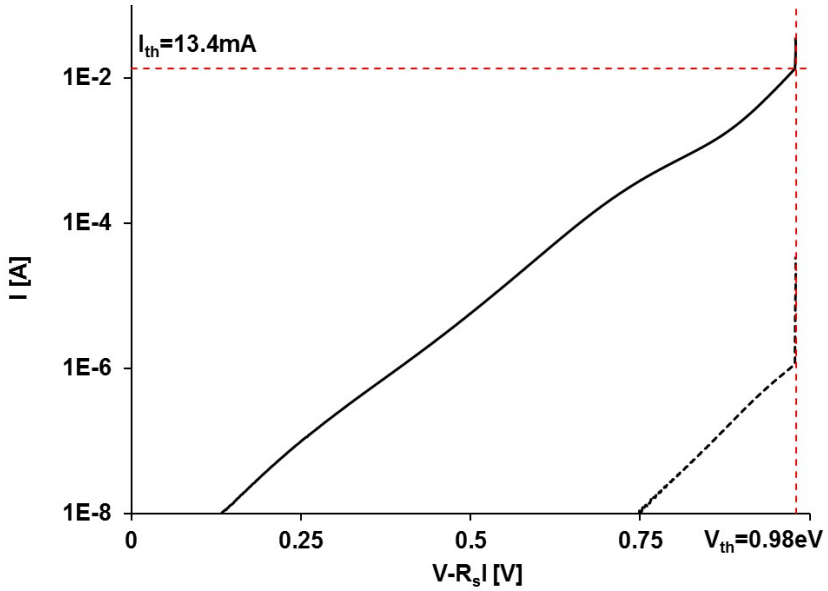

Figure 1.13: The total laser current and the monitor current in logarithmic scale vs. the voltage reduced of the effect of the series resistance.

3. Plotting the current I as a function of the reduced voltage $V = V_L - R_S I$ clearly displays a kink whose coordinates are (V_{th}, I_{th}), as showed in fig.1.13.

4. At last, as announced in 1.1.5.3, the coupling constant K allows to reconstruct the internal radiative current I_{ph}, at any injection level, as (1.60) (fig.1.14).

5. The double plot of I and I_{ph} as functions of the same reduced voltage V (fig.1.13), and the current-current plot $I_M(I)$ (fig.1.15) give the final format for the DC characteristics.

About the last point, the choice of not normalizing I_M to I_{ph} in the current-current version of the power-current curve follows the suitability to preserve the effects of losses on the measured emission, that would be lost by that normalization

A final comment should be reserved to the popular dV/dI and IdV/dI curve, often recommended [Ch 2.8.5 in [31] and paragraph 1.4] to point out non-idealities in real laser diodes.

The point is that they are usually plotted as functions of the laser current I. This neglects the many information encoded in the low injection range, where, for instance, latent degradation mechanisms can early mark their own presence.

If one also plots the same curves as functions of the applied voltage V, as here proposed, the full information of the $I > I_{th}$ range are preserved, and in addition the lower range can be fruitfully investigated.

In fig.1.16, indeed, the ideal differential curves give both the series resistance R_S and the ideality factor n multiplied by the thermal voltage $V_T = kT/q$. One particular feature of this ideal IdV/dI plot is that for $I > I_{th}$ it aligns with a straight line intersecting the origin of the axes.

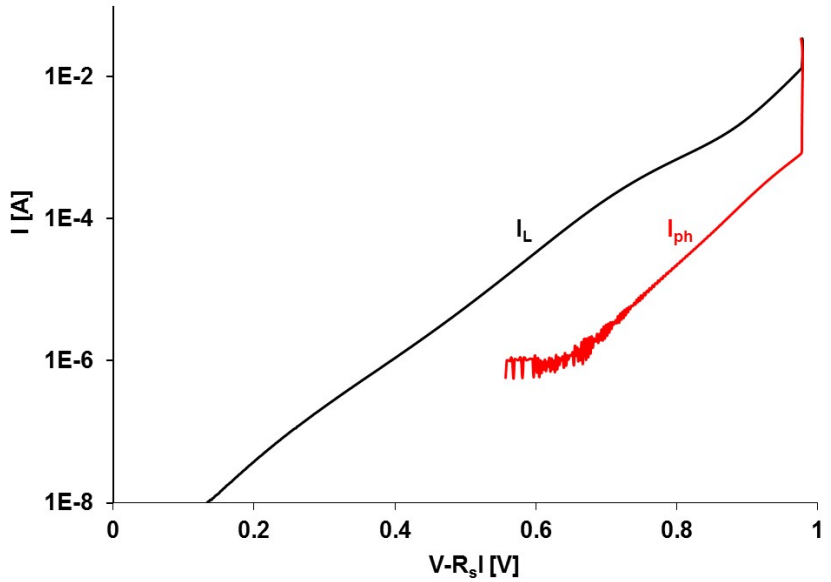

Figure 1.14: The total laser current and the photonic component of the current in logarithmic scale vs. the voltage reduced of the effect of the series resistance.

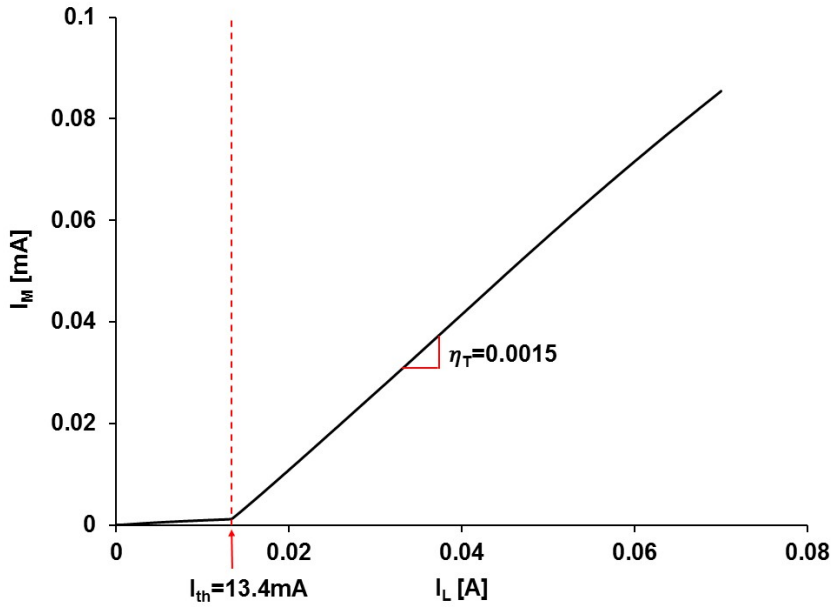

Figure 1.15: The total laser current vs. the monitor current

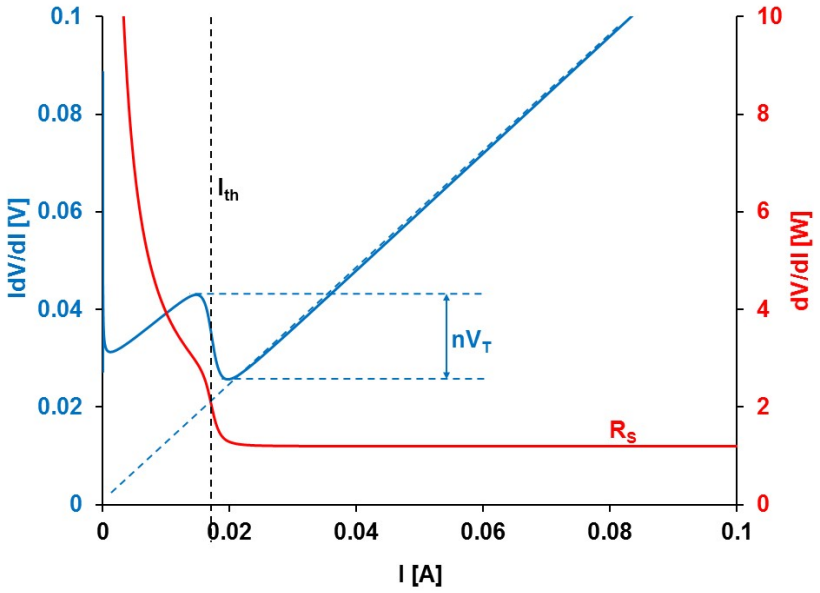

Figure 1.16: The standard differential curves dV/dI and IdV/dI

As a complement, fig.1.17 gives the IdV/dI curve as a function of the voltage V, superimposed to the $I(V)$ curve. The vertical bands corresponds to the three areas A,B,C in fig.1.10, and the bold lines refer to the reduced abscissa $V - R_S I$, while the thin lines refer to the external voltage V.

It is interesting to observe that now the areas A and B, invisible in fig.1.16, display evident features, and even more that the straight dashed line, that overlaps the IdV/dI plot for $I > I_{th}$, crosses the horizontal axis exactly at $V = V_{th}$, one of the important parameters of the device.

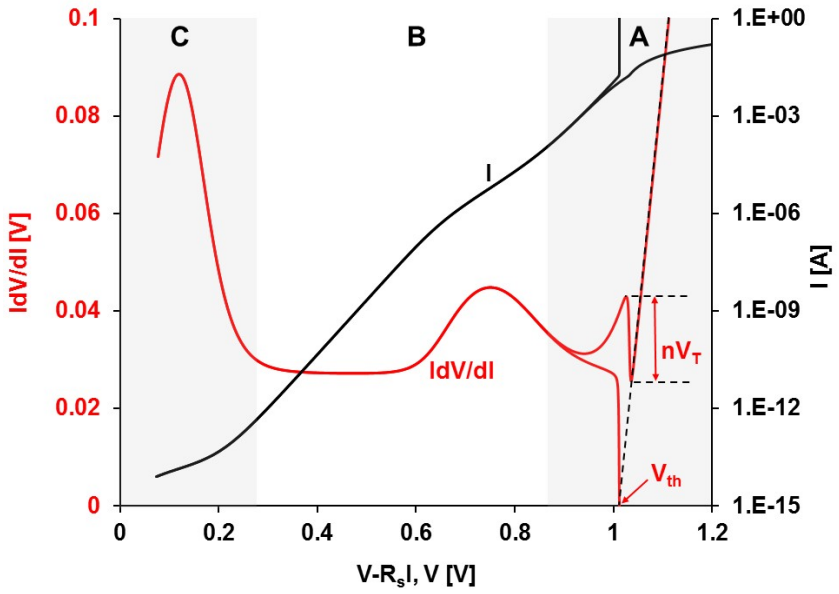

Figure 1.17: The curves I and IdV/dI as functions of both V and $V - R_S I$.

1.1.6.2 Optical characteristics

The integral measurement of the emitted optical intensity, described in the previous subparagraph, needs to be complemented by spectral measurements. Contrary to the $I(V)$ measurements, for which a new protocol has been proposed, the measurement procedures do not ask for any modification with respect to the standard. Anyway, the new interpretation and formulas for gain, that will be proposed in the next paragraphs, will allow to take advantage of some popular methods, based on spectral measurements (as the Hakki-Paoli method [37]), for proposing a significant extension of the measurable gain values. This will be the subject of paragraphs 1.3 and 1.4.

1.1.7 Refinements of the basic model.

Real devices are not ideal, and even this paragraph required to embed several non-radiative or lateral, or shunting currents in the main body of the model. Three cases will be here considered: first of all the presence of Multiple Quantum Wells, indeed the model assumes the same approximations that lead, for instance from eq.2.43 to eq.2.45 in [31]. Here the number of wells N_W simply multiplies the gain value for a single quantum well. In other words, a sort of effective volume is introduced, summing all QWs. It is rough, but it is also common in textbooks. Within such approximation, currents are the same as in the basic model, apart from the effective volume.

Then the big puzzle of the non-unitary ideality factor and the apparent reduction of R_S at increasing current beyond are going to be discuss in the next paragraphs of this Chapter.

The choice has also been made to not deal with thermal effects. It is assumed that the available literature on this subject does not need any revision, at least on the basis of the present model.

1.2 Optical gain in single-mode laser diodes

Optical gain in semiconductor laser diodes (LDs) is a function of both the light frequency and the injection level, and its measurement enters the characterization and monitoring procedures for such devices. To this purpose, the most popular methods have been proposed by Hakki and Pauli [37], Cassidy [38], Henry, Logan and Merritt [39] or Hofstetter and Faist [40].

Anyway, each of the listed methods is essentially spectral, and strictly applies to multi-mode emitters. When one moves to single-mode LDs, as Distributed Feed Back (DFB), Distributed Bragg Reflector (DBR) or externally-tuned laser emitters, none of those methods does work.

This paragraph aims to deal with modal gain, that is optical gain at a given frequency.

It seems a much simpler task than handling general gain, because the main complexity in gain equations comes from the spectral dependence of many parameters. Modal gain g at a fixed frequency is just a function of the injection level, that, in turn, is usually represented by the laser current I.

We are then going to study $g(I)$, a function that is known in advance to display some very simple features: it grows monotonically with I; it has a minimum g_m that is negative and corresponds to the absorption α_{abs} of the un-pumped ($I = 0$) material; it is null when I leads stimulated emission to just balance absorption, which defines the so-called transparency condition; it becomes positive beyond transparency and, finally, it saturates when g equates the total optical loss coefficient α_T. Despite that simplicity, the curve $g(I)$ does not exist in literature. Several empirical formulas are instead available, each missing at least one of the features of the real function.

Moreover, the experimental methods for measuring modal gain at saturation require the comparison of a pair of devices with identical structure and different cavity length [34], a request easily fulfilled by a device manufacturer but not by an end user.

The following subparagraphs will first resume the most popular equations for gain available in literature. They will then propose both a working formulation for $g(I)$ and a protocol for its measurement, based on the results of a laser model published in some previous papers [1–3], that are described and somewhat refined in paragraph 1.1.

Particular attention will be paid to the comparison of the old and new formulations. This will allow to explain why empirical formulas work so well, and will also grant some "fitting parameters" in that formulas with a sound physical significance.

Finally, the measurement protocol will be demonstrated for the real cases of a 850 nm VCSEL and two 1310 nm DFB edge emitters, one with ridge and one with Buried Heterostructure (BH) technology.

1.2.1 Gain equation in literature

1.2.1.1 The double population model

The most complete equation for gain, starting from the theoretical form that links that quantity to both frequency and quasi-Fermi levels, appears in [41, 42], and is the only one that preserves the separate populations of electrons and holes, and then also the concept of population inversion.

Referring in particular to [42], the expression is

$$g = A\frac{\lambda_0^2}{8\pi n_r^2}\left[f_e(1-f_h)\right]N_\nu^2\left[1-\exp\left(\frac{h\nu-(\phi_n-\phi_p)}{kT}\right)\right] \tag{1.78}$$

Here, for the sake of the next discussion, the notations of [1–3] have been used, but the term-to-term correspondence with the quoted reference holds. In particular: g is the gain function, A is the Einstein's coefficient for spontaneous emission, λ_0 is the photon wavelength in vacuum, n_r is the refractive index of the active region, f_e and f_h are the Fermi distribution for, respectively, electrons and holes, N_ν^2 is their joint density of states, $h\nu$ the photon energy, kT the thermal energy, and ϕ_n and ϕ_p the quasi-Fermi levels for, respectively, electrons and holes.

Equation (1.78) predicts both a lower and upper limit for g that, in a specific note in [42], are shown to have the same absolute value and opposite sign, up to state that, at complete population inversion "what was absorption becomes gain".

This is not true. On one side, indeed, the low-injection approximation (un-pumped material), that assumes a completely filled state in the valence band and a completely empty state in conduction band, is acceptable, together with the conclusion that gain in the un-pumped material is negative, and coincides with its natural absorption. But, on the other hand, the upper limit requires a completely filled state in the conduction band and a completely empty state in the valence band, which is physically impossible. Moreover, the saturation at $g = \alpha_T$ does not appear, and the link with the injected current I is not explicit. Anyway, this is the only equation that indicates upper and lower bounds for gain.

1.2.1.2 The linear and logarithmic models

The strictly modal gain g is described by four empirical models, reported and discussed in detail in [43]. The most relevant of them, for the sake of the present study, states the dependence of g on the logarithm of the ratio J/J_{tr} between the injected current density J and its value J_{tr} at transparency.

The approximation of such model to the first order leads to the linear model that is widely recognized as less accurate, but, nevertheless, is assumed for a calculation of the threshold current density J_{th} in [25], that is reported in so many textbooks, by substituting g with its saturation limit α_T.

Two more models, logarithmic and linear, are reported, referring gain not to the current density J but to the carrier density n and its value n_{tr} at transparency. It is the same reference [25] that shows how the J and n models can be harmonized by assuming the bi-molecular (band-to-band) recombination dominant, and properly adjusting the empirical fitting parameters.

In conclusion, all the available empirical formulas for gain can be efficiently represented by the logarithmic model, where, using the total current I instead of its density J one has the equation (1.58), that introduces the empirical fitting parameter g_0, also implies the definition of the threshold current I_{th} (1.59) [43] as that value of I for which gain g exactly balances the total optical losses α_T.

It is evident that the gain equation (1.58) may behave well only close to transparency and also that is monotonic, as requested, but it fails in predicting upper and lower boundaries for g.

Nevertheless, its consequence (1.59) has been experimentally validated along decades. This challenges any new model to behave equally well, before pretending to replace such consolidated representations.

1.2.2 New equation for Gain

The model proposed in [1–3], is described and partially refined in the paragraph 1.1. It embraces the whole injection range of a laser diode and includes the threshold condition as a sharp but not abrupt transition between the LED and the laser regimes. It has been first applied to point out the peculiar characteristics of the radiative component I_{ph} of the total current I and its relationship with the other currents. The model is here applied to modal gain, with the aim of finding a formulation able to remove the limitations of the previously recalled equations. We will start with equations (1.27) and (1.28) in the paragraph 1.1, that indicates

the gain function as:

$$g = g_m \frac{1 - \exp\left(\dfrac{h\nu - qV}{kT}\right)}{\left[1 + \exp\left(\dfrac{h\nu - qV}{2kT}\right)\right]^2} \tag{1.79}$$

It is just a cumbersome exercise to show that this expression is exactly the same as (1.78). It is indeed sufficient to first express g_m by means of (1.23), then to use (1.15) to express B/c, and finally recognize the appearance of the term $f_e(1-f_h)N_\nu^2$ by means of (1.6), (1.7), (1.8) from paragraph 1.1. The identification of qV with the separation of the quasi-Fermi levels leads to the final result.

An equivalent form of (1.79) will be more useful for the following steps:

$$g_m \tanh\left(\frac{qV - h\nu}{4kT}\right) = g_m \frac{\exp\left(\dfrac{qV - h\nu}{2kT}\right) - 1}{\exp\left(\dfrac{qV - h\nu}{2kT}\right) + 1} \tag{1.80}$$

As said, this equation, by itself, does not tell anything new with respect to (1.78), apart from attributing a physical meaning to the parameter g_m: for the un-pumped material ($qV = 0$), the exponentials are extremely small in comparison with unity (at least for real photon energies at normal temperatures) so that

$$g_{min} = -g_m = \alpha_{abs} \tag{1.81}$$

This tells that g_m is the absolute value of the absorption coefficient α_{abs} for the un-pumped material.

Anyway, in order to obtain a self-consistent expression that includes all features of gain, it is advisable to invert (1.80) to express the exponential as a function of g/g_m.

$$\exp\left(\frac{qV - h\nu}{2kT}\right) = \frac{1 + \dfrac{g}{g_m}}{1 - \dfrac{g}{g_m}} \tag{1.82}$$

Now, the exponential on the left side of (1.82) is identical or very close to all exponentials appearing in the definition of the current components I_{ph} and I_{nr} as indicated in paragraph 1.1.

The first equation (1.38), neglecting the negative unity in the numerator, and using (1.43), (1.25) and (1.36), may be written as

$$I_{ph} = I_0 4R \frac{\exp\left(\dfrac{qV - h\nu}{kT}\right)}{R\left[\exp\left(\dfrac{qV - h\nu}{2kT}\right) + 1\right]^2 + \left[1 - \exp\left(\dfrac{qV - h\nu}{kT}\right)\right]} \tag{1.83}$$

where

$$I_0 = qVol\Delta\nu g_m \left(\frac{2\pi n_r}{\lambda_0}\right) \tag{1.84}$$

results to be the value of I_{ph} at transparency $qV = h\nu$. Its expression has been obtained by neglecting the negative unity also in the denominator of the black-body (1.14).

The other current I_{nr} can be suitably rewritten, starting from (1.51), neglecting again the negative unity and using (1.56)

$$I_{nr}(V) = I_{th0} \exp\left(\frac{qV - h\nu}{kT}\right) \tag{1.85}$$

As pointed out in paragraph 1.1, it should be also noticed that the coefficient I_{th0} corresponds to the value of this current I_{nr} at transparency, $qV = h\nu$.

Now, (1.82) allows to eliminate the exponentials from (1.83) and (1.85), and to express the total current (1.52) as

$$I = I_{th0}\left(\frac{1 + \dfrac{g}{g_m}}{1 - \dfrac{g}{g_m}}\right)^2 + I_0 \frac{\left(1 + \dfrac{g}{g_m}\right)^2}{1 - \dfrac{g}{\alpha_T}} \tag{1.86}$$

This is an inverse relationship that expresses the total current I as a function of the gain g, and that cannot be inverted in a simple form. Anyway it is possible to plot the $g(I)$ curve, that clearly displays several important features:

1. $\partial I/\partial g$ is positive, that means a monotonic relationship between I and g, for all gain values $g < \alpha_T$.

2. Gain g has a minimum when $I = 0$, that corresponds to $g = -g_m$.

3. At transparency, when gain vanishes, the current is $I = I_{th0}+I_0$, in agreement with the definition of the constants I_{th0} and I_0.

4. If $\alpha_T > g_m$ gain saturates (infinite current) at $g = g_m$.

5. If $\alpha_T < g_m$ gain saturates at $g = \alpha_T$.

With regard to the last two points, relative to the values of α_T and g_m, it can be easily checked that the denominator of (1.38) may vanish only if $R < 1$, that is (1.36) only if $\alpha_T < g_m$. This condition is the requirement for lasing, and then the value $g = \alpha_T$ is the saturation limit for gain in semiconductor lasers, and corresponds to the requirement that gain balances optical losses.Would be $R \geq 1$, no population inversion could be achieved. The diode would only emit as a LED, and the upper limit for gain would be given by g_m, as predicted by [42].

Equation (1.86) is then the first gain equation able to include all its features.

1.2.3 Comparison with previous models

For the sake of comparison with literature, the following alternative form, obtained by (1.80) and (1.85) will be useful:

$$g = g_m \frac{\sqrt{I_{nr}} - \sqrt{I_{th0}}}{\sqrt{I_{nr}} + \sqrt{I_{th0}}} \tag{1.87}$$

This formula links gain g to the sole non-radiative current I_{nr} (and its value I_{th0} at transparency), but hides the saturation limit. The latter is implicitly recovered when it is realized that the first term on the right-hand side of (1.86) is exactly I_{nr} and that, in a properly designed laser diode achieving threshold, g clamps at $g_{clamp} = \alpha_T$. The maximum of I_{nr} is then

$$I_{nr,MAX} \equiv I_{th} \tag{1.88}$$

This is the definition of the threshold current I_{th}, as reported in detail in [1–3] and in (1.55). Direct substitution of (1.88) and (1.55) into (1.87) gives back the gain saturation limit.

Equation (1.87) has a practical importance because of the mentioned dominance of I_{nr} in the whole sub-threshold range, that includes the transparency value I_{th0}. This dominance may safely lead to identify I_{nr} with the total current I when empirical formulas are looked for. In other words, the form

$$g \approx g_m \frac{\sqrt{I} - \sqrt{I_{tr}}}{\sqrt{I} + \sqrt{I_{tr}}} \tag{1.89}$$

where I_{tr} is the value of the total current I at transparency, may be considered a practical approximation of (1.87) when the accuracy in current measurements is not better than about 1%. In this way, the given result for g can be compared with the various expressions, available in literature, that refer the gain g to the total current I. In particular, formulas (1.89) and (1.55) should be compared, respectively, with (1.58) and (1.59). The difference is striking and the wide experimental confirmation of (1.59) seems to ultimately support the validity of the old models with respect to the new one. However, the new formulas give account for gain saturation, while (1.58) seems to allow g to increase with I without any limit. It seems hard to exploit the benefits of the two versions.

The surprising result comes from the power expansion of the competing formulas. Let us start with (1.58) and (1.89): they mathematically agree only for the common prediction that gain vanishes at transparency $I = I_{tr}$. Anyway, close to transparency, we have for (1.58)

$$g = g_0 \ln \frac{I}{I_{tr}} = g_0 \left[\left(\frac{I}{I_{tr}} - 1 \right) - \frac{1}{2} \left(\frac{I}{I_{tr}} - 1 \right)^2 + \frac{1}{3} \left(\frac{I}{I_{tr}} - 1 \right)^3 - \frac{1}{4} \left(\frac{I}{I_{tr}} - 1 \right)^4 + \right.$$
$$\left. + O \left(\frac{I}{I_{tr}} - 1 \right)^5 \right] \tag{1.90}$$

while for (1.89)

$$g = g_m \left[\frac{\sqrt{\frac{I}{I_{tr}}} - 1}{\sqrt{\frac{I}{I_{tr}}} + 1} \right] = \frac{g_m}{4} \left[\left(\frac{I}{I_{tr}} - 1 \right) - \frac{1}{2} \left(\frac{I}{I_{tr}} - 1 \right)^2 + \frac{5}{16} \left(\frac{I}{I_{tr}} - 1 \right)^3 + \right.$$
$$\left. - \frac{7}{32} \left(\frac{I}{I_{tr}} - 1 \right)^4 + O \left(\frac{I}{I_{tr}} - 1 \right)^5 \right] \tag{1.91}$$

It follows that if we identify the phenomenological fitting parameter g_0 with

$$g_0 = \frac{g_m}{4} \tag{1.92}$$

the competing expression will coincide at the first and second order, while the difference of their third order term is as small as that between 5/16 and 1/3, and between 7/32 and 1/4 for the fourth order term. This means that any experiment confirming (1.58) in its range of validity, near transparency, will also confirm (1.89) that, in turn, does not differ numerically from its exact formulation given by (1.87).

Being the threshold current I_{th} close to I_{tr}, this conclusion also apply to threshold current measurements.

This last particular case has been investigated in a previous paper [36], where optical losses were modifed on a 1310 nm edge emitter by a Focused Ion Beam, and I_{th} was monitored. The experiment and its results will be reported in detail in the next paragraph 2.2. Here we can anticipate that the experiments, indeed, confirmed the expected results in a range where the two competing formulas for $g(I)$ are completely undistinguishable.

A final comment must be given for (1.92): it assigns a physical meaning to the phenomenological "fitting parameter" g_0 of [43]. The factor 1/4 is not accidental: it corresponds to the transparency value of the absorption term in (1.27), so that g_0 assumes the role of the absorption coefficient measured at transparency, that is when absorption exactly balances stimulated emission.

1.2.4 Experimental method

The procedure proposed in [35] and in 1.1.6 is the most straightforward also for gain measurement. Plotting I, I_{nr} and I_{ph} as functions of the internal voltage $V - R_S I$, it is possible to identify the values of I_{th0} and I_0 as the values of, respectively, I_{nr} and I_{ph} that correspond to the transparency voltage V_{tr} (Fig.1.18).

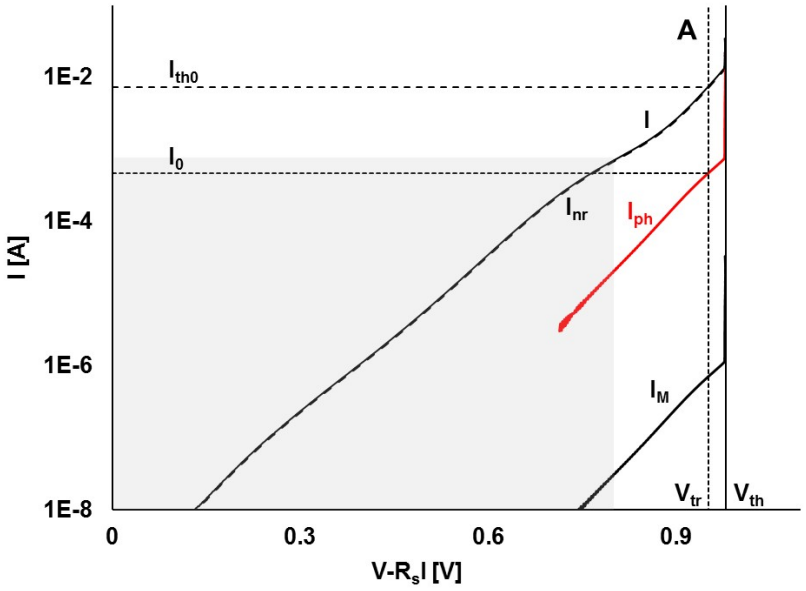

Figure 1.18: The identification of I_{th0} and I_0 on the measured characteristics.

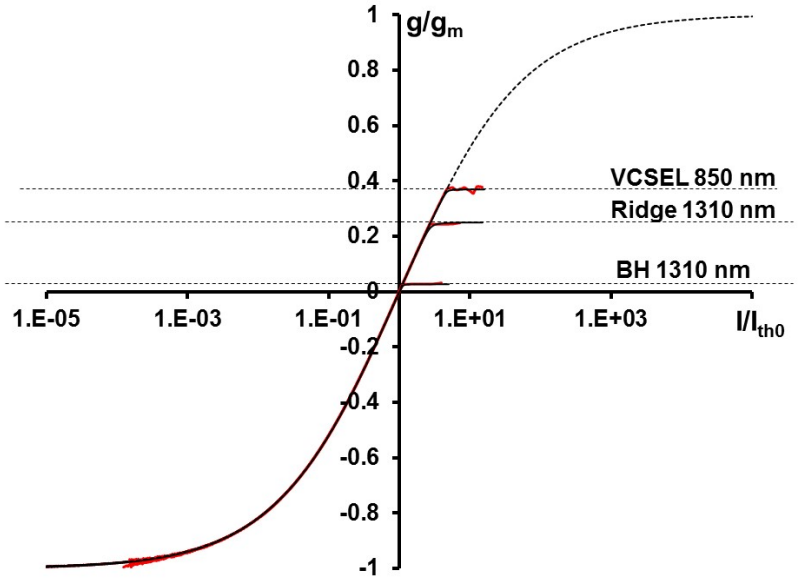

Figure 1.19: The normalized experimental gain curves (red lines) of three laser diodes, compared with the calculations (thin lines) of (1.89) and of (1.86). Once indicated the value of the ratio $R = \alpha_T/g_m$ in (1.86), the experimental and the calculated curves are undistinguishable. The saturation values for the ratio R are 0.37 for the VCSEL, 0.25 for the ridge emitter and 0.025 for the BH device.

The original I_M has been preserved, to show the upscaling factor required to reconstruct I_{ph}. Anyway, the latter remains so low with respect to I_{nr} in the sub-threshold range, that I and I_{nr} look undistinguishable, which justifies the approximation of (1.87) with (1.89), as far as saturation is not involved.

1.2.4.1 The normalized curves and the universal function

The available experimental values of $I_{nr}(I)$ and the calculation of I_{th0} allow to draw the normalized gain g/g_m as a function of the normalized current I/I_{th0} according to (1.87).

Fig.1.19 reports the normalized experimental gain curves for a VCSEL emitting at 850 nm, and two edge emitters at 1310 nm, one in Buried Heterostructure (BH) and one in Ridge technology.

It is interesting to observe the dashed line calculated by means of (1.89), that is replacing I_{nr} with I. It draws a symmetrical universal curve on which the experimental values of the normalized gain must lay for any device. What remains peculiar of each device is the level at which the ratio g/g_m saturates.

Equation (1.86) is the key result in this paragraph that includes all features of modal gain as a function of the injected current. Its alternative forms (and in particular (1.87)), have been successively presented and discussed for the sake of comparison with the previous formulas found in literature.

The cardinal point of the given results is the Current-Voltage relationship shown in [1–3], and the peculiarity of (1.83), the $I_{ph}(V)$ characteristics for the radiative component of the total current I. It is the vanishing condition for the

denominator in that equation that switches up the LED-laser transition, and then gain saturation, in the whole theoretical frame.

After these results we start further investigations, in order to extrapolate the value for the modal gain g_m. The first attempt will be presented in the next subparagraph.

1.2.5 Gain versus current in single mode laser diode.

Numerous investigation based on electrical and optical characterization have been intensively used to characterize and determine failure mechanisms in laser diodes [40,44–48]. The analyses in this paragraph 1.2 and in the next subparagraph 2.2.1 with the references [2,3,35,49,50] have considered the gain measurement with electrical measurement approach. In particular, paragraph 1.2 it is focused on the measurement of gain g as a function of the laser current I, first pointing out how and why the available theories and methods fail for single-mode emitters, as DFB and DBR structures. It then gave account for an experiment where, inducing controlled modifications with a FIB, the empirical relationship between optical losses and threshold current was nicely confirmed. Finally, it proposed a new theoretical formula that on one side is proven to numerically coincide with the empirical ones, and on the other side indicates an experimental method for measuring gain in single-mode devices.

The last sub-subparagraph 1.2.4.1 pointed out the main practical limitation of the whole study: the impossibility to decouple the measured gain g from a scale factor g_m.

This subparagraph aims to remove that limitation, by the combined use of the new measurement method for $g(I)$ and the Hakki-Paoli method [37,51] that, since 40 years, provides spectral measurement of gain for Fabry Perot laser diodes.

The multimodal sub-threshold spectrum of some DFB devices will be shown acting as one of the best candidates for absolute gain measurement, according with the Hakki-Paoli (HP) or other techniques reported in [37,38,51], at some few different current levels. The results, measured at the operating frequency at which the devices are tuned for single-mode lasing, compared with the corresponding values of the continuous $g(I)/g_0$ curve, obtained by means of the new method, allow to calculate g_0. The perfect superposition of the HP values onto the continuous curve, after upscaling it by g_0, validates once more the proposed extended model.

The goal of this subparagraph will be to demonstrate a much simpler way for gain measurement as a function of the injection current in single-mode emitters. This, in turn, aims to ease both characterization and failure Analysis in such devices.

1.2.5.1 The measurement of g_m

As it has been said previously equation (1.86) corresponds to an improvement of the proposed new model, that allows to demonstrate the existence of upper and lower limits for the function $g(I)$. Anyway, it does not decouple g from g_m (or, equivalently, from g_0).

A nice solution to this problem comes from the observation that at suitable currents $I < I_{th}$ the spectrum even of a Distributed Feedback (DFB) device is

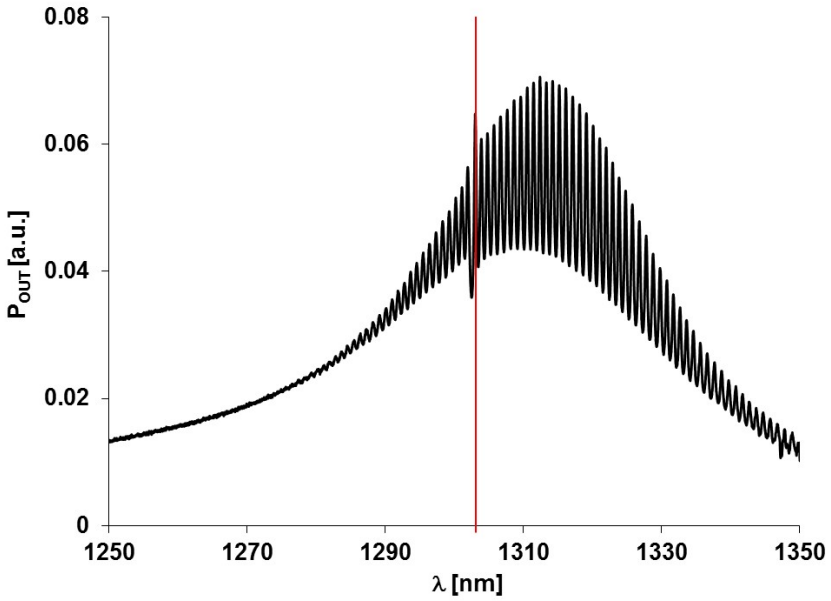

Figure 1.20: Multi-modal spectrum of a 1310 nm InP-based DFB laser diode for $I < I_{th}$ measured at transparency $qV_{tr} = h\nu$.

dominated by the Fabry-Perot resonances (fig.1.20). The spectral measurement (fig.1.20) has been made with the equipment HORIBA Jobin Yvon, 1250M Series II, High resolution Spectrometer, with spectral dispersion equal to $0.65nm/mm$ (with slit near $3\mu m$). For experiment the resolution is close to $20pm$ for a constant current close to $8mA$. Considering such current levels, the HP method can be applied to get the absolute value of g at any frequency in the spectrum, at a constant current I.

On a practical ground, only a limited set of values of I provides a good SNR for the measured spectral $g(\nu, I)$. Anyway, it should be obvious that, tuning on the DFB peak frequency ν, those values must coincide, apart from a multiplying constant, with those from (1.86). That constant is g_m, and it is defined by data fitting.

The result is shown in fig.1.21, where the dots represent the HP measurements, while the continuous curve corresponds to the plot of (1.87), after the determination of I_{nr} and I_{th0} according to sub-subparagraph 1.1.5.2. The plot clearly shows the upper and lower bounds of the absolute gain, while the inset allows to appreciate the nice fitting of the two sets of data. The minimum value of g, corresponding to the absorption coefficient for the un-pumped material at the reference frequency set by the DFB grating, results to be $g_m = 650cm^{-1}$, while the total loss coefficient, giving the saturation upper boundary for gain, results to be $\alpha_T = 140cm^{-1}$.

The proposed method undoubtedly an added-value for both manufacturers and end-users dealing with the possibility to extract the gain value of Laser diodes using a quite nice and simple technique from the spectrum measurements. This approach is more efficient for laser diode devices where laser diode is not directly accessible and some additional optical losses, due to packaging, must be taking into account. The combined use of the current-voltage measurements and of the Hakki-Paoli methods allows for at least a good estimate of gain in single-mode

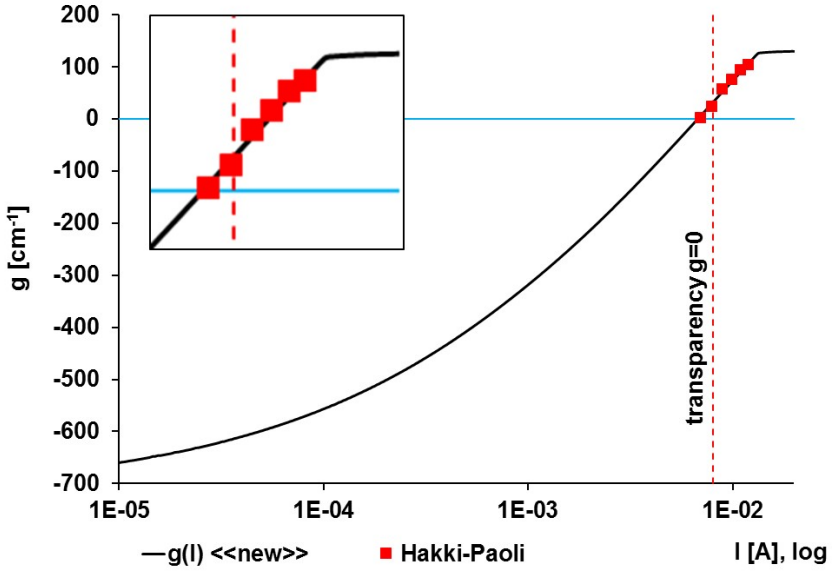

Figure 1.21: $g(I)$ in logarithmic horizontal scale measured by the Hakki-Paoli and the new method.

laser diodes removing the need of comparing devices of different lengths [31], or even of opening the package. The good fitting of the Hakki-Paoli data by the $g(I)$ continuous curve on one side experimentally validates once more the theoretical laser model underlying the new proposed method for measuring g, and on the other side shows the complete removal of the ultimate limitation that affected it, as pointed out at the beginning of this subparagraph.

It is then possible, from now, to include gain measurement among a set of non-destructive characterization techniques available not only at the device designer level, but also for qualification reliability engineers. Going back to the theoretical model, the lower gain limit should only depend on material properties as fundamental as the value of the Einstein coefficient for absorption and stimulated emission and on the joint density of states for electrons and holes involved in radiative direct transitions. On the other hand, the upper gain limit should mostly depend on optical losses, a strictly device-specific parameter that includes the internal losses, not due to absorption, and photon escape from the active region (including the escapes that the confinement factor Γ accounts for). It is then expected that the most part of the known laser degradation mechanism will affect the upper limit of gain, leaving its lower limit and the whole intermediate curve unchanged.

This novel method will allow to verify such expectations. In any case, it is a new tool for a direct insight into the relationship between causes and effects in laser diodes. Such study represents a significant part of the general Design for Reliability (DfR) effort carried out to produce efficient and reliable high power devices at the industrial level.

1.2.6 Gain versus voltage in single mode laser diode.

This subparagraph 1.2.6 proposes a practical method for complete gain measurement in DFB laser diodes and it is complementary to the method proposed in the previous subparagraph 1.2.5 . It is non-destructive and does not require any reference device. It includes the whole range of continuous gain values, from its minimum to saturation, passing through the transparency condition. The method makes gain suitable for monitoring time-evolving processes, as degradation kinetics in Reliability tests.

This subparagraph follows the approach to gain calculation mentioned by Agrawal and Dutta [52], that refers to the original study by Lasher and Stern [41] that has been, in turn, summarized by Casey and Panish [53]. We propose to overcome the shortcoming pointed out by [52] for which that approach "provides only the small-signal gain, and so gain-saturation effects cannot be treated", by using the concept of junction voltage, introduced by Paoli and Barnes [54]. The result will be an experimental curve, ranging continuously from the negative minimum corresponding to the un-pumped state, passing through the transparency condition and finally clearly saturating at a constant maximum. One undefined multiplying constant will then be calculated by comparing that curve with some experimental gain values measured by the standard Hakki-Paoli method [37], whose suitability for DFB devices will be discussed. The list of other methods for gain measurements is left to specific papers available on literature [44].

1.2.6.1 Gain and voltage equations

Verdeyen [42], based on [41, 52, 53], proposes for gain the expression (1.78). From this equation we now proceed with the following steps:

a) Set

$$g_m = A\frac{\lambda_0^2}{8\pi n_r^2}N_\nu^2 \tag{1.93}$$

This is a gain coefficient, depending on the frequency ν, that collects all information on the effective density of states.

b) Following Paoli and Barnes [54], define

$$V_j = V - R_S I \tag{1.94}$$

where V and I are, respectively, the forward voltage and current of the laser diode, and R_S is the series resistance of the device.

c) Introduce an explicit for the product of the Fermi functions in (1.78)

$$\begin{aligned}[f_e(1-f_h)] &= \frac{1}{\left[\exp\left(\frac{E_e-\phi_n}{kT}+1\right)\right]\left[\exp\left(\frac{\phi_p-E_h}{kT}+1\right)\right]} = \\ &= \frac{1}{\exp\left(\frac{h\nu-qV_j}{kT}\right)+2\exp\left(\frac{h\nu-qV_j}{2kT}\right)\cosh(\epsilon)+1}\end{aligned} \tag{1.95}$$

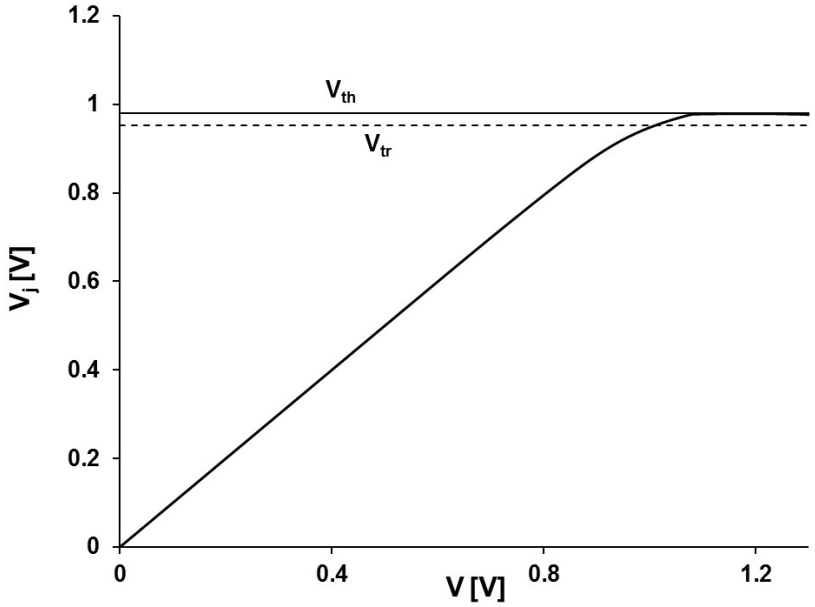

Figure 1.22: Experimental plot of the junction voltage V_j in a 1310 nm InP-based DFB laser diode. Its saturation value V_{th} is compared with the transparency voltage $qV_{tr} = h\nu$.

where the parameter ϵ is defined as (1.9) and E_e and E_h are the electron and hole energies involved in the optical transition $E_e - E_h = h\nu$.

For undoped $In_{1-x}Ga_xAs_yP_{1-y}$ lattice-matched to InP, it can be demonstrated that, in the Boltzmann approximation for carrier densities, $\epsilon \leq 1$ for transitions involving light holes, and one order of magnitude less for heavy holes. The possibility and effect of larger values of ϵ for relevant doping and/or high injection levels, for which the Boltzmann approximation does not hold, will be considered in the next discussion. The final result of the indicated steps is the definition of the function

$$H = \frac{g}{g_m} = \frac{1 - \exp\left(\dfrac{h\nu - qV_j}{kT}\right)}{1 + 2\cosh(\epsilon)\exp\left(\dfrac{h\nu - qV_j}{2kT}\right) + \exp\left(\dfrac{h\nu - qV_j}{kT}\right)} \tag{1.96}$$

1.2.6.2 Gain measurement

Equation (1.94) allows to draw V_j from experimental data. Fig.1.22 refers to a 1310 nm DFB laser diode for which $R_S = 7.7\Omega$ has been measured. Inserting now the experimental values of V_j in (1.96), after having calculated ϵ for the given material and measured $h\nu$ form the single-mode emission above threshold, we can draw the relative gain function g/g_m. In order to get the absolute gain function g, the constant g_m must be obtained.

For this task, we take advantage of the evidence (fig.1.23) of clear Fabry-Perot (FP) resonances in the sub-threshold Amplified Spontaneous Emission (ASE) spectrum, and of the correspondence of the DFB peak with one of the FP maxima. The

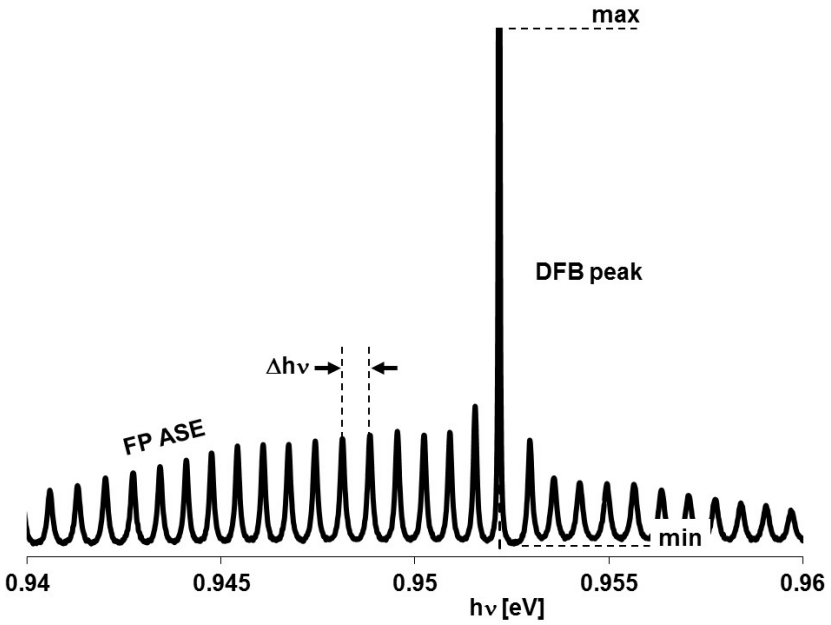

Figure 1.23: ASE spectrum of the DFB in the sub-threshold range.

final discussion will demonstrate that in this situation the Hakki Paoli method [37] can be applied also to the DFB peak. According with that method, the ratio r between the max and min indicated in fig.1.23 leads to measure the quantity

$$S = \ln\left(\frac{\sqrt{r}+1}{\sqrt{r}-1}\right) = L\alpha_T - Lg \tag{1.97}$$

where L is the length of the optical cavity, and α_T is the total loss coefficient.

About α_T, it is assumed to include all internal losses α_i and mirror losses α_m, being the latter often represented by means of the sole mirror reflectivities R_1 and R_2, typical of a pure Fabry-Perot (FP) cavity, whose length is L

$$\alpha_T = \alpha_i + \alpha_m = \alpha_i + \frac{1}{L}\ln\frac{1}{\sqrt{R_1 R_2}} \tag{1.98}$$

The physical length L could be directly measured from one reference device. It was done by Scanning Electron Microscopy, resulting $L = 258\mu m$.

Anyway, we proceeded also with the FP resonances, measuring the Free Spectral Range (FSR), that is the spacing $\Delta h\nu$ between maxima in Fig.1.23, that is linked to Optical Path Length (OPL) nL.

$$nL = \frac{hc}{2\Delta h\nu} \tag{1.99}$$

where h is the Planck's constant, c the light speed in vacuum and n the refractive index. It resulted $nL = 0.0903cm$, that indicates $n = 3.5$, a perfectly acceptable value for the given material and optical frequency. The joint use of (1.96) and (1.97) leads to the linear relationship

$$S_i = L\alpha_T - Lg_m H_i \tag{1.100}$$

I	V	V_j	S	HL	HH
6.98	1.003	0.949	2.297	-0.022	-0.018
8.03	1.018	0.956	1.889	0.039	0.030
9.01	1.030	0.961	1.292	0.088	0.070
10.05	1.043	0.966	0.964	0.134	0.106
11.13	1.056	0.97	0.629	0.176	0.140
12.11	1.067	0.974	0.431	0.210	0.167

Table 1.2: Experimental measurements of terms in (1.100).

Where the suffix i indicates that several measurements can be performed at different injection levels. Table 1.2 reports a set of such measurements, where H was calculated for both the case of light holes (HL) and heavy holes (HH). For both cases (1.100) was used for a least square fit.

The difference in the last two columns is due to the different value of ϵ, that on one side modifies the curve described by (1.96) and on the other leads to different values for its minimum g_m. It interesting is to observe Fig.1.24, that plots both curves vs. the applied voltage V and also the experimental gain values measured by means of the Hakki-Paoli method. The two curves are the same curve for the whole positive range of the gain function, and also for an extended range below the transparency, much more extended than the range explored by the Hakki-Paoli method.

Moreover, it could be shown that setting $\epsilon = 0$, one would obtain a curve undistinguishable from that of the light holes. Even more, any other value of ϵ, including the extreme ones corresponding to degeneracy in the doping level, would lead to the same result: beyond some negative gain level, all fitting curves do coincide.

The practical meaning of Fig.1.24 is that a simplified version of (1.96) should be proposed, holding for all the practically important gain values, with the exception of its deep range close to the minimum:

$$g = g_m \frac{1 - \exp\left(\frac{h\nu - qV_j}{2kT}\right)}{1 + \exp\left(\frac{h\nu - qV_j}{2kT}\right)} = g_m arcth\left(\frac{h\nu - qV_j}{2kT}\right) \tag{1.101}$$

In order to better visualize the various excitation levels involved in this study, Fig.1.25 reports the standard L-I curve of the same device as in fig.1.22, fig.1.23 and fig.1.24. The threshold current is measured at about 13 mA. The box HP indicates the range of excitation values at which the spectra have been measured for applying the Hakki-Paoli method. It should be appreciate that all them are

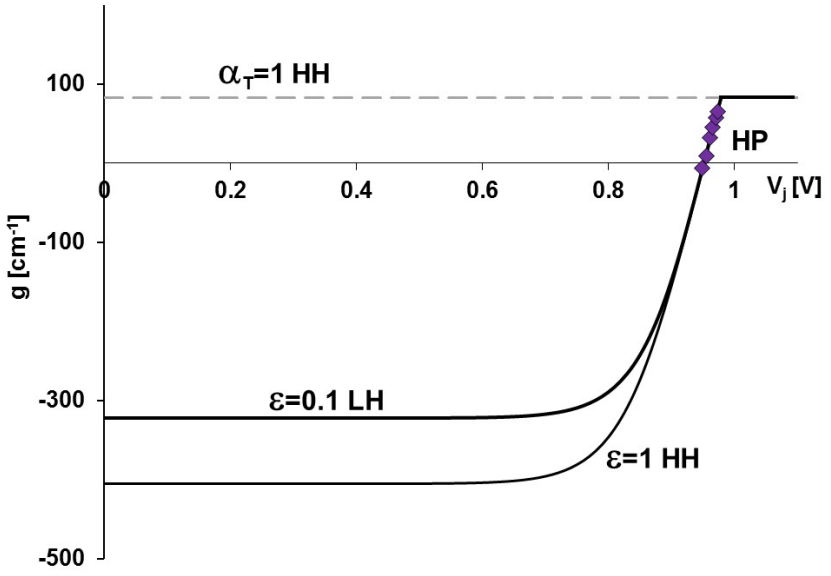

Figure 1.24: Absolute gain measurement for two values of the parameter ϵ. HP indicates the experimental values calculated by the Hakki-Paoli method.

lower than threshold, so fulfilling the recommendation issued by Cassidy [38] with respect to possible effects of the resolution of the spectrometer when spectra are measured above-threshold.

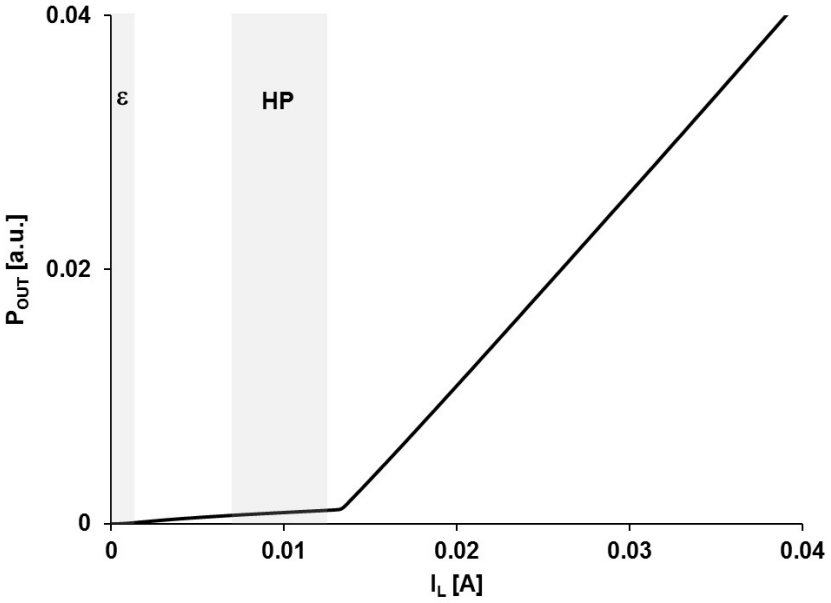

Figure 1.25: The general L-I curve for the DFB laser diode under investigation. The box HP indicates the injection range for the Hakki-Paoli method, while the box ϵ indicates the low current values for which gain curves, as in Fig.1.24, can depend on the actual value of ϵ.

But, even more important, the use of sub-threshold data in (1.100) leads to

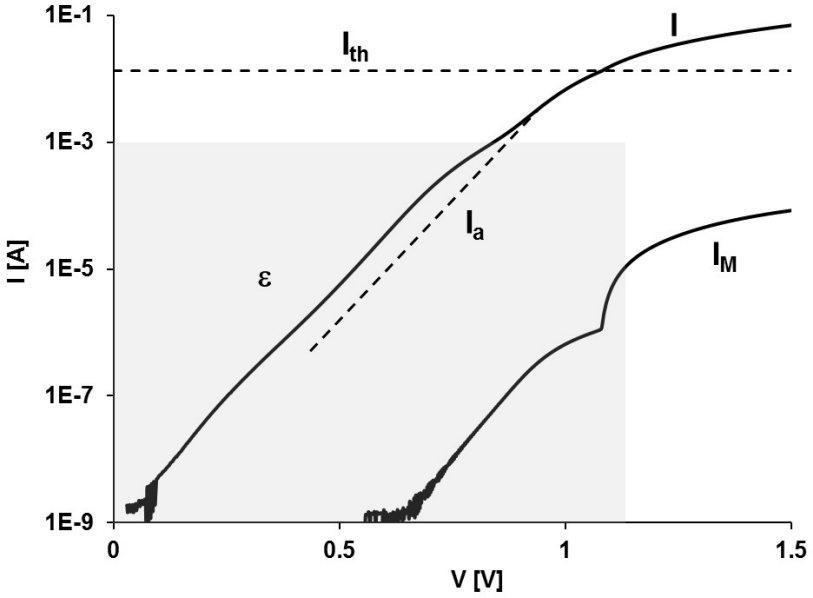

Figure 1.26: The box indicates the range of voltage and current where the actual value of ϵ modifies the gain curves. The dashed line I_a indicates the current of the active area [2]. The extra current is due to lateral currents, not completely confined under the ridge. I_M is the current measured from the monitor diode.

the determination of α_T as a coefficient in a linear relationship, not necessarily related to any saturation. It is then relevant to observe that that same numerical value comes out from the gain equation when the threshold voltage $V_j = V_{th}$ is introduced in (1.96), no matter the value of ϵ.

Finally, it is also interesting to observe that the region where ϵ makes the difference in gain formulas corresponds to the low injection range where, in a ridge structure, even current confinement is not complete, as shown in fig.1.26.

1.2.6.3 Hakki-Paoli method and DFB

The last considerations have defined the boundaries of application of (1.95), one of the crucial points of this study. The other most important issue is the suitability of the Hakki-Paoli method for DFB devices. This requires a slightly different approach than the standard one that operates within the so-called Coupled-Wave framework [55, 56]. The Coupled Wave Theory (CWT) gives nice results for the DFB reflection coefficient, up to replace the product R_1R_2 that defines the combined mirror reflectivity in a pure FP cavity with a more complicated but elegant expression that includes those same reflectivity coefficients and the DFB-specific reflectivity. Nevertheless, if one tries to use the solution of the CWT for calculating the optical field after the multiple round-trips, one never gets what Fig.1.23 shows, and in particular, an enhanced DFB peak castes onto the FP pattern.

For the limited sake of this study, we will first consider the DFB peak in Fig.1.23 as essentially *tuned* to one of the existing FP maxima. This means that one can assume that the cavity length L is an integer multiple of the DFB grating pitch a. If this holds, it is sufficient to recall that in the HP method [37] and in the

appendix C with the new mathematical reconsiderations, the amplitude F of the travelling wave whose propagation is considered after several round trips is given by

$$F(x) = F_0 \left[\exp\left(-\frac{\alpha_T - g}{2} x \right) \exp(ikx) \right] \tag{1.102}$$

and this leads to a final intensity

$$\mid F \mid^2 = \frac{\mid F_0 \mid^2}{1 + \exp(-2(\alpha_T - g)L) - 2\exp(-(\alpha_T - g)L)\cos(2kL)} \tag{1.103}$$

from which maxima and minima are calculated and lead to (1.97). We replace the plane wave of (1.102) with the Bloch solution

$$F(x) = \exp\left(-\frac{\alpha_T - g}{2} x \right) \left[\exp(ikx) \sum_m F_m \exp\left(i\frac{2\pi m}{a} x \right) \right] \tag{1.104}$$

It can be easily verified that, after several round trips of length L multiple of a the result in (1.103) is simply modified in its numerator, where $\mid \sum_m F_m \mid^2$ replaces $\mid F_0 \mid^2$. Provided one assumes that the DFB resonance, due to the finiteness of the cavity, has a linewidth large enough to include the next minimum, the HP method results suitable for gain calculations.

The proposed method essentially aims to extend the range of practical measurements of modal gain to DFB laser diodes, validating and extending the Hakki-Paoli method, originally developed only for FP devices. The measurement procedures are non-destructive and can be applied to packaged devices whose construction details are unknown.

The role of details as band asymmetries or even material doping have been shown to be relevant only in the very low current range, as illustrated in fig.1.25 and fig.1.26.

This result is also relevant for a model developed and applied during the past years [2,3,35,49,50], where the approximation corresponding to $\epsilon = 0$ is implicitly assumed. This subparagraph shows up to what extent this can be acceptable also for that general model.

1.3 Clamp Voltage and ideality factor in laser diodes

The proposed model for laser diodes was applied to the decomposition of the experimental characteristics of several laser diodes into their fundamental components. This pointed out a problem involving the ideality factor and the clamp voltage. The two quantities indicate largely different values of the internal voltage, not explained or predicted by any theory. The solution of the puzzle requires going back to points as fundamental as the meaning of locality of band-to-band transitions in quantum or bulk active regions

This paragraph deals with a puzzle that troubled the authors along a couple of years, after having published [1–3], the new theoretical model for the DC characteristics of a laser diode (LD). The initial prompt, and the main application field of

such a new model, was the search for an interpretation tool for the evolving characteristics of a LD under degradation [35]. In particular, the model attempted the numerical fit of the experimental DC curves by adjusting the relevant coefficients of a set of equations strictly derived by physical considerations. The protocol described in subparagraph 1.1.6 [35] illustrates how to decode the experimental data and reconstruct, for instance, the separate contribution of the radiative and non-radiative phenomena to the overall conduction.

Compared to that model, two experimental points remained puzzling: the apparent continuous reduction of the series resistance beyond the threshold condition, and the measured internal threshold voltage as the upper limit of the sub-threshold domain. The former will be discussed and solved specifically in a next paragraph, while the latter is the subject of this section.

The kernel of the problem can be summarized as follows: experimental data for several different laser diodes show that the pure radiative component I_{ph} of the total laser current I exactly behaves as in a Shockley diode with an ideality factor $n > 1$. This is not surprising for a MQW structure, as it will be discussed in the following subparagraphs, and simply states that the effective internal voltage V_{in} driving the optically active material is n times lower than the voltage V applied to the electrical junction. But the threshold condition, that is the experimentally observable clamp of the junction voltage $V = V_{th}$, always occur at $qV_{th} \approx h\nu$, where q is the electron charge and $h\nu$ is the peak photon energy, and not at $V = nV_{th}$, as the sub-threshold domain predicts.

The simplest explanations based on ohmic effects or parasitic currents fail after simple considerations, and the problem stands in its full evidence.

The paragraph will start from experimental measurements on a real device, according with the protocol described in 1.1.6 and [35], and will then summarize the results of the model reported in 1.1 [1–3] that are relevant for this work.

The attempt to fit theory with experiments will point out the puzzling question of the effective voltage. With the aid of further experimental data, belonging to both bulk and Quantum Well active area devices, it will be proposed an interpretation, that calls into play concepts as fundamental as the locality of photon-charge interaction.

1.3.1 Experimental data and modeling

Fig.1.18 displays the experimental characteristics of an edge-emitting DFB laser diode in ridge technology tuned at 1310 nm. This representation follows the protocol proposed in the subparagraph 1.1.6.

Moreover, the displayed voltage range focuses, in this paragraph, on the injection levels close to threshold, and neglects the lower current range (highlighted area on the left), due to lateral conduction paths. Those lateral currents are relevant only in the sub-mA range for a device as in fig.1.18, and are not significant for this study. Anyway, they have been duly considered and completely modeled in [2].

Several other features of fig.1.18 should be commented. The threshold voltage V_{th} now appears as a vertical asymptote for all currents, while the threshold current I_{th} is the corresponding value of the current I. The quoted references refine the last

statement, showing that the real definition of the threshold current is the value that the sole I_{nr} assumes at $V = V_{th}$. The small contribution of the radiative current I_{ph} to the total current I in the sub-threshold range, experimentally confirmed in fig.1.18, makes the identification $I \approx I_{nr}$ reasonable for practical cases. Anyway, both theory and direct inspection of the numerical data from experiments show that I_{nr} does clamp at the value $I_{th} = I_{nr}(V_{th})$ (1.54), while I continues increasing, because of (1.52), following the increase of I_{ph} even when voltage clamps. This particular feature of I_{ph} is possibly the most peculiar result of the cited model, that describes that current by means of the formula (1.46), The reference voltages in fig.1.18 are, respectively, the transparency voltage

$$V_{tr} = \frac{h\nu}{q} \tag{1.105}$$

at which stimulated emission balances absorption, and gain is null, and the threshold voltage can be rewritten from (1.41):

$$V_{th} = V_{tr} + \frac{2kT}{q} \ln\left(\frac{1+R}{1-R}\right) \tag{1.106}$$

that is the value of the internal voltage at which the denominator in (1.46) vanishes. It is evident from (1.106) that $V_{th} > V_{tr}$ and that the condition for voltage clamping at a finite value, that is for achieving the laser regime, is $R < 1$.

For the case given in fig.1.18, one has $V_{th} = 0.993$, $V_{tr} = 0.947V$, and, at room temperature, $R = 0.42$.

It is intriguing the parallelism (that means the proportionality) of all currents in the sub-threshold range in fig.1.18, and have discussed it in the previous paragraph 1.1. Anyway, for the scope of this part, the sole I_{ph} is relevant, so that we will focus on it in the following.

The plot of I_{ph} calculated from (1.46) and the experimental measurements as in fig.1.18 will show, in the next subaragraphs, a nice qualitative agreement: the sub-threshold range (when exponentials in the denominator of (1.46) are negligible with respect to the unity) displays a Shockley-like behavior, that is an exponential dependence of current on voltage. As far as the voltage approaches the threshold limit (1.106), the current I_{ph} increases rapidly, up to dominate over all other currents, and the non-radiative I_{nr} blocks (1.54).

1.3.2 Ideality factor and threshold voltage

When one moves to a more quantitative analysis, two differences appear between theory and experiments: the transition at threshold is sharper in the experimental curves than in the theoretical ones, and the slope of the sub-threshold branch in real data is significantly lower than predictions.

Measuring the slope of I_{ph} in the sub-threshold range in fig.1.18, one gets an ideality factor $n = 1.4$, instead of the expected $n = 1$. At a first glance this seems not a problem: many diodes show non-unitary ideality factors, and even the seminal work of Shockley [15] predicts that, in case of recombination inside the depletion layer (that is the case for optical emitters, although radiative

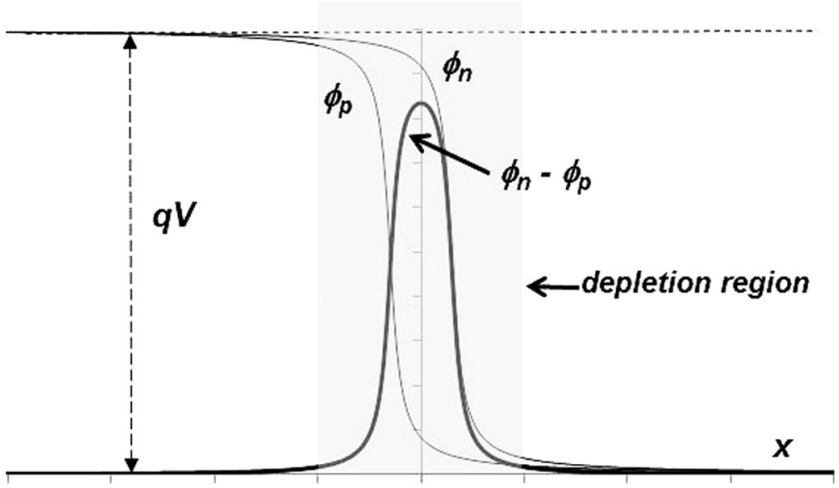

Figure 1.27: Quasi-Fermi levels ϕ_n and ϕ_p in a junction where all recombination takes place inside the depletion region. Their difference is everywhere lower than the junction bias qV.

recombination hopefully overcomes trap-driven transitions), the ideal voltage V appears reduced.

The interpretation, indeed, of a value $n > 1$ could be that recombination leads several carriers to be lost before they reach the region where the dominant recombination rate takes place, as represented in fig.1.27. This means that the leading current appears to depend not on $\exp(qV/kT)$, but on $\exp(qV/nkT)$, with $n > 1$. This would simply require to re-define the"internal voltage" that appears in (1.52) as a fraction of the nominal voltage, even after having removed the ohmic contribution.

Here the problem arises that a reduced voltage would also re-scale the value of both V_{tr} (1.105) and V_{th} (1.106), which does not appear in experimental data.

In order to clarify the last point, fig.1.28 shows an attempt to use (1.46) for fitting data of fig.1.18. The bold lines represent the cases of $n = 1$ and $n = 1.4$. The corresponding values for both V_{tr} and V_{th} are brought into evidence. It should be noticed that the last case shifts the transparency voltage V_{tr} at more than $1.3V$, which is well beyond the observed value of V_{th}.

To support the statement that the measured V_{tr} really depends on V and not on V/n, we can recall the results obtained in an experiment [36] where a Focused Ion Beam (FIB) was used to modify the optical losses in a 1310 nm ridge laser diode, and then to change both V_{th} and I_{th}. The modified thresholds not only followed the theoretical expectations, but also allowed to extrapolate their values to the ideal case of no-losses, when threshold and transparency coincide. It resulted $V_{th0} = V_{tr} = 0.947V$, that is exactly the value of $h\nu/q$.

In other words, the sub-threshold range looks depending on a reduced voltage ($n > 1$), while the threshold voltage seem to follow the full voltage ($n = 1$). The two requirements by no means can be simultaneously fulfilled in (1.46).

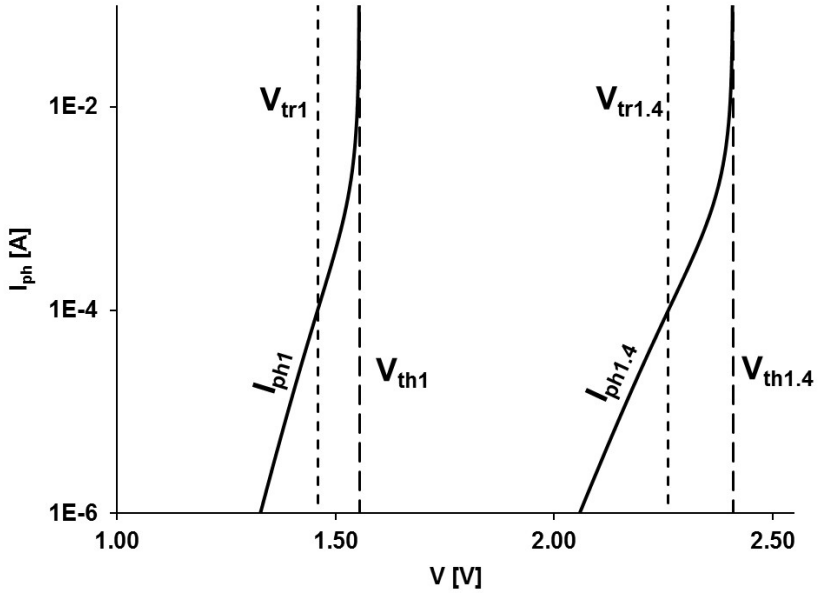

Figure 1.28: I_{ph} curves calculated, by means of (1.46) for $n = 1$ and $n = 1.4$, trying to fit experimental data of Fig.1.18.

1.3.3 Curve fitting

The first step toward the solution of the puzzle is to observe that a suitable superposition of several functions I_{ph}, as given by (1.46), can lead to properly fit the experimental curves.

Let us start with fig.1.29, referring to a 850 nm GaAs-based VCSEL, that is known to have a single active layer, thick enough to be considered closer to a bulk layer than a Quantum Well. The transparency voltage is accordingly calculated as $V_{tr} = 1.459V$, while the threshold was measured at $V_{th} = 1.555V$. This is compatible with the theoretical $n = 1$ curve, with a loss/gain ratio $R = 0.7$.

The sub-threshold branch, on the other hand, shows an ideality factor $n = 1.55$, and the transition appears sharper than the expectation from (1.46). Anyway, a very good fit results from a suitable linear combination of two I_{ph} curves, one depending on V/n and one on V. The first nearly completely recovers the sub-threshold range, while the second, that defines the threshold voltage, is suitably scaled down, in order to adjust the transition. It is not necessary here to grant this patchwork with too much significance: it is just a phenomenological observation that will call for deeper analysis in the following.

A second example (fig.1.30) is a 1310 nm DFB laser, as for the case in fig.1.18, but in Buried Heterostructure (BH) technology.

The obvious question is about the physical meaning of the superposition of just two theoretical and conflicting curves to get proper fitting of experimental data. To this purpose, fig.1.31 may help. It has been calculated superimposing not two curves, but a continuous set of curves I_{ph} spanning a given interval n_1, n_2 of values of the ideality factor n, weighted by an adjustable peak function $P(n)$:

$$\int_{n_1}^{n_2} P(n) I_{ph}\left(\frac{V}{n}\right) dn \tag{1.107}$$

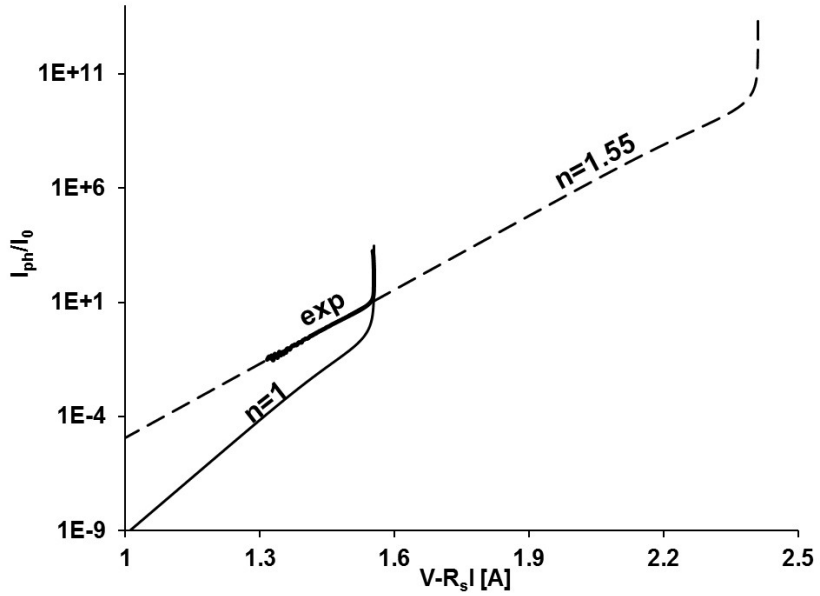

Figure 1.29: Experimental I_{ph} (bold line) for a 850 nm VCSEL and the two fitting curves (thin lines), calculated from (1.46).

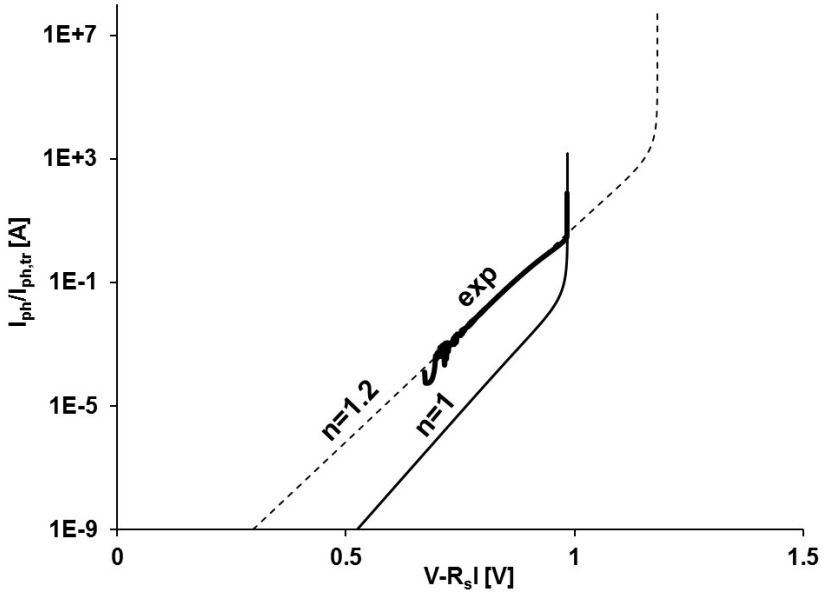

Figure 1.30: The same as in Fig.1.29 for a 1310 nm BH DFB laser diode.

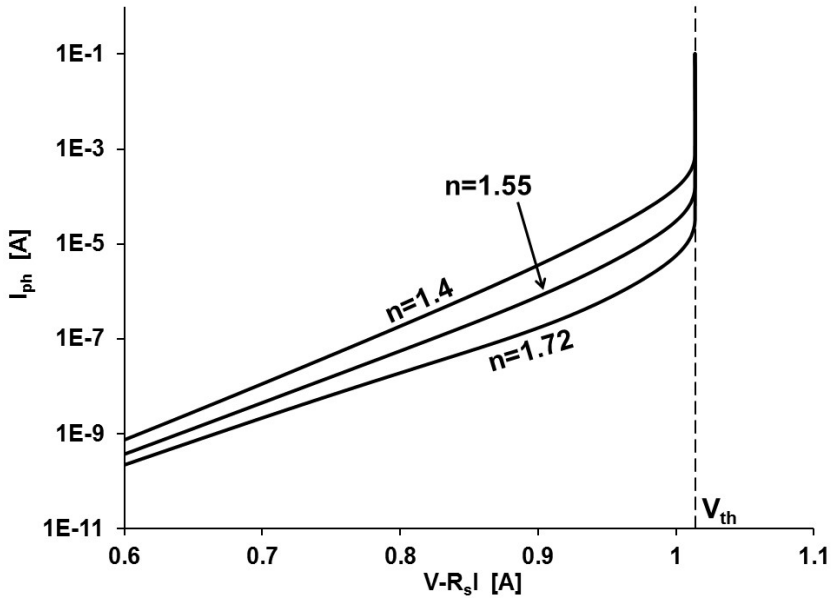

Figure 1.31: The continuous superposition in (1.107) gives curves with different slope for different shapes of the peak function $P(n)$, but with the same threshold voltage, corresponding to the threshold of the I_{ph} function with the lowest value of n.

The specific case reported in figure refers to n ranging from 1 to 2, and a gaussian peak function P with $\sigma = 0.1$,whose maximum is shifted from $n = 1$ to $n = 1.5$ and $n = 2$. The resulting I_{phTOT} curves display, for $V < V_{th}$, a slope corresponding, respectively, to $n = 1.72$, $n = 1.555$ and $n = 1.4$. The relevant result is that all curves display the same threshold V_{th} of the component $I_{ph}(V)$, corresponding to the minimum value $n = 1$.

The scope of (1.107) is to represent, at least qualitatively, a situation similar to fig.1.27, where several different separations of the quasi-Fermi level concur to the total recombination rate. The result is a curve that strictly resembles the ideal I_{ph}, keeping the correct threshold voltage while the ideality factor deviates from unity.

It is then possible to imagine that a suitable choice of the extremals of the integral and of the shape and position of the peak function P in (1.107) can fit real data.

1.3.4 Ideality factor

At a first glance, in order to explain $n > 1$, in LEDs or laser diodes, three other causes could be considered, besides the distributed recombination inside the active layer represented in fig.1.27: ohmic effects, diffusion currents, and Shockley–Read–Hall (SHR) recombination. Anyway, the first have been removed by introducing the reduced abscissa $V - R_S I$, and in any case no ohmic effect can reduce V to the same V/n at any injection level. On the other hand, diffusion currents have been considered since the original papers [1–3] as the residual Shockley current due to incomplete recombination inside the active region, and have been

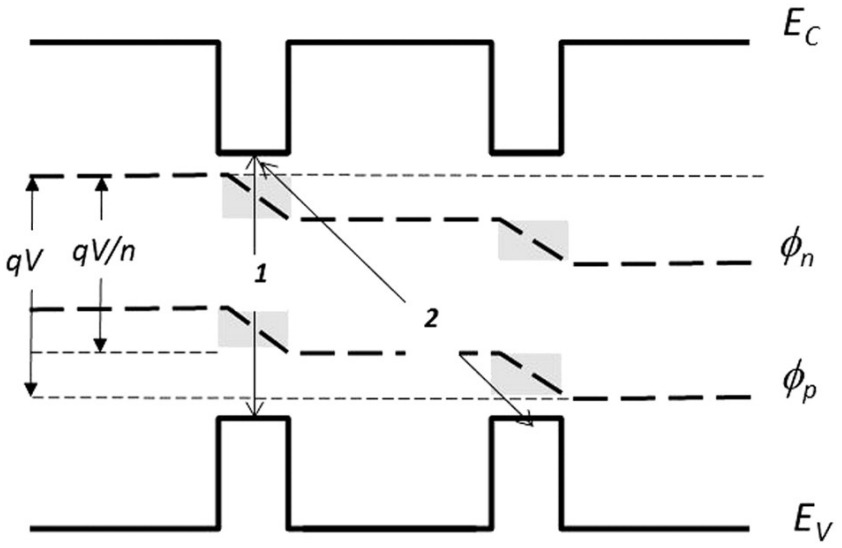

Figure 1.32: Local and non-local transitions in an ideal double Quantum Well

shown to be negligible in real devices. Finally, the Shockley–Read–Hall mechanisms could justify non-unitary values for n, but limited to the sole non-radiative components (because none of such recombination mechanisms contributes to light emission), while we are investigating the ideality factor of the sole radiative current I_{ph}, no matter the behavior of any other current in the laser diode.

1.3.5 Non-local interactions

All rate equations for photon emission rely on the joint densities of electrons and holes, that is, they imply "bimolecular" recombination [31]. This, in turn, calls into play the full separation of the quasi-Fermi levels, and never a fraction of it. The theoretically expected clamp of such separation and the observation of a clamping voltage in the $V - R_S I$ representation identifies the measured internal voltage with $\phi_n - \phi_p$, and brings back to the problem of the origin of an ideality factor $n > 1$.

The superposition in (1.107) and fig.1.31 partially solves the problem, showing as a distributed recombination across the active layer can both justify the non-unitary ideality factor and the occurrence of a fixed threshold voltage. But it gives, indeed, the correct threshold voltage only if the lowest limit in the integral is exactly $n_1 = 1$. This means that transitions involving the full separation of the quasi-Fermi levels must be included in the range of the possibilities. Looking again at fig.1.27, this seems impossible.

The point is that, in fig.1.27, we consider each recombination rate ruled by the difference between the quasi-Fermi levels calculated at the *same position*. In other words, we invoke strictly *local* interactions.

The situation is, if possible, even more evident if we consider a Multi Quantum Well. Fig.1.32 describes an ideal double quantum well, that is supposed to be immersed in the middle of the depletion region of a Heterojunction Diode, and draws the qualitative behavior of the quasi-Fermi levels, assuming for simplicity that recombination only takes place inside each well.

It should be evident that none of the wells "feels" the complete separation of the quasi-Fermi levels, as ref. [58] clearly shows for LED devices. In other words, any attempt to bring any QW first to transparency and then to threshold, would require to apply a total voltage to the MQW stack equal to or higher than $qV = nE_g$. This holds until we consider local transitions, as the vertical arrow, labeled "1" in fig.1.32. But if we accept the idea that also the transition labeled "2" has a non-null probability, then the whole building of the previous subparagraph 1.3.3 gains physical soundness.

Anyway, this last transition should be handled with care. It cannot be a two-step event, for instance, first tunneling from one well to the other, followed by local recombination. In this case, the tunneling would "filter" the flux of charge, allowing only part of the carrier densities to penetrate the other well. This would, in turn, reduce the quasi-Fermi levels, i.e., for electrons, leading back to the reduced separation.

On the contrary, we could suppose that the tunneling is so probable that electrons from the well on the left, in fig.1.32, will flood the well on the right, and the same for holes on the reverse direction, without significant reduction of their density. By the way, this is one of the ways for reading Quantum-Cascade devices. But, would this be the explanation, then also the recombination rate in the sub-threshold range should follow the full separation qV of the quasi-Fermi levels.

The point is that, in order to have a transition at full separation qV and $n > 1$, we should consider that the population of electrons on the left well can interact with the population of holes in the one on the right. Only in this case we can achieve transparency applying a voltage that is $V_{tr} = h\nu/q \approx E_g/q$, and a measurable threshold V_{th} that is only few percent higher than V_{tr}.

Furthermore, the evidence of a non-unitary ideality factor, given by the sub-threshold branches of all experimental cases, states that such a non-local transition should be much less probable than local processes. This is the meaning of the relative position of the two I_{ph} curves in both figs. 1.29 and 1.30: the component depending on V must be much lower than $I_{ph}(V/n)$ in the sub-threshold range. This makes sense: local transitions are likely to be much more probable than non-local ones. It seems reasonable that such situation may be common to all diodes, and not peculiar of laser diodes.What is peculiar is that, in optical emitters, the radiative component I_{ph} behaves as described by (1.46), with its vertical increase at threshold. This feature allows a current, that should be negligible in all other cases, to become dominant as far as the bias reaches the threshold V_{th}.

It seems necessary to accept in full the ultimate consequence of the Uncertainty Principle that leads to non-locality of the interaction. If one considers the different linewidth of the spontaneous and stimulated emission, it follows that the sharp definition of the electron–hole transition energy for a stimulated process requires an uncertainty in the carrier position larger by far than the thickness of the active regions, no matter if bulk, QW or MQW. On the contrary, the much wider lineshape of the spontaneous transitions allows locality to keep some meaning, and classical (including MQW transitions) recombination rates between carriers may be distinguished by their position.

The non-local interaction is of course not new, and is based on the overlap of the electron and hole wave functions in quantum-sized solid-state structure sys-

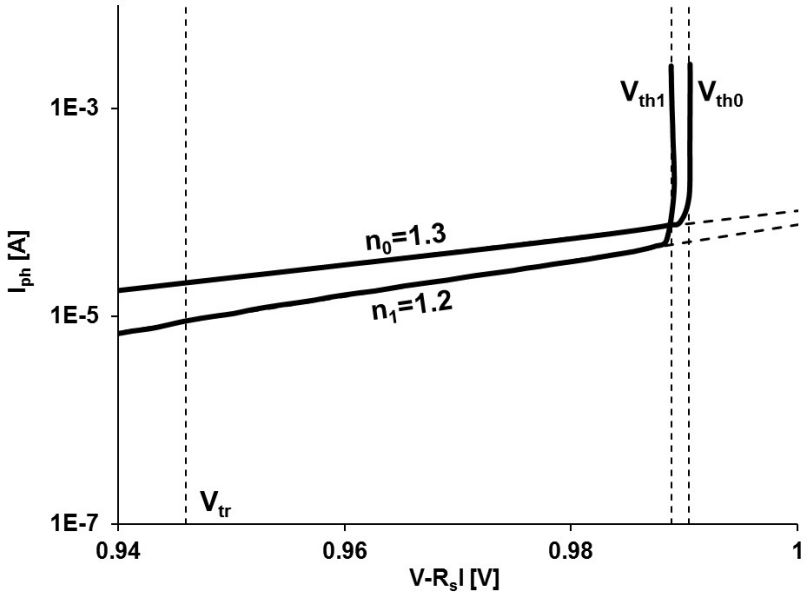

Figure 1.33: Effects of 3 MeV proton irradiation on a 1310 nm InP edge emitter. Curve 0: before irradiation. Curve 1: after irradiation.

tem. It is mentioned in several experiments as Quantum Coupling, for explaining observations in closely spaced Quantum Dots and micro-cavities (see ref. [59, 60] for examples).

Anyway, in the current paragraph, non-locality is called into play for explaining features as simple as DC characteristics displayed even by commercial optoelectronic devices. Its novelty should be then surprising, because of the decades of science and technology in this field. It may be useful to consider that two things allowed to point out the problem: a) the availability of (1.46), that predicts the behavior of I_{ph} continuously across the whole injection range and embeds the threshold condition as a computable consequence of theory, and b) the reference of the quasi-Fermi levels to the measurable applied voltage V, that brings down a laser diode to the practical playground of device engineering.

1.3.6 Application: proton irradiation on a 1310 nm DFB

The proposed update of an existing model for laser diode DC characteristics has been applied to the case of an InP-based DFB laser diode emitting at 1310 nm, that was irradiated by $3MeV$ protons for studying the effect of radiations on optical emitters for space applications. The complete report of that experiment, that shows the evidence of diffusion kinetics after irradiation, is presented in 3.4 and [61]. The result relevant for this paragraph is summarized in fig.1.33, where the sole I_{ph} is plotted, before and just after irradiation, versus the reduced voltage $V - R_S I$ as for the previous cases. For the sake of clarity, no calculated curve has been added, although excellent results can be easily obtained by the extended model, as reported for all previous cases. This allows focusing on the experimental evolution of the laser characteristics.

Contrary to the large majority of degradation cases, the threshold voltage V_{th1}

of the damaged device decreases with respect to its initial value V_{th0}, which should indicate a small reduction of the optical losses inside the cavity. In fig.1.33 V_{tr} indicates the ideal threshold voltage in case of no losses. In the sub-threshold range, on the other hand, the intensity of the radiative current reduces, which is typical of a smaller quantum efficiency of the active region. But the most intriguing figure is the reduction also of the ideality factor.

It is beyond the scopes of this paragraph even to attempt the physical interpretation of the observed characteristics, that display some puzzling features. The role of the proposed example is to point out that, at least in some particular cases, the accurate analysis of some degradation kinetics must include the possibility of changes also of the ideality factor. The proposed extended model operates in that direction.

The study of the electrical characteristic and Trans-characteristics of commercial laser diodes pointed out a contradictory determination of the separation of the quasi-Fermi levels in the sub-threshold and above the threshold ranges. Several practical explanations have been considered, all based on classical arguments in Physics of Solid State Devices. Nevertheless, only the reference to deep Quantum Mechanical concepts as non-locality of photon-induced electron–hole transitions seems to be able to fully solve the contradiction.

A fascinating experiment could be imagined to verify the proposed interpretation: would it be possible to build a laser diode with two Quantum Wells of different bandgaps, and provided that the selection rules allow the "non-local" transitions, then lasing would take place at a photon energy different from the characteristic emission of each of the two wells.

1.4 Incomplete threshold and effective R_S.

The previous paragraph 1.3, dealing with the puzzle of the ideality factor, opened the series of the refinements required for practical application of the general model. This paragraph will deal with another point that shares, with the previous one, a common issue: the observed clamp voltage V_{th} in real devices [57]. That voltage is predicted to be a constant (1.41), and its experimental value should be given by first calculating the series resistance R_S by means of the differential curve dV/dI as shown in fig.1.12, and then re-plotting the general current-voltage characteristics as a function of the reduced voltage $V - R_S I$: all current components I_{nr}, I_M, I_{ph} measured for $I > I_{th}$ should then align along a vertical line, exactly located at the abscissa $V = V_{th}$. The problem in real devices is that the value of R_S should be itself a constant for $I > I_{th}$, but it is not. The series resistance, indeed, seems to monotonically decrease as the current I increases. This phenomenon has been observed by several authors in the past [62–64] but non completely justified. This section will start with the statement of the problem by analysing experimental data for a real device. It will then propose a solution with two different approaches: one strictly analytic, based on a network of distributed elements, that is still in process and for this reason reported in Appendix D, and one numerical based on a limited number of discrete components reported in the next subparagraph 1.4.3.

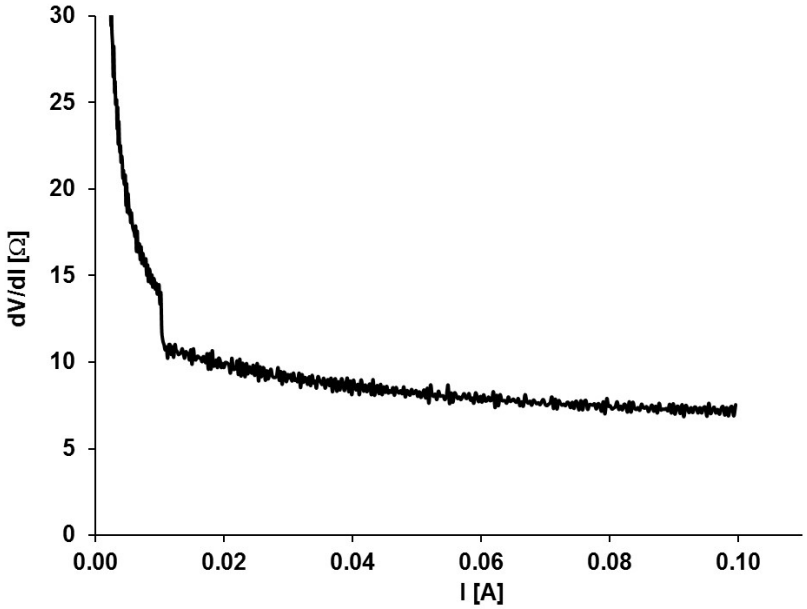

Figure 1.34: First derivative dV/dI as a function of the total current for a DFB-LD 1310nm.

1.4.1 Experimental data

The core of the problem can be summed up in this way: experimental data for different kind of laser diodes show progressive and monotonic reduction of the series resistance beyond the threshold. This was not so evident in fig.1.12, but appears relevant in cases as in fig.1.34. It is evident that R_S is not a constant but presents a drastic decrease with the increase of the current. In more detail, it is possible to notice that at threshold the corresponding R_s is about 10.1Ω, but after $80mA$ the value of the resistance falls at about 6.9Ω, a reduction of 30%. As a consequence, the plot of the current, as a function of the voltage without the effect of the R_s shows an overturning rather than a fixed clamp voltage (fig.1.35) [1, 2].

Generally, this phenomenon is attributed to thermal effects, but this looks impossible, because the resistance should increase, and not decrease, with temperature. Anyway, also an experimental proof has been obtained to support that preliminary conclusion. DC or pulsed measurements in pulse conditions have been collected for a same device, in order to discriminate the thermal effects. The conditions of the pulsed measurements are:

- pulse width $1\mu s$
- pulse current level $100mA$
- delay time $1ms$

The red line in fig.1.36 is the measurement in pulsed mode while the black line refers to DC conditions. It appears evident that no thermal effect can be responsible for the observed anomaly in the dV/dI curve. For this reason, it is possible to conclude that the decrease of the series resistance can not be ascribed to thermal effect.

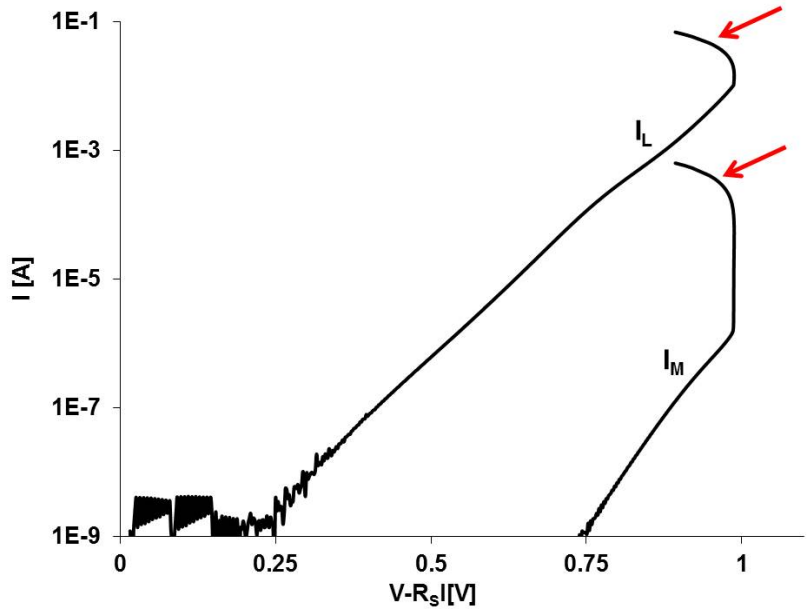

Figure 1.35: Total laser current and monitor current as a function of the voltage reduced of the effect of the series resistance.

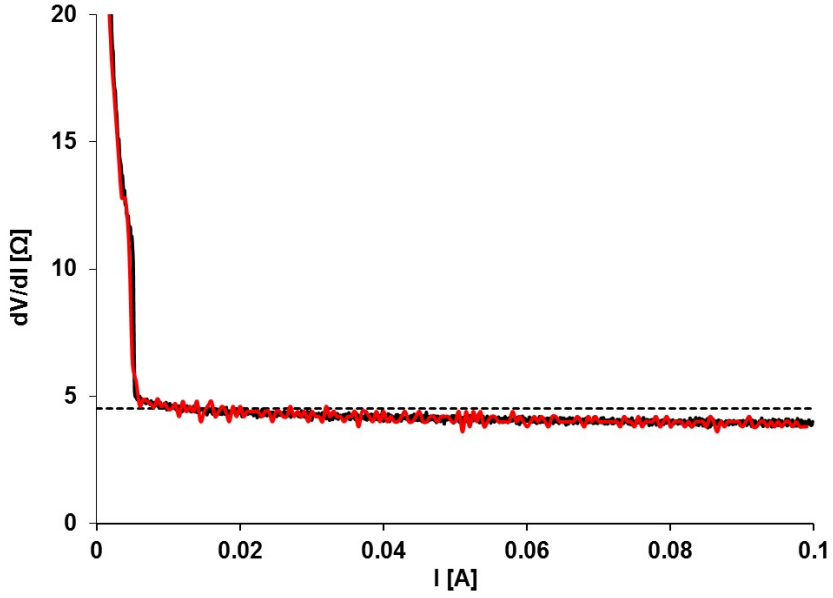

Figure 1.36: First derivative plot from measures in pulse and continuous condition.

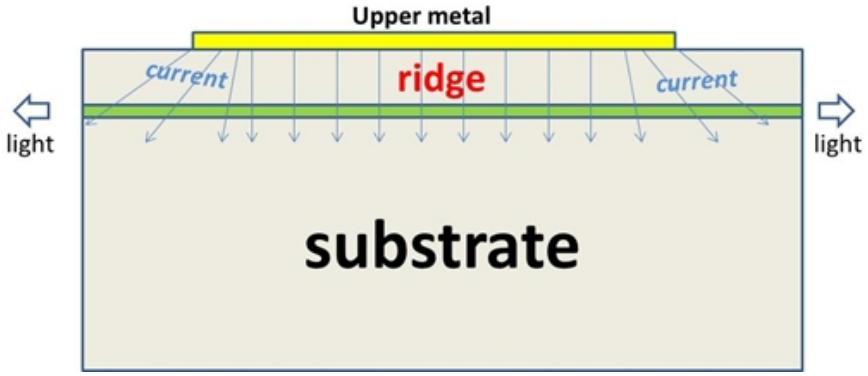

Figure 1.37: Different current paths from the upper metal contact to the electrical junction

The reason for the apparent reduction of R_S has been then investigated starting from the hypothesis that the active region under the long and narrow ridge does not reach the lasing threshold at the same time everywhere. The cause of that inhomogeneity should be the different current paths from the upper metal contact to the electrical junction (fig.1.37), that are associated to different ohmic voltage drops. The construction made in fig.1.8 for dealing with lateral currents may help: the junction line (that in this case fig.1.37 runs along the length of the optical cavity, while in fig.1.8 it was transversal to it) can be imagined made of several identical "diodelets" whose mutual connection and that with the equipotential metal contact is made of small ohmic resistors. In this structure, the threshold condition first appear at the diode elements close to the metal contact. When the metal voltage further increases, the voltage of those elements will remain clamped, but the threshold will be likely to propagate laterally, also modifying the apparent total series resistance.

1.4.2 Parameters from real devices

The parameters entering the two models that have been developed are strictly linked to the physical and geometrical characteristics of real devices; in particular, the device chosen for the study is an InP-based Directly-Modulated-Distributed Feed Back (DM-DFB) edge-emitting laser diode, whose high modulation speed is achieved by a very narrow ridge, manufactured quite close to the active region (fig.1.38).

The typical geometrical proportions, evaluated on real devices, are reported in the draft of fig.1.39.

Assuming a uniform resistivity ρ inside the ridge, h is the height of the ridge itself, L is the length of the area connected to the metalization and Z is the corresponding width. Considering the series resistance, which corresponds to the series resistance measured at the threshold from experimental data, one has

$$R_S = \rho \frac{h}{LZ} \tag{1.108}$$

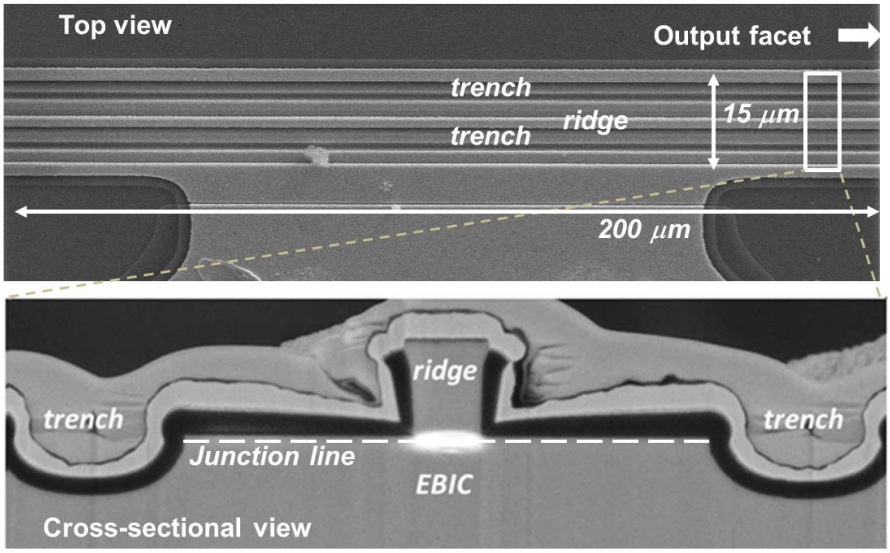

Figure 1.38: Top view and cross-sectional view of a DM-DFB Edge Emitter laser diode.

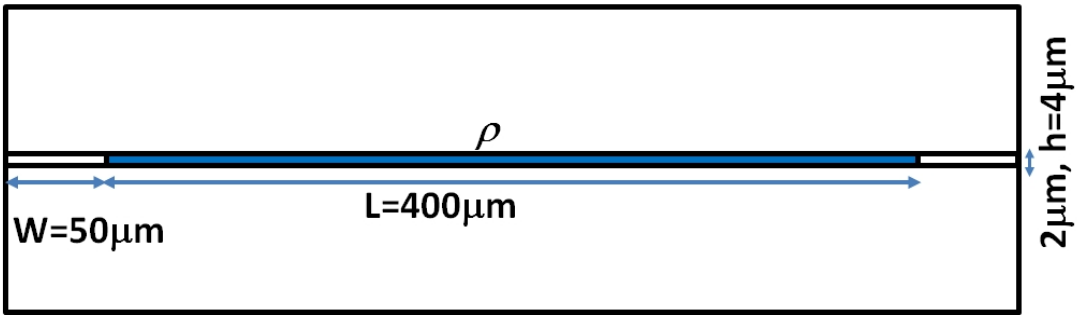

Figure 1.39: Typical geometrical proportion of a device with ridge structure.

The total resistance of the lateral path is

$$R_L = \rho \frac{W}{hZ} \tag{1.109}$$

We can simplify some expressions by introducing the coefficient

$$R_0 = \frac{\rho}{Z} \tag{1.110}$$

so that

$$R_S = R_0 \frac{h}{L} \tag{1.111}$$

$$R_L = R_0 \frac{W}{h} \tag{1.112}$$

1.4.3 The discrete numerical model

The first check of the hypothesis of a propagating threshold can be done by a simple numerical model, where a network of discrete identical elements, connected

by ohmic links, represents the various parts of the real device. We start from a base element as in fig.1.40 (a) [1–3,35,36,57], that represents the diodes responsible for the the radiative and non-radiative currents in a small section of the active area, and the corresponding ohmic path towards the metal contact. This element is here graphically simplified as indicated in fig.1.40 (b).

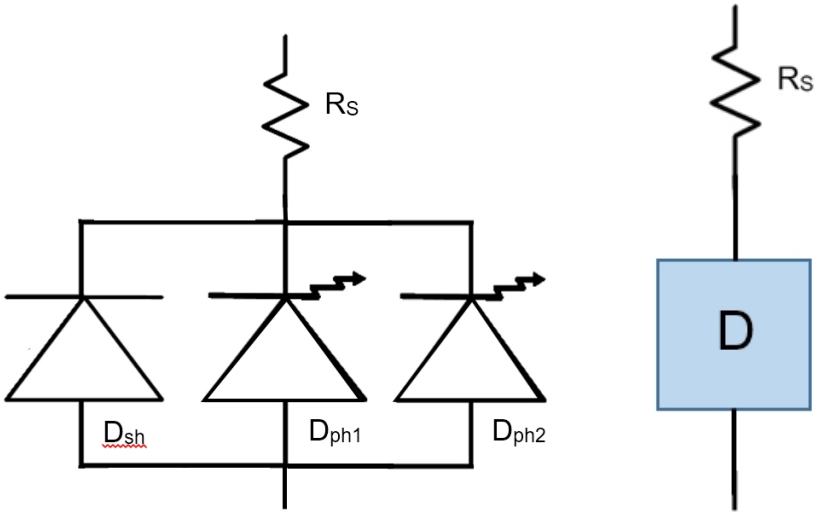

Figure 1.40: The historical model (a) and the schematic symbol (b) to identify it in the new simulation.

Ten base elements have been linked as shown in fig.1.41. The first element of the circuit represents the section under the ridge, that is assumed equipotential. In other words, that first element is equivalent to several parallel identical elements that, in turn are equivalent to a single diode and a single resistor suitably dimensioned. The network of the other elements, on the contrary, represents the terminal part (s) of the ridge, where currents flow after some ohmic path. The values of the vertical and horizontal ohmic elements follow the definitions (1.108)-(1.112) and the number of elements, as well as the equivalent area of each diode is taken proportional to the area of the first diode.

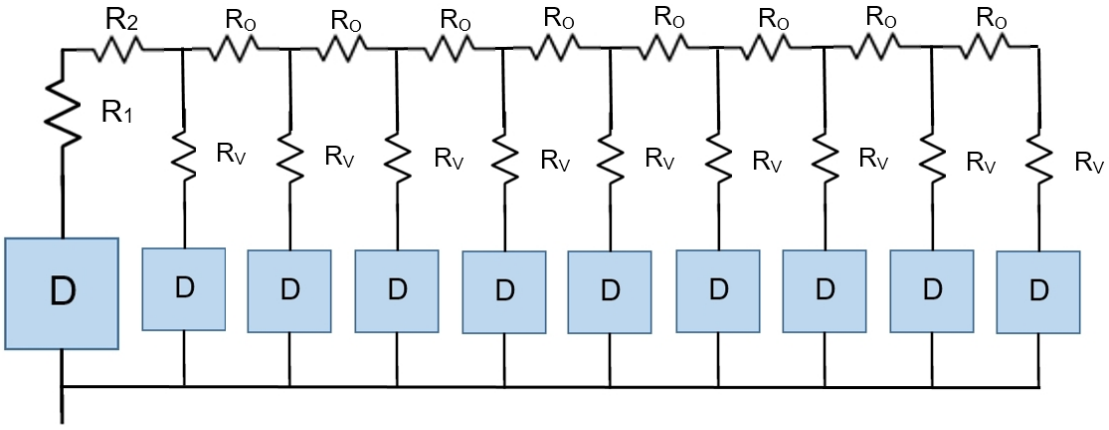

Figure 1.41: The model simulated with LTspice.

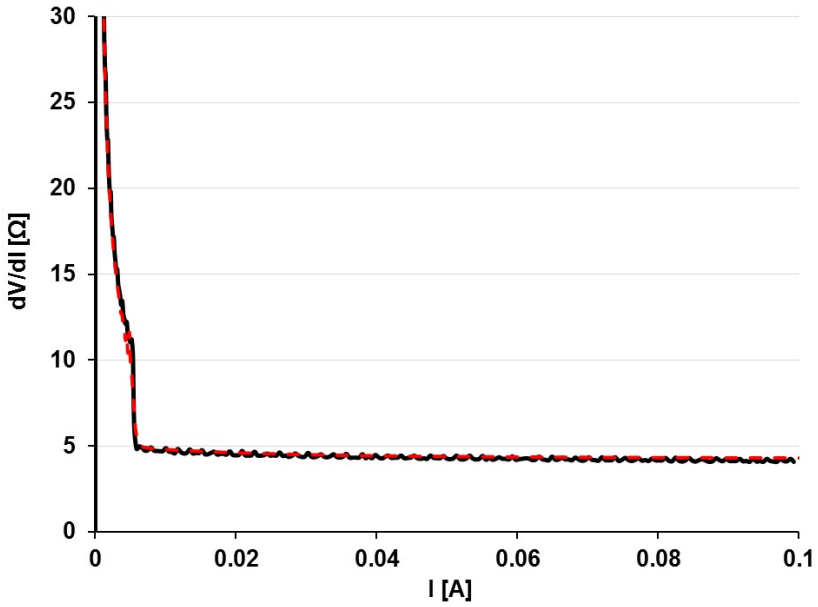

Figure 1.42: The resulting simulation (red curve) superimposed to the experimental curve (black). The same decreasing of the dV/dI is evident after the threshold with the increasing of the current.

The predicted electrical behavior of this structure is reported in fig.1.42 and fig.1.43, that, respectively, show the differential dV/dI and the current-voltage characteristics in the reduced-voltage representation. The calculated curves perfectly fit the experimental ones in the relevant region $I > I_{th}$.

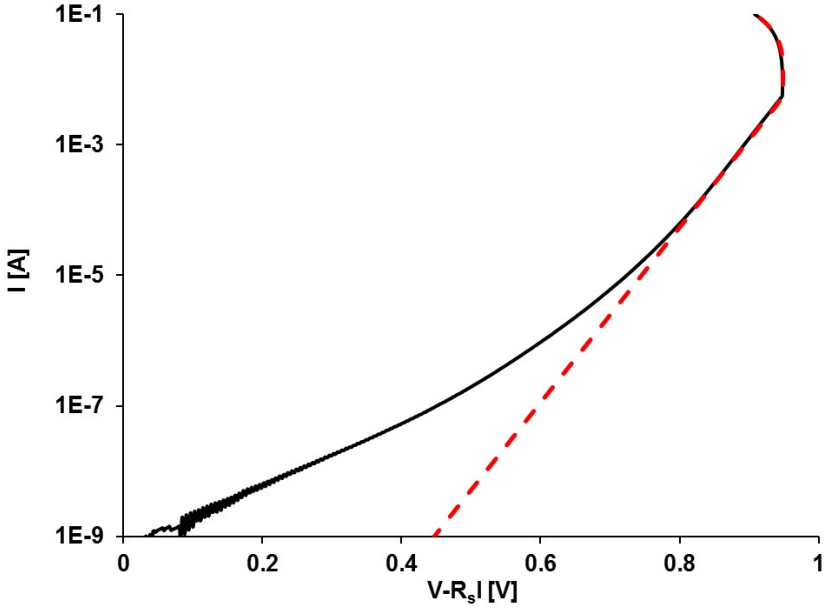

Figure 1.43: The simulation (red curve) is perfectly superimposed on the experimental curve (black) for high level of injection. Beyond the threshold the overturning of both the curves is evident.

This nice result can be further appreciated if one checks the voltage of each diode element. It results that as soon as the first element, the main body of the laser device, reaches the threshold, none of the lateral elements did the same. Then, when current and voltage increase, each lateral diode reaches its own threshold and clamps to the same threshold voltage V_{th}. In fig.1.44 the diamond markers indicate the achievement of threshold by each new lateral diode. The interpretation now is simple: the threshold propagates since its first appearance, involving more and more area of the ridge. The corresponding voltage clamp also propagates, and this results in an apparent progressive reduction of the series resistance, and in an apparent reduction of the clamp voltage.

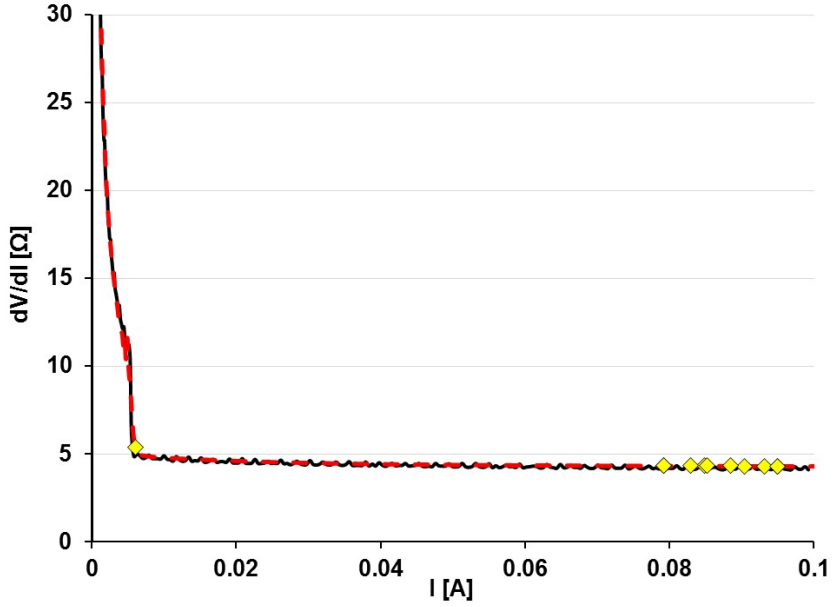

Figure 1.44: The resulting simulation (red curve) superimposed to the experimental curve (black), the yellow points represent the clamp of the elements.

This phenomenon, that could be marginal at a first glance, indicates that injection (and then gain) is not uniform even in a simple device. In paragraph 3.2 it will be shown as non-uniform light distribution can give, in advanced devices, dramatic effects, as the excitation of higher optical harmonics. This is a very recent result, and the correlation between the latter event and the electrical effects described in this paragraph is still under investigation.

Conclusions

This Chapter looks at the fundamental characteristics of laser diodes under a new point of view, and proposes several conclusions that embed, and never contradict, the widespread knowledge, evolved along more than 50 years. The connection of the sub-threshold and the above-threshold ranges, including the self-determination of the threshold condition, is possibly its most useful result.

The availability of a working model for the full injection range enables numerical simulations, parameter fitting and monitoring of degradation kinetics. A

suitable method for proficiently measuring real devices has been recalled. This new method essentially aims to extend the range of practical measurements of modal gain to DFB laser diodes, validating and extending the Hakki-Paoli method, originally developed only for FP devices. The measurement procedures are non-destructive and can be applied to packaged devices whose construction details are unknown.

Non idealities have been indicated, deeply discussed and solved. The roadmap for further investigations has been proposed all along the Chapter.

Chapter 2

Validation experiments by electron microscopy.

Introduction

During the years of PhD the Author had the opportunity to access different microscopy techniques. In particular four of them have been applied for physical investigations at microscope level:

- FEGSEM (Field Emission Gun Scanning Electron Microscopy)
- FIB (Focused Ion Beam)
- EBIC (Electron Beam Induced Current)
- TEM/STEM (Transmission Electron Microscopy/Scanning Transmission Electron Microscopy) FEGSEM and FIB were available on the same instrument, in the so-called Dual Beam configuration.

2.1 The optical trans-characteristics and XEBIC at the SEM

The prompt for this study came from some field failures of a kind of 1310 nm laser diodes, mounted in the Transmitter Optical Sub Assembly (TOSA) of a 10 Gbit/s trans-receiver.

The correlation with some stress-related root cause was suspected, but its exact identification remained puzzling. Thermomechanical effects have been considered, as a possible source of defects, but for the sake of completeness also more subtle mechanisms have been investigated, as stress-related inhomogeneity in electron, hole and photon concentrations, due to local distortion of band-gap E_g and (which is the same) refractive index n.

The failed devices were severely damaged, and then some experiments have been performed on similar reference devices. Being direct measurement of the spatially-resolved values of E_g and/or n not possible on a finished device, two complementary approaches have been considered, investigating the DC electro-optical characteristics and the charge distribution under forward injection.

2.1.1 Experimentals

2.1.1.1 The devices

The device chosen for the study is an InP-based Directly-Modulated-Distributed Feed Back (DM-DFB) edge-emitting laser diode, whose high modulation speed is achieved by a very narrow ridge, manufactured quite close to the active region, and two deep lateral trenches cutting the active and the confinement layers (fig.2.1).

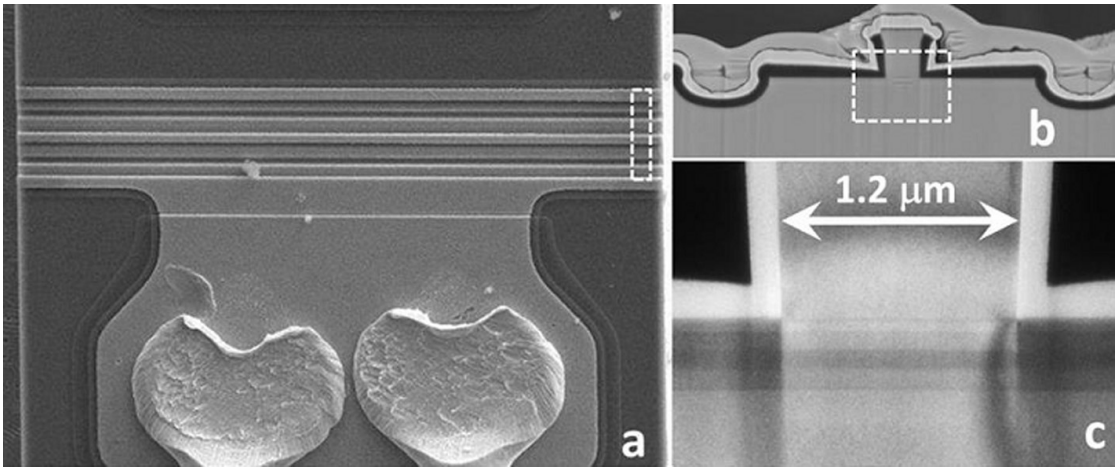

Figure 2.1: SEM plan view (a), cross-section (b) and TEM (c) on the device under test.

2.1.1.2 Burnout

The figure 2.2a shows the TEM images of the failure. The damage is shown in plan-view, with the lamella cut parallel to the epitaxial layers, and including part of the basement of the ridge (fig.2.2b is the same as fig.2.1c, rotated by 90°. The dashed box in b indicates the upper and lower edges of the lamella displayed in a).

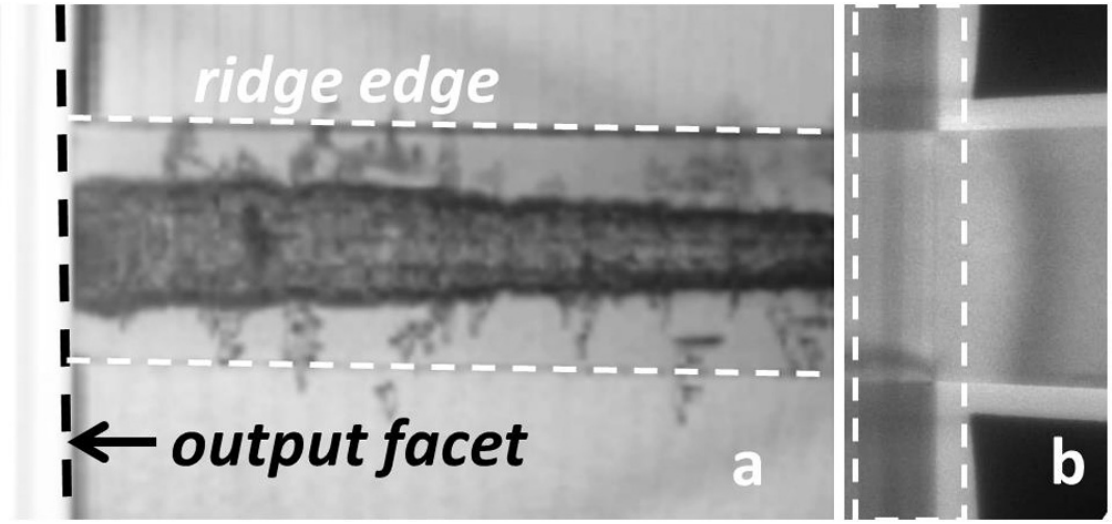

Figure 2.2: TEM on the burnout catastrophical optical damage (a). Position of the edges of the lamella are shown in (b).

The damaged area describes a severe event where melting and re-crystallization took place, leading also to the lateral spread of some insulated dislocations, quite consistent with the interpretation of a Catastrophical Optical Damage (COD).

An extensive literature exists about CODs (see for instance [65]), always indicting the optical power density as the firing quantity for the failure mechanism. The point here is to detect how the high-speed technology introduces something able to locally increase such power density.

2.1.1.3 Case study by transcharacteristics

The novelty is here the deeper insight that the trans-characteristics (1.60) allow, for the present case.

Fig.2.3 shows the $I_M(V)$ experimental plot, and its expected behavior (line a) from the theoretical model here derived in [2]. The difference is evident at the transition across the threshold. The kink in the experimental I_M recalls the knee in the total current I in fig.1.18, suggesting that also in this case the "active element", able to reach its own threshold, is a much smaller one (line c).

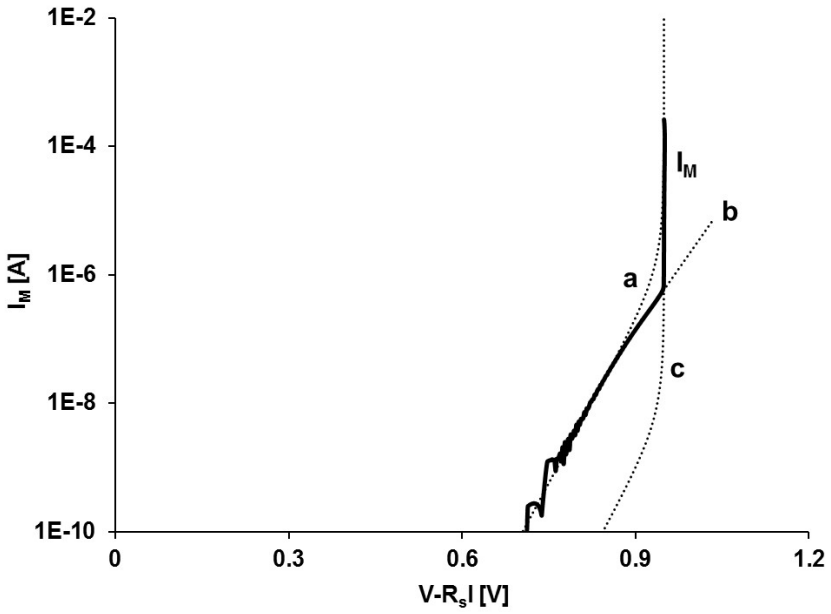

Figure 2.3: The experimental I_M deviates from its theoretical expectation for a uniformly pumped active area (a). It results perfectly fitted by the sum of the ideal curve (a) shifted downward (c) to refer to a much smaller area and a current-limited contribution (b).

Numerical fitting of experimental data indeed, shows the composition of a theoretical curve at much lower intensity (line c), but displaying the threshold, and a larger conduction curve (line b), perfectly fitted by the same formula that allows to describe the sub-mA range of I in fig.1.18. That formula, derived in details in [3], describes the characteristics of a resistive transmission line made of diodes identical to the light emitting one and infinitesimal extension.

Anyway, lateral conduction across the diode areas at the sides of the ridge cannot be invoked to give account for fig.2.3: it is indeed the plot of what occurs

inside the real active area, under the ridge. Nevertheless, the behavior, although on a different scale, seems quite similar.

The nature of this phenomenon is likely to be less simple than a simple resistive path, and must be investigated by local techniques. In any case, the interpretation of fig.2.3 is simple and severe: only a part of the active region reaches the population inversion, and then drains all other current further injected into the device. The optical density then crowds in smaller areas than designed, which in turn increases the probability for any degradation mechanism enhanced by optical and/or electrical power density.

2.1.2 Confirmation by EBIC

Expectations get an interesting confirmation by EBIC (fig.2.4), measured at a fresh cross-section of the active region performed by FIB. The signal distribution dramatically changes when the device is inclined or perpendicular with respect to the beam axis. Beam voltage and current are exactly the same for the two cases. A continuous EBIC line appears for the inclined case, while it is completely confined under the ridge in case of perpendicular imaging. It should be here recalled that EBIC maps the junction activity when it is forward biased at a level similar to current injection in EBIC conditions. Carrier generation takes place only partially inside the depletion region under inclined imaging, while is nearly completely collected under perpendicular orientation.

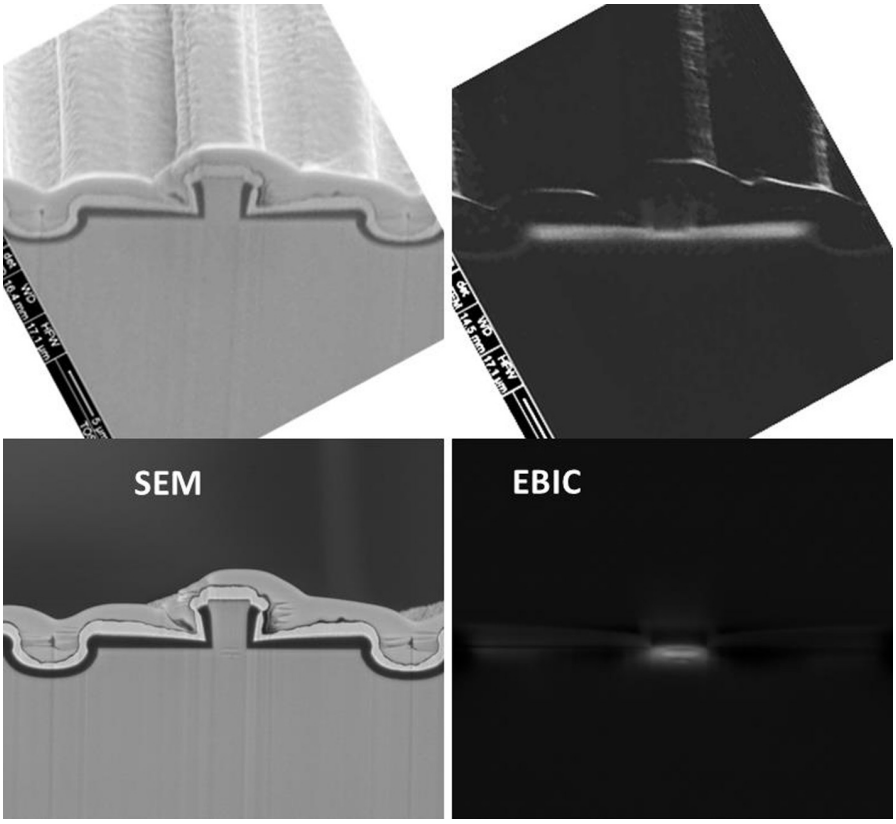

Figure 2.4: SEM (left) and EBIC (right) of a FIB-cross-sectioned front view of the device. Inclination changes the charge collection

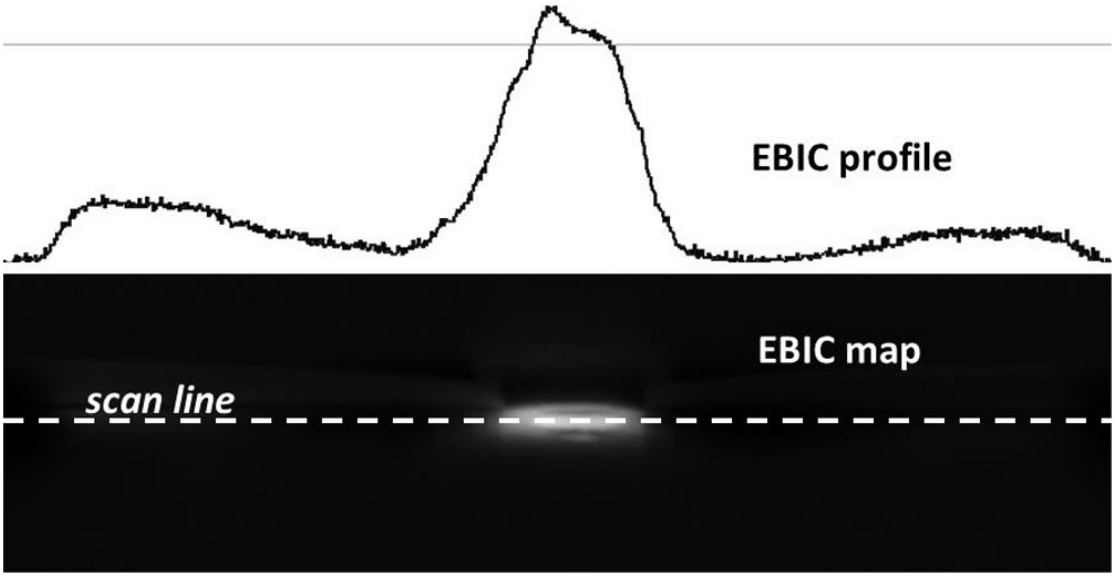

Figure 2.5: Linescan of the EBIC signal.

It is then the second case that can tell something relevant for our investigation. When the linescan of the EBIC signal along the active layer is drawn (fig.2.5), it shows

1. a peak inside the area under the ridge
2. lower maxima and minima at both sides.

The asymmetry of the EBIC map could even be attributed to some possible residual tilt along the horizontal direction, but the two pointed out features remain. The first is perfectly consistent with the analysis of fig.2.3. The second tells that the edges of the ridge introduce some distortion in charge collection, that is likely to be attributed to lattice strain.

2.1.3 Longitudinal strain

The last consideration allows to look at another puzzling failure case with some interest. The figure 2.6 shows the failure of another laser diode, with quite similar characteristics and application as for the previous case. Here an evident burnout occurred not at the mirror facet, but well inside the ridge, just at the edge of a thicker Au metalization covering the thinner metal.

The device is, as for the other device, a DM-DFB laser diode, and the role of longitudinal strain should be here considered.

If the thick metal edge introduces some local strain, then both the bandgap and the refractive index are locally modified.

The DFB corrugation would then look no more periodic, but locally chirped. The effect of chirping is known [66,67], and is used to create wide band Distributed Bragg Reflectors (DBR) in monolithic tunable lasers.

In our case, the distortion creates a virtual partially reflecting mirror under the thick metal edge, and makes it prone to parasitic light scattering.

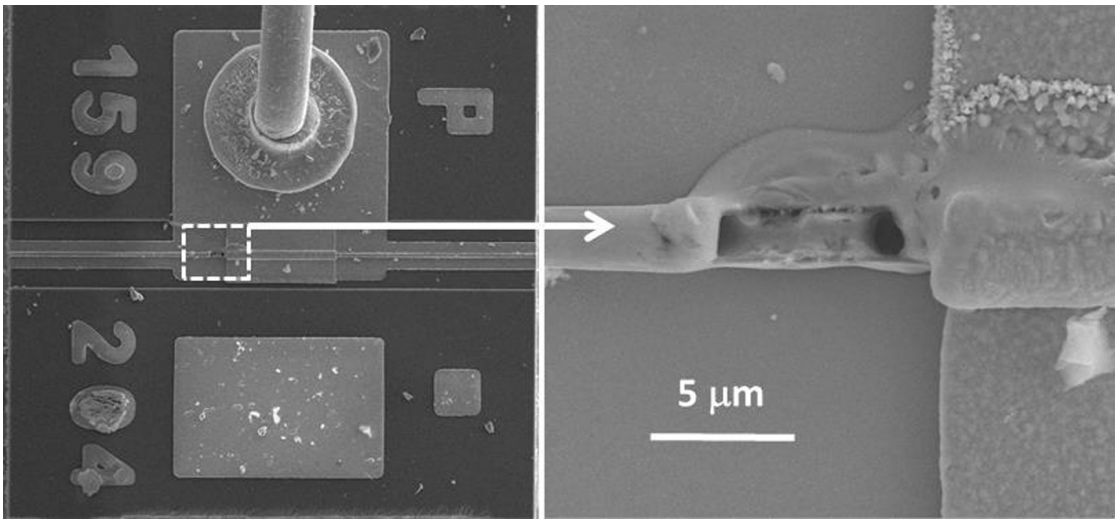

Figure 2.6: A burnout on a DFB device occurring inside the ridge length, at the step of a thick metalization over the thinner one.

The introduction of trans-characteristics to support a case study is not a new proposal, and caused some discussion, for instance, when [3] was presented for the first time.

The current paragraph tries to show that details in the trans-characteristics carry information not directly available in the standard $I(V)$ and $P_{OUT}(I)$ plots. In particular, the former does not distinguish between the light emission and the other recombination mechanisms, while the latter, dealing with light power, draws the dependence on I on a linear scale that hides detail in the whole sub-mA range, that, on the contrary, carries a lot of information.

In any case, the foundation of all the proposed applications is the theoretical treatment of the "pure radiative current" I_{ph} given in paragraph 1.1 and [2], that allowed to draw lines a and c in fig.2.18 of this paragraph. It is the only available model, at our knowledge, that leads the balance equation for photons to current–voltage characteristics spanning the whole current range that includes, and predicts, the threshold condition and the voltage clamping. It is this unique feature of I_{ph} that prompts the considerations in the previous sub-subparagraph 2.1.1.3.

2.2 FIB-induced electro-optical alterations in a DFB InP laser diode

2.2.1 FIB to modify the internal optical losses.

This section summarizes the work done during the preparation of the final thesis for the Author's graduation. Most of the results have been published in two separate papers at a past Conference [35, 36], but are here collected in a more self-consistent form. The final part will deal in with the new gain model reported in paragraph 1.2. It is a consequence of a much larger study, carried out mainly by the Tutor of the Author [2, 3] that mostly confirms or simply redraws many

consolidated results, but also, in some points, achieves important differences, at least under the formal point of view. Optical gain is one of such points, and probably also the best way to compare the new theory with the known ones.

A new method has been here applied, based on a Focused Ion Beam (FIB), to modify the sole internal optical losses in a commercial DFB device. Consistently with the available theories, such modification causes measurable changes in both the threshold current and the total optical efficiency. The expected mathematical relationship between these last quantities is then verified on the experimental data, which also defines a quite effective graphical test to check if really FIB only altered the internal optical losses. After validation, the numerical parameters extracted from the experiments allow for a calibrated plot of gain as a function of the injection level.

Finally, going back to the different gain models, the experiment itself is shown prone to be re-designed for the sake of validating or discarding each of them. The experimental data available up to now are, at the same time, disappointing but also exciting, because they stop just at the very limit that would decide about the two most conflicting competitors. This addresses the planned next steps and perspectives of this work.

2.2.1.1 Experimentals

The device selected for the test is a commercial InP-based DFB laser emitting at 1310 nm, originally mounted in a Transmission Optical Sub-Assembly (TOSA), for telecom applications. The structure of the injection region is made of a ridge configuration with a high aspect ratio, centered on the top of a planar epitaxial stack, limited at both lateral sides by deep tranches. Fig.2.7 shows the top view of such device and the polished cross-section of the vertical structure with the EBIC signal superimposed in order to locate the junction depth and also the width of the injected area. The selected area for successive FIB experiments is also shown.

Fig.2.8 describes the planning of the FIB modification: a vertical trench should cut one of the sides of the ridge, far from the longitudinal edges (mirrors) of the optical cavity, and close enough to the cavity to possibly modify the optical propagation of the lateral evanescent waves, but not so much to interfere with current injection. The alternate and inclined layers on the edges of the ridge allow to easily monitor the actual position of the cut.

The choice of the position of the cuts far from the mirror edges aims to avoid any perturbation to the reflectivity. This is also the reason for choosing a DFB, that is a device locked to single-mode operation: any alteration in the cavity shape in, say, a Fabry-Perot configuration would have modified the mode distribution, complicating the gain studies.

Fig.2.9 shows the comparison between the real FIB action and the expected one, which confirms that the hole is at the side of the ridge, does not intersect the current injection area, but is located at about $1\mu m$ from the optical gain region, where the side tails of the electromagnetic fields surely penetrate.

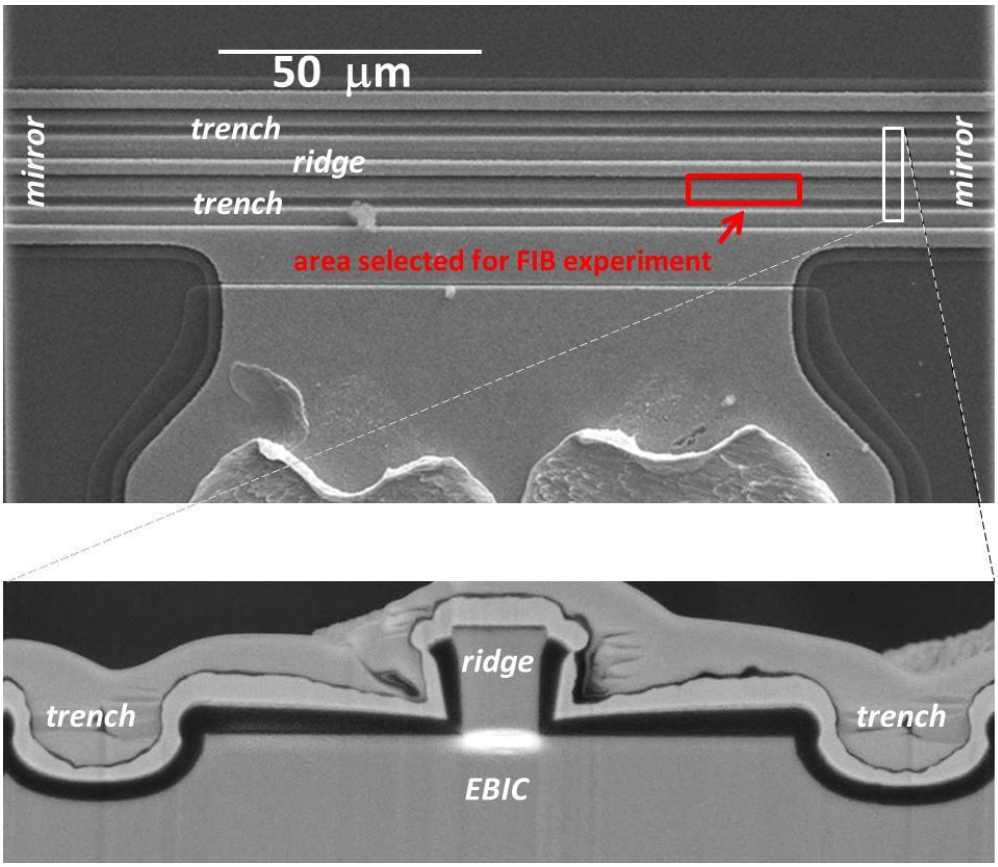

Figure 2.7: Top and cross-sectional views of the laser diode. EBIC locates the depth and width of the actual current injection area.

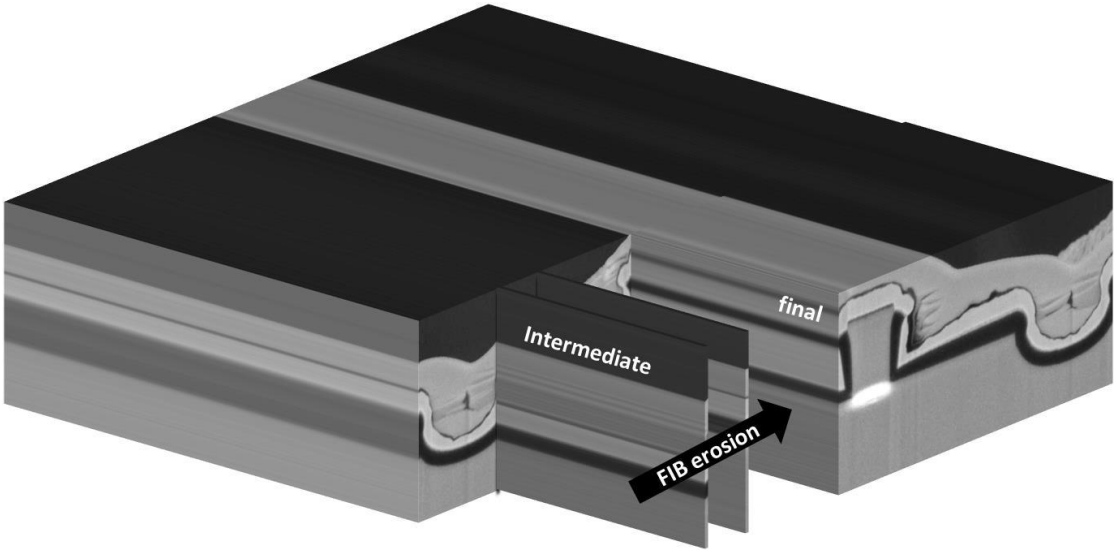

Figure 2.8: Design of the FIB modification. The final surface is recognized by its peculiar stack of layers.

FIB was applied twice, allowing the second step to increase the length of the erosion by 50% with respect to the first one. Laser monitor characteristics have been measured on the specimen as received and after each FIB step.

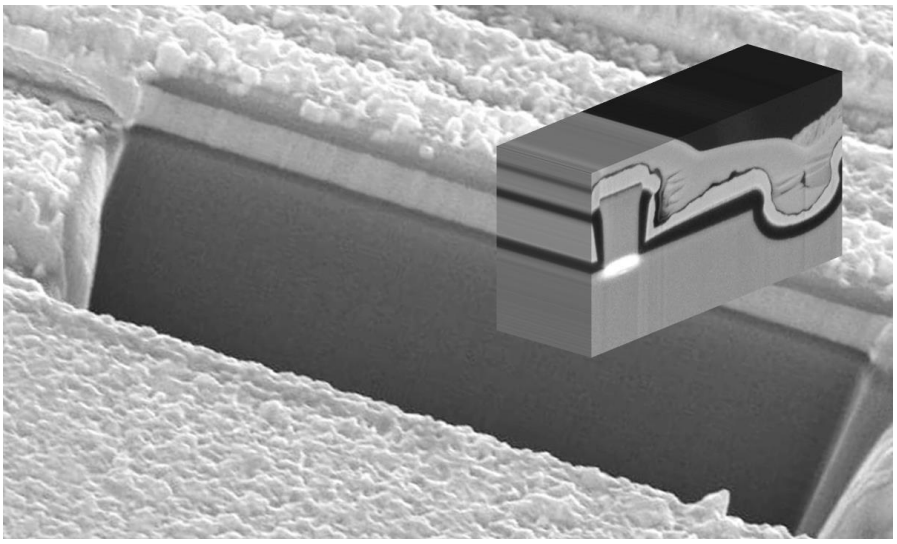

Figure 2.9: Design of the FIB modification. The final surface is recognized by its peculiar stack of layers.

2.2.1.2 Threshold current and optical efficiency

As a result of the experiment, three curves have been obtained for the power-current plot.

Fig.2.10 reports such plot, drawn in terms of the monitor current I_M as a function of the laser current I. It is evident that the FIB induced both an increase of the threshold current I_{th} (given in fig.2.10 as the intercept of the inclined lines with the horizontal axis) and a corresponding decrease of the total optical efficiency η_T (that here is represented as the differential ratio dI_M/dI for $I > I_{th}$. The obvious relationship holds with optical power: $P_{OUT} = I_M h\nu/q$).

Both effects are largely expected because of the lumped empirical equations (1.59) and

$$\eta_T = \eta_C \frac{\alpha_m}{\alpha_T} \tag{2.1}$$

The coupling efficiency η_C measures the fraction of light that, leaving from the laser facet, actually creates light into the monitor diode; α_T and are α_m, respectively the total and the mirror loss coefficients.

Equations (1.59) and (2.1) clearly states that, given a set of measured couples (I_{th},$1/\eta_T$) as from fig.2.10, the linear relationship holds

$$\begin{cases} \ln(I_{th}) = \ln(I_{th0}) + \eta_0 \dfrac{1}{\eta_T} \\ \\ \eta_0 = \eta_C \dfrac{\alpha_m}{g_0} \end{cases} \tag{2.2}$$

Fig.2.11 shows the perfect alignment of the experimental pairs along the theoretical curve, and also indicates the predicted value of I_{th0}, corresponding to the ideal zero-loss case $\alpha_T = 0$, that allow to draw $g(I)/g_m$ in fig.2.12. The alignment of the experimental points, and its extrapolation to zero-loss, should be considered the validation of the hypothesis that mirror losses have not been involved. The point

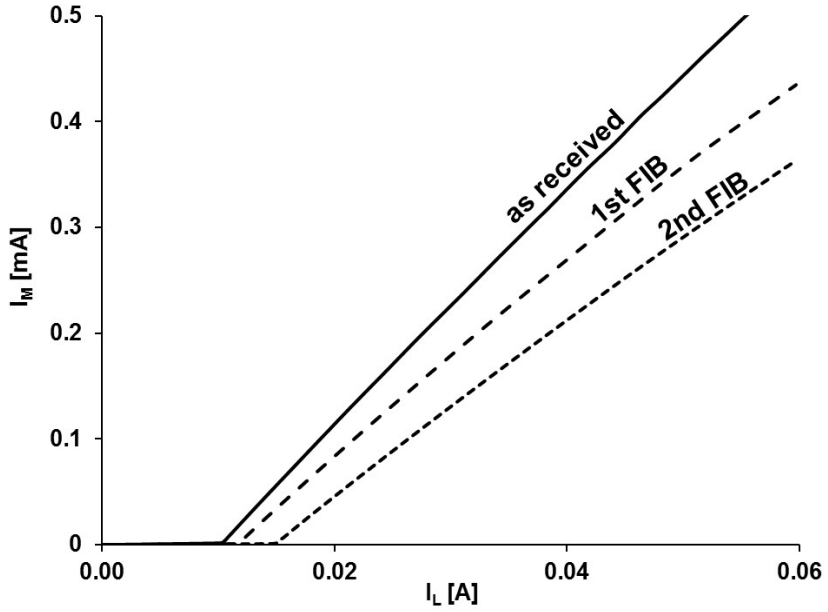

Figure 2.10: The evolution of the power-current characteristics during the experiment

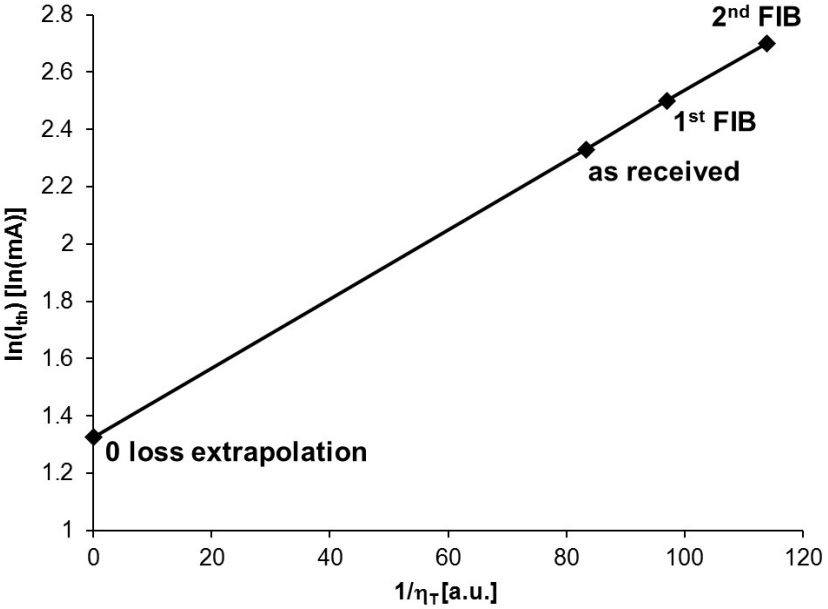

Figure 2.11: Experimental data plotted onto the theoretical curve (1.5)

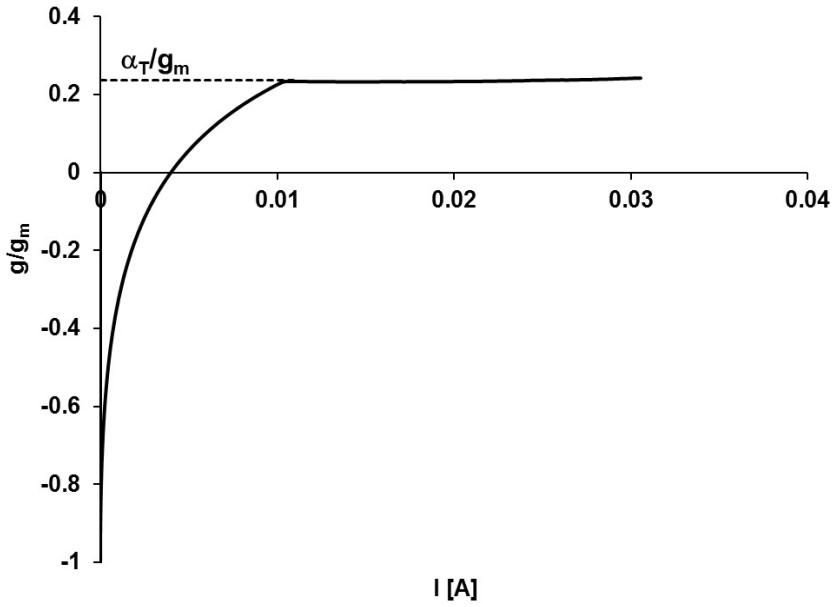

Figure 2.12: Experimental gain as a function of the injected current, that clerly show the upper limit of saturation at α_T/g_m

is that, even if the physical mirrors have not been touched by the FIB action, their reflectivity could change if wavelength have been even slightly affected. The sole confidence that the DFB grating locks the cavity mode can sound fairly sufficient. It is then advisable to recall fig.2.13, from ref. [36], that compares the different results of the plots as in fig.2.11 when pure internal losses (a) or also mirror losses (b) are introduced. The experiments in this case refer to a completely different case (external cavity tunable lasers), that allowed both choices, but the result is of striking evidence.

2.2.1.3 Competing models and design of an experiment

The stimulating results of the last sub-subparagraph seem to open a conflict with evidence. The best way to point out the problem is to compare the different expressions for the threshold current. The alternative formulas (1.59), (2.1) and (1.55), (1.56) seem indeed to say quite different things, and the nice alignment shown in fig.2.11 and 2.13, based on the exponential form (1.59), clearly supports that popular and widely accepted model. Nevertheless, the empirical origins of (1.59) and (2.1) should be compared with the theoretical foundation of (1.55) and (1.56) that, in turn, is consistent with the gain analysis reported by ref. [79], where upper and lower bounds are predicted for g.

The rather surprising discovery has been that the power expansions of (1.59) and (1.55) near the transparency condition (zero losses) lead to identical results at the zero, first and second order, and that the coefficients of next few orders differ for very small quantities [36].

This is put into evidence in fig.2.14, where the same as fig.2.11 has been re-plotted as a function of the ratio α_T/g_m (proportional to the abscissa in fig.2.11). The available experimental points do not decide which of the two models holds.

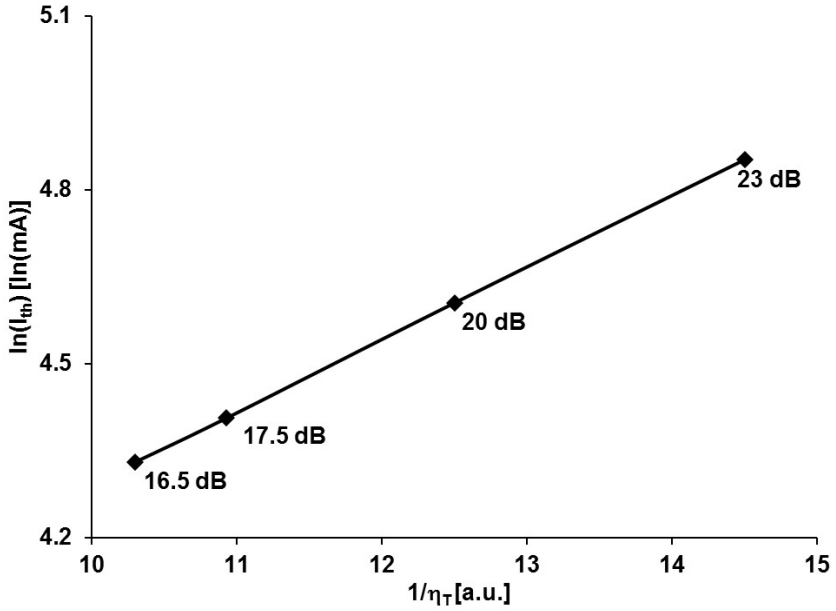

(a) Pure internal losses in a tunable laser (from ref. [36]).

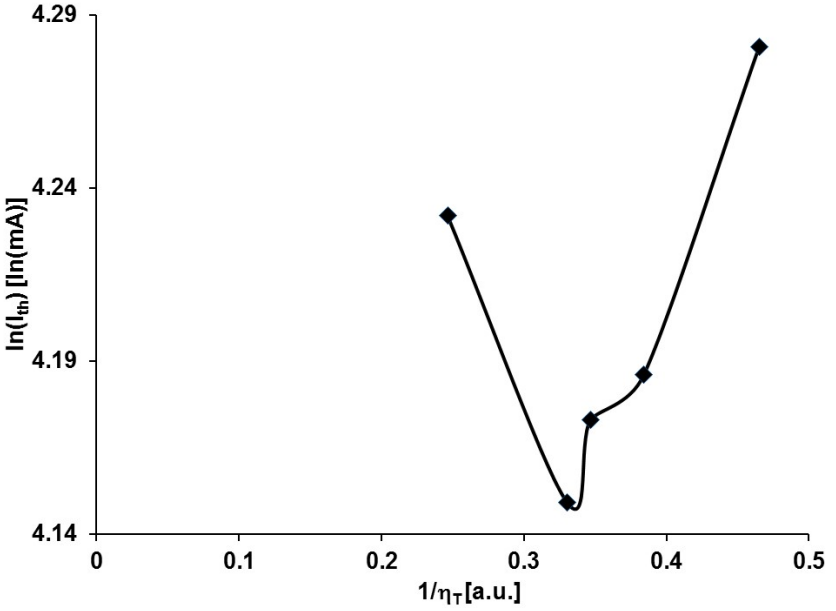

(b) Internal and mirror losses in a tunable laser (from ref. [36]).

Figure 2.13: Different result of the plot of fig.2.11 when pure internal losses (a) or also mirror losses (b) are introduced.

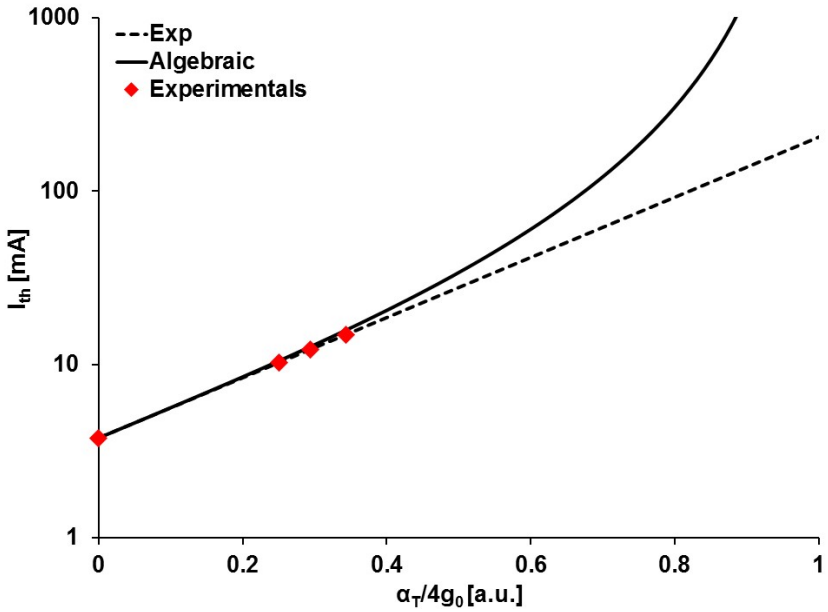

Figure 2.14: The same as fig.2.11 with the experimental points plotted onto the competing exponential and algebraic models for I_{th} given, respectively, by (1.59) and (1.55).

An experiment leading to even a small further increase in the FIB-induced losses seems ready to answer the question. Unfortunately, the increase of FIB modifications introduces parasitic parallel current paths, that modify the whole procedure for extracting parameters as indicated in ref. [35] and shown in fig.1.18. This task is not beyond any possibility, and it is deeply described in the next subparagraph 2.2.2 and [49]. If successful, it will strongly validate the whole theory presented in [2, 3].

2.2.2 FIB-induced electrical alteration.

On the basis of the experiment discuss in the previous subparagraph 2.2.1, in which it has been used FIB to induce local modification in a single-mode edge emitting laser operating at 1310 nm, and that led to a method for estimating gain parameters. In this experiment, the final FIB modification introduced large variation in electrical characteristics that were not analysed in detail, and even seemed to contradict the basic laser model that the experiment itself aimed to confirm. This part focuses on this puzzling point, and solves it with a circuital hypothesis, a circuit simulation and a direct inspection by XEBIC.

Until now it has been studied the variation of the gain coefficients in some kinds of single-mode laser diodes. One kind was made of a 1310 nm edge emitting DFB InP-based device, progressively modified by FIB erosion at one side of the optical cavity. The evolution of both the threshold current and the optical efficiency were monitored, and shown to be due to the sole variation of the internal optical losses.

Anyway, when looking at the full set of available data, that also included the evaluation of the series resistance R_S and the internal threshold voltage V_{th} (corresponding to the separation of the quasi-Fermi levels required to achieve lasing),

the last FIB-induced state showed really puzzling figures, including a reduction of qV_{th}, as for a reduced optical loss. Moreover, such last experimental result seemed to destroy the underlying DC model progressively developed and applied during the last few years.

This subparagraph analyses this puzzling point, proposes its solution and shows an experimental XEBIC [78] observation that validates the conclusions.

2.2.2.1 Experimentals

The measurement of gain coefficients [36] in single-mode laser diodes involves the threshold current I_{th} and the total efficiency η_T, both obtained by the L–I curves by interpolating the experimental data, with the well-known linear formula [31]

$$L = \eta_T(I - I_{th}) \tag{2.3}$$

and using them, for different couples I_{th}, η_T, in the empiric relationship (1.58) [31]. As previously said, the alignment of the experimental data along a straight line confirms that only internal losses lead to changes in α_T. Such analysis led to the curve in fig.2.11 in subparagraph 2.2.1, that seems to fully confirm all expectations.

The last point is important because many results obtained insofar have been based on an equivalent circuit [2] that, after a common series resistance, links in parallel several elements representing, separately, the light emitting "diode", the non-radiative currents, the lateral currents flowing at low injection at the sides of the active region. Removal of such a series resistance is then a starting step for any deeper analysis of the electrical end electro-optical characteristics.

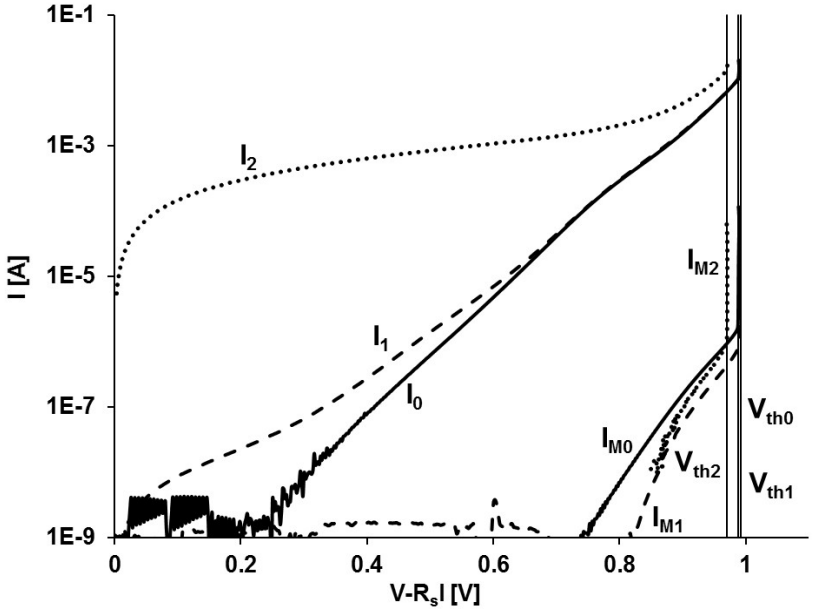

Figure 2.15: I and I_M characteristics at the initial state (0), after the 1st FIB (1) and after 2nd FIB (2).

When one performs such step for the initial state, after the first FIB and after the second FIB, one obtains the result shown in fig.2.15. Here both the laser

current I and the relative monitor diode current I_M are plotted vs. the separately calculated reduced voltage $V - R_S I$, at the initial step (suffix "0"), the first FIB ("1") and the second FIB ("2"). Also the corresponding threshold voltages V_{th} are put into evidence.

The surprising result was that after the last FIB, the clamp voltage V_{th2} appeared to decrease, while the threshold current increased, in evident conflict with the statement about their relationship.

The evidence, in current I_2, for a parasitic shunting ohmic path, roughly corresponding to some 700Ω, addresses the qualitative interpretation. Anyway, the preservation of alignment of the highest point in fig.2.11 with the others remains puzzling, if relevant extra-currents are invoked.

2.2.2.2 Analysis

When one considers the configuration in fig.2.16, where the block L represents the laser diode, large values of the shunt resistance R_0 correspond to the initial state, and the resistance itself can be neglected. FIB is likely to introduce both optical effects, by modifying the lateral losses, and electrical effects in terms of a parasitic shunting path along the walls of the grooved trench. Such electrical effects can be neglected when confined to the sub-mA range, as for current I_1 in fig.2.15. In this case, in fig.2.16 the lateral resistance R_0 can be omitted, and the dV/dI characteristics correctly give the overall series resistance R_S when measured at $I > I_{th}$.

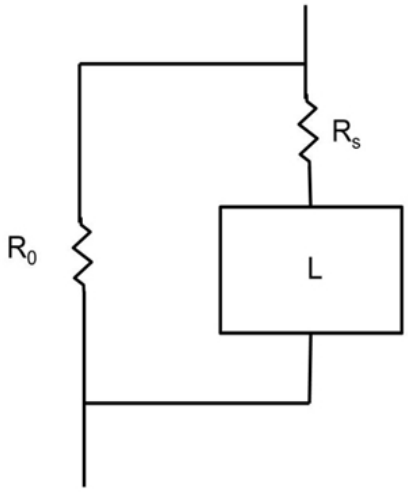

Figure 2.16: The simple circuit for describing fig.2.15.

On the contrary, the last curve I_2 shows a dominant leakage current, that does not physically involve the optically active region, but drains current enough to perturb the $I(V)$ relationship in the whole device.

It is matter of trivial circuit analysis to see that, when the element L in fig.2.16 clamps at its internal clamp voltage V_{th}, not only I_{th} but also η_T and the externally measured value of itself V_{th} change depending on the critical ratio $R_0/(R_S + R_0)$.

More precisely, if the known relationships for V and I_M hold for the initial state (no shunting path) for $I > I_{th}$, the appearance of the parallel path changes

them into

$$\begin{cases} V = \dfrac{R_0}{R_0 + R_S}(V_{th} + R_S I) \\ \\ I_M = \dfrac{R_0}{R_0 + R_S}\eta \left(I - \left(\dfrac{R_0}{R_0 + R_S} I_{th} + \dfrac{V_{th}}{R_0} \right) \right) \end{cases} \tag{2.4}$$

The result is that the functional relationships between the measurable quantities V, I, I_M remain the same, and that the four constants V_{th}, I_{th}, R_S, η seem to change their value, mostly depending on the value of the ratio $R_0/(R_S + R_0)$ that for the given case amounts to about 0.985. The correspondence between old and new parameters is:

$$\begin{cases} V_{th} \to \dfrac{R_0}{R_0 + R_S} V_{th} \\ \\ R_S \to \dfrac{R_0}{R_0 + R_S} R_S \\ \\ \eta \to \dfrac{R_0}{R_0 + R_S} \eta \\ \\ I_{th} \to \dfrac{R_0}{R_0 + R_S} I_{th} + \dfrac{V_{th}}{R_0} \end{cases} \tag{2.5}$$

Here is the explanation of the apparent reduction of the clamp voltage V_{th}: the lateral path kids the electrical model, and emulates the original simple pure serial scheme with false values for the key parameters. Not only the clamp voltage, but even the series resistance R_S seems to reduce, challenging any physical interpretation, upon FIB milling of the laser surface.

But what is possibly more intriguing is that the qualitative effect of the parasitic path is that it simultaneously *increases* the threshold current I_{th} and *decreases* the total optical efficiency η. This is just what one expects from an increase of optical losses, the foundation of fig.2.11 and a key point in ref. [36].

It is then natural to wonder if the third point in fig.2.16 is a true effect of pure optical losses, or if it is somewhat affected by electrical effects, or even if it is only an electrical effect.

One way at least to infer the answer is to check if, supposing a tentative R_x for the parasitic shunt resistance, one can reproduce or approach the former state I_{M1} starting from the measured values of I_{M2}, by means of the inverse of (2.5).

Fig.2.17 shows an intermediate situation, that confirms that the variations from state 1 to state 2 *can* be reproduced by mere electrical means. The choice of a suitable value for R_x allows to continuously recover all intermediate states between 1 and 2. Such a possibility does not say, in principle, that nothing optical took place after the second FIB, but prevents from separating the optical from the electrical effects.

It should be noticed that this states that the third point in Fig.2.11 is possibly unreliable, and that the FIB method can be safely applied only when evidence exists that no electrical alterations took place at currents higher that the mA range.

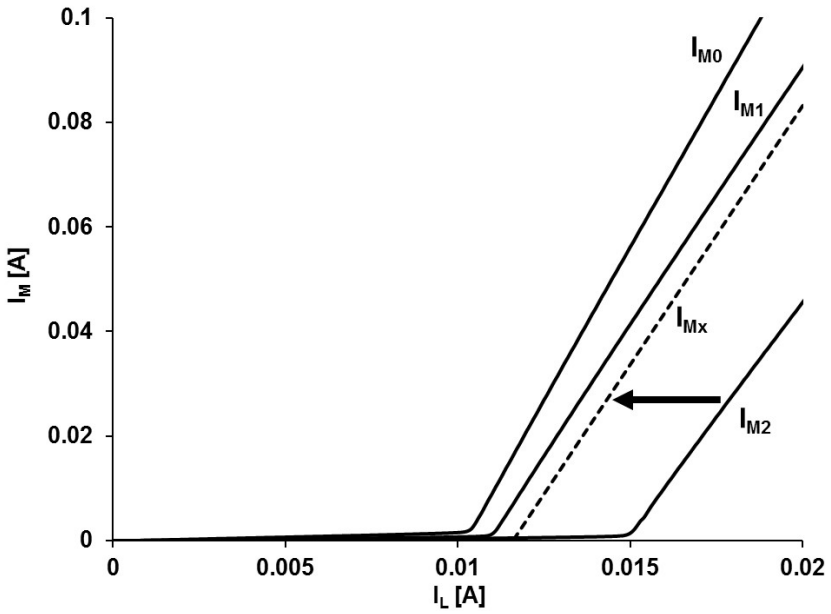

Figure 2.17: The last curve I_{M2} can be brought to recover the previous state, I_{M1},by adjusting the electrical parameters of the shunting path.

Finally, fig.2.18 shows a XEBIC map superimposed onto the corresponding SEM image on the polished facet of the device under test after the final FIB. The edges of the floating blocking layer disappear on the left side, that is just the side where FIB created its trenches [36], confirming with full experimental evidence the hypothesis of a more and more important shunting path, shorting the lateral junction, growing during FIB action.

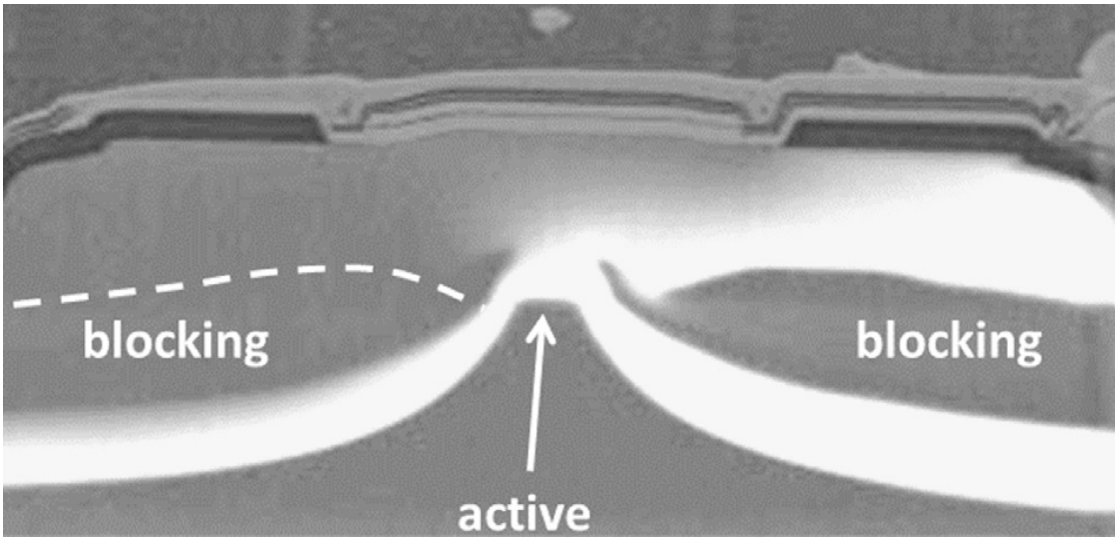

Figure 2.18: XEBIC confirms the expected shunted path by cancelling the upper blocking junction signal on the left side, where FIB grooved a trench.

Conclusion

Several different aspects of the theoretical model have been investigated by means of experimental microscopical methods. In the first paragraph strain-related alteration of charge and photon distribution have been investigated, prompted by the occurrence of some failures in high modulation speed lasers. The physical analysis of some reference devices points out the real distortion of charge collection uniformity. This phenomenon has also been identified on the trans-characteristics of the devices, that are demonstrated to carry information enough to reveal possible risks in a non-destructive way.

Then starting from the analysis of these field failures in single-mode laser diodes for telecom application, that are consistent with the so-called Catastrophical Optical Damage (COD) mechanism. The attempt to replicate such mechanism by controlled FIB-induced local damage required, for its interpretation, the much general revision of fundamental concepts as gain and losses in laser diodes.

Finally the puzzling set of measurements in the FIB-modified laser diode has been shown to be explained by a modified equivalent circuit, and confirmed by EBIC. This raises some warnings in applying the FIB method, as reported in [36], when evidence for electrical alterations appear in the mA range of the laser current, which also defines a criterion for validating data in such FIB-based experiments.

Chapter 3

Laser Diode degradation.

Introduction

Moving to failure physics of laser diodes, the original prompt for developing the model of Chapter 1, we will first modify each of the model parameters and predict the effects on the measurable characteristics. Then we will consider a number of real degradation cases, looking for correspondence between experiments and theory. Where possible, we will propose the link between the two approaches, by describing the physical mechanism in terms of multiple parameter alterations. It will be explained how the model really addresses failure analysis, becoming a powerful tool in diagnostic for such devices and finally some unusual case of failure will be reported.

3.1 Degradation modeling in laser diodes.

After recalling fundamentals of the model for laser devices, this paragraph illustrates an application on a real device. The result is the measurement of a number of important parameters, related to physics and technology of a laser diode, which is in turn useful to address the failure analysis in case of degradation.

The model [1–3] developed for laser diodes is able to describe its DC characteristics (voltage, current, emitted optical power). Its possible main feature is to display the threshold condition in a self-consistent way, and to relate it (and its variations under degradation) to specific parameters as internal and external optical losses, the intrinsic single-mode emission frequency, the coupled density of states of electrons and holes, the saturation current of the Shottky-like characteristics in the sub-threshold LED regime, etc.

Degradations can then be investigated by modifying one or more of those parameters, looking for their fingerprints on the measurable characteristics.

Anyway, the most practical utility should travel the inverse path: from real characteristics, find the numerical values for fundamental parameters, related to possible failure mechanisms. If, indeed, it is of fair utility to appreciate the increase of the threshold current or the decrease of the optical efficiency, it would be quite useful to "decode" those degradation modes in terms of evidence for say, some modified reflectivity at the mirror facets, or a clear increase of the non-radiative recombination rate inside the optical cavity.

This paragraph focuses on a practical procedure for measuring the relevant parameters entering the model, and tests it on an experimental case of a good device. Its application on specific induced degradation case will be summarized in the final section.

3.1.1 The effect of parameter variation

The equivalent electrical circuit for a laterally-confined structure as described in Chapter 1 splits the total area of the junction into several parallel diodes (fig.3.1). Three of them represent the optically active region: one corresponds to the non radiative component of the current, that displays a typical Shockley behavior; the other two diodes represent the photonic components of the current, one responsible for the sub-threshold region ($n > 1$) and the other responsible for the threshold ($n = 1$), as described in subparagraph 1.2.5.

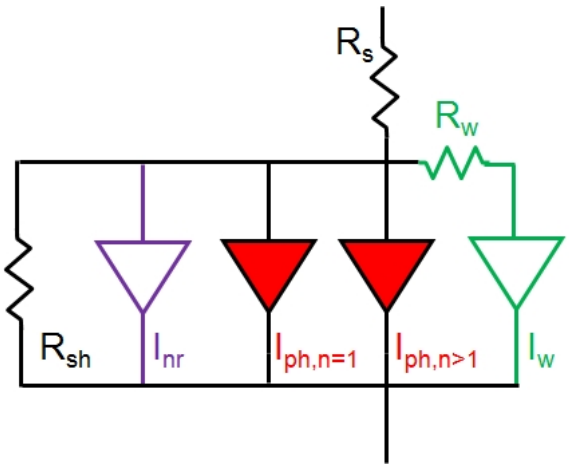

Figure 3.1: The equivalent circuit for an Edge-Emitters laser diodes.

The lateral component of the current is also taken into account by the last diode (whose current is I_W) which is in turn resistively connected, to the central "optically active" diodes. This resistor, indicated as R_W, represents the average of the ohmic effects (current paths across semiconductor material) on the lateral current [2]. Fig.3.1, also includes a common series resistor R_S that globally takes account for contact and wire connection resistances, and a shunt resistor R_{sh}, that is likely to be very high, to describe possible resistive paths parallel to the junction, as for surface conduction or even very small vertical spikes inside the epitaxial layers connecting the p and the n sides (as for native or etch pits related to them). This "marginal" element is important, for instance, to describe some dramatic effects of a severe failure mechanism as ESD, that causes the local perforation of the junction, and results in a dramatic decrease of the original value of R_{sh}.

The proposed circuit in fig.3.1 has proven well suitable also to describe the electrical characteristics of LEDs, in which case the only difference is the presence of a single photonic diode, that never reaches the laser threshold. Table 3.1 reports the current equations corresponding to each branch, as, derived in Chapter 1 and here reported for simplicity.

Equations	**Parameters**
$I = \dfrac{V}{R_S}$	R_S
$I_{R_{sh}} = \dfrac{V}{R_{sh}}$	R_{sh}
$I_{nr} = I_{nr0} \exp\left(\dfrac{qV}{nkT}\right)$	I_{nr0}, n
$I_{ph_{n=1}} = I_{ph0} R \dfrac{\exp\left(\dfrac{qV}{kT}\right) - 1}{R\left[\exp\left(\dfrac{qV - h\nu}{2kT}\right) + 1\right]^2 + \left[1 - \exp\left(\dfrac{qV - h\nu}{kT}\right)\right]}$	I_{ph0}, $h\nu$, R
$I_{ph_{n>1}} = I_{ph0n} R \dfrac{\exp\left(\dfrac{qV}{n_{phn}kT}\right) - 1}{R\left[\exp\left(\dfrac{qV - h\nu}{2n_{phn}kT}\right) + 1\right]^2 + \left[1 - \exp\left(\dfrac{qV - h\nu}{n_{phn}kT}\right)\right]}$	I_{ph0n}, $h\nu$, n_{phn}, R
$I_W = \dfrac{kT}{qR_W}\left[\sqrt{1 + 2\dfrac{R_W I_{W0}}{kT/q} \exp\left(\dfrac{qV}{n_W kT}\right)} - 1\right]$	R_W, I_{W0}, n_W

Table 3.1: Current Equations for each branch of the electrical model, with the corresponding parameters.

It is interesting to observe the effect of each single parameter on the DC electrical and optical characteristics.

The following set of images 3.2-3.13 show the effect of a single-parameter variation on a) the optical power-current curve (the so-called L-I curve) and b) on the current-voltage curve. The latter plots both the total current I (in black) and the photonic current I_{ph} (in red) as functions of the laser total voltage V. In other words, no reduced voltage is used for the abscissa (in order to keep the effects of the series resistance into evidence). The only minor differences with the standard procedure in measuring laser diodes is the logarithmic scale for the vertical axis in the $I(V)$ plot and the inclusion of I_{ph} in the same plot. Arrows are placed to highlight the relevant variations in each plot, directed in the direction of the increasing value of the parameter under test. For instance, in fig.3.2 R_S is considered. It is the series resistance that takes into account the resistive path between the metal contact and the active region. Its increase gives (fig.3.2) a peculiar modification of the current-voltage characteristics (arrowed) without any evidence on the Light-Current curve.

Even this first observation is interesting, because many times, looking for degradations, the sole L-I curve is considered, focusing all attention on the threshold current and the optical efficiency, that is on the voltage coordinate of the "knee" and on the slope of the over-threshold branch. In the given example, one parameter, namely R_S, would be able to dramatically change without any effect on the L-I curve. The reliability issue, related to degradation mechanisms likely to involve the metal-semiconductor connection, would be completely hidden, even prevent-

ing from any screening possibility, for instance, by means of thermal tests during qualification or incoming inspection.

Similar to the given case, all other parameters are then considered in the following images.

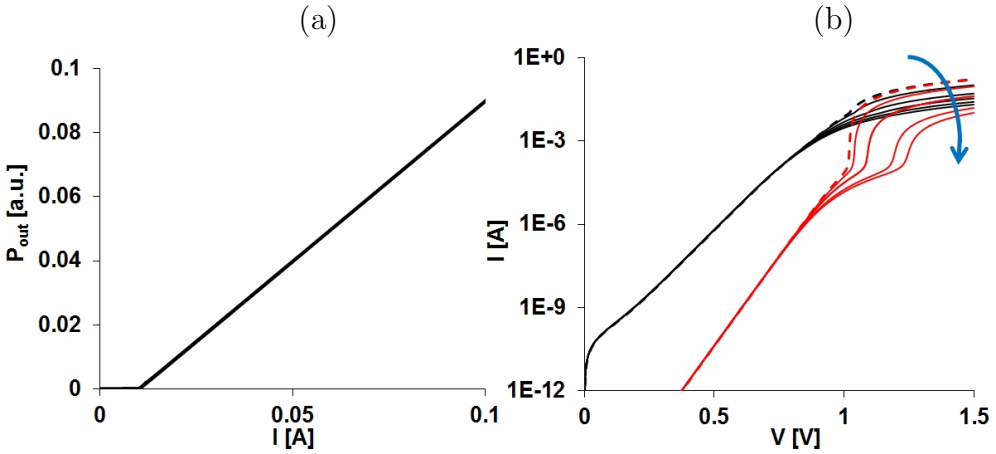

Figure 3.2: Variations of parameter R_S.

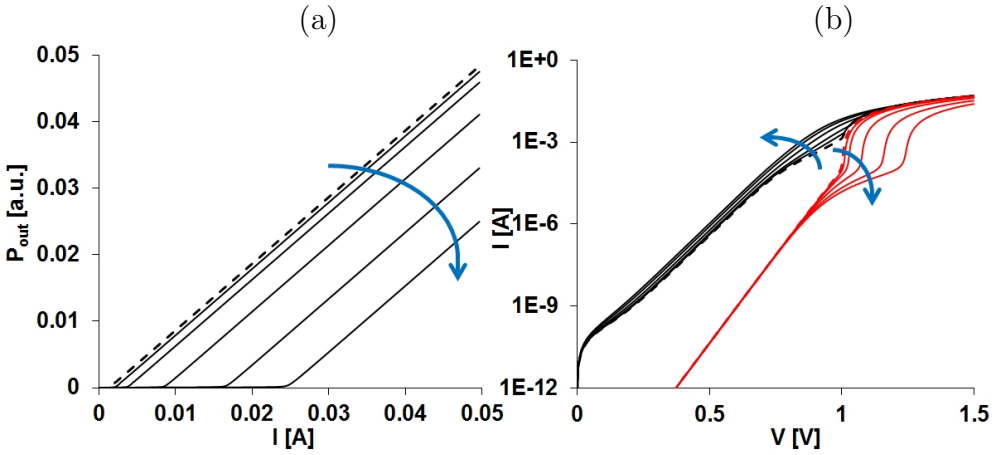

Figure 3.3: Variations of parameter I_{nr0}.

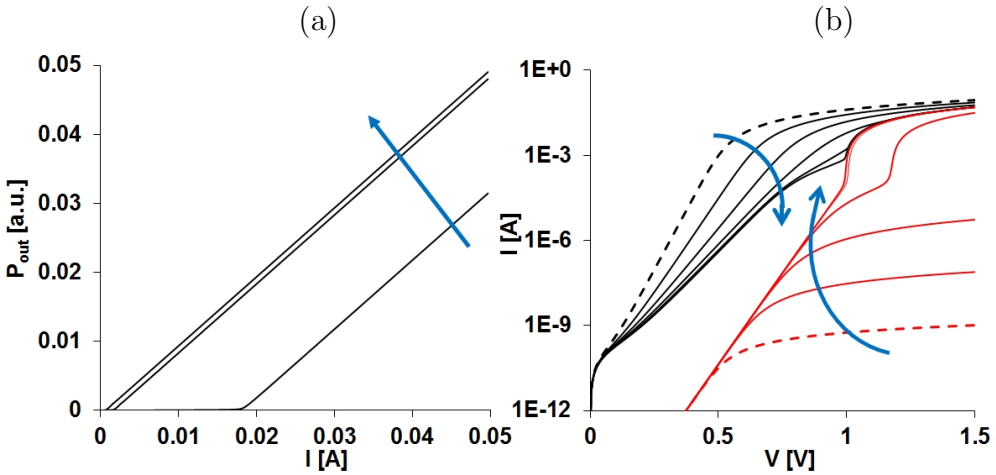

Figure 3.4: Variations of parameter n.

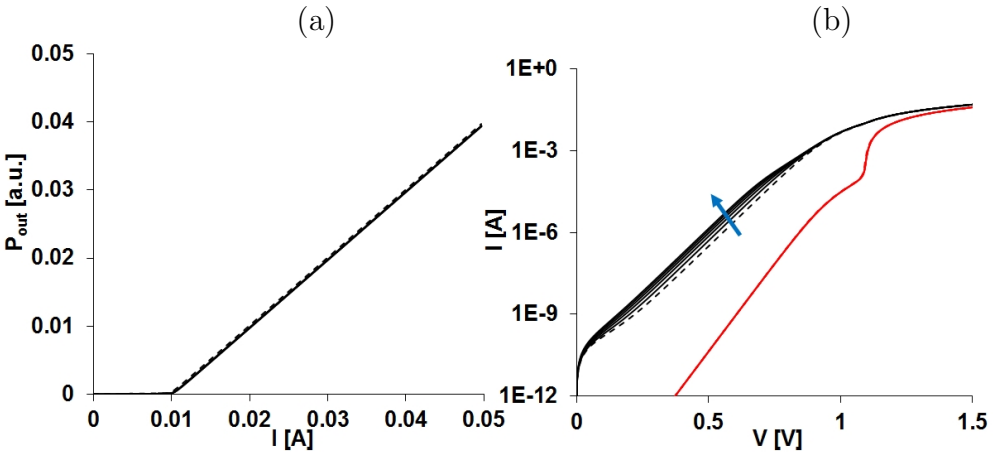

Figure 3.5: Variations of parameter I_{W0}.

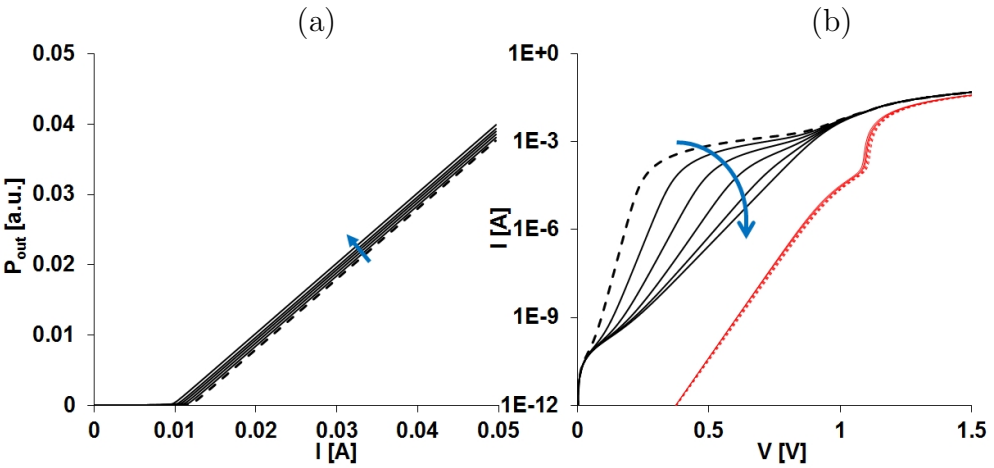

Figure 3.6: Variations of parameter n_W.

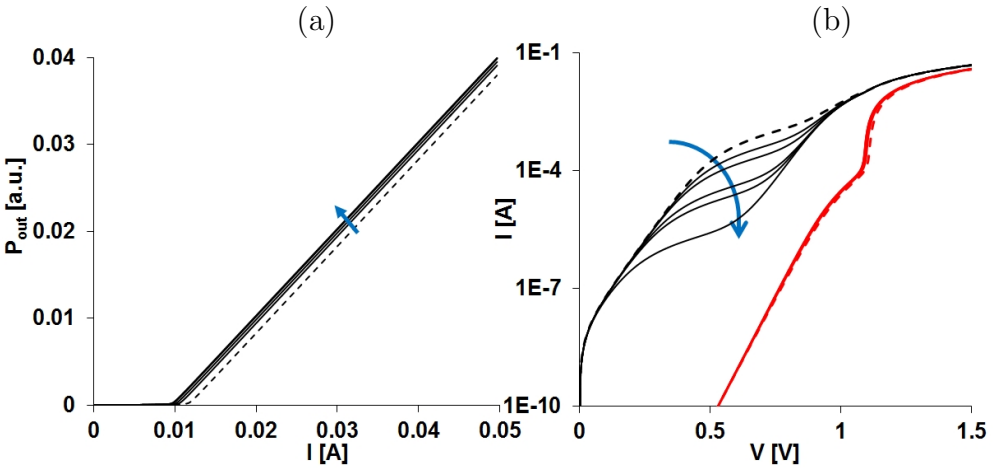

Figure 3.7: Variations of parameter R_W.

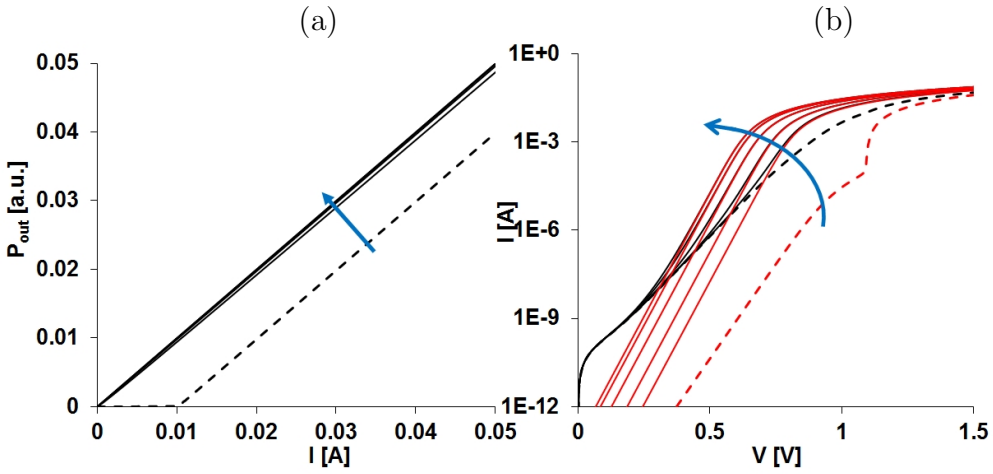

Figure 3.8: Variations of parameter I_{ph0}.

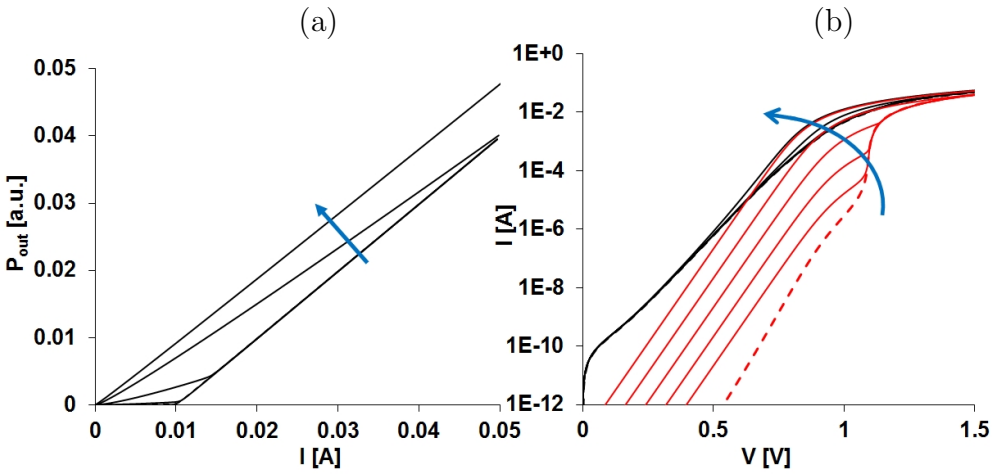

Figure 3.9: Variations of parameter I_{ph0n}.

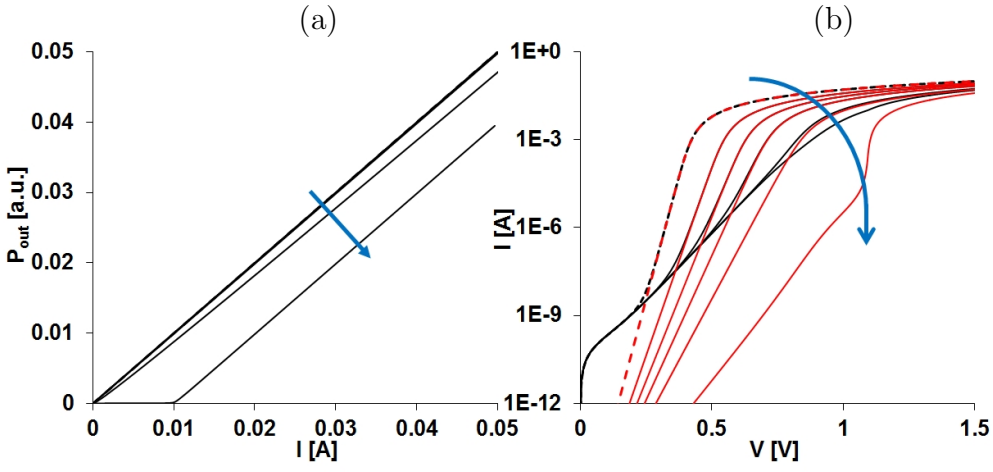

Figure 3.10: Variations of parameter n_{phn}.

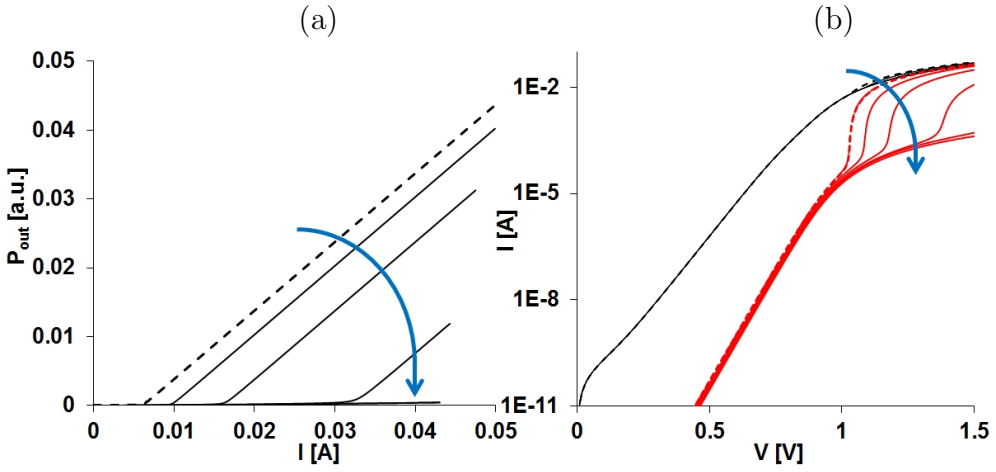

Figure 3.11: Variations of parameter R.

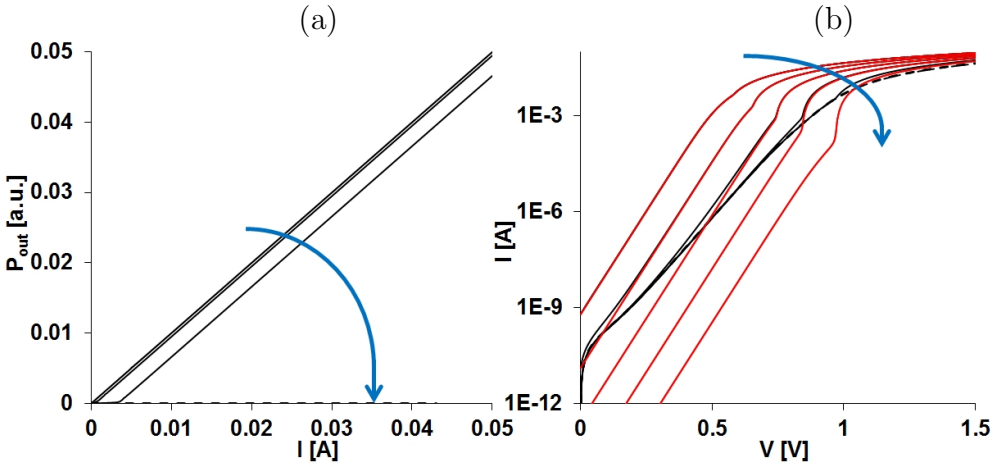

Figure 3.12: Variations of parameter $h\nu$.

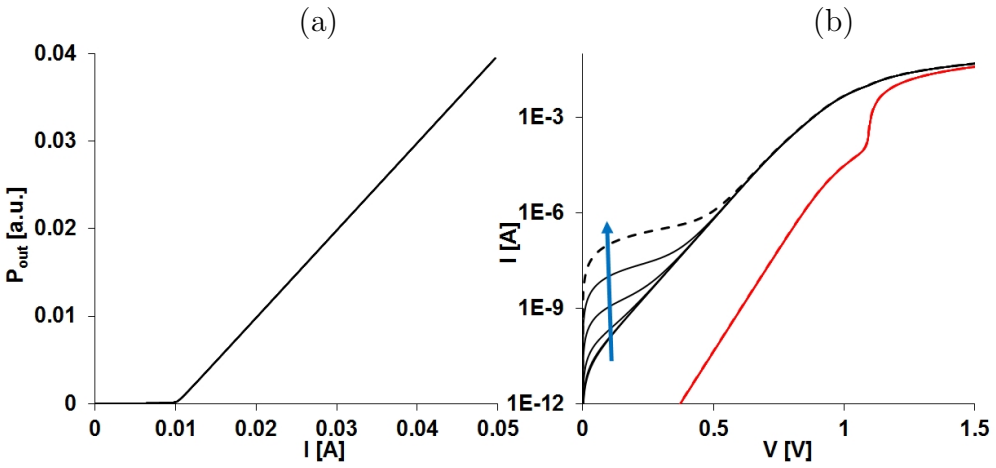

Figure 3.13: Variations of parameter R_{sh}.

Each case could be considered point by point, but the graphical evidence is in itself clear enough. Some specific points will be here highlighted.

a) Several single-parameter variations have no correspondence with any physical degradation mechanism. For instance, an increase of the saturation current I_{ph0} of the "photonic diodes" has no counterpart in the historically documented cases, and hardly can be imagined as the consequence of an evolving failure.

b) The most part of the single-parameter effects predicts for the LI curves or no changes at all, or the mere increase of the threshold current, which is contrary with the most widespread experience, that indicates as degradations reduce light emission by both increasing the threshold current and decreasing of the optical efficiency.

c) Some latent phenomena, as for the leakage current (value of the shunt resistance R_{sh}), would be completely missed not only in the LI curve but also in the $I(V)$ curve is the linear vertical scale is employed, as usual. This is the reason for proposing the log scale.

3.1.2 Parameter extraction from experimental curves

The focus of this paragraph is mostly on the procedure for extracting the relevant parameters from experimental curves. In particular, values for R_s, V_{th}, I_{th}, R, $h\nu$, I_{th0} has been described in the subparagraph 1.1.6. Meanwhile I_{nr0}, n, I_{W0}, n_W, R_W, I_{ph0}, I_{ph0n}, n_{phn}, have been found accessible by superimposition of experimental curves and simulated and this is the main topic for this subparagraph.

The electrical model gives the opportunity to individuate all the current components of real laser diodes. For example, considering the experimental measurements of a real laser diode Edge-Emitter, that emits at 1310nm, in fig.3.14, and considering the method described in chapter 1, in which the transparency values of the current and of the voltage have been pointed out, the values of the parameters can be extrapolate and are reported in table 3.2.

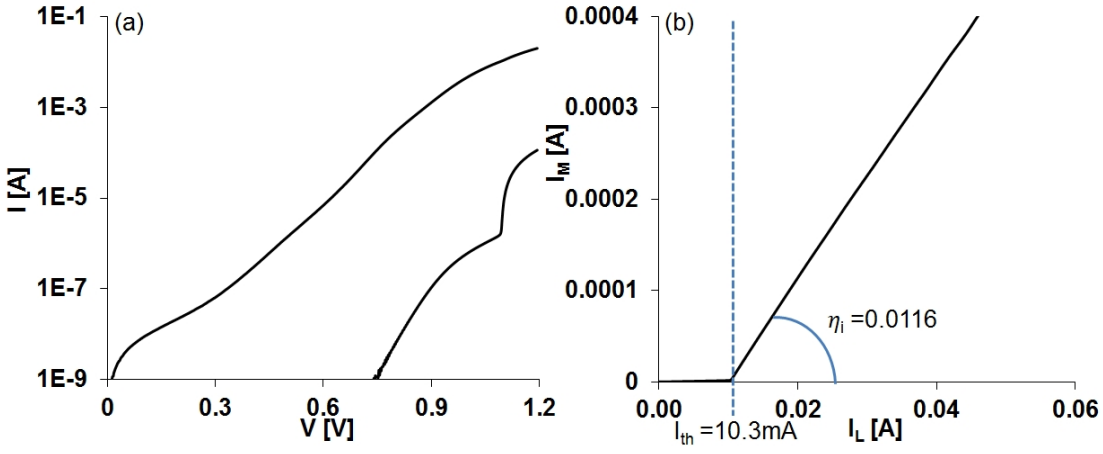

Figure 3.14: (a) The $I(V)$ characteristics and (b) the proportional optical power characteristic measured for a real laser diode.

Parameter	Value
R_S	10.3Ω
I_{th}	10.3mA
η_i	0.0116
K	86
V_{th}	0.99V
R	0.32
$h\nu$=V_{th0}	0.947eV
I_{th0}	3.9mA

Table 3.2: Extracted values of the parameters by using the method illustrated in the paragraph 1.1.6.

The total laser current I and the photonic component I_{ph} as a function of the reduced voltage $V - R_S I$ are reported in fig.3.15. Starting from these electrical characteristics every current component can be identified in the electrical model in fig.3.1 by best fit of the parameters.

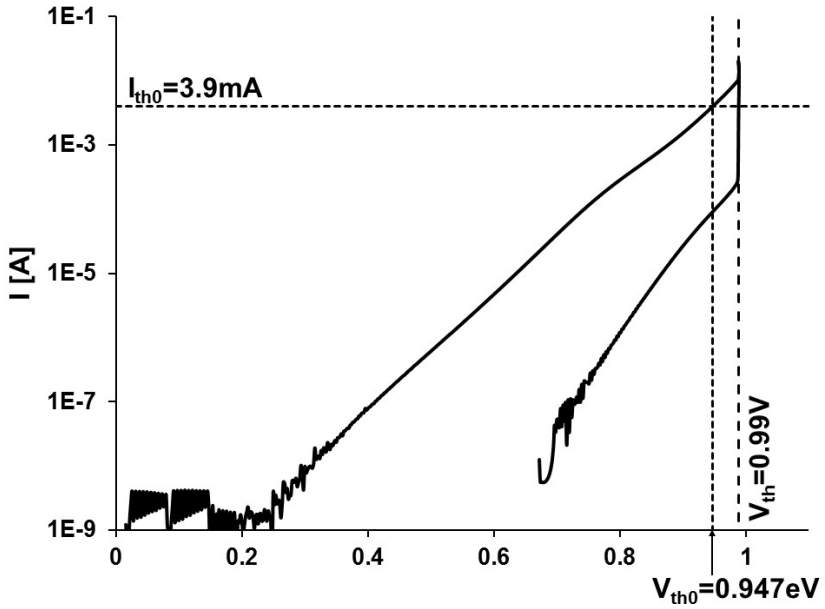

Figure 3.15: The I and I_{ph} characteristics vs. the reduced voltage $V - R_s I$.

Fig.3.16 shows the calculated currents; by using the equation for each component reported in tab.3.1, they are superimposed to the experimental curve mea-

sured. Table 3.3 reports the best fit values for the relevant parameters entering the model.

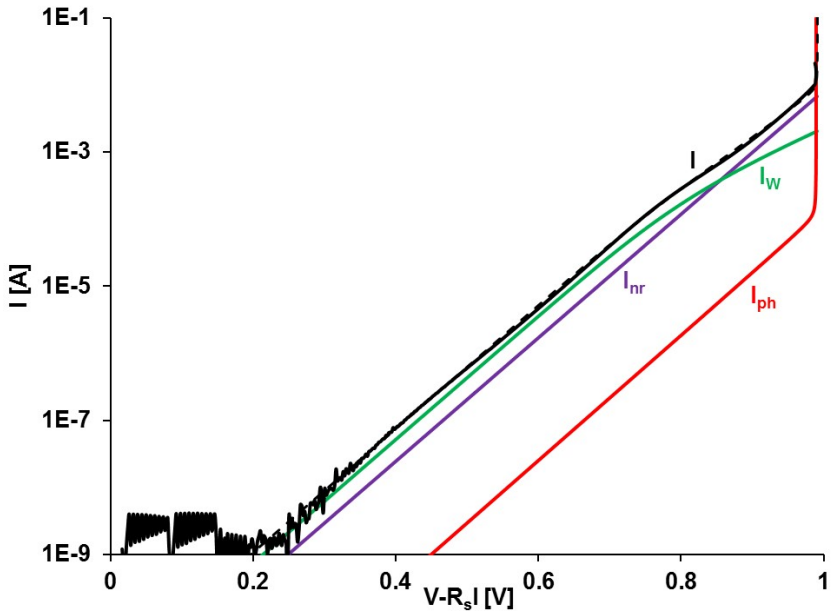

Figure 3.16: Simulated currents for the equivalent model in fig.3.1 compared to the experimental characteristics (black) measured for a real device (fig.3.14). The red line refers to the photonic component, the green one to the lateral flow and the violet curve describes the non radiative component of the current, in this case the shunting resistance is so high that does not contribute for low level of injection.

Parameter	**Value**
I_{nr0}	5pA
n	1.82
R_W	150Ω
I_{W0}	10.7pA
n_W	1.82
I_{ph0}	0.7μA
n_{phn}	1.82
R_{SH}	10TΩ

Table 3.3: The best fit values for the relevant parameters entering the model.

3.1.3 Physically induced parametric changes.

At this point it is evident that this procedure may be of the upmost utility when parameter variations are involved, that is in case of degradation, to address Failure Analysis. This part reports the case of subparagraph 2.2.1 and the comparison between all the parameters before and after the first and the second FIB action. The first step is to compare the electrical measurements of the laser diode as received and after the first FIB. The results are reported in fig.3.17.

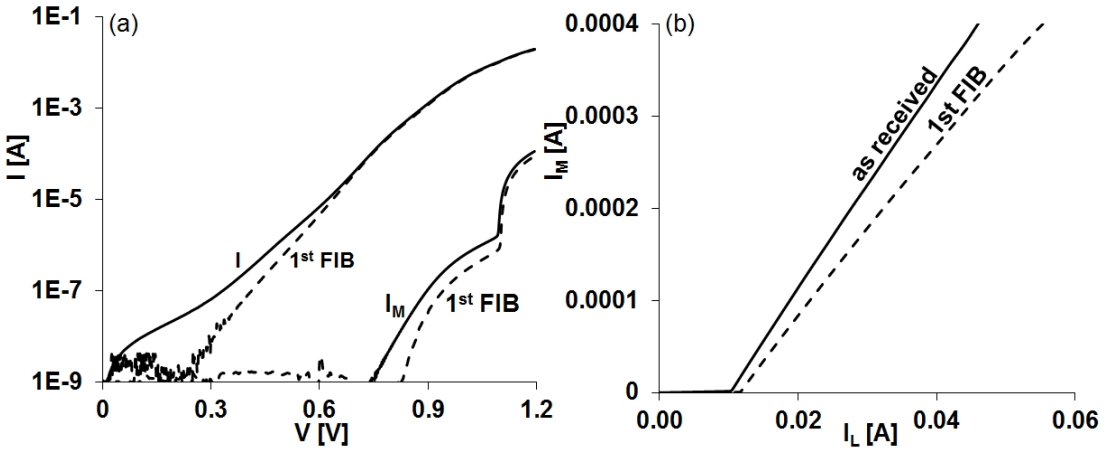

Figure 3.17: (a) Comparison between the experimental measurements $I(V)$ and $I_M(V)$ before (bold line) and after (dashed line) the first FIB action. (b) Comparison between the experimental measurement $I_M(I_L)$ before (bold line) and after (dashed line) the first FIB action.

At first glance, this measurements allow to observe that after the first FIB action:

- in fig.3.17a:
  - for low level of injection a shunting resistive path is created,
  - for high level of injection there are not change and the R_S appears the same,
  - the monitor current after the FIB is lower than the monitor current before the FIB, this predicts a reduction of the photonic current.
- in fig.3.17b:
  - an increase of the threshold current,
  - a decrease of the total efficiency.

The second step is to extrapolate all the parameters for the measurements after the first FIB action, and to compare these values with the values obtained for the device as received, in table 3.4 these two sets of values are reported.

Parameter	**as received**	**1st FIB**
R_S	10.3Ω	10.3Ω
I_{th}	10.3mA	11.6mA
η_i	0.0116	0.00983
K	86	102
V_{th}	0.99V	0.99V
R	0.32	0.32
$h\nu$=V_{th0}	0.947eV	0.947eV
I_{th0}	3.9mA	4.13mA

Table 3.4: Extracted values of the parameters by using the method illustrated in the subparagraph 1.1.6 for the laser diode as received and after the first FIB action.

Figure 3.18, that plots the total current and the photonic component as a function of the reduce voltage, allows to make another important observation: it seems that the threshold voltage does not change, but it depends from $h\nu$ and $R = \alpha_T/g_m$. The first one in this situation can not change, but R, that depends from the total losses, changes as described in 2.2.1. This effect is caused because the variation is so small (less the 10% as can be seen from the difference of the two threshold currents), that is not appreciable in the V_{th}, in which the dependence from the total losses is inside of a logarithm function (1.106).

Finally, also for this case fig.3.19 shows the simulated currents of each component and they are superimposed to the experimental curves measured, table 3.5 reports the best fit values for the relevant parameters of this case.

The values of the parameters, together with the plots in fig.3.17 and fig.3.18, allow to confirm that for high level of injection the curves, before and after the FIB step, are perfectly superimposed, the non-radiative and the lateral components of the current do not present modifications. The presence of a lower resistive shunting path, parallel to the circuit, causes an increase of the current for low level of injection. Finally, the current in the active region, the photonic current, shows a decrease, already noticed from the reduction of the monitor current after the FIB and confirmed by the decrease of the value of I_{ph0}. The non variation of the series resistance is important too, indeed it corresponds to the Ohmic path of the ridge, but, as described in 2.2.1, the FIB action does not touch the ridge, so the R_S does not have reasons to change.

In conclusion, in this section it has been shown how the powerful tool of the mathematical model is useful for the analysis of laser diode. The variations of each parameter allow to determinate which component of the current is changing

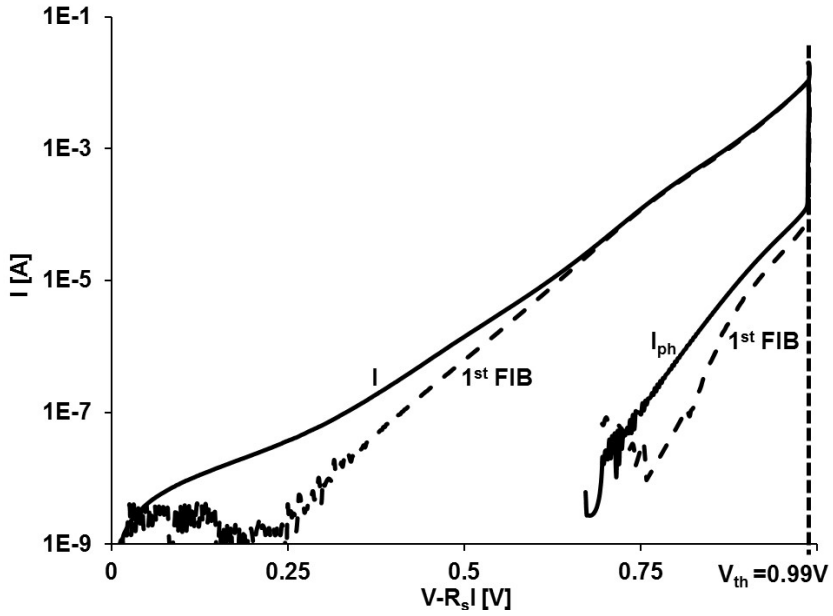

Figure 3.18: Comparison between the $I(V - R_sI)$ and $I_M(V - R_sI)$ of the device before (bold line) and after (dashed line) the first FIB action.

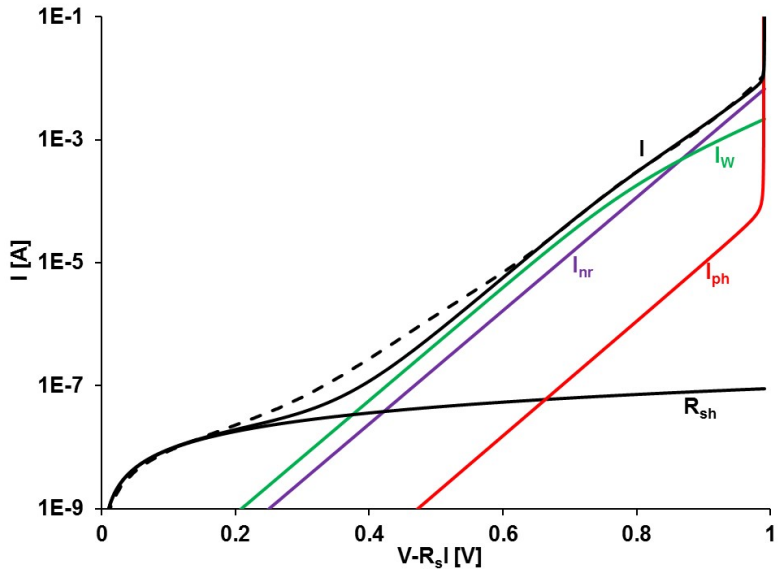

Figure 3.19: Simulated currents for the equivalent model in fig.3.1 compared with the experimental characteristics (bold black line) of laser diode measured (fig.3.17). The red line refers to the photonic component, the green one to the lateral flow the violet curve describes the non radiative component of the current and the back thin curve describes the shunting contribution.

Parameter	as received	1st FIB
I_{nr0}	5pA	5pA
n	1.82	1.82
R_W	150Ω	150Ω
I_{W0}	10.7pA	12pA
n_W	1.82	1.82
I_{ph0}	0.7μA	0.4μA
n_{phn}	1.82	1.82
R_{SH}	10TΩ	11MΩ

Table 3.5: The best fit values for the relevant parameters entering the model for the laser as received and after the first FIB step.

and this gives the possibility to oriented the actions for the failure analysis in the next steps. The application of the model is quite easy and the method to extract all the parameters has been detailed presented, by using some experimental measurements on a Edge-Emitter laser diode. Finally to show the validity of the model, a comparison has been made between a virgin laser and the same laser with a defect induced by FIB. The extraction parameters, by using the proposed model, allows to make a complete analysis of the case.

3.1.4 Multiple parameter changes in COD.

A second example of application of this method is given from the most frequent case of failure in laser diode: the Catastrophical Optical Damage. Indeed this kind of failure has a fingerprint and it is easily recognizable from the parameters and the electrical curves evolutions before and after a COD event. In figure 3.20a the electrical characteristics $I(V)$ in logarithmic scale for a laser diode before (red line) and after COD (black line) are reported. In the zoomed figure 3.20b, a crossing between the two electrical curves is evident.

This point had puzzled the expert designers of an important international company, which whom the Department of Electrical and Electronic Engineering of Cagliari collaborates. Actually the explanation of this effect, by using the method reported in this paragraph, is quite simple.

By using the electrical model and the equation of all the current components, the crossing effect has been simulated by the variation of two parameter (fig.3.21a and 3.21b):

- increasing the saturation current of the non radiative diode I_{nr0}

- and increasing the total losses α_T

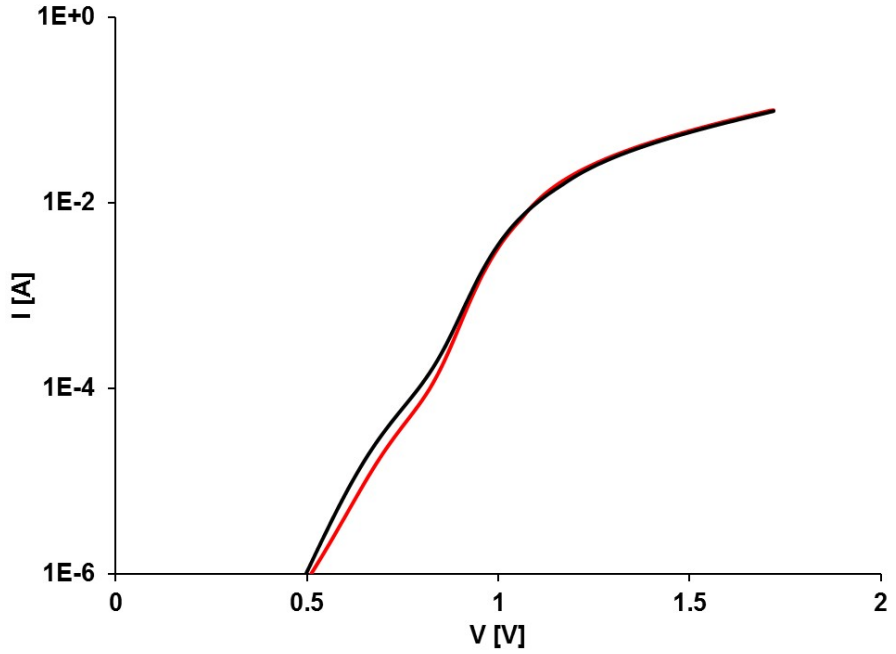

(a)

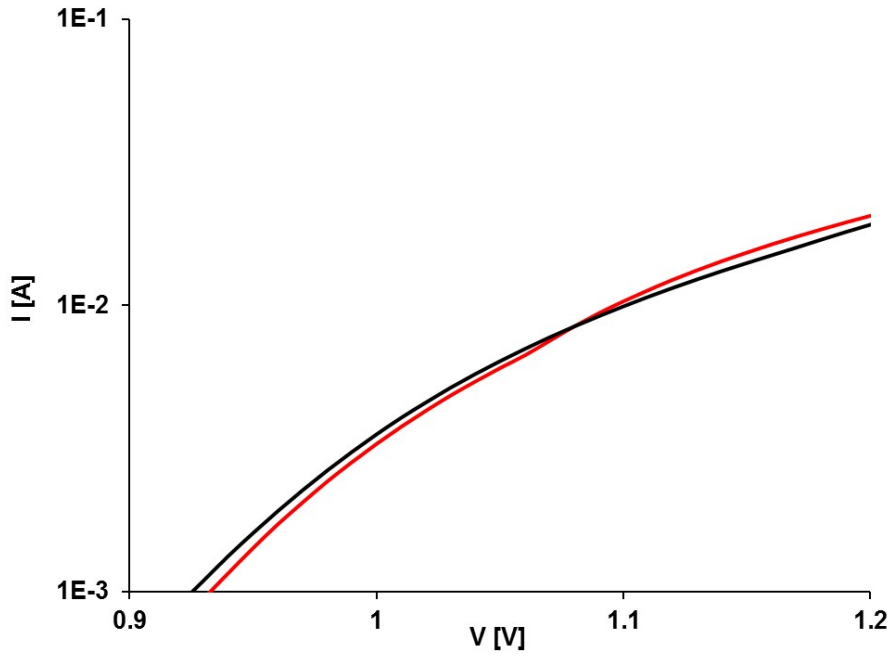

(b)

Figure 3.20: Experimental electrical characteristic for a LD before (red) and after COD (black) (b) and the zoomed area of the crossing between the two curves (b).

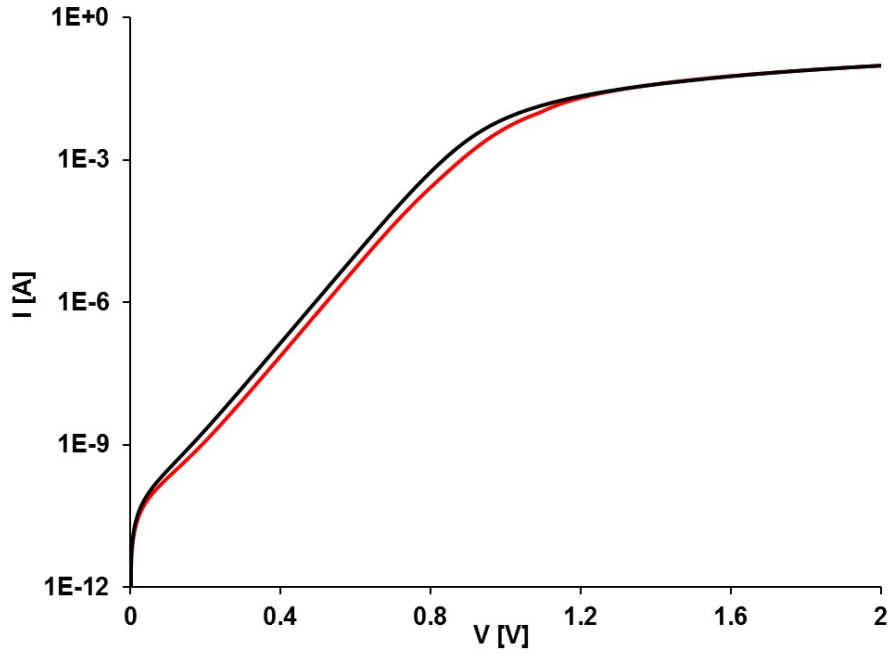

(a)

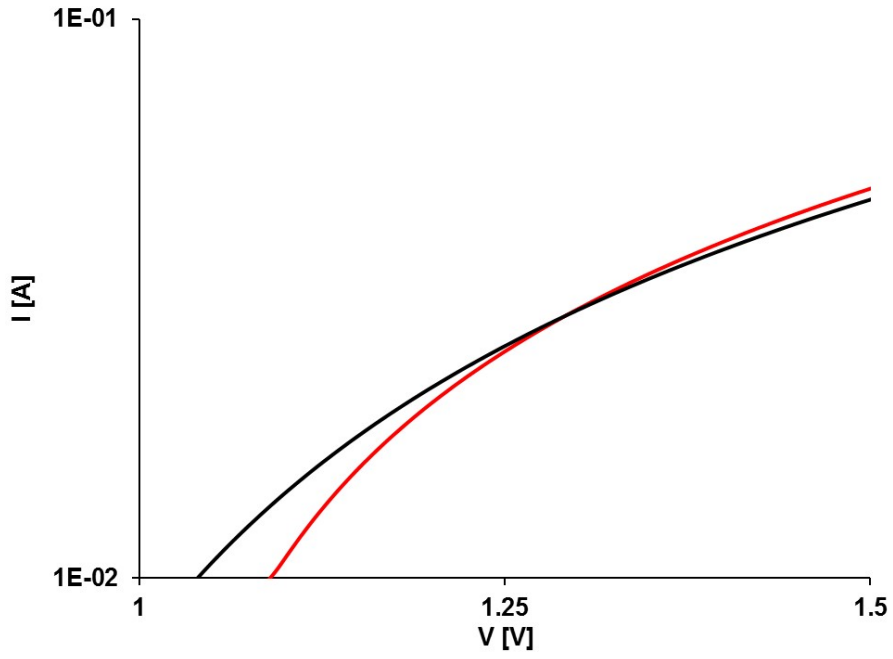

(b)

Figure 3.21: Simulated electrical characteristic for a LD before (red) and after COD (black) (b) and the zoomed area of the crossing between the two curves (b).

This is exactly the description of a failure in the active region as the COD is. Without using electron microscopy, just looking the electrical characteristic $I(V)$, with the electrical model described in Chapter 1 and in this paragraph 3.1, it is possible to recognize a COD from some other events.

3.2 Side mode excitation in single-mode laser diodes.

The Author, during the three year of PhD, managed also with some particular kind of laser diodes for high power application and some unusual case of failure analysis. In this paragraph it will be presented a double-peaked spectrum in some DFB laser diodes that is demonstrated to relate to axially confined Catastrophic Optical Damage (COD), followed by the excitation of a transversal optical mode. The melting-regrowth kinetics of CODs also reveals another possibility of COD-induced side optical modes in a fiber DBR pump laser diode.

The appearance of a double peak in the spectrum of some single-mode laser diodes, failed during their operating life, has been the prompt for a study that reveals the possibility for multi-mode oscillation of the optical field in commercial devices. This study required to recall and summarize the most peculiar features of the so-called Catastrophic Optical Damage (COD) [65, 80–95], in term of spatial and temporal evolution of the associated melting-regrowth process.

It resulted a surprising correlation between CODs and side mode excitation: not only the initial case is easily explained as a COD-induced higher-order lateral mode, but a second case, occurring in some pump laser diodes, externally tuned by means of a fiber Distributed Bragg Reflector (DBR), revealed a quite complex evolution, starting with a COD that induces a vertical higher-order mode that in turn causes a second-level COD. The conclusion that CODs can induce modifications of the optical cavity, able to excite higher harmonics, would probably confine this study to the field of the curious cases. But the observation of a completely reversed relationship, where lateral multi-modes are the origin of a peculiar COD in a state-of-the-art Distributed Feed Back (DFB) structure, flags an alarm on the possibility for mode hopping even in single-mode devices.

The paragraph will first consider the simple case of the double peak in the DFB device, showing the structure of the CODs in planar, transversal and longitudinal views. The transversal features will be referred to a study that has been published a long time ago [96], because of its role in safely identifying a real COD and in particular its regrowth kinetics after the initial melting. The quantitative shift of the second peak will be shown to be consistent with the excitation of the second lateral mode of a Hermite-Gaussian beam [97, 98] for the specific material and geometries.

The COD kinetics will be the key for decoding the second case. In particular the regrowth under Liquid Phase Epitaxy (LPE) conditions will explain the observed distribution of defects and lattice-matched areas in the molten/regrown region as the final effect of the second COD.

Finally, the surprising case of side-mode-induced-COD will be shown and demonstrated.

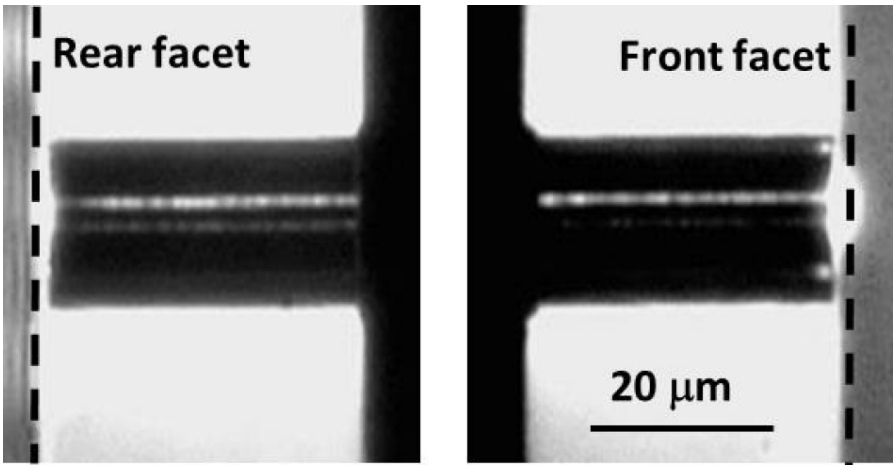

Figure 3.22: EL image of the rear and front facets of one of the failed devices, showing regular light emission.

The paragraph does not aim to discuss the origin of the initial CODs in any of the first and second cases: several authoritative papers have been published on that subject, some of which are listed in the bibliography [65, 80–95].

3.2.1 COD-induced higher-order modes

3.2.1.1 Experimental observations

Some InP-based 1310 nm DFB laser diodes failed during field operation. Their optical power resulted reduced and noisy, but all devices still reached the lasing threshold, and their Electroluminescence (EL) images confirmed light emission from both facets (fig.3.22).

The most surprising feature was the appearance of a second peak in the light spectrum when the laser current was increased beyond approximately 50 mA, as shown in fig.3.23. The second peak was at a wavelength 1.3 nm shorter than the original peak, which survived at its original position

Plan View (PV) STEM analysis was carried out on the rear facets of one of the failed devices (fig.3.24).

The evident damage starts from the facet itself and propagates inside the optical cavity along its central axis, leaving two regions of regular material at its upper and lower sides.

The interpretation of the observed spectrum is then straightforward: at low injection current, the light oscillation inside the damaged segment of the active cavity is mostly switched off, and the surviving cavity on the left sustains the regular oscillation at the wavelength fixed by the DFB corrugation. It is useful to recall here that, in a DFB, the facets do not play the role of mirrors, being the optical feedback supplied by the Bragg diffraction distributed along the whole cavity. The effect of the damaged axial stripe is to reduce the lifetime of the electron-hole pair by increasing the local non-radiative recombination, and to attenuate the optical field by absorbing the incoming photons generated elsewhere.

At higher injection conditions, the attenuation of the fundamental transversal mode, that continues to survive, allows the first lateral mode, whose maxima are

symmetric with respect to the axis, to setup.

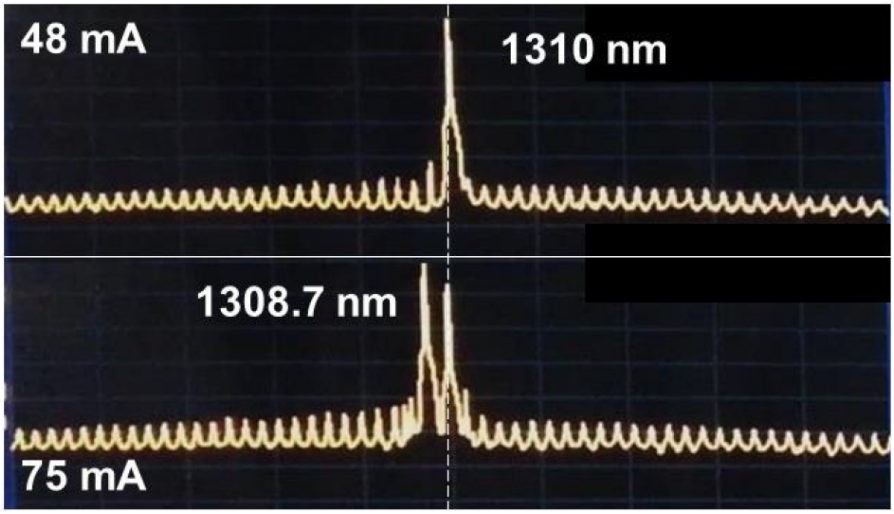

Figure 3.23: Spectrum at two different driving currents of the same device of fig.3.22.

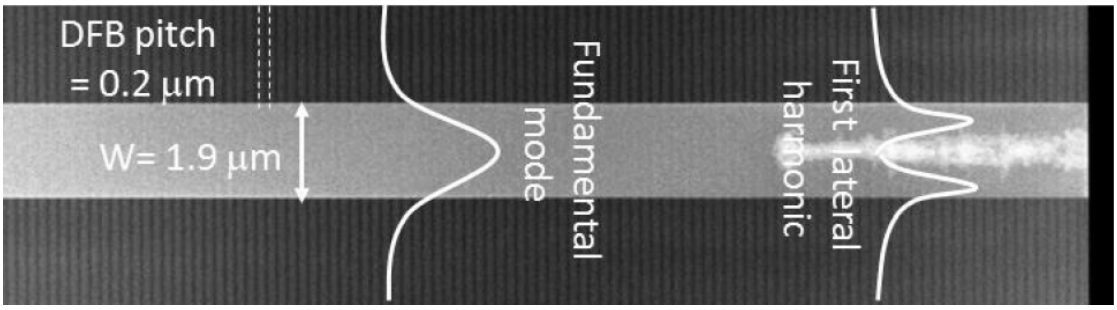

Figure 3.24: PV STEM on the rear facet of a failed device, showing a typical COD propagating from the right-hand side boundary of the optical cavity to inside.

3.2.1.2 Peak separation and the Hermite Gauss functions

The second peak in fig.3.23 seems to indicate that a second wave, with a wavelength shorter by 0.1% with respect to the fundamental one, travels longitudinally along the laser cavity.

Anyway, such a *longitudinal* wave would never resonate with the existing DFB grating, whose measured pitch of 0.211μm strictly corresponds to the 1310 nm wavelength in vacuum when a refractive index n=3.10 is assumed, well suitable for the InGaAsP mixture of the active Multi Quantum Well (MQW) region.

The only possibility is that a *transversal* component of the oscillation is responsible for the new peak. At a first glance, one could consider a sinusoidal wave whose longitudinal half-wavelength corresponds to the pitch d of the DFB grating and, in its fundamental mode, has the width W of the ridge as the transversal half wavelength. In this case, it is easy to demonstrate that the effective wavelength

λ_0 would be defined by

$$\frac{2n}{\lambda_0} = \sqrt{\frac{1}{d^2} + \frac{1}{W^2}} \tag{3.1}$$

The transversal next mode would display a wavelength λ_1 given by

$$\frac{2n}{\lambda_1} = \sqrt{\frac{1}{d^2} + \frac{2}{W^2}} \tag{3.2}$$

Unfortunately, this calculation predicts, for the given figures, a second peak shifted by some 20nm with respect to the fundamental mode.

The solution comes from the more accurate representation of the optical wave in terms of Hermite-Gaussian beams [97, 98], that more realistically represent the lateral confinement, in a ridge-guided structure, as a smooth function and not as a sharp wall.

It is standard practice in Photonics to derive for the fundamental mode the expression

$$\frac{2n}{\lambda_0} = \frac{1}{d}\left(1 + \frac{\alpha}{q}\right) \tag{3.3}$$

Where q is the number of periods of the DFB structure (and then is a very large number, in the order of 1000) and a is a parameter, depending on the ridge width W, the refractive index n and the vertical confinement factor G, that ranges between 0 and 1. The next transversal harmonic brings the wavelength λ_1 to the new value

$$\frac{2n}{\lambda_1} = \frac{1}{d}\left(1 + 2\frac{\alpha}{q}\right) \tag{3.4}$$

The difference $\lambda_0 - \lambda_1$ is exactly in the range of the observed peak shift.

Moreover, the intensity distribution calculated for the fundamental and the first transversal mode by the Hermite-Gauss functions exactly follows the qualitative shapes reported in fig.3.24.

3.2.2 COD structure and regrowth kinetics

The planar view of fig.3.24 shows some interesting features of a COD, that are completed in fig.3.25 by the longitudinal cross-section (LX view) of the damaged region of a second device of the same group.

It is necessary to enlarge the LX image (fig.3.26) to appreciate the alternate regions where the MQW stack survives or disappears, distributed with same periodicity of the DFB grating.

The disappearance of the MQW and the absence of any extended lattice defect indicate a melting/regrowth process, driven by the optical field as a thermal source. One could say that the COD brands the crystal with the shape of the standing wave of the optical field.

This is also the reasons for the preservation of such detailed figures as in fig.3.26, without complete destruction of the whole device: as soon as the material reaches its melting point, light generation locally and suddenly switches off, and the fused region cools down.

The cooling phase is quite interesting: the original different materials of the active region and of the confinement layers are now blended together in a liquid

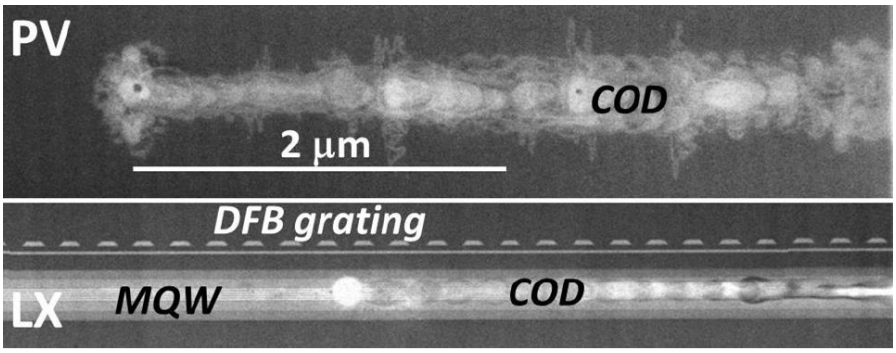

Figure 3.25: PV and LX STEM on the rear facets of two failed devices.

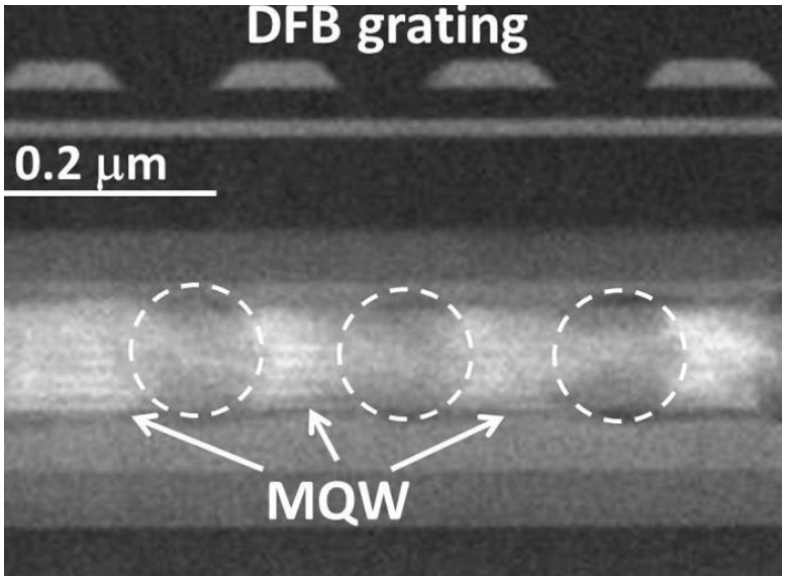

Figure 3.26: Deatil of the LX .view of fig.3.25, showing the alternate surviving or disappearing (circled) MQWs.

phase, and are confined inside several *meltingpots* shaped as the isothermal surfaces generated by the optical field and whose boundaries preserve the lattice of the solid structure. This means that the intermixed materials, cooling down, solidify under Liquid Phase Epitaxy (LPE) conditions starting from the liquid/solid interfaces to inside, according with some complicate phase diagrams that will segregate the lowest melting material to the middle of the regrown region.

This is very well illustrated by an old TEM LX image (fig.3.27) of a suddenly failed strained-lattice (SL) single quantum well (SQW) InGaAs/AlGaAs pump laser diode emitting at 980 nm [99]. The melting process started from overheating of linear defects (misfit dislocations) that instantaneously released the strain of the SL active layer after the penetration of climb dislocations from outside because of Recombination Enhanced Defect reaction (REDR). For the sake of the present study, the interesting point is that the misfit dislocations inside the active layer, because of enhanced photon absorption, became hot rods creating cylindrical isothermal surfaces around them. After melting, the regrown material perfectly replicated the surrounding lattice, but cancelled the active layer. Only a residual

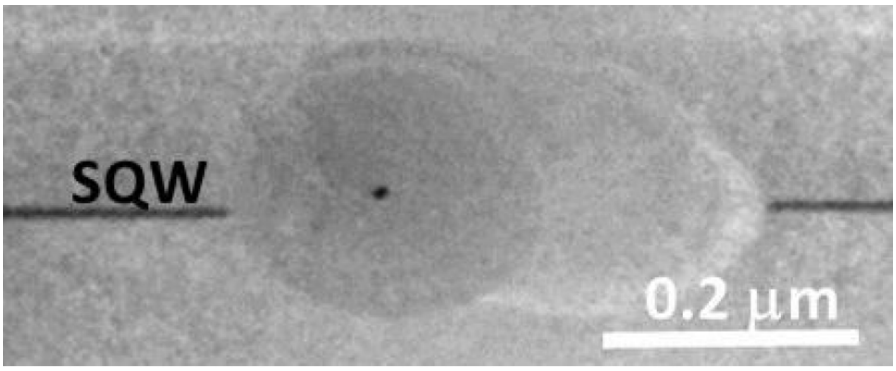

Figure 3.27: Cross-sectional TEM of a molten/regrown SL SQW region.

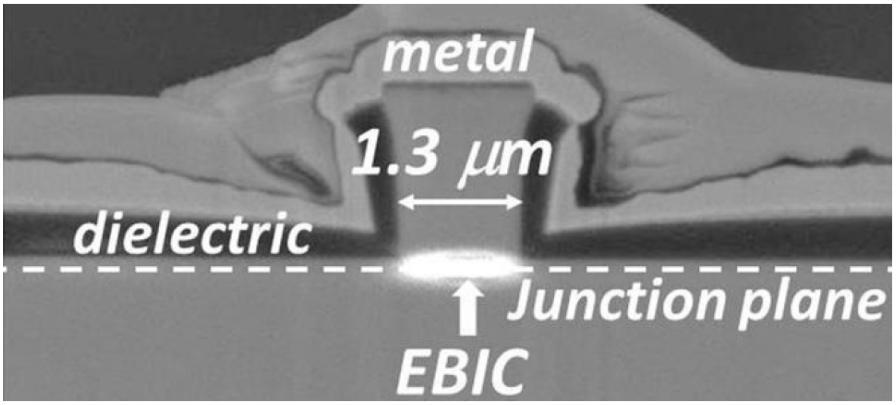

Figure 3.28: Transversal EBIC distribution in a ridge structure (from. Ref. [78])

spot of the low melting In-rich phase appears in the middle of one of the reacted regions.

When the same regrowth kinetics are considered for the molten region of fig.3.26, one should take into account the transversal distribution of the optical energy, predicted by the Hermite-Gauss functions, that is an astigmatic Gaussian bidimensional function. In other words, the circles in fig.3.26 should be considered as cross-sections of ellipsoids.

Fig.3.28 (from [78]) shows the EBIC distribution in the Transversal Cross section (TX view) of a laser diode with ridge confinement. The EBIC signal exactly maps the current distribution under the ridge in forward bias conditions [100] and then also the optical field intensity.

Depending on the position where the ellipsoids are cut in TX view, one may have a situation as in fig.3.29, where the damage is strictly confined in the middle of the active region, where the optical field has its maximum, or a larger intersection as in fig.3.30, where the ellipsoid occupies a large part of the active region.

The dislocations appearing in fig.3.30 at both sides of the COD are also evident in PV (fig.3.25), and should be considered as secondary effect of the intense and fast melting/regrowth event onto the surrounding material.

Anyway, the most interesting feature is that, as for the case of fig.3.27, the most part of the material inside the ellipse is perfectly matched to the surrounding lattice. Only a thin line of defects runs along the major axis of the ellipse. This

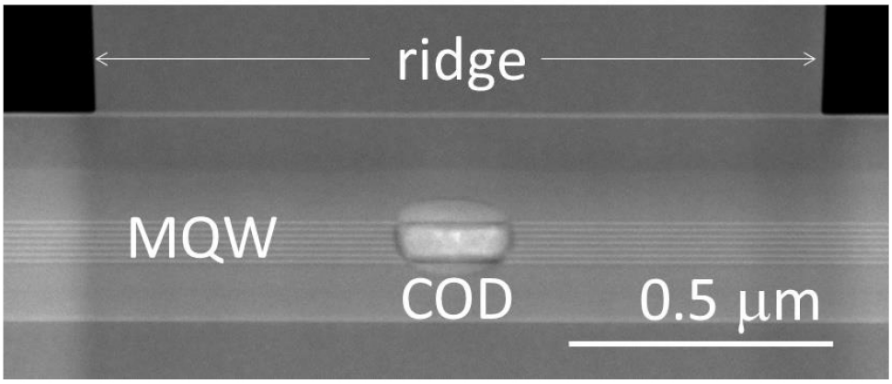

Figure 3.29: TX TEM view of a highly confined COD.

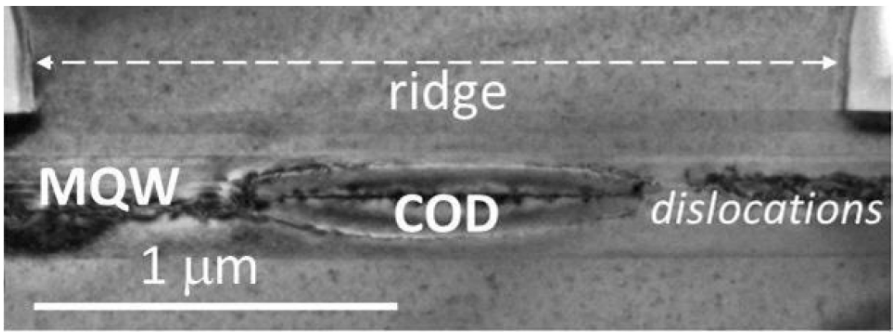

Figure 3.30: TX TEM view of a laterally extended COD.

is the fingerprint of the melting/regrowth process in TX view, and was studied and published since 1991 [96], when dealing with ElectroStatic Discharges (ESD) in Buried Crescent (BC) InP(InGaAsP) laser diodes. The liquid-solid wavefronts that evolve during the solidification process start from the elliptic boundary and proceed as in fig.3.31. The calculation has been carried out, as in the quoted reference, on the basis of the Euler equations [96] for the propagating wavefronts in a system where the growth speed only depends on the local orientation of the interface. The predicted surface quickly develop two cusps along the major axis of the ellipse, whose motion define the locus of the points where the upper and lower wavefronts collapse, and where the low-melting material segregates in a mixture that cannot more be matched to the surrounding lattice.

3.2.3 Double COD and side modes

The previous detailed study of the structure of a COD is the key for understanding a puzzling situation occurred in a set of high power 980 nm pump laser diodes, tuned on a single mode by means of an external fiber DBR.

The PV (fig.3.32) showed a continuous stripe of defects, without any periodicity, extending for several tens of micrometers

It should be evident that the intersecting ellipses cannot coincide with any isothermal surface. Moreover, the defective area occupies a large part of the intersecting regions, but does not extend upwards. The remaining part of the ellipses is made of lattice-matched material, as shown by fig.3.32, where the central bright

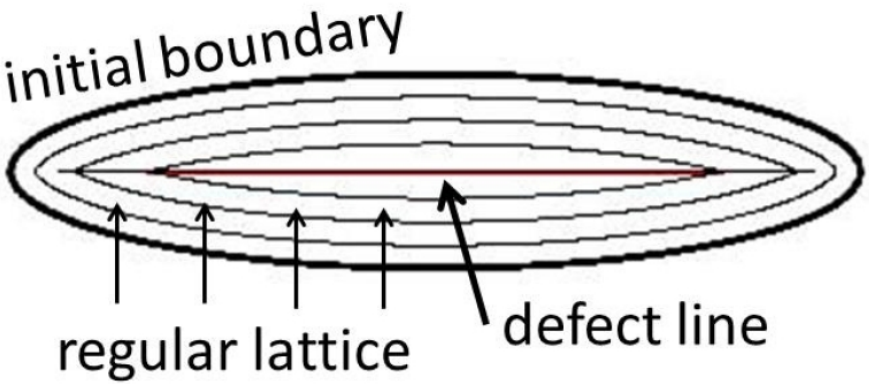

Figure 3.31: Calculated evolution of the liquid/solid boundaries in a COD.

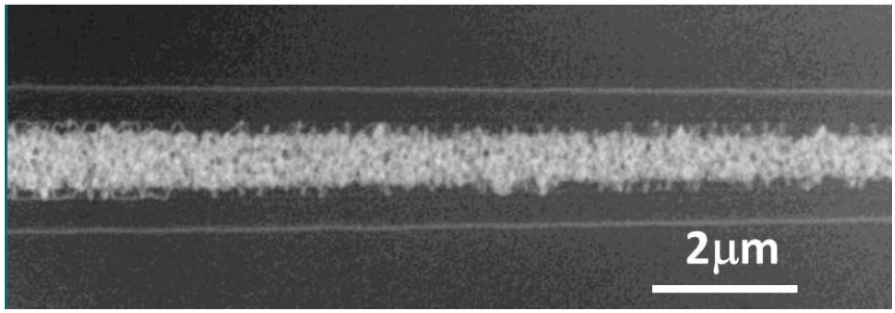

Figure 3.32: STEM PV of extended defects in a failed high power 980 nm pump laser diode.

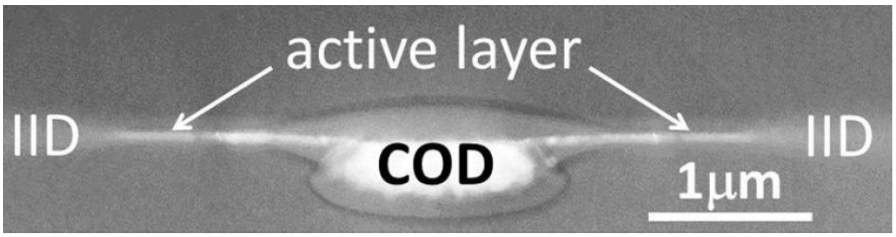

Figure 3.33: STEM TX of the defects in fig.3.32. The lateral IID labels indicate the Impurity-Induced-Disordering used in this device for lateral confinement.

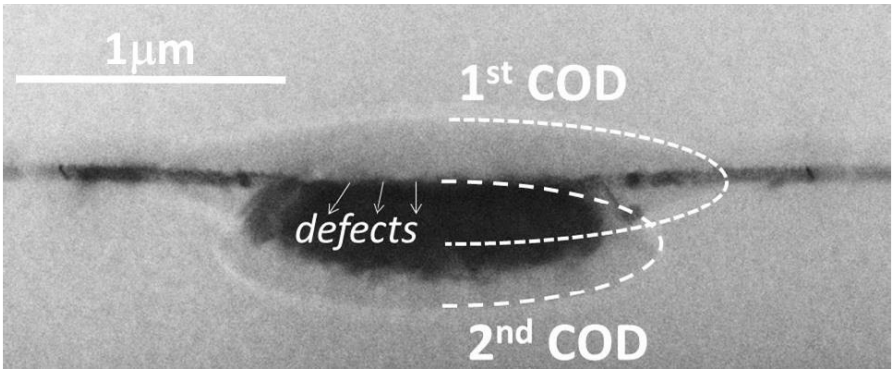

Figure 3.34: Two step kinetics for the case of fig.3.32, 3.33.

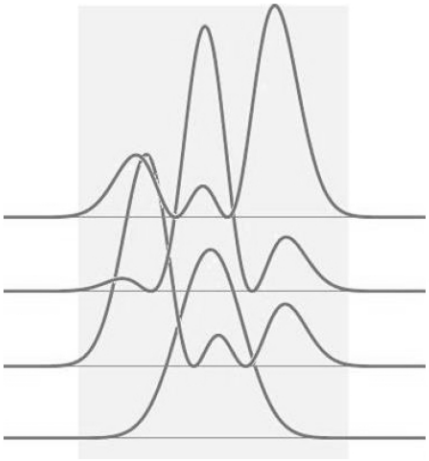

Figure 3.35: Asymmetric field distribution by different combination of the first transversal Hermite-Gauss harmonics.

stripe corresponds to the defects inside the ellipses, and the two thin horizontal white lines are the boundaries of the upper ellipses in fig.3.33. No kinetics are known able to create such a structure during a single melting/regrowth event.

The solution, on the contrary, appears clear if we suppose two events. The first is a standard COD, and creates the ellipse aligned with the active layer. This will have the same structure described in the previous subparagraph 3.2.2. But we then need to suppose that the light did not disappear in this area, but that an intense optical beam traveled below the molten/regrown region, and that caused a second COD. This second COD will melt the second elliptic region, and here is the key point: the upper side of the new liquid/solid interface runs along the defect line of the first ellipse. The LPE process evolving from here does not replicate a perfect lattice, but will cause a complex network of twins and thread dislocations to fill the space between the major axes of the two ellipses (fig.3.34).

The question is: how can the optical field move away from the active region? The answer is likely to be, again, in the higher order transversal modes, as in the first case, with the difference that here it is a vertical transversal mode that is called into play. This requires a larger amount of energy than for activating and horizontal lateral higher mode, but, on the other side, the device is designed exactly for high power operations. Also the presence of a single ellipse in the secondary COD, instead of two symmetrical ones over and below the active layer is easily explained. It is indeed very easy to obtain asymmetric beams by allowing mode interference. For instance, fig.3.35 shows three possible field distributions obtained by differently combining the first three transversal Hermite-Gauss orders T00, T10 and T20, always keeping the same total power distributed among modes.

It is interesting to observe as the excitation of higher transversal modes can focus a peak of energy also in a narrow central peak, reaching a local density higher than in the sole fundamental peak for which the device has been designed. This last observation can be an alternative explanation of the very confined COD in fig.3.29.

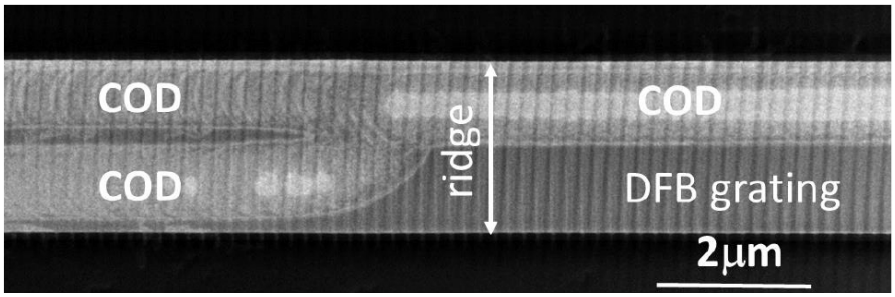

Figure 3.36: STEM PV of a DFB structure showing a COD separated into two parallel paths.

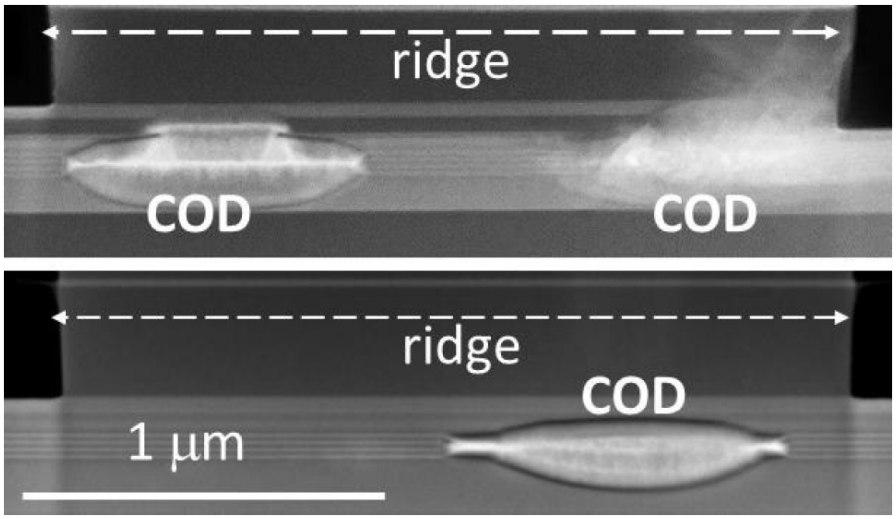

Figure 3.37: STEM TX of the same device as in fig.3.36 at both the double and the single path CODs.

3.2.4 Lateral-mode-induced COD

The last subparagraph 3.2.3 could be summarized in two sole images, fig.3.36 and fig.3.37. They belong to a high power 1310 nm DFB structure that failed during High Temperature Operating Life (HTOL) test. They show a long COD, propagating along several tens of micrometers, split into two parallel rails, that converge in a single rail, occupying half the width of the ridge guided area. The cross section identifies as real CODs two symmetric elliptic regions, with all the features described in the previous subparagraph 3.2.2.

Here the difference with the previous cases is striking: the COD is not the cause, but the effect of the higher-order transversal optical mode. No primitive damage has been found on this and other devices of the same group, but only the observed long damaged paths, that in turn cannot be anything else than molten/regrown regions following the optical intensity.

The first two cases reported in this subparagraph can be considered just complicate effects of a very well-known failure mechanism as a COD. Nevertheless, their detailed study allows to progressively investigate the structure of a COD, pointing out some of its structural peculiarities that make its individuation absolutely safe.

It is then possible to bring the results of the last subparagraph and in particular

of fig.3.36 and 3.37 to their ultimate interpretation: single mode laser structures may host transversal multi-modes. It is not sure that when this happens it also leads to a COD. In this case, the performances of the device would be severely affected in terms of dispersion figures in fiber optic communications.

It is not the aim of this subparagraph to investigate the origin of such multi-modality, leaving this subject to a more accurate investigation. It can be said that the common point for all cases seems to be the high power: even the first case, involving a device operating at low power, reveals the higher-order mode by a second peak that only appears when the driving current increases. More precisely, it seems that the high optical power density is the trigger for higher harmonics, which not only includes the high power devices, but also the low power ones whose active region is highly confined vertically and laterally.

Also any design solution or process flaw that can break the axial symmetry of the optical cavity is indicted for exciting th extra-modes. In this directions some studies are in progress, involving integrated optical devices, where the coupling elements can become critical for this new failure mechanism.

3.3 ESD tests on 850 nm GaAs-based VCSELs

Forward and reverse HBM, MM, CDM ESD tests have been performed on 850-nm VCSELs, together with EOS and overpower test. The physical analysis of the tested devices showed a variety of damages not easily correlated to the measured electro-optical degradations. The solution requires the detailed interpretation of the observed physical mechanism, by means of electron microscopy and device modelling, that also in this case it helps with the solution of the physical interpretation for the mechanisms of failures.

The qualification plan for telecom application of commercial GaAs-based VCSELs emitting at 850 nm included several transient electrical stress tests: forward and reverse ESD tests according with the Human Body Model (HBM), the Charged Device Model (CDM) and the Charged Machine Model (MM) , Surge test and Over Power (OVP) test [101–106]

Several failures have been detected by the simple monitoring of the current leakage at reverse bias. Anyway, the attempt to correlate the leakage level with the polarity, timing and intensity of the applied stress was not able to point out more than a fair relationship between stress intensity and leakage. Moreover, when physical analysis was performed first by forward Electro Luminescence (EL), and reverse-bias emission microscopy (EMMI) and then by FIB-assisted Electron Microscopy (at both the SEM and the STEM), the pattern of the observed damages complicated even more the situation. It happened, indeed, that some damage patterns, well known in VCSEL literature [107–113], appeared in devices with extremely different leakage levels, and even in devices that passed the pass/fail test after the stress.

The last observation on one side calls for an explanation, and on the other side rises a warning about the possibility that some devices pass the ESD tests but that the test themselves introduce the seed for delayed degradation during the operating life

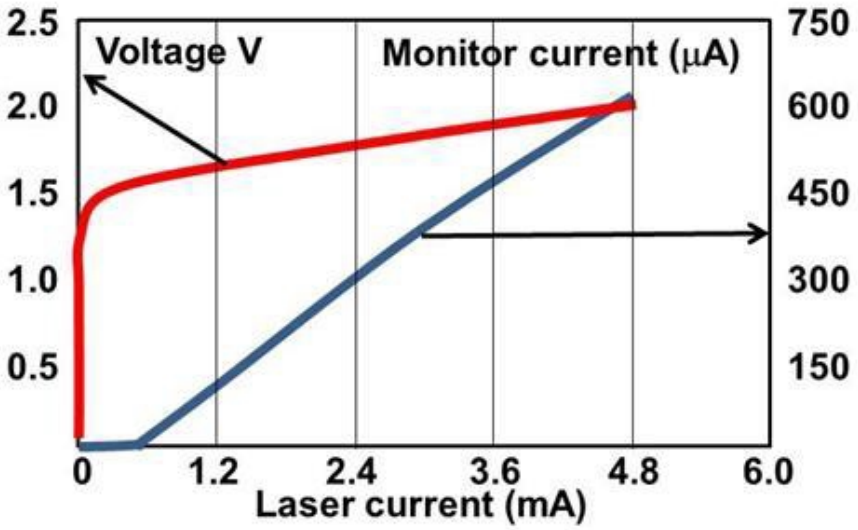

Figure 3.38: Electro-optical DC characteristics of a typical VCSEL before the stress test.

This paragraph aims to strictly focus on the correlation between physical damage and electrical properties. It will first summarize the set of tests, and illustrate the most evident and also the most contradictory results. Then it will introduce a simple circuital interpretation for the type and location, and the observable electrical effects, of the observed physical damage.

3.3.1 Devices, ESD tests and failure modes

The devices are commercial VCSELs for telecom applications, whose internal structure includes upper and lower Distributed Bragg Reflectors (DBR) with respect to the active plane. The latter, in turn, achieves laterally confined emission by means of a partially oxidized Al-rich epitaxial plane, that leaves only a nearly circular central area accessible to the injection current (see next subparagraph 3.3.2 for some physical details). Despite the sharp selection of the longitudinal oscillation operated ny the DBR, the light emission is expected to allow several lateral modes, for the sake of a better (lower) beam divergence.

The typical electrical and optical DC characteristics of one of the devices are reported in fig.3.38. On such devices, transient electrical tests have been planned, whose complete set is reported in tab.3.6. The forward or reverse polarity of the stress have been indicated by, respectively, the + or the – sign. A leakage level larger than $2\mu A$ at a reverse bias of $-5V$ was used as a pass/fail criterion after the tests. The highlighted cells in the last column, indicate devices that passed the test, having a leakage lower than the preset failure criterion. It should be noticed that, apart three cases (highlighted cells in the last column), all devices failed, according with the given criterion.

Some correlation is evident, for instance between the leakage level and the maximum stress in HBM tests. Anyway this does not hold, for instance, for Over Power (OVP) tests, where the highest electrical degradation occurs for the less severe stress. When one tries to solve the puzzle for the OVP test by observing

n.#	**Test**	**Conditions**	**Leak. at -5V**
1	OVP	20mA / 10s, 50mA / 10s	453μA
2	OVP	20mA, 24mA, 36mA, 42mA / 10s	752μA
3	OVP	30mA / 10s	>2mA
4	surge+	24mA/5ms/10, 42mA/5ms/10	normal
5	surge+	60mA/5ms/15	6.31μA
6	surge-	10mA/5ms/10, 20mA/5ms/10	big
7	HBM-	0-200V / 6	4.59μA
8	HBM-	0-200V / 6	4.64μA
9	HBM-	0-1000V / 200V step	0.835μA
10	HBM-	0-1000V / 200V step	243μA
11	HBM+	1400V-5000V / 200V step	>2mA
12	HBM+	1400V-5000V / 200V step	>2mA
13	HBM+/-	2000V	20.2μA
14	HBM+/-	2000V	11.3μA
15	CDM+/-	fail 740V	5.42μA
16	CDM+/-	fail 730V	5.65μA
17	CDM+/-	pass 440V	1.15μA
18	MM+/-	fail -500V	5.69μA
19	MM+/-	fail -500V	9.87μA
20	MM+/-	pass 300V	296nA

Table 3.6: Tests and results.

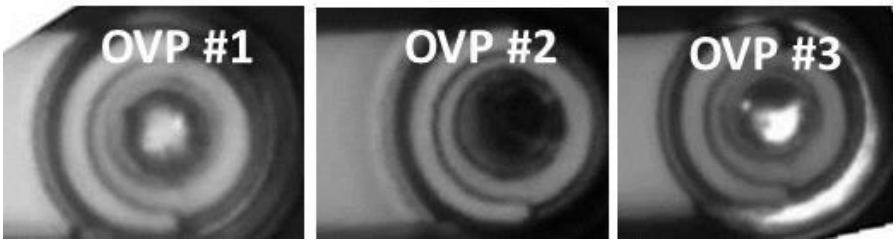

Figure 3.39: EL images of the residual light emission for the three devices stressed by the OVP test (see Table 3.6).

the EL emission (fig.3.39) of the three devices #1,2,3, one gets even more confusing data, because, for instance, device 3 is much more leaky than device 2, but has also much more residual light emission.

The set of measurements in fig.3.38 and 3.39 is everything is possible to do without opening the package, and then is also the available set of actions for screening purposes. Any further insight requires destructive actions, starting from the package.

Spectral analysis is usually not considered among this set, because of the several unpredictable lateral modes intrinsically allowed by the design itself of a VCSEL, even during regular operation.

3.3.2 Physical analysis

As a preliminary step, the vertical structure of the devices has been reconstructed at the SEM after FIB-assisted cross-sectioning (fig.3.40).

For the failed devices, EL was used to drive 200 keV STEM analysis in Z-Contrast (ZC) mode, sometimes in Planar View (PV), sometimes in cross-sectional (X) view. This method has been nicely illustrated and applied in [113]. It takes advantage of the capability of analyzing thick specimens, up to 1 micrometer for our devices, preserving information from scattering phenomena as for the standard Diffraction Contrast, but without the constraint of thin lamellas. This allows to include the whole 3D extension of several defects, as the next examples will show.

The different tests caused several different patterns of physical damage, and different degrees of electro-optical degradation. The puzzling point is the apparent poor correlation between physical damage and optical degradation.

Fig.3.41 reports two kinds of physical, damage, corresponding to two levels of reverse HBM ESD test.

The first case, despite the evident damages, did not show any significant change in the optical characteristics (threshold current and optical efficiency), and a small leakage of less than $5\mu A$ at $-5V$. The second case, on the contrary, displayed the total loss of optical emission and a leakage at $-5V$ as large as about $240\mu A$.

The conclusion seems evident: the higher stress creates the damage external to the oxide window, and that kind of damage is responsible for the main electrical and optical degradation.

Anyway, the situation resulted much more articulated. A second device stressed at $1000V$ reverse HBM test did not show any change after the test, but, after some ageing, it approached the same failure modes of the previous device. A variety

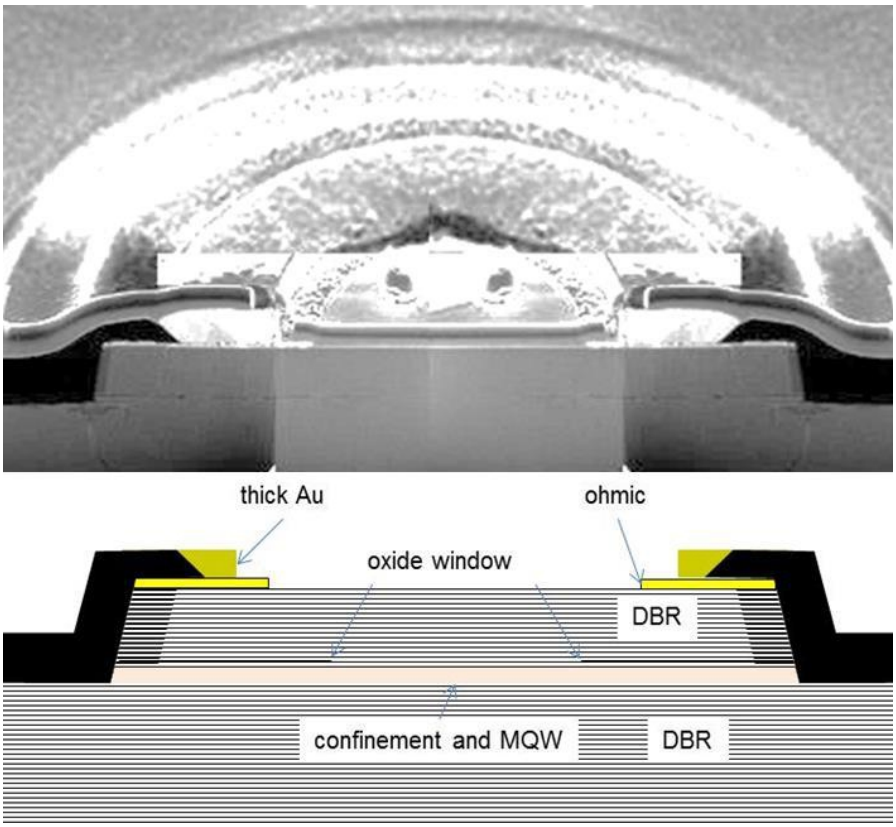

Figure 3.40: Cross-sectional view of one of the tested VCSELs at the SEM (upper side) and reconstructed transversal structure.

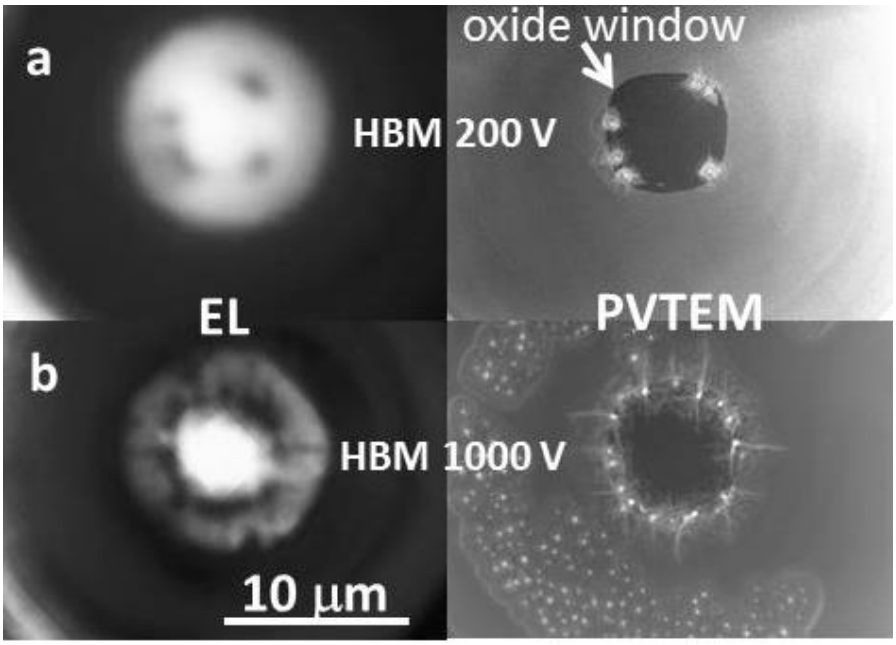

Figure 3.41: Electro Luminescence (EL) and Planar View TEM (PVTEM) on two devices after reverse HBM test at a) 200 V (#7 in Table 3.6) and b) 1000 V (#10).

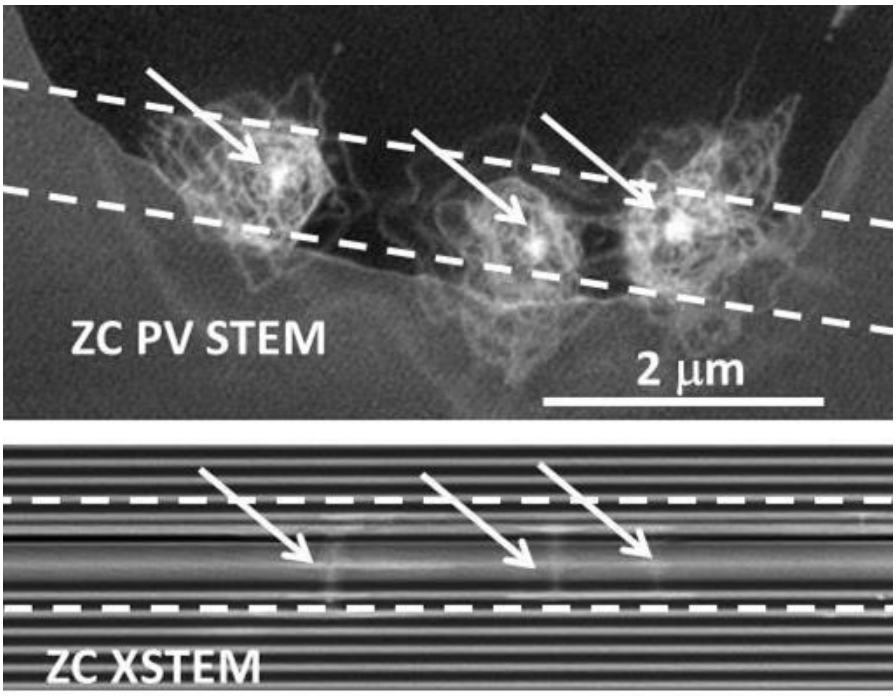

Figure 3.42: Plan View (PV) and Cross-sectional view (X) at the STEM in Z-Contrast (ZC) of two similar sets of three ESD-induced defects (arrowed) as for specimen in fig.3.39a. The dashed lines in each image indicate the approximate thickness of the specimen in the other, that then results to include the whole 3D extension of the defects.

of combination was then discovered between the applied stresses, the physical evidence and the detectable optical and electrical failure modes.

The structural analysis of the defects showed as the spots appearing along the internal rim of the oxide windows are vertical structures surrounded by nested systems of dislocations (fig.3.42).

Such structures, in themselves, are not sufficient to cause any relevant electrical effect, because of their complete immersion inside the depletion region of the *pn* junction, or any optical effect, because of their location at the boundaries of the optical cavity.

Nevertheless, they are likely to become nucleation points for larger defects during the operating life of the devices, as shown in fig.3.43, where a fatal network of dislocations clearly evolves from a single local damage point into a Dark Line Defect (DLD) structure. Also the damages observed in fig.3.41b, outside the oxide window, may appear at a different extent, but always involve the perforation of the oxide. For the weaker cases, the perforation creates small molten regions that, cooling down, are likely to preserve the dominant local doping , and then re-build a parasitic *pn* junction that keeps the measured leakage limited (fig.3.44).

Of course, high levels of stress can lead directly to a faulty state. What is interesting is the fact that some defects may occur without any external manifestation. Also the types of transient stress may be different, leading to quite similar degradation states. For instance, fig.3.45 reports the result of a surge test, where the device, after the stress, passed the electrical and optical tests. It was only the EL

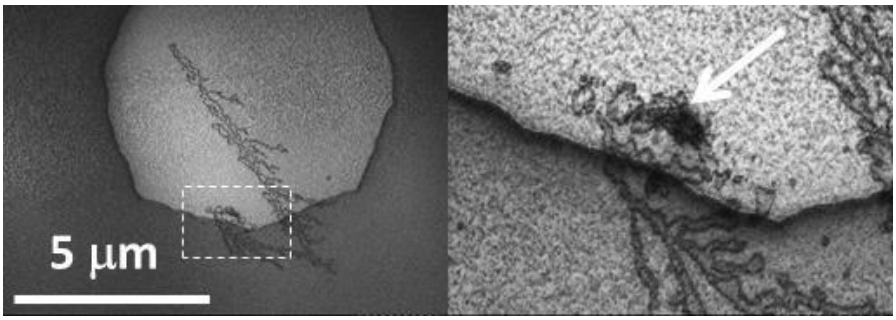

Figure 3.43: DLDs evolving from a local damage.

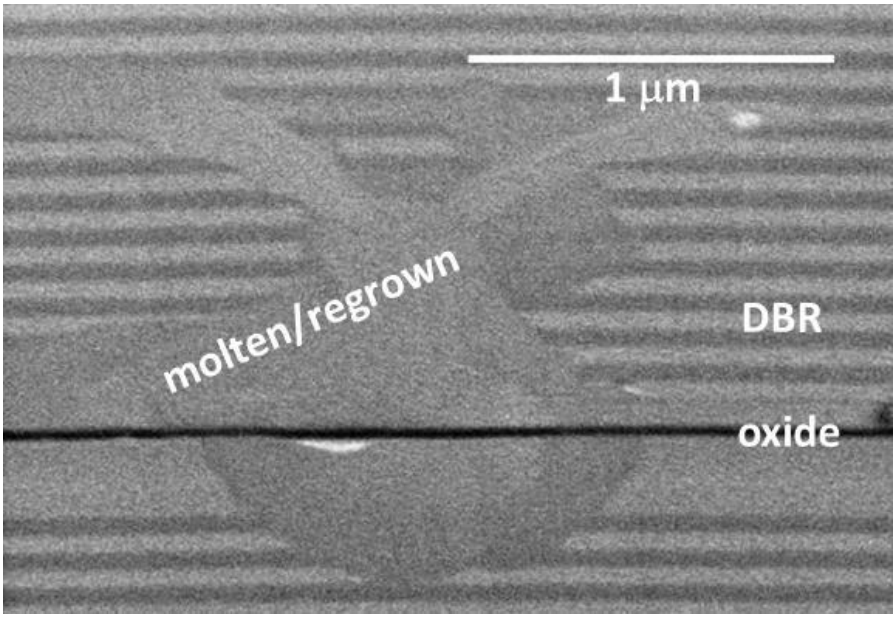

Figure 3.44: Transversal view of an oxide damage, with the evidence of melting and regrowth of the stack of layers of the Distributed Bragg Reflector (DBR).

inspection, and the following TEM analysis, that revealed the same microscopic damage as for the $200V$ HBM test reported in fig.3.41a.

3.3.3 Electrical model

In order to describe the distribution of the stress during the transient events, the model reported in fig.3.46 has been developed. It is obviously an over-simplified model, that tries to summarize with a unidimensional resistive network of parallel elements what is a structure that has a circular symmetry. It then qualitatively describes what happens along a radius of the VCSEL circular structure. The rightmost element in fig.3.45 then represents the geometric center of the device, where the only allowed current flow is vertical, while for any other element also a lateral flow must be allowed. The numerical values associated to each element have been selected in order to reproduce under DC and AC the measured values for the real devices.

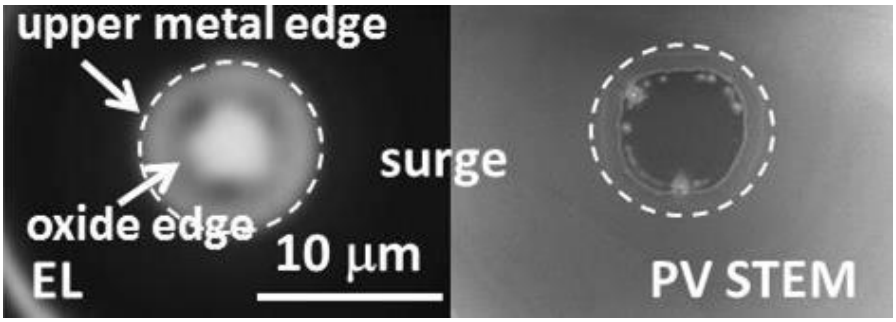

Figure 3.45: Results of a forward surge test, to be compared with fig.3.41a.

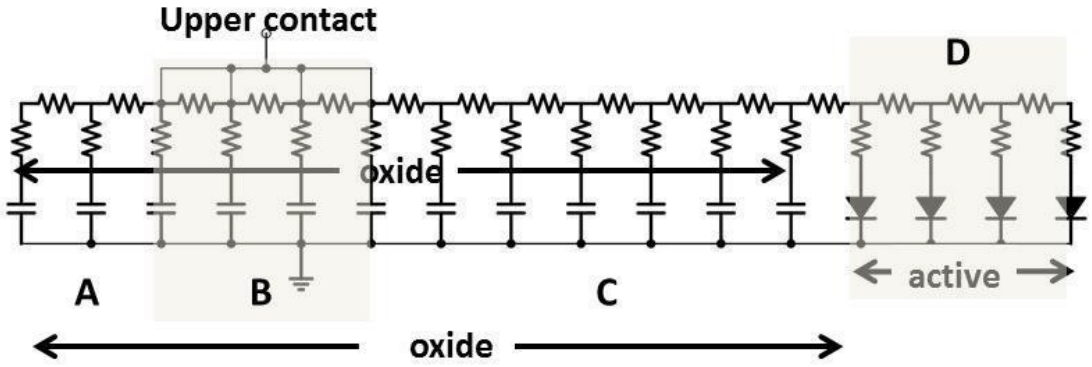

Figure 3.46: A resistive network model for the VCSEL, representing the radial distribution of electrical elements. Four regions, A,B,C,D are highlighted, corresponding to different regions shown in fig.3.40.

Several situations have been simulated by means of the circuit in fig.3.46. The most clarifying example refers to the case of a reverse HBM stress, as for the experimental cases of fig.3.41. First of all, each node in the circuit will sustain a transient that has the general time evolution as in fig.3.47

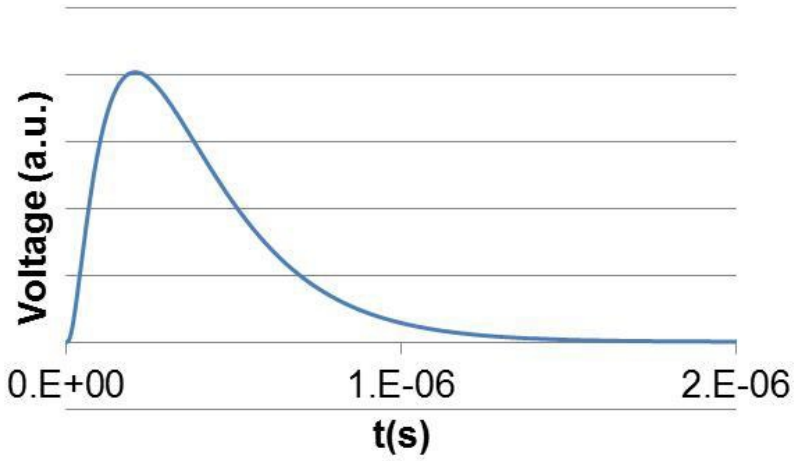

Figure 3.47: Time evolution of the EDS discharge at a generic node in the circuit in fig.3.46

The increasing voltages across the nodes during the rising time is shown in fig.3.48.

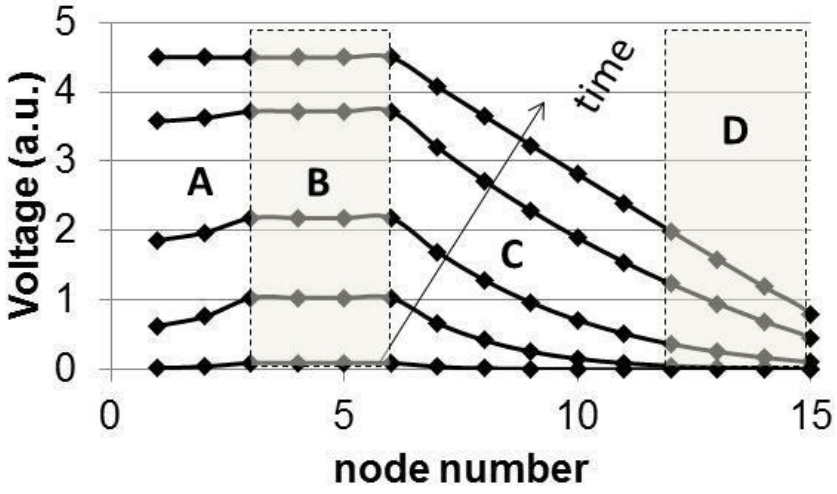

Figure 3.48: Rising voltage transient across the capacitors and diodes in fig.3.46

The four regions A,B,C,D of fig.3.46 and 3.48 can be identified on the same damage pattern of fig. 3.41b, as shown in fig.3.49. The white spots in region D are of the same type as in fig. 3.42, while those in region B belong to the type of fig.3.44.

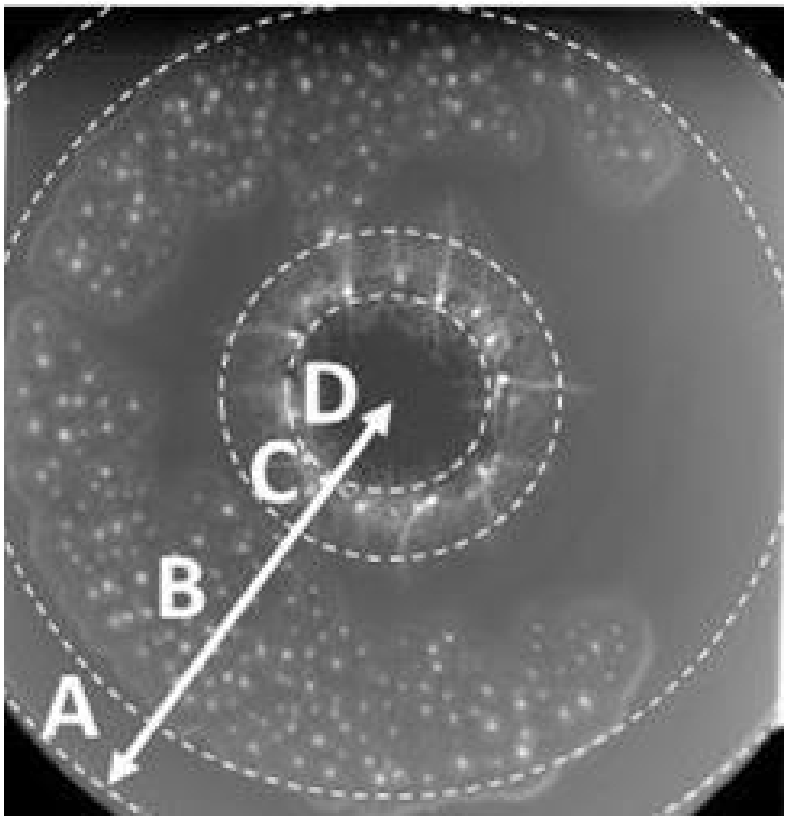

Figure 3.49: The four regions A,B,C,D of fig.3.46 and 3.48 correspond to different damage patterns on real cases (same specimen as in fig.3.41b).

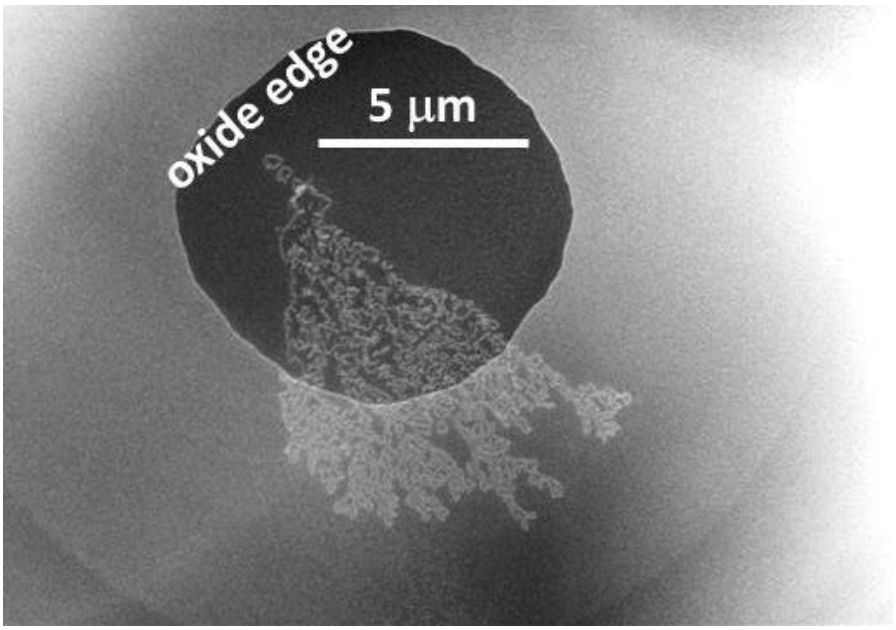

Figure 3.50: STEM Plan view of a dislocation network evolving form a single point inside the active region, likely to *not* be caused by ESD.

The section proposed several results from ESD tests on commercial VCSEL devices. It focused on the problem of identifying the type, structure and spatial distribution of the observed physical damage.

Several conclusions follow the proposed analysis. First of all, two kinds of defects are shown to appear, whose structural details are given, respectively, in fig.3.42 and 3.44. Both occur, as expected, at the places of maximum field in the oxidized regions A,B,C and in the active region D. All of them appear as the result of current filaments, causing a small damaged core and a surrounding region that is mostly made of nested dislocations for the active region and of extended fusion/solidification areas in the oxidized areas.

The thresholds for the two kinds of failures indicate that the weakest structure is the edge of the active region (as shown by fig.3.41 and fig.3.45). Failures across the oxide are always related to excess leakage, and their occurrence also causes an optical faulty state, in terms of reduced light emission.

On the contrary, failures in the active region can occur as silent damage, not detected by the standard optical or electrical screening methods. Their risk for device reliability is illustrated by fig.3.43, where DLD defects are likely to evolve from small defective areas close to the oxide edge. The effectiveness of EL in individuating cases as in fig.3.45 strongly suggests to introduce Electro Luminescence as a screening procedure whenever possible, if ESD risks are involved.

It is not marginal also what that same on DLD evolution conclusion do exclude. Cases as in fig.3.50 and fig.3.51 have been often claimed as the result of ESD stress, possibly due to incorrect handling. Based on the proposed analysis, on the contrary, ESD hardly justifies such interpretation: dislocations evolve, as in fig.3.42, from a small point, but the point is in the wrong place and its nucleus does not correspond to any of the structures shown in fig.3.41.

Even more, in fig.3.51 nothing leads to any relationship with ESD events:

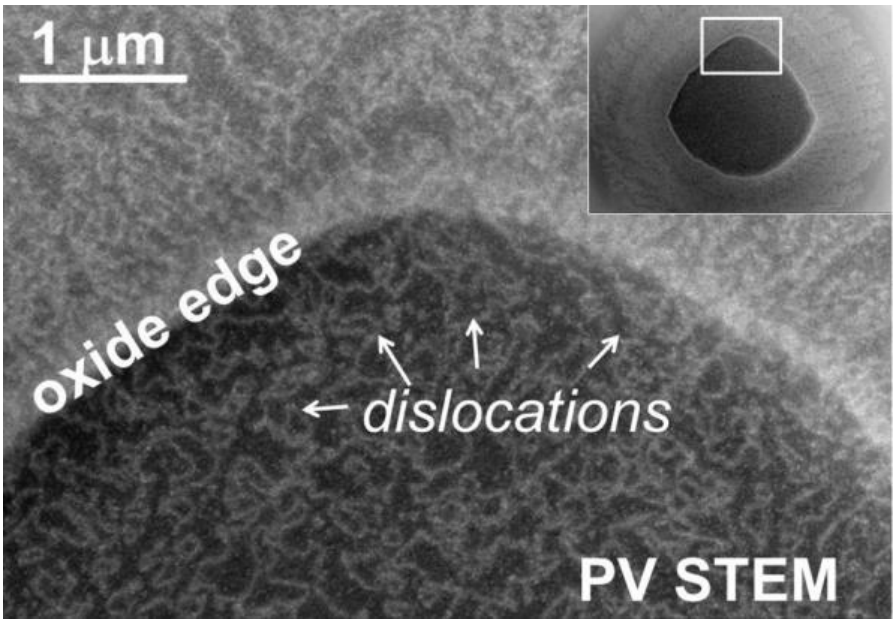

Figure 3.51: STEM Plan view of a uniform dislocation network, occupying the whole active window and extending outside, attributed to ESD.

a uniform network of dislocations floods the active area, possibly evolving from native defects at epitaxy or, more probably, from the oxidized edge. Nevertheless, the Manufacturer concluded his own Failure Analysis, requested by the end user, with the words: "The crystal damage coincides with ESD high current path. So this failure was undoubtedly caused by ESD because no other mechanism would produce this same crystal damage pattern".

The evident contradiction of the last statement with the reported results also puts the question of ESD as the most frequent indicted culprit for any failure, at least in the Manufacturer-Customer commercial relationships. The repeated occurrence of cases of questionable failure analysis reports has been discussed since a long time [114–117], and also recently [118] , and points out the opportunity of demonstrating the proposed conclusions on the basis of scientific evidence.

In conclusion, the section focused on part of the puzzling results obtained from several transient tests on VCSELs, and more specifically on the physical and electrical characterization of the damaged regions. The limited number of specimens in each test does not allow to draw statistical conclusions. Anyway, the study allows on one side to confirm a severe warning for possible ESD-induced latent damage, and on the other to invoke some caution in indicating ESD for any failure.

3.4 Proton Irradiation Effect in Commercial Laser Diodes

The effects of radiation on semiconductor light emitters have been investigated by several Authors [119–123] mostly to assess the reliability of such devices in aerospace applications. In this paragraph it will be presented these effects and the

interpretation of the results will be aided by the model for laser diodes described in the previous chapters.

Effects are expected to be direct and immediate, with a clear alteration of the laser performances related to the irradiation parameters. Anyway, also long-term effects are considered, because of the known attitude of solid state emitters to host the growth of extended, fatal defects starting from small and initially negligible seeds.

The strategy for a coordinate study of early and long-term effects is rather clear: the selected samples, once duly measured before and after irradiation, should be monitored during a period of operating life, possibly accelerated by means of high temperature and/or high current. What such a strategy undertakes is that each degradation phase is irreversible, no matter if due to the primary irradiated particles or to some internal growth of lattice defects. Anyway, some Authors recognize that some recovery of the initial conditions may take place a certain time after irradiation, and this leads in general to the recommendation of starting the operating life tests immediately [123, 124].

This paragraph is focuses on recovery effects. The laser characteristics of two different devices, after 3MeV proton irradiation, indeed, were found to evolve on a daily time scale even for unbiased samples at room temperature.

Moreover, that time evolution displayed some quite peculiar features that prompted to consider the spatial redistribution of the implanted protons, and in particular to identify a diffusion process.

This explanation, well supported even by a simple theoretical model based of the classical diffusion equation, in turn puts many more questions on both the physical side and the hardness assurance protocols.

The next subparagraph will start with the description of the two devices, of their measurement protocols and of the irradiation setup. Then, the time-evolving characteristics will be reported and interpreted.

The solution of the diffusion equation will be trimmed on the geometries of the two kind of lasers, introducing a suitable Green function able to vanish on the physical boundaries of the chips. The comparison of the calculated and measured results will suggest some further refinements.

Finally, the open questions will be listed and discussed, in order to plan the future work.

3.4.1 Experimental setup

3.4.1.1 Laser diodes

The devices employed for the experiment are an edge emitter and a VCSEL (Vertical Cavity Surface Emitting Laser), both for telecom applications.

The first is an InGaAsP/InP Distributed FeedBack (DFB) device tuned at 1310 nm, mounted on a typical Transmission Optical Sub-Assembly (TOSA) that includes a photodiode as a monitor of the emitted optical power (fig.3.52).

The top and front views of a real device of this family are shown in fig.3.52. The latter is a SEM image with the superposition of the EBIC (Electron Beam Induced Current) that maps the position of the junction line, that completely embeds the optically active layer.

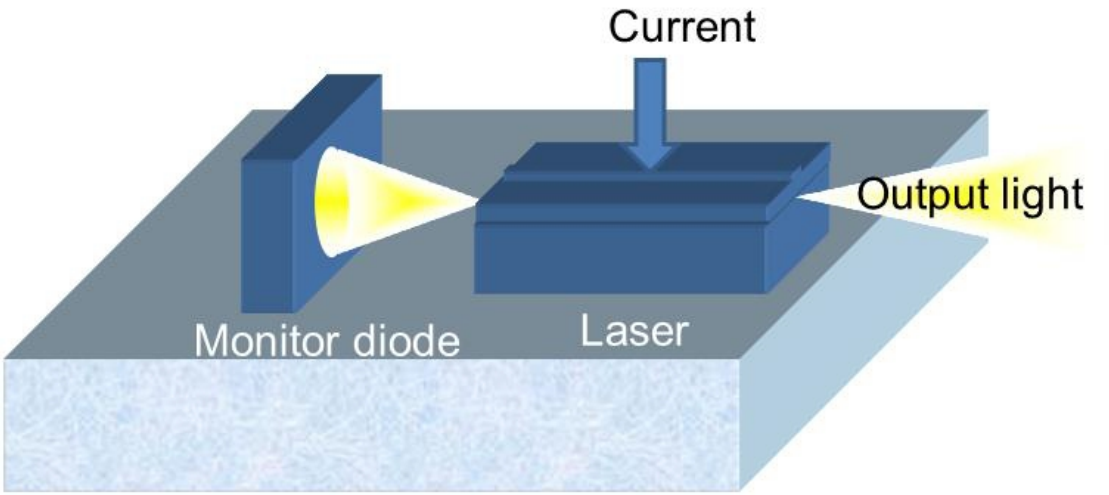

Figure 3.52: Assembly of the laser/monitor pair in a TOSA configuration.

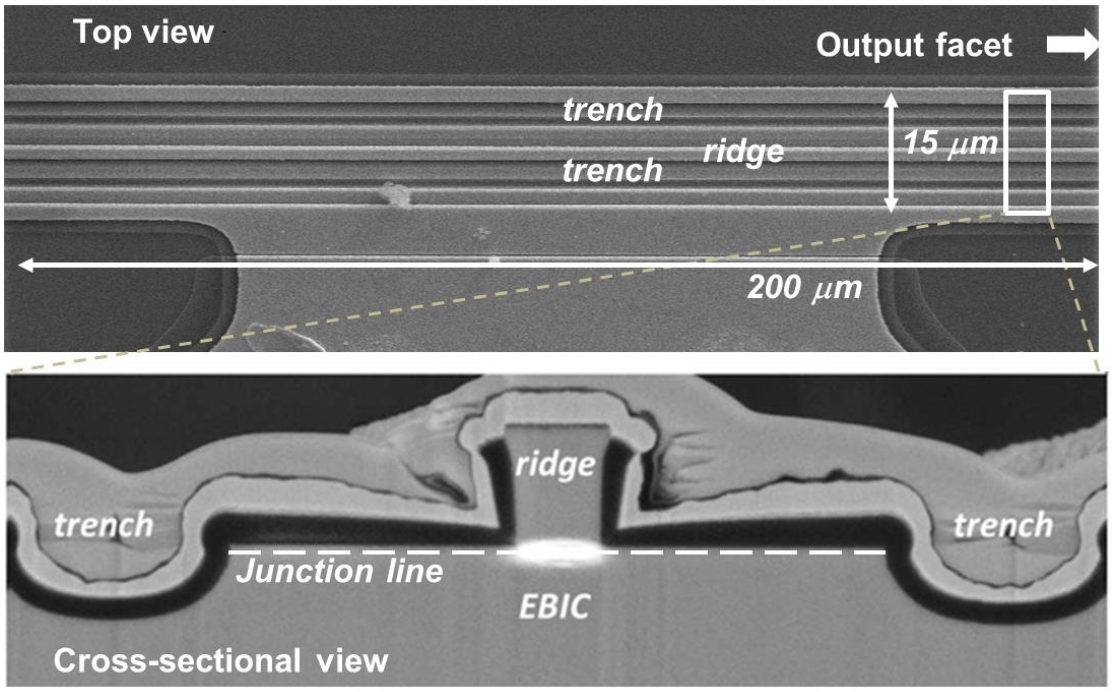

Figure 3.53: Top and cross-sectional views of the 1310 nm edge-emitting laser diode.

The second device is a vertical emitter, based on the AlGaAs/GaAs system that includes upper and lower Distributed Bragg Reflecting (DBR) stacks to tune the light emission at 850 nm.

The structure is reported in fig.3.54, while fig.3.53 shows a cross-section of a real device, obtained by FIB (Focused Ion Beam) milling.

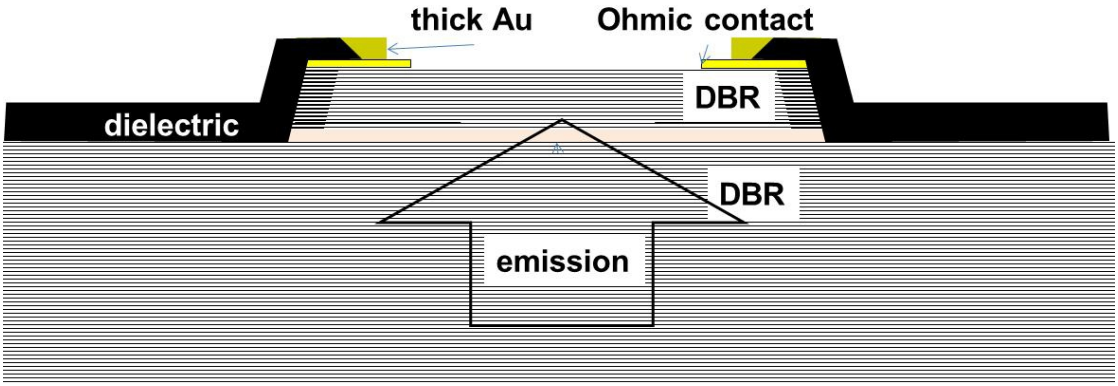

Figure 3.54: Schematic structure of a VCSEL.

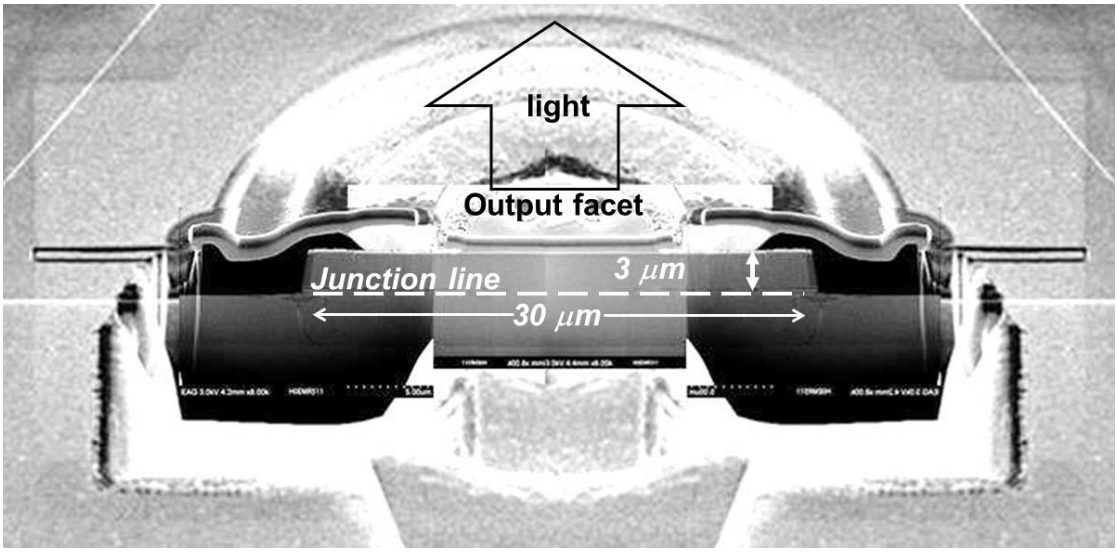

Figure 3.55: Patchwork of SEM images of the cross-section of a VCSEL.

3.4.1.2 Irradiation and measurements

We have performed $3MeV$ protons irradiation in vacuum at the CN accelerator of the INFN National Laboratories of Legnaro, Italy. The proton beam was perpendicular to the laser output facets. This means that in the ridge laser the axis of the proton beam was parallel to the junction plane, while in the VCSEL it resulted perpendicular.

The proton fluence was $3\text{x}10^{12} particles/cm^2$ for the InP edge emitter and for the GaAs VCSEL.

The proton beam projected range was about $60\mu m$ for both devices, meaning that the proton peak distribution was well inside the $200\mu m$ length of the edge emitter (see fig.3.53) while it was much deeper than the electrically active junction, that is also the optically active layer, in the VCSEL case.

The devices have been measured before the experiment, and then in four steps just after irradiation, namely after two hours, one week, two weeks and one month.

They have never been biased apart for the very short time of their measurement.

The measured parameters were: the laser current I, the corresponding voltage V, and the photocurrent I_M measured at the monitor diode for the ridge-emitter (see fig.3.52) and at an external photodiode for the VCSEL, respectively. As said this current is proportional to the optical power P_{OUT}, so that the plot of $I_M(V)$ gives the light-current curve. For both devices the monitor current was up-scaled, following the protocol indicated in subparagraph 1.1.6, that allows to eliminate the conversion losses of the monitor diode. This is important for the edge-emitter, where the monitor diode itself is exposed to the proton flux, this causes a reduction of the conversion efficiency of the monitor diode that is compensated by the up-scaling procedure.

In order to better illustrate the obtained radiation results, from fig.1.15 we remind two relevant parameters I_{th} and η_T, which are commonly related [43] to the internal optical loss coefficient α_i, to the loss coefficient from the emission facet α_m, and to their sum, the total loss coefficient $\alpha_T = \alpha_m + \alpha_i$, by the empirical formulas (1.59) and (2.1).

3.4.2 Results

Figures 3.56 and 3.57 reports the resulting light-current curves before irradiation (dashed curves), just after irradiation (1), after two hours (2), one week (3), two weeks (4), and one month (5).

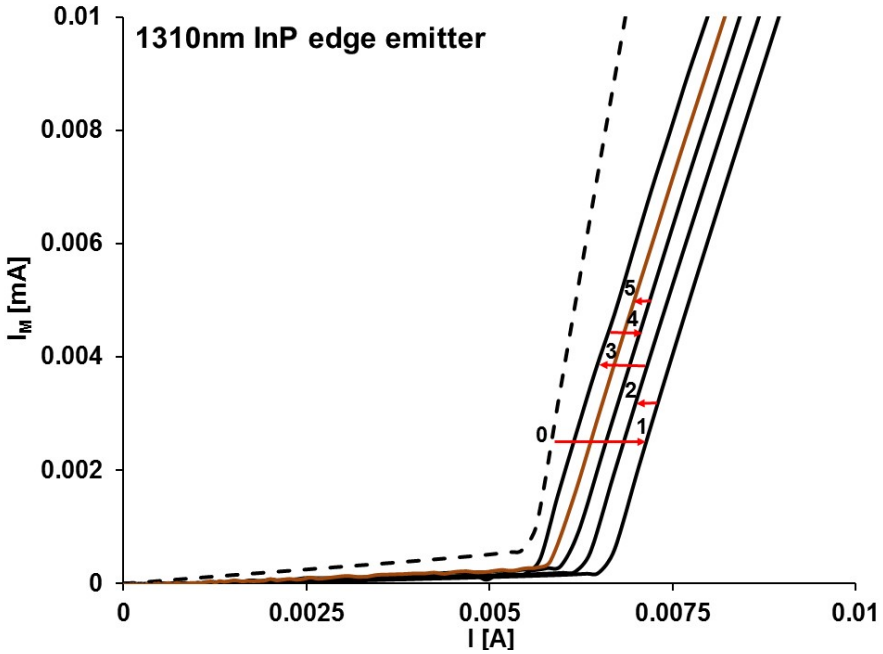

Figure 3.56: Light-current characteristics after irradiation for the 1310nm InP Edge Emitter. The dashed lines represent the pre-irradiation condition.

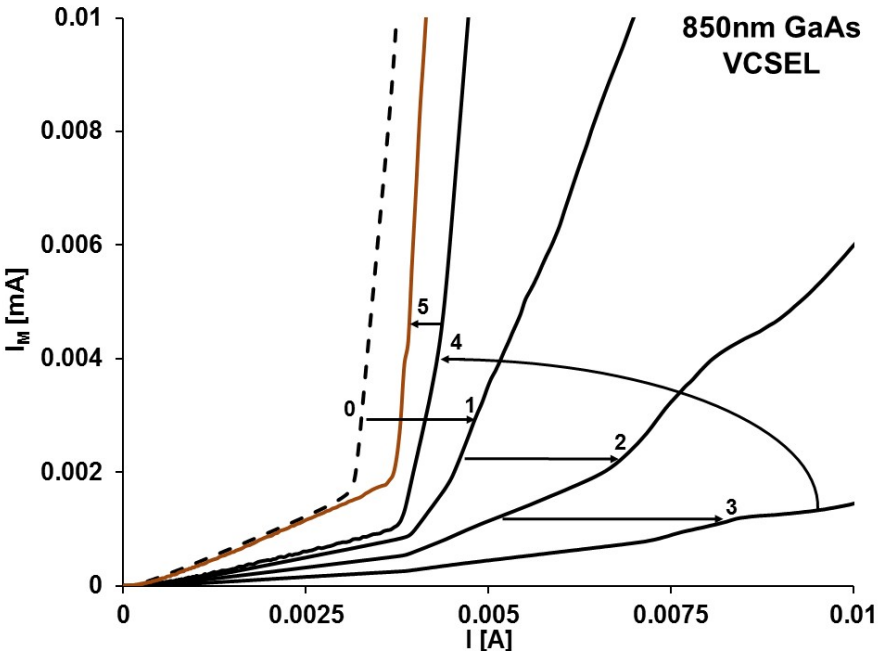

Figure 3.57: Light-current characteristics after irradiation for the 850nm GaAs VCSEL. The dashed lines represent the pre-irradiation condition.

The immediate effect of proton irradiation is aligned with literature results: for both devices the threshold current increases and the efficiency decreases. This is a common situation in laser diode degradation, that is related to the appearance of non-radiative centers inside the active region. Such defects, indeed, cause a strong increase of the internal optical losses, and then of the total loss coefficient α_T that appears in (1.59), without modifying the other parameters.

The following evolution is by far more puzzling and intriguing under many points of view. First of all, after the first measurement, the evolution is opposite in the two devices during the first room temperature annealing week (curves 2 and 3): the edge emitter tends to recover the initial state, while the VCSEL continues to degrade. After two weeks (curve 4) the characteristics of both devices invert their evolution. This happens at a small extent for the edge emitter, that returns to an intermediate state between step 2 and 3, but much more for the VCSEL that jumps to half the initial degradation, midway between states 0 and 1.

After one month (lines 5), both devices result closer to their initial states than at the previous step 4. In addition, some details appear, specific for each device. After irradiation the slope of all states (1,2,3,4,5) remains the same for the edge emitter. On the contrary, for the VCSEL not only the slope greatly changes, but states 2 and 3 seem even to have no threshold current.

The detailed interpretation of the observed features is challenging, because it requires to understand the interaction mechanisms active at microscopic level, how the geometry and relative orientation of the proton beam and the laser layers enter the problem and which phenomenon causes the time evolution (and following which kinetics). Yet, some important conclusion can be given even at a general level.

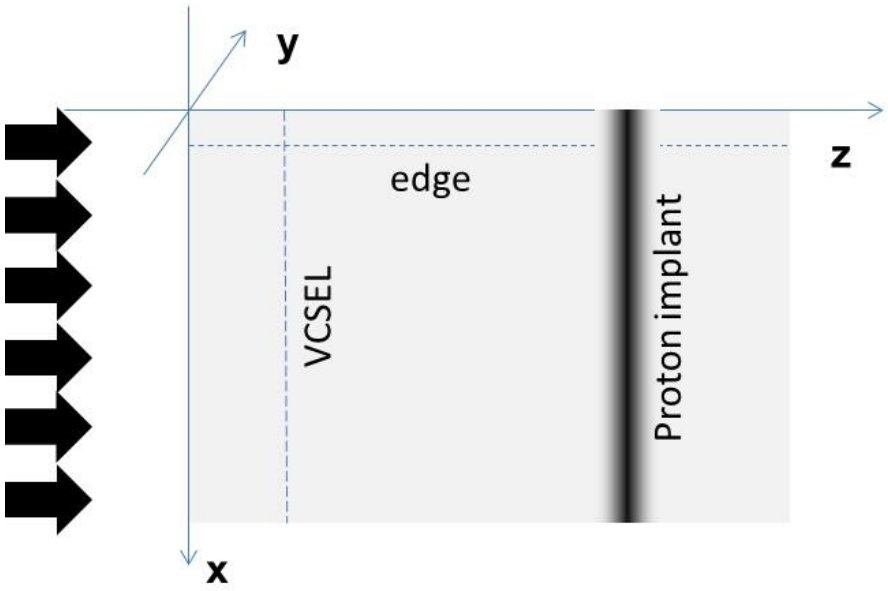

Figure 3.58: Model for proton implant and diffusion in both the VCSEL and the edge-emitter laser diodes.

Non-permanent damage

First of all, the kind of damage induced by the proton irradiation is, concerning its effect on optical properties, non-permanent. This follows the evident large recovery shown by both devices: on the other hand, the lattice damage hardly would disappear at room temperature along one month. This fact is also in agreement with previous observations, reporting some post irradiation recovery [125].

Second, also local activation/deactivation of interstitial protons (for instance because of electron capture or binding with dopant atoms) should be excluded. It is indeed difficult to imagine a mechanism that in one device enhances the optical effects of protons (the initial evolution of the VCSEL) and in the other (the ridge emitter) case goes in the opposite direction.

The working hypothesis that answers many, but not all, questions is related to the diffusion of protons introduced by irradiation.

Proton diffusion hypothesis

If protons diffuse from their initial position after implantation, and we consider the geometries of the two experiments (fig.3.58), we can study, at least at qualitative level, the expected kinetics of the optical performances.

We assume that the proton density inside the optically active layer causes the increase of the non-radiative recombination, that results in an increase of the optical losses (coefficient α_T) and of the term I_{tr}, that is shown in paragraph 1.1 to be determined, indeed, by the amount of non-radiative events.

In order to calculate the proton density, we assume that the proton profile is approximated by a single layer at a depth equal to the projected range (that is, we lead the projected struggle to vanish). This approximation can be easily removed for a more accurate calculation, but the main results appear even at this

simplified level. We also assume that protons escape from the physical boundaries of the chips, which forces their density to zero at the laser surfaces. The thickness of the devices is assumed infinite, if compared with the penetration range of the implanted particles, and the beam intensity is assumed uniform across the whole width of the chips.

The definition of the mathematical problem is given by the classical diffusion equation for the proton concentration C:

$$\frac{\partial C}{\partial t} = D\nabla^2 C \tag{3.5}$$

where D is the diffusion coefficient and t is the time. The solution is represented in terms of the superposition given by the triple integral over the three orthogonal space coordinates:

$$C(x,y,z,t) = \iiint C_0(x_0,y_0,z_0)G(x,y,z,x_0,y_0,z_0,y)dx_0dy_0dz_0 \tag{3.6}$$

provided the Green function G, corresponding to the solution of the problem for a point source located in x_0, y_0, z_0, is known for the given domain.

For an unlimited and uniform three-dimensional domain, the solution is known:

$$C(x,y,z,x_0,y_0,z_0,t) = \frac{1}{\sqrt{(4\pi Dt)^2}} \exp\left[-\frac{(x-x_0)^2+(y-y_0)^2+(z-z_0)^2}{4Dt}\right] \tag{3.7}$$

For the domain indicated in fig.3.58, the Green function H satisfying the boundary conditions on the $x = 0$ and $z = 0$ planes is easily obtained from (3.7) and the image method:

$$\begin{aligned} H(x,y,z,x_0,y_0,z_0,t) = G(x,y,z,x_0,y_0,z_0,t) - G(x,y,z,-x_0,y_0,z_0,t) + \\ +G(x,y,z,-x_0,y_0,-z_0,t) - G(x,y,z,x_0,y_0,-z_0,t) \end{aligned} \tag{3.8}$$

The total density C obtained from (3.6) is then integrated over the active layer half plane, indicated for each devices by the corresponding dashed lines in fig.3.58.

The result is summarized in fig.3.59, where the proton concentration is plotted as a function of the parameter Dt. A rough estimate of the diffusion coefficient D can follow the observation that the inversion in the VCSEL characteristics occurs between 1 and 2 weeks. This gives for D an estimate of about $10^{-11} cm^2/s$ consistent with literature [126]. For the edge emitter the optically active defects are expected to decrease with time, while for the VCSEL a "wave peak" is predicted, with an initial increase of the density, because of diffusion from the high concentration deep region, followed by a continuous decrease. The most part of the observed features is consistent with the proposed diffusion model.

Anyway, several details still require some deeper investigation. Among them: step 4 and the slopes of the light-current curves for the edge-emitter, and the apparently missing threshold current of the VCSEL at steps 2 and 3. All these issues will be discussed in the future in a new extended paper, as well as the role of the radiation induced lattice damage in correlation with the proton diffusion.

In conclusion, proton irradiation on two kinds of commercial laser diodes has shown optical effects evolving in time. The different geometries of the two devices,

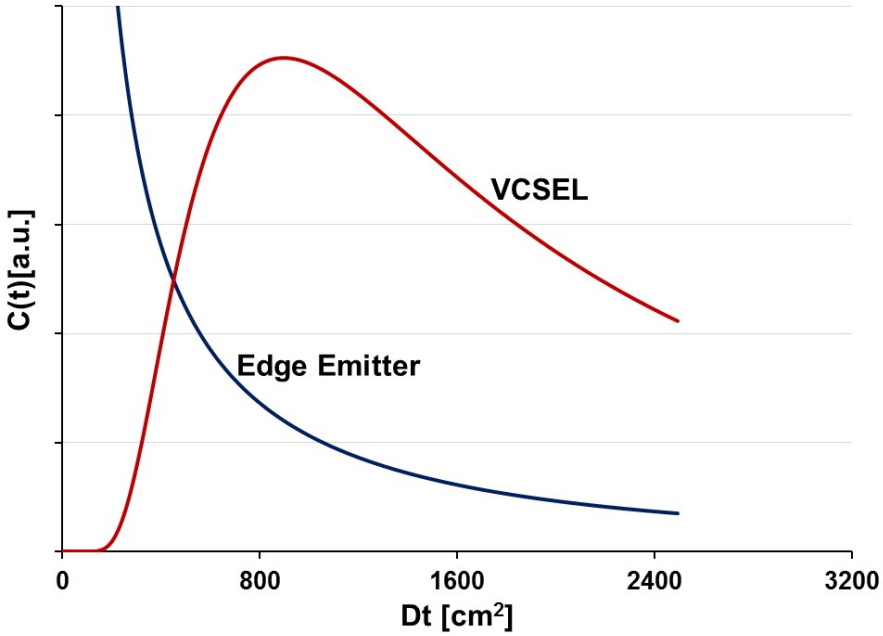

Figure 3.59: Calculated time evolution of the total proton density at the active regions of both the edge emitter and the VCSEL, according to the diffusion model.

and in particular the orientation of their planar active region with respect to the proton beam, caused completely different effects.

A simple model pointed out a proton diffusion process as the basic mechanism driving the observed kinetics. Several open question still ask for more detailed investigations, starting from the root mechanism that leads protons to affect the electro-optical properties of a laser diode.

The possibility of a permanent damage associated to proton irradiation can be investigated by accelerating the diffusion process by a suitable storage of the irradiated devices at high temperature, without any bias.

In any case, despite the many open questions, the conclusion follows that any lifetest on proton-irradiated laser diodes should carefully consider that, if the implanted dose is supposed to cause the growth of extended defects, it changes in time. The same lifetest started at once or one day (or one week) after irradiation may lead to totally different results.

3.5 1060nm seed laser diodes in pulsed operation: performances and safe operating area

The general model developed in Chapter 1 deals with low power devices. No thermal effects related to high power have been included. During the discussion of the anomalous dV/dI, discuss in paragraph 1.4, a pulsed measurement method has been applied to validate the hypothesis of low power condition. This opened the door to experimental studies on power devices. The following part will describe some preliminary experiments aiming to point out the most relevant adjustments that the model will require when facing the high power domain.

New phenomena are observed in the optical response of InGaAs/AlGaAs 1060nm Laser Diodes (LDs) and Laser Diode Modules (LDMs) driven under high peak current condition: two segments of parasitic oscillations appear in the optical response of every tested LD and LDM, when increasing the current above two respective thresholds. We designed a test bench devoted to the near-field and time-spectral analysis of LD optical responses under such conditions. A correlation was found between the presence of the first segment of oscillations on the optical response, a widening of the near-field profile and a temporal broadening of the LD spectrum [127, 128].

Lifetime and reliability estimation of Laser Diodes (LDs) and Laser Diode Modules (LDMs) used under CW conditions have been extensively studied by many research groups [129, 130]. However, for fiber Laser seeding applications, the use of pulsed commercial 1060nm LDMs offers a large flexibility compared to others techniques (ex. EO modulator) [131]. In order to limit nonlinear effects (Ex. Brillouin, noise) caused by a high amplification gain of the fiber Laser, it is required that LDs be driven under high peak overcurrent (>>2A), short pulse duration (<100ns) and high repetition rate (>100kHz) conditions [132]. Nevertheless, the behavior and life expectancy of these LDs under such conditions is not well established. A few studies have been carried out on the reliability of some 1060nm Laser diode, rated for a pulsed current of 2A max, demonstrating their ability to withstand higher driving current conditions (2.35A [133], or even 3.5A [134]).

Our work is based on determining the reliability of InGaAs/AlGaAs 1060nm CW LDs under such conditions by the extraction of Electro-Optical (EO) characteristics (I-V, P-I, DoP etc.) and the monitoring of their changes during pulsed ageing tests. In this context, we observed new behavior when LDs and LDMs are driven under high peak-current conditions: damped pseudo-oscillations were observed on the optical pulse response of the Laser diode, when increasing the driving current above a critical threshold and larger than the maximum ratings. This effect is non-linear, and is therefore expected to cause undesired effects on the output pulse of the fiber Laser [135]. In order to understand the origin of those oscillations and to discuss their potential influence on the operation range of seed LDs, we studied three types of LDs with different packaging architecture: 10 butterfly LDMs (numbered from #1 to #10) with a Fiber Bragg Grating (FBG) photo-inscribed in the core of the optical fiber, 10 butterfly LDMs without FBG, and 11 Chip on Submount (CoS) LDs. Optical pulse responses of each Laser diode are characterized through dedicated test benches:

- time pulse response,
- near-field analysis (only for CoS)
- time-spectral analysis of these diodes when driven under overcurrent and short-pulse conditions.

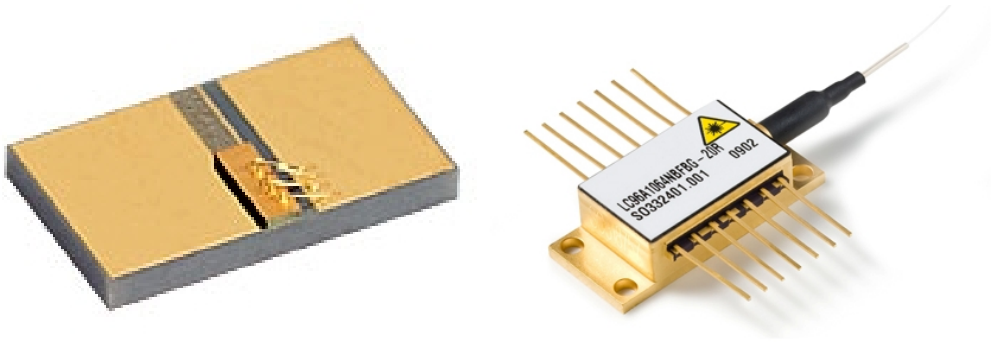

(a) (b)

Figure 3.60: Example of LDs packages: a) CoS LD and b) butterfly LDM.

3.5.1 Optical characterizations at high peak current pulsed conditions

As the drive current increases, and for a constant pulse duration of 100ns, two time intervals of oscillations (namely "A" and "B") appear on the optical responses of all the tested diodes, regardless packaging architecture (fig.3.61). A strong part-to-part variability is observed on the current threshold triggering the 1st time interval of oscillations (I_{thA}) varying from 2.8A to ∼11A. However, this value is quite constant between LDs originating from the same manufacturing batch, regardless of the final packaging of the die.

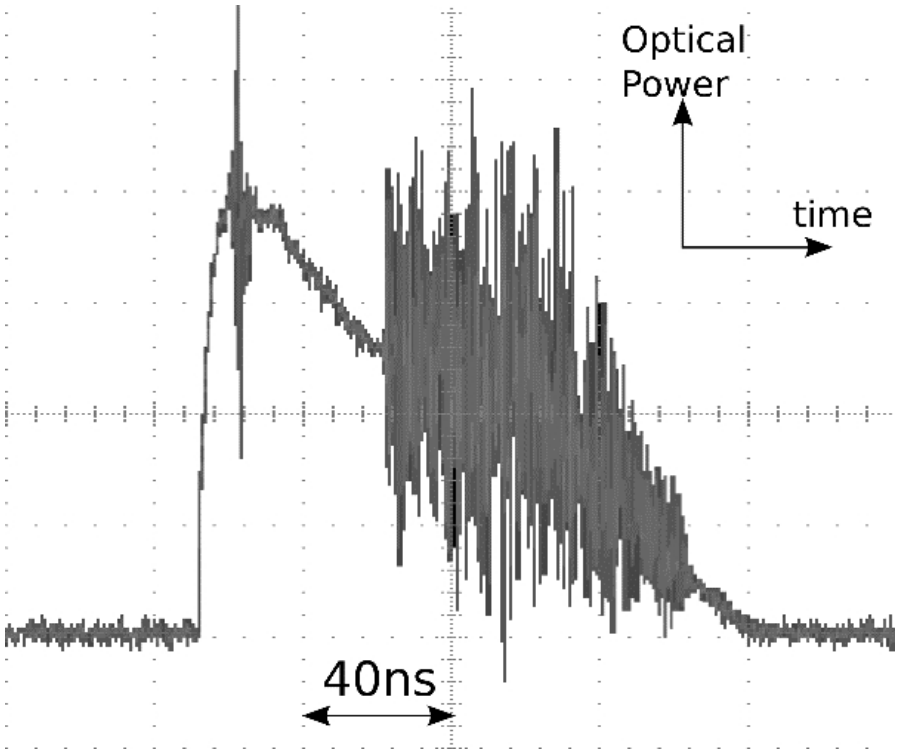

Figure 3.61: Parasitic oscillations on the optical response of a CoS LD, driven at a current of 8.76A. Two segments of oscillations ("A" and "B") are clearly observed (40ns/div).

While measuring the spectrum of these LDs and LDMs under high current pulsed conditions, a widening of the output spectrum has been observed specifically when driving these LDs and LDMs over their I_{thA} threshold. Therefore we conducted a time spectral analysis to understand the dynamics of the temporal variations of the spectrum over the A-type oscillations threshold. The time-spectral test bench realized, described in fig.3.62, is based on a time slicing of the optical responses using an Electro-Optical Modulator (EOM) synchronized with a pulsed LD driver (2-12A, 100ns). The output of the EOM is sent to an optical spectrum analyzer (OSA). By generating a variable delay between the LD output pulse and the EOM driving signal, time spectral charts of the LD output pulse are achieved versus current conditions. Near-field pattern imaging of CoS Lasers front facet is also characterized using a high magnification microscope system, based on a 20x microscope objective coupled with a dedicated NIR camera.

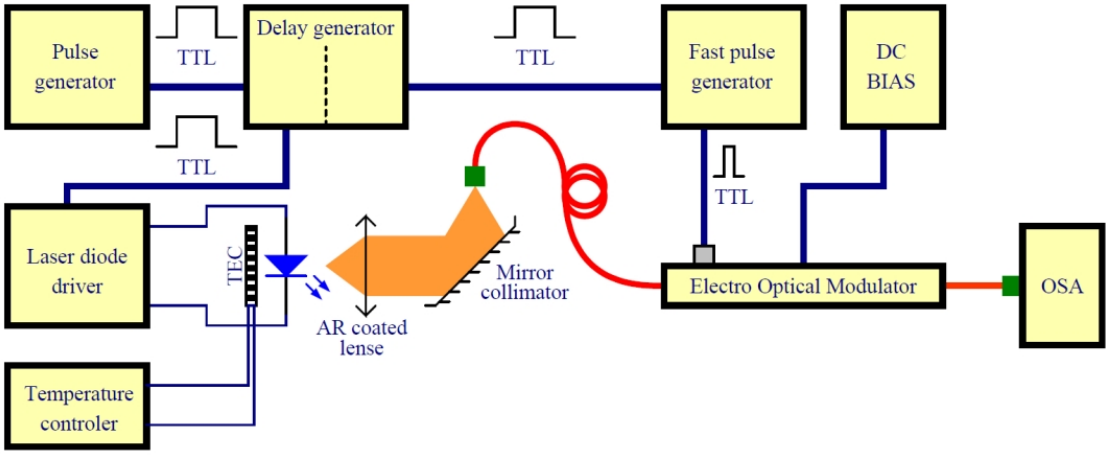

Figure 3.62: Designed time-spectral analyzer.

A relationship between the value of I_{thA} and the near-field profile widening of the optical pulse is demonstrated, as reported on fig.3.63a and fig.3.63b. In contrast, the occurrence of the second time interval of oscillations has not any effect on the near field profile, suggesting a different origin for these oscillations. fig.3.64a and fig.3.64b summarizes the time-spectral analysis results. As reported on fig.3.64a, the maximum intensity of the pulse spectrum is located at 1060nm as expected. At the beginning of the Laser pulse, the optical spectrum is relatively wide, and rapidly narrows afterwards, so that the spectrum of the impulsion reaches a steady state after ten nanoseconds. This large spectral width at the beginning of the impulsion is explained by the multi-modal character of the gain switching emission [136]. However, when the LD is driven with a peak current higher than I_{thA}, a temporary broadening of the optical spectrum is observed, as shown on fig.3.64b (I_{thA}=8.3A, I_{LD}=9A), within a range from 15ns to 25ns after the beginning of the Laser pulse. This exactly matches the Atype oscillations zone occurring above this specific driving current, thus confirming a relationship between the occurrence of A-type oscillations on the optical response of a Laser diode and a spectral broadening of the optical pulse.

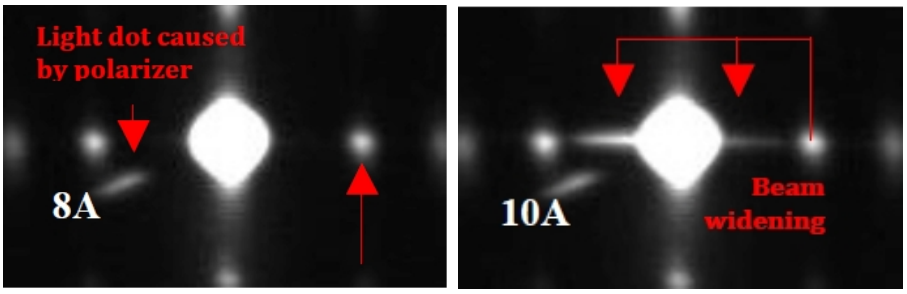

(a) (b)

Figure 3.63: Near-field profile of a CoS diode driven a) below and b) above I_{thA} = 9.5A.

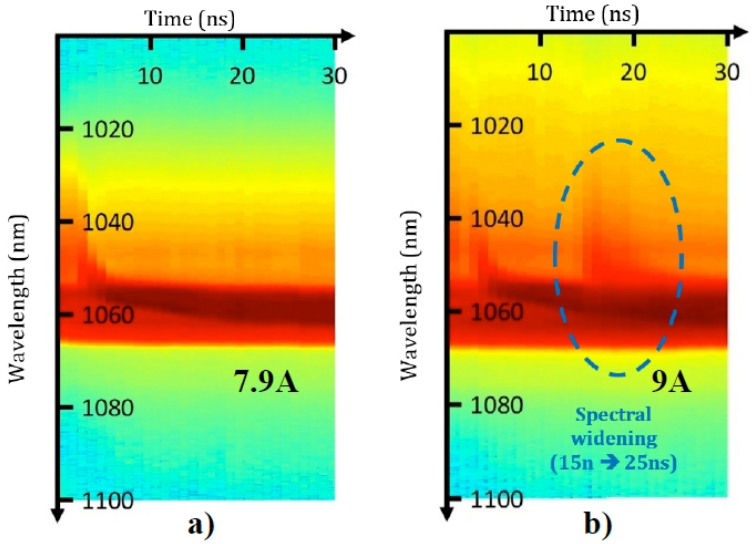

Figure 3.64: Time spectral analysis of a CoS LD output pulse, driven a) below and b) above I_{thA}=8.3A.

3.5.2 Aging results

In order to determine a potential relationship between the value of I_{thA} and the Safe Operating Area (SOA) of these LDs, three LDMs (LDM #4, LDM #1, LDM #9, without FBG and with different values for I_{thA} (3.9A, 7A, 11.2A respectively), have been aged under step-stress accelerated pulsed conditions (variable current and ageing time, 100ns, 200kHz). The aging setup is shown in fig.3.65. After each step of the aging test, the I_{thA} and I_{thB} values have been measured.

Up to now, six ageing steps have been realized (6A/72h, 6A/120h, 6.5A/120h, 6.5A/380h, 7A/120h, 7.5A/120h), as seen on fig.3.66. No modification of the value of I_{thA} or I_{thB} have been observed. However, after the "V6bis" aging test (7.5A, 120h), the LDM #4 failed during the I_{thA} and I_{thB} measurements. This LDM is the one with the lowest I_{thA} value. Through these preliminary investigations, both the robustness of these devices is demonstrated over a large current pulse magnitude compared to operating peak current (x 3.5). Aging tests are in progress

especially to assess the behavior of the two other Laser diodes above 7.5A and the relationship between stress current level and their respective intrinsic I_{thA} values.

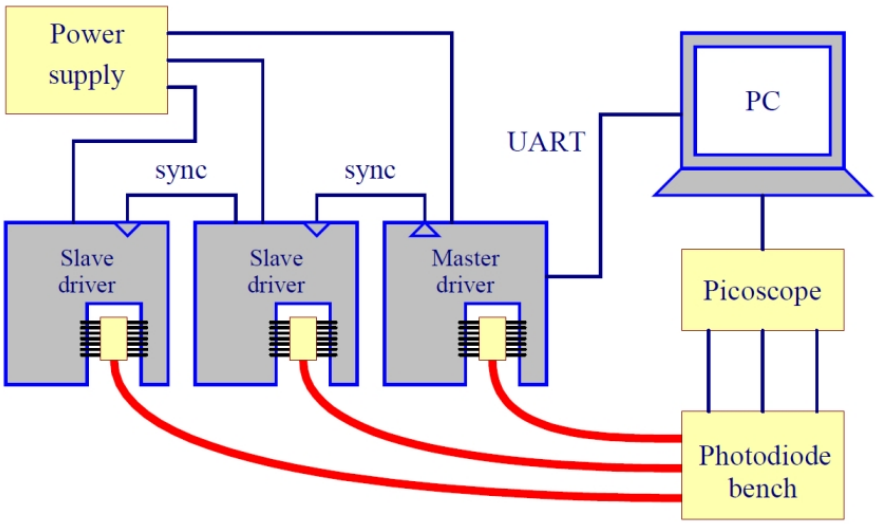

Figure 3.65: Aging setup

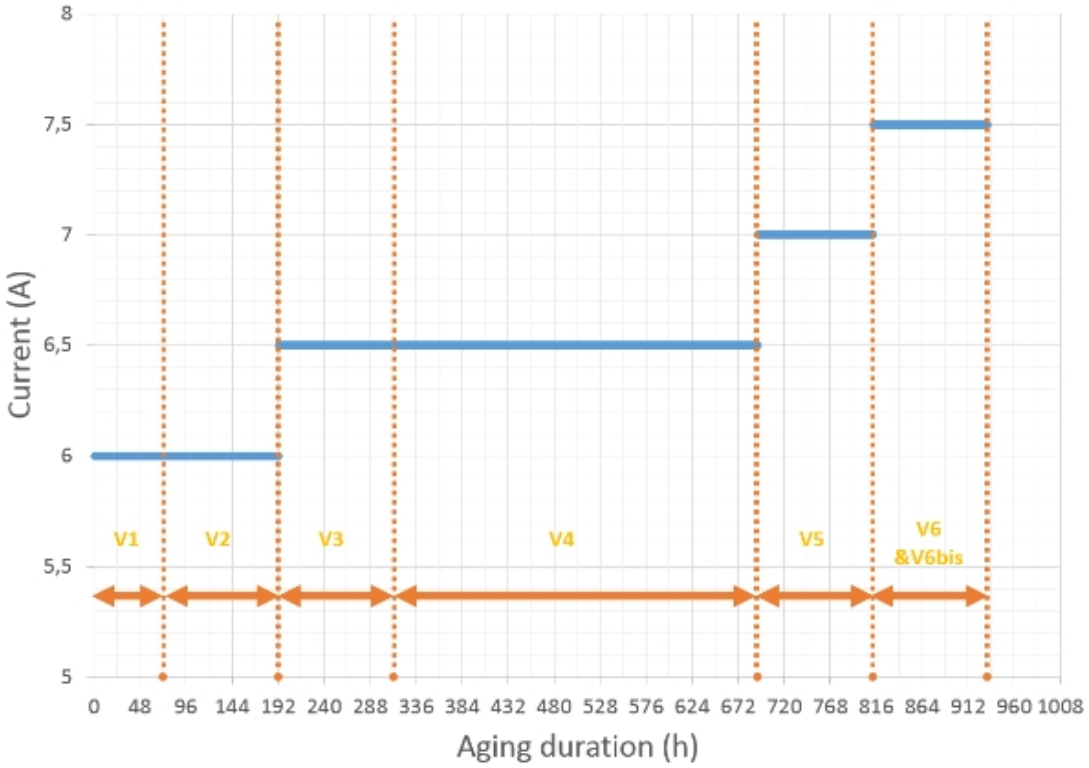

Figure 3.66: Step-stress conditions. For the "V6" and "V6bis" aging test, the same aging conditions have been successively applied to the LDM with the highest I_{thA} value, and then to the two remaining LDMs.

The absolute optical output power and relative optical output power variation of the LDM1, LDM4 and LDM9 diodes are monitored during the four ageing processes. The results of two of them are summarized below:

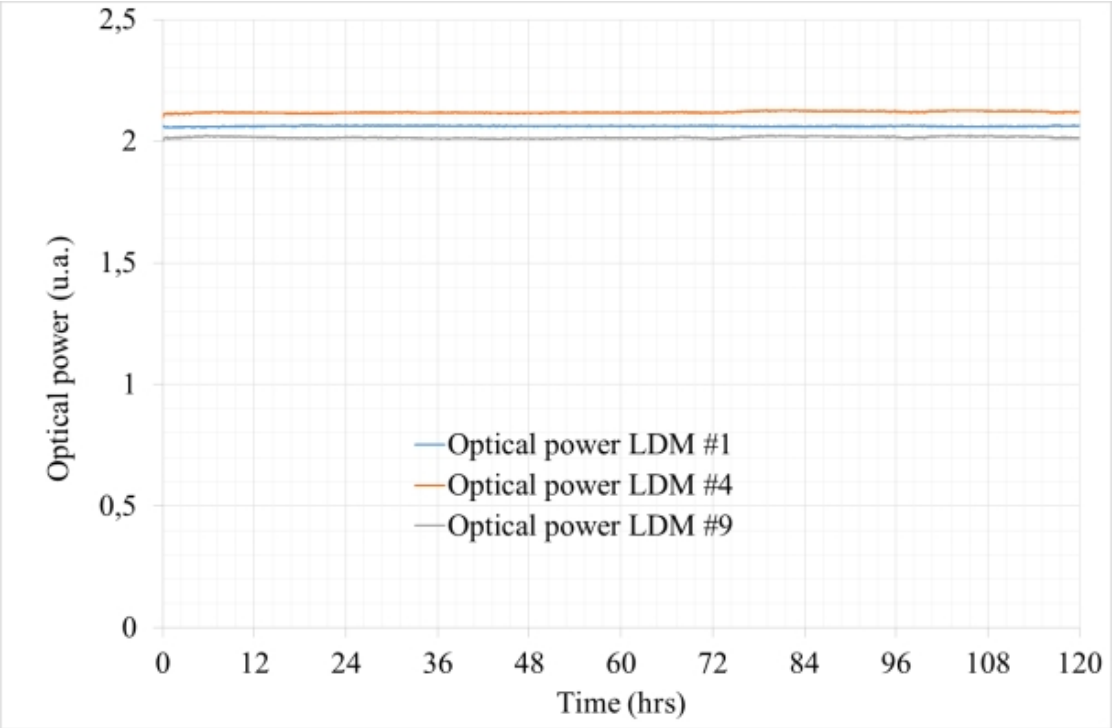

(a)

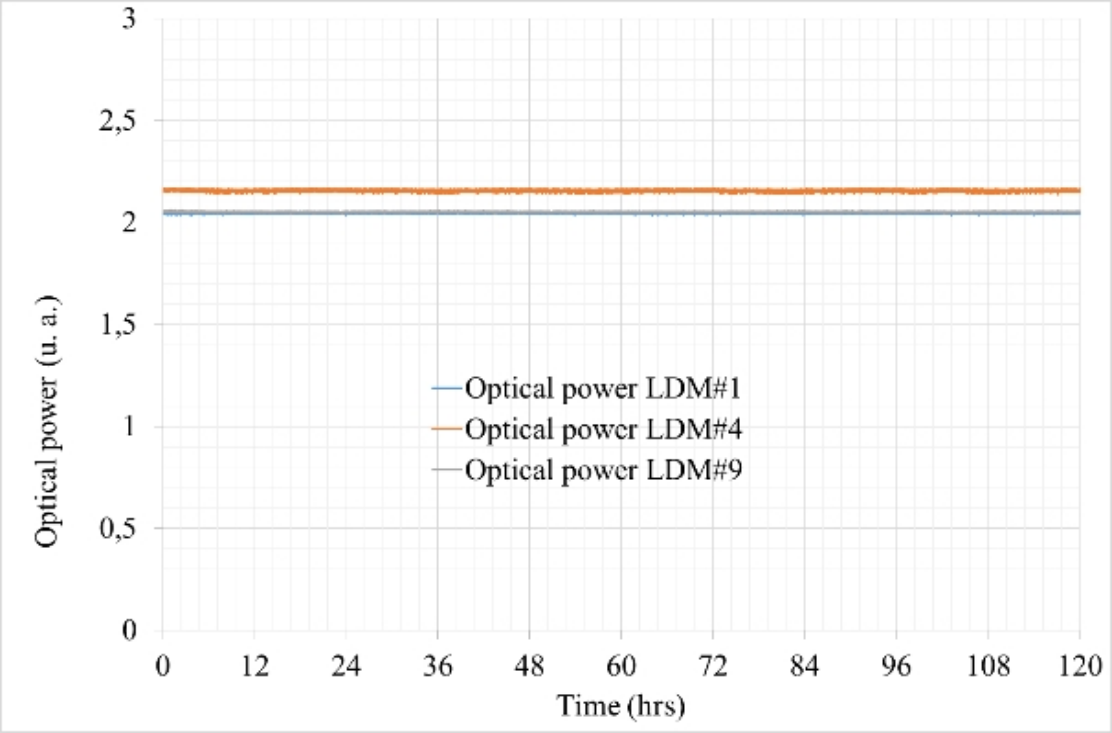

(b)

Figure 3.67: Optical power monitoring during a) the "V3" and b) the "V5" ageing test.

As seen on fig.3.5.2 and fig.3.5.2 small fluctuations of the optical power are observed all along every ageing tests. However, no long term decrease of any Laser

diode output power was highlighted.

Investigations were carried out to understand the origin of A-type oscillations of the optical response of LDs or LDMs when driven under high current/short pulses conditions. In this context, we supplied three batches of Laser diodes, with different packaging, and measured the respective threshold current value over which these oscillations appeared (I_{thA} and I_{thB}). We observed a strong batch-to-batch variation in the value of I_{thA} and not for I_{thB}. We discussed the possible origins of the A-type oscillations, and we conducted a near field profiling and spectral / time spectral analysis of the LDs optical responses. Indeed, a correlation was observed between the occurrence of A-type oscillations and the spectral widening of the LDs optical response. Time spectral analysis was conducted, which highlighted a link between A-type oscillations and a temporal broadening of the pulse spectrum. Step-stress ageing tests were then carried out on three LDMs without FBGs. One device failed after an ageing test carried out at 7.5A during 120h. However, the same ageing conditions have had no effect on the two remaining devices, that could withstand such severe driving conditions. Furthermore, no modification of their I_{thA} and I_{thB} values have been observed yet. Further aging tests must be carried out on several devices with low and high I_{thA} values in order to highlight or revoke a relationship between the SOA of a device and its I_{thA} value.

Conclusions

In conclusion, in this last Chapter a list of failures, that the Author has studied in the years of the PhD, has been reported. In subparagraph 3.1.3 have been reported two practical cases in which the parameters extraction, before and after some catastrophic event, could be useful to individuate failure mechanisms and in some particular case, the method proposed could be the best way to address failure analysis.

In the second part the case of the double-peaked spectrum in some DFB laser diodes is demonstrated to relate to axially confined Catastrophic Optical Damage (COD), followed by the excitation of a transversal optical mode. The melting-regrowth kinetics of CODs also reveals another possibility of COD-induced side optical modes in a fiber DBR pump laser diode.

The third case reported the test performed on 850-nm VCSELs forward and reverse HBM, MM, CDM ESD, together with EOS and overpower test. The physical analysis of the tested devices showed a variety of damages not easily correlated to the measured electro-optical degradations. The solution required the detailed interpretation of the observed physical mechanism, by means of electron microscopy and device modelling.

The fourth case about the proton irradiation on two kinds of commercial laser diodes has shown optical effects evolving in time. The different geometries of the two devices, and in particular the orientation of their planar active region with respect to the proton beam, caused completely different effects. In this case a simple model pointed out a proton diffusion process as the basic mechanism driving the observed kinetics.

Finally, the atypical phenomenon observed on the optical response of InGaAs/AlGaAs 1060nm Laser Diodes (LDs) and Laser Diode Modules (LDMs) driven under

high peak current condition: two segments of parasitic oscillations appear on the optical response of every tested LD and LDM, when increasing the current above two respective thresholds. For this case it has been studied the possible origins of the oscillations observed, and we conducted spectral and time spectral analysis of the LDs optical responses. A temporal spectral broadening, associated with the occurrence of "A" type oscillations, was highlighted. Up to now, neither a drop in the optical power of the LDs aged nor a variation in their and values, before and after the ageing tests, were observed. The aged LDs were able to withstand the chosen ageing conditions without any noticeable decrease of their performances.

General conclusions

The kernel of the proposed study is the open problem of correlating failure modes and failure mechanisms in laser diodes. It is known in failure analysis and, in particular for photonics, that a gap exists between observations (failure modes) and physical roots of degradation (failure mechanisms).

The answer to this issue prompted to develop that self-consistent model that has been referred to and summarized in this Thesis.

The conclusion has been the validation of the basic model, and its quantitative application to real cases.

The focus of the model has been shown to deal with the $P_{OUT}(I)$ electron-optical characteristics, but it resulted also able to deal with a larger set of parameters, as the proprieties of lateral areas concurring to current conduction and confinement.

The combined observation of both current and voltage thresholds became important, as well as the Shockley-like parameters that rule over the whole sub-threshold region of the I(V) characteristics of a real laser diode. Those parameters result to be strongly related to photonic devices physics as well as failure physics: saturation current increases because of the reduction of carrier lifetime; the emission factor points out the fraction of carriers recombining inside or outside the depletion region; the series resistance speaks about the contact interfaces, etc.

A method for measuring the most part of those parameters, electrical and optical, is then proposed, as a starting point before facing real failures. Along that line, simple steps as reducing the external to the internal voltage led to direct insight and measurement of the voltage threshold. All parameters shown in Chapters 1 and 2, and their numerical values, come as a result of that decoding procedure.

In the last part of the Thesis some demonstrations on real cases have been given in detail, in which single parameters have been tested as independently as possible. It is the case of the FIB modification that induced defects on the lateral sides of a laser, showing modifications of the threshold current and the total efficiency without any variation of total losses. These steps of practical cases helped to confirm and improve and the model.

Here was the aim and, hopefully, the strength of this three years of PhD: to perform and perfect the model and the method proposed in the last decade by Vanzi et al.

Appendix A

The role of band asymmetry

In order to discuss the role of the asymmetry parameter ϵ, as defined in (1.9), we will limit ourselves to the simple case of density of states of an ideal Quantum Well, that is a step function for both electrons and holes.

$$\begin{cases} g_e = \dfrac{m_e}{\pi\hbar^2} E_e > E_C, 0 \; otherwise \\ \\ g_h = \dfrac{m_h}{\pi\hbar^2} E_e < E_V, 0 \; otherwise \end{cases} \tag{A.1}$$

From (1.1) and (1.4) we obtain

$$\frac{E_e + E_h}{2kT} = \frac{E_C + E_V}{2kT} + \frac{m_h - m_e}{m_h + m_e} \frac{h\nu - E_g}{2kT} \tag{A.2}$$

On the other hand, for an undoped semiconductor the total number of electrons equates the total number of holes, so that

$$\int_{E_C}^{\infty} n(E_e) dE_e = \int_{-\infty}^{E_V} p(E_h) dE_h \tag{A.3}$$

Using the definition of carrier densities given in Tab.1.1, and (A.1) for the densities of states, one obtains

$$\frac{\phi_n + \phi_p}{2kT} = \frac{E_C + E_V}{2kT} + \ln\left(\sqrt{\frac{m_h}{m_e}}\right) = \frac{E_i}{kT} \tag{A.4}$$

where the independence of the result on the applied bias V allows to identify the mean value of the quasi-Fermi levels as the Fermi level E_i itself at equilibrium for the undoped material. The result is:

$$\frac{(E_e + E_h) - (\phi_n + \phi_p)}{2kT} = \frac{m_h - m_e}{m_h + m_e} \frac{h\nu - E_g}{2kT} - \ln\left(\sqrt{\frac{m_h}{m_e}}\right) \tag{A.5}$$

It is clear that for ideal symmetric bands (equal effective masses) this value is null, and then (1.6) would be exact.

For asymmetric bands the two terms on the right-hand side of (A.5) partially compensate, depending on the displacement of the peak emission $h\nu$ with respect to the energy gap E_g.

The maximum absolute value is reached for the non-broadened distribution of states, where that displacement is null, which makes the first of the two terms to vanish. In any case, some non-null value of ϵ must be considered. The effect of ϵ has been duly reported for all the relevant results previously obtained, but it can be summarized as follows

1) The sub-threshold range of all currents, including the radiative current I_{ph} is not directly affected.

2) The threshold voltage V_{th}, at given peak frequency, temperature and optical losses increases with increasing ϵ.

3) The threshold current I_{th} also increases with increasing ϵ, simply because it depends on V_{th}.

Some further effects are caused by band asymmetry where the product of the effective masses, instead of their ratio that defines ϵ, enters into play. This is the case of the gain coefficient gm (1.30). This leads to the supplementary results:

1) Absorption increases with increasing g_m (1.28)

2)Gain saturation is not affected, because of its upper limit at $g = \alpha_T$.

3) The radiative current I_{ph} increases also in the sub-threshold range, because the term $I_{sh0} = I_{ph0}(R/R + 1)$ in (1.48), (1.49) is proportional (equations (1.36) and (1.47)) to $\alpha_T g_m/(\alpha_T + g_m.)$

The first and third results obviously follow the consideration that increasing the product of the effective masses simply means the increase of the joint density of states, and then the rate of optical transitions.

The previous considerations have a great relevance when one considers not only band asymmetry, but also the multiplicity of the valence band, and in particular the existence of the light and heavy hole sub-bands (the split-off band will be here neglected because of its lower population, that is assumed to marginally affect the main transition rates). Each sub-band contributes to optical transitions, giving rise to two specific radiative currents I_{phl}, and I_{phh} that adds to build up the total I_{ph}.

The light-hole contribution I_{phl} has a lower "saturation current" in the sub-threshold range than the heavy-hole term I_{phh}, but displays a lower threshold voltage than the latter. As an example a numerical evaluation can be given for the $In_{1-x}Ga_xAs_yP_{1-y}$ lattice-matched to InP to give emission at 1310 nm, as in the previous fig.1.5 and 1.6, applying the parameter evaluation summarized by [32], Ch.3. One gets $\epsilon = 0.33[(h\nu - E_g)/2kT] - 0.34$ for transition between conduction band and the light-hole band, and $\epsilon = 0.79[(h\nu - E_g)/2kT] - 1.06$ when, on the contrary, transitions involve heavy holes.

If we refer the results to the ideal case $\epsilon = 0$, for room temperature, $h\nu = E_g = 0.9466eV$, and $R = 0.4$, that would lead to $V_{th} = 0.9905V$, we obtain the results listed in Table A, where the saturation current, the threshold voltage and the threshold current are referred to the ideal case of symmetric bands.

When we realize that it is the lower threshold voltage to rule over the whole

	Relative I_{sh0}	Relative V_{th}	Relative I_{th}
$\epsilon = 0_{\text{(symetric band)}}$	1	1	1
$\epsilon = -0.34_{\text{(light holes)}}$	1	1	1
$\epsilon = -1.06_{\text{(heavy holes)}}$	1.34	1.012	1.6

Table A.1: Relative values of the relevant parameters for the symmetric band model and the asymmetric models involving light and heavy holes.

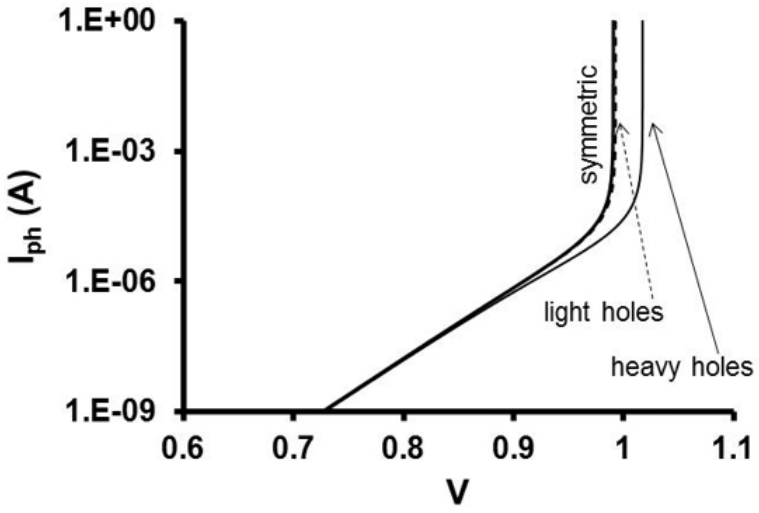

Figure A.1: Expected I_{ph} at the laser transition for the symmetric band model, and for the light or heavy hole transitions in the 1310 nm emitter of fig.1.6.

system, this means that threshold is governed by the light-hole transitions. For threshold voltages close to 1 V and threshold currents about 10 mA, the use of the approximation $\epsilon = 0$ would then give an error of 1 mV on V_{th} and of 0.4 mA on I_{th}. FigA.1 draws and compares the three calculated plots of I_ph. The symmetric band approximation results nearly undistinguishable from the light-hole transitions.

This is the reason for considering the simpler version of the model, corresponding to the non-realistic band symmetry approximation, an excellent tool for practical applications. The only point to be kept in mind is that, for the given case, the sub-threshold values of I_{ph} will result some 30% lower in the theoretical model than in experiments.

Appendix B

Dimension of the join densities

A comment can be made about the physical dimensions of the joint densities. Based on the standard definitions

$$\begin{cases} n = \int_{E_C}^{\infty} n(E_e) dE_e \\ \\ p = \int_{-\infty}^{E_V} p(E_h) dE_h \end{cases} \tag{B.1}$$

one should first change the energy variables into frequency ones

$$\begin{cases} E_e = E_C + \dfrac{m_h^*}{m_h^* + m_e^*}(h\nu - E_g) \\ \\ E_h = E_V - \dfrac{m_e^*}{m_e^* + m_h^*}(h\nu - E_g) \end{cases} \tag{B.2}$$

and then identify

$$\begin{cases} n_\nu = h\dfrac{m_h^*}{m_h^* + m_e^*} n \left(E_C + \dfrac{m_h^*}{m_h^* + m_e^*}(h\nu - E_g) \right) \\ \\ p_\nu = h\dfrac{m_e^*}{m_h^* + m_e^*} p \left(E_V - \dfrac{m_e^*}{m_h^* + m_e^*}(h\nu - E_g) \right) \end{cases} \tag{B.3}$$

in order to have $n = \int_{E_g/h}^{\infty} n_\nu d\nu$, $p = \int_{E_g/h}^{\infty} p_\nu d\nu$

The last step is to define the joint density as

$$p_\nu n_\nu = \int p_\nu n_{\nu_1} \delta(\nu_1 - \nu) d\nu_1 \tag{B.4}$$

This makes the joint densities dimensions $cm^{-6}t$ an $\left[\int p_\nu n_\nu d\nu\right] = cm^{-6}$. It should be clearly reminded that $\int p_\nu n_\nu d\nu \neq pn$

Anyway, those densities never appear, but always combined with other terms, including the Einstein coefficients that have been introduced. It will then be left to the dimensional analysis of the ultimate results to properly recognize the suitable dimensions of the relevant terms.

Appendix C

The Hakki-Paoli consideration.

This appendix has the espouser to reconstruct the Hakki Paoli formula and to compare it with 1) The similar equations that define the total losses and the gain saturation limit 2) The result of the New Model for the laser spectrum.

C.1 Hakki-Paoli method

Let the field F_0 describe the amplitude and phase of the optical field at the beginning of the round trips, in some point of the cavity. After the first round trip of length $2L$ the twice reflected wave F_1 adds to the initial field in the same point

$$F_1 = F_0 \left[\sqrt{R_0 R_1} \exp\left(-\frac{\alpha_T}{2} 2L\right) \exp\left(ik2L\right) \right] \tag{C.1}$$

where R_1 and R_2 are the power reflectivities of the two mirrors, α is the net power absorption coefficient (and for this reason, in an amplitude calculations we use the square root of R_1 and R_2 and $\alpha/2$ in the propagation exponential). The wave propagation constant is k. After the second trip the additional field F_2 is

$$F_2 = F_1 \left[\sqrt{R_0 R_1} \exp\left(-\frac{\alpha_T}{2} 2L\right) \exp\left(ik2L\right) \right] = F_0 \left[\sqrt{R_0 R_1} \exp\left(-\frac{\alpha_T}{2} 2L\right) \exp\left(ik2L\right) \right]^2 \tag{C.2}$$

Summing over all trips:

$$\begin{aligned} F = \sum_{n=0}^{\infty} F_n = F_0 \sum_{n=0}^{\infty} \left[\sqrt{R_0 R_1} \exp\left(-\frac{\alpha_T}{2} 2L\right) \exp\left(ik2L\right) \right]^n = \\ = \frac{1}{1 - \left[\sqrt{R_0 R_1} \exp\left(-\frac{\alpha_T}{2} 2L\right) \exp\left(ik2L\right) \right]} \end{aligned} \tag{C.3}$$

The intensity of the field is now

$$|F|^2 = |F_0|^2 \frac{1}{\left|1 - \left[\sqrt{R_0 R_1}\exp\left(-\frac{\alpha_T}{2}2L\right)\exp\left(ik2L\right)\right]\right|^2} =$$

$$= |F_0|^2 \frac{1}{1 - \left[\sqrt{R_0 R_1}\exp\left(-\frac{\alpha_T}{2}2L\right)\exp\left(ik2L\right)\right]} \frac{1}{1 - \left[\sqrt{R_0 R_1}\exp\left(-\frac{\alpha_T}{2}2L\right)\exp\left(ik2L\right)\right]} =$$

$$= |F_0|^2 \frac{1}{1 + R_1 R_2 \exp\left(-2\alpha L\right) - 2\sqrt{R_1 R_2}\exp\left(-2\frac{\alpha}{2}L\right)\cos\left(2kL\right)} \quad \text{(C.4)}$$

This means that the intensity, because of positive or negative interference, will oscillate between the two values

$$|F|^2_{min} = |F_0|^2 \frac{1}{\left[1 + \sqrt{R_1 R_2}\exp\left(-\alpha L\right)\right]^2} \quad \text{(C.5)}$$

$$|F|^2_{MAX} = |F_0|^2 \frac{1}{\left[1 - \sqrt{R_1 R_2}\exp\left(-\alpha L\right)\right]^2} \quad \text{(C.6)}$$

Following Hakki-Paoli, let us calculate the ratio

$$r_i = \frac{|F|^2_{min}}{|F|^2_{MAX}} = \frac{\left[1 + \sqrt{R_1 R_2}\exp\left(-\alpha L\right)\right]^2}{\left[1 - \sqrt{R_1 R_2}\exp\left(-\alpha L\right)\right]^2} \quad \text{(C.7)}$$

now, it is possible to calculate the expression

$$\frac{1}{L}\ln\frac{\sqrt{r_i}+1}{\sqrt{r_i}-1} = \alpha - \frac{1}{L}\ln\sqrt{R_1 R_2} \quad \text{(C.8)}$$

If it defines the total reflectivity as

$$R^2 = R_1 R_2 \quad \text{(C.9)}$$

it is possible to obtain:

$$\frac{1}{L}\ln\frac{\sqrt{r_i}+1}{\sqrt{r_i}-1} + \frac{1}{L}\ln R = \alpha \quad \text{(C.10)}$$

This is what Hakki-Paoli call the net gain ΓG_i.

C.2 Etalon

Let us write the cosine in the alternative form

$$\cos\left(2kL\right) = 1 - 2\sin\left(kL\right) \quad \text{(C.11)}$$

this leads to

$$|F|^2 = |F_0|^2 \frac{1}{1 + R^2 \exp(-2\alpha L) - 2R \exp\left(-2\frac{\alpha}{2}L\right) \cos(2kL)} =$$
$$= |F_0|^2 \frac{1}{\left[1 + R^2 \exp(-2\alpha L) - 2R \exp\left(-2\frac{\alpha}{2}L\right)\right] + 4R \exp\left(-2\frac{\alpha}{2}L\right) \sin^2(kL)} \tag{C.12}$$

This means

$$|F|^2 = |F_0|^2 \frac{1}{\left[1 - R \exp(-\alpha L)\right]^2 + 4R \exp(-\alpha L) \sin^2(kL)} =$$
$$= \frac{|F_0|^2}{\left[1 - R \exp(-\alpha L)\right]^2} \frac{1}{1 + \frac{4R \exp(-\alpha L)}{1 - R \exp(-\alpha L)} \sin^2(kL)} \tag{C.13}$$

Looking at the dependence on positive or negative interference, it is obvious that it is given by the last ratio, so that we can write the maximum as before (corresponding to the minima of the $\sin^2$ function), and all other values as a modulation of the maximum:

$$|F|^2_{MAX} = |F_0|^2 \frac{1}{[1 - R \exp(-\alpha L)]^2} \tag{C.14}$$

$$|F|^2 = |F|^2_{MAX} \frac{1}{1 + \frac{4R \exp(-\alpha L)}{1 - R \exp(-\alpha L)} \sin^2(kL)} \tag{C.15}$$

The modulating term is quite nice. Let us call it T. If we consider the case of zero losses, and express the wavenumber k in terms of the light wavelength in vacuum λ and of the refractive index n, we get

$$T = \frac{1}{1 + \frac{4R}{[1 - R]^2} \sin^2\left(2\pi \frac{n}{\lambda} L\right)} \tag{C.16}$$

This is exactly the transmission function of an Etalon, whose thickness is L, and whose reflectivity of the single interface is R. It makes sense, because an ideal Etalon is supposed to be transparent ($\alpha = 0$), without any gain or absorption. The term $4R/[1 - R]^2$ corresponds to the *finesse* of the Etalon. Unfortunately it is usually indicated by the letter F, that we will not introduce here, for avoiding confusion with the field.

C.3 The meaning of α

From (C.1) it should be clear the α is the net power attenuation coefficient that includes everything adds or subtracts intensity along the round trip. It excludes the mirror losses (coefficient α_m), but includes the internal losses (coefficient α_i), and the absorption losses (coefficient $\alpha_a bs$) as well as, with a negative sign, the pure

gain coefficient (coefficient G). The standard definition of the total loss coefficient α_T, that also enter the L-I equation, is

$$\alpha_T = \alpha_i + \alpha_m \tag{C.17}$$

It follows that in the Hakki-Paoli theory the definition of α is

$$\alpha_{HP} = [\alpha_i + \alpha_{abs} - G] = \alpha_i - g = (\alpha_T - \alpha_m) - g = \left[\alpha_T - \frac{1}{2L}\ln\left(\frac{1}{R_1 R_2}\right)\right] - g \tag{C.18}$$

This is important, because at threshold $g = \alpha_T$, so that

$$\alpha_{threshold} = -\frac{1}{2L}\ln\left(\frac{1}{R_1 R_2}\right) = \frac{1}{L}\ln\left(\sqrt{R_1 R_2}\right) \tag{C.19}$$

and (C.1) at threshold becomes

$$F_1 = F_0\left[\sqrt{R_1 R_2}\exp\left(-\frac{\alpha}{2}2L\right)\exp\left(ik2L\right)\right]_{threshold} = F_0\exp\left(ik2L\right) \rightarrow |F_1|^2 = |F_2|^2 \tag{C.20}$$

The square modulus confirms that the intensity after the first round trip is the same as at its beginning. It is the steady-state condition, that requires that gain balances losses for sustaining the optical oscillation within a lossy cavity. It follows that the definition of transparency is NOT $g = 0$, but $g = \alpha_i$.

Appendix D

The distributed model

With reference to fig.D.1, we describe a network of vertical elements that represent the same element of the discrete numerical model (par.1.4.3) but in each of its two possible states: the laser diode elements are or clamped at their threshold voltage (in this case they are represented by a voltage generator fixed at V_{th}) or their bias is lower than V_{th}, and then they are represented by a standard Shockley diode. The horizontal connection, as in the discrete model, describes the metal contact (region A) as an equipotential line, connecting all elements in parallel. It is assumed that the device has reached its "first" and main threshold, that is the transition to the lasing condition of the whole part of the active area directly covered by the metal contact. It is then assumed that also some of the neighboring diodes, out of the direct vertical contact to the metal layer, have reached their own threshold and then have a clamped voltage. This is region B in fig.D.1. Last, a region C includes all those diode elements that did not reach the threshold. The extension W of the joint B and C region is physically defined by the geometry of the device, while the extension H of the sole C region (leaving $W - H$ for the extension of region B) is unknown. H will result as the key parameter ruling over the determination of bot voltages and currents in the proposed model.

Recalling the definitions of par.1.4.3, let R_S be the total series resistance of the sole region A (1.108). The total resistance of the B+C path will be R_L (1.109).

Assuming dx as the horizontal distance by the vertical elements, each vertical resistor in fig.D.1 r_V will have a value

$$r_V = R_0 \frac{h}{dx} \tag{D.1}$$

Each horizontal resistor r_L it will be

$$r_L = R_0 \frac{dx}{h} \tag{D.2}$$

In region A the vertical component of the current is easily given by the Ohm's law

$$I_A = \frac{V - V_{th}}{R_S} \tag{D.3}$$

This current will be complemented by the horizontal current that will flow towards regions B and C, that will be indicated, in the next section, as I_{in}.

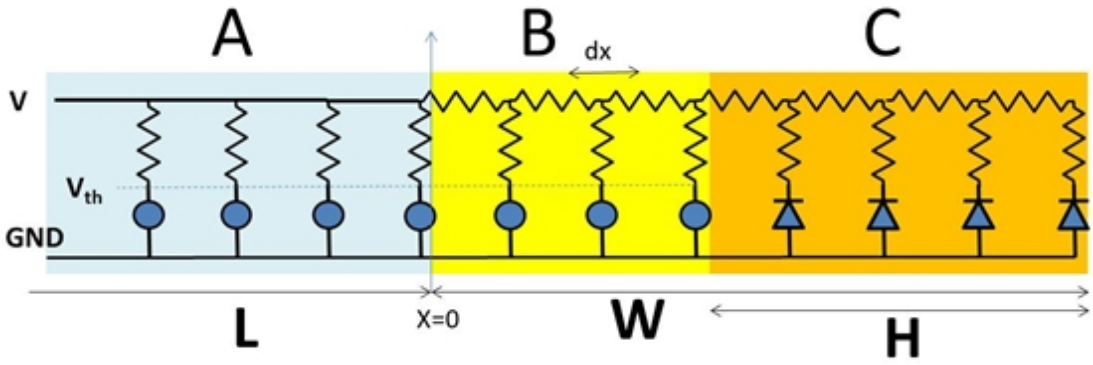

Figure D.1: Electrical model for the distributed model, the voltage generators represent the diodes clamped yet, the total resistance path represent the effective distribution of resistances in the system.

When the diodes of region A just reach their threshold, a current I_{th} will flow that allows to define the external threshold voltage V_A

$$V_A = V_{th} + R_S I_{th} \tag{D.4}$$

We also express the saturation current of the diodes by means of the threshold condition:

$$I_{th} = I_{VS} \exp\left(\frac{V_{th}}{V_T}\right) \tag{D.5}$$

that can be reversed

$$I_{VS} = I_{th} \exp\left(-\frac{V_{th}}{V_T}\right) \tag{D.6}$$

The current I_{th} so defined will be not exactly the real threshold current of the device, but describes what should be its value if the lateral side W were of negligible extension. The measured threshold current will accordingly be $I_{th} + I_{in}(V_A)$.

Let us now proceed with the analysis of regions B and C.

Region B

In region B, let $I(x)$ be the current flowing across the horizontal resistors and with

$$i_V = \frac{V - V_{th}}{r_V} = \frac{V - V_{th}}{R_0 h} dx \tag{D.7}$$

The current flowing along one of the vertical paths. Between the points x and $x + dx$ we have:

$$\begin{cases} V(x + dx) = V(x) - r_L I(x) \\ \\ I(x + dx) = I(x) - i_V \end{cases} \tag{D.8}$$

That is:

$$\begin{cases} V'(x) = -\dfrac{R_0}{h} I(x) & \text{(D.9a)} \\ I'(x) = -\dfrac{V - V_{th}}{R_0 h} & \text{(D.9b)} \end{cases}$$

Differentiating the first:

$$V''(x) = -\frac{R_0}{h} I'(x) = \frac{V - V_{in}}{h^2} \tag{D.10}$$

whose solution is

$$V(x) - V_{th} = A \exp\left(\frac{x}{h}\right) + B \exp\left(-\frac{x}{h}\right) \tag{D.11}$$

from which

$$I(x) = -\frac{1}{R_0}\left[A \exp\left(\frac{x}{h}\right) - B \exp\left(-\frac{x}{h}\right)\right] \tag{D.12}$$

Now, we set the initial boundary conditions in $x = 0$ as the definitions of the voltage V_{in} (that corresponds to the voltage of the metal contact) and of the current V_{in} (that is the current to be added to I_A in order to get the total current I)

$$\begin{cases} V(0) = V_{in} \\ \\ I(0) = I_{in} \end{cases} \tag{D.13}$$

This gives

$$\begin{cases} A + B = V_{in} - V_{th} \\ \\ A - B = -R_0 I_{in} \end{cases} \tag{D.14}$$

and then

$$\begin{cases} A = \dfrac{V_{in} - V_{th} - R_0 I_{in}}{2} \\ \\ B = \dfrac{V_{in} - V_{th} + R_0 I_{in}}{2} \end{cases} \tag{D.15}$$

This allows to rewrite the current and voltages in region B as

$$\begin{cases} V(x) - V_{th} = [V_{in} - V_{th}] \cosh\left(\dfrac{x}{h}\right) - R_0 I_{in} \sinh\left(\dfrac{x}{h}\right) & \text{(D.16a)} \\ I(x) = I_{in} \cosh\left(\dfrac{x}{h}\right) - \left[\dfrac{V_{in} - V_{th}}{R_0}\right] \sinh\left(\dfrac{x}{h}\right) & \text{(D.16b)} \end{cases}$$

It should be noticed that the solution is not yet completely defined, because of the complete independence of the constants I_{in} and V_{in}. It is necessary to solve the current-voltage equations also in region C and set the final boundary condition and the connection with region B for reaching the final result, that is the current-voltage relationship $I(V_{in})$ of the complete structure. Anyway, it is interesting to have some insight in advance, considering the extreme case for which B extends

for the whole lateral length W, that is considering H=0 and no region C. In this case, the final value of the lateral current $I(W)$ would be null, and then

$$[V_{in} - V_{th}] \cosh\left(\frac{W}{h}\right) = R_0 I_{in} \sinh\left(\frac{W}{h}\right) \tag{D.17}$$

The total current would then be

$$I = I_A + I_{in} = [V - V_{th}] \left[\frac{1}{R_S} + \frac{1}{R_0 \tanh\left(\frac{W}{h}\right)}\right] \tag{D.18}$$

This result indicates that final value of the equivalent of the series resistance dV/dI would be smaller than its value just at threshold

$$R_{eff} = \left[\frac{1}{R_S} + \frac{1}{R_0 \tanh\left(\frac{W}{h}\right)}\right]^{-1} = R_S \frac{R_0 \tanh\left(\frac{W}{h}\right)}{R_0 \tanh\left(\frac{W}{h}\right) + R_S} \tag{D.19}$$

Region C

In this region C the vertical conduction involves diodes. For a generic element at location x:

$$\begin{aligned} i_V = I_V \frac{dx}{L} = I_{VS} \frac{dx}{L} \exp\left(\frac{V(x) - r_V i_V}{V_T}\right) = I_{VS} \frac{dx}{L} \exp\left(\frac{V(x) - R_0 \frac{h}{dx} I_V \frac{dx}{L}}{V_T}\right) = \\ = I_{VS} \frac{dx}{L} \exp\left(\frac{V(x) - R_0 I_V \frac{h}{L}}{V_T}\right) \end{aligned} \tag{D.20}$$

As for region B, we have

$$\begin{cases} V(x + dx) = V(x) - r_h I(x) \\ I(x + dx) = I(x) - i_V \end{cases} \tag{D.21}$$

From which

$$\begin{cases} V'(x) = -\frac{R_0}{h} I(x) & \text{(D.22a)} \\ I'(x) = -\frac{I_V}{L} & \text{(D.22b)} \end{cases}$$

The difference comes from the explicit expression of the second equation

$$I'(x) = -\frac{I_{VS}}{L} \exp\left(\frac{V(x) + R_0 h I'(x)}{V_T}\right) \tag{D.23}$$

Let us differentiate again

$$I''(x) = I'(x)\left(\frac{V'(x) + R_0 h I''(x)}{V_T}\right) = \frac{I'(x)V'(x)}{V_T} + \frac{R_0 h I'(x) I''(x)}{V_T} \tag{D.24}$$

Substituting for V' by means of the first equation:

$$I'' = -\frac{R_0}{hV_T} I I' + \frac{R_0 h}{V_T} I' I'' \tag{D.25}$$

The general integral is readily obtained:

$$I' = -\frac{R_0}{2hV_T} I^2 + \frac{R_0 h}{2V_T} I'^2 + c \tag{D.26}$$

Would h be null, we would be in the same case of the lateral currents (no vertical ohmic paths) [2] that is summarized in (1.77). As for that case, let us write the integration constant c as proportional to some current term I_0, that should be defined by the boundary conditions.

$$I' = -\frac{R_0}{2hV_T}(I^2 + I_0^2) + \frac{R_0 h}{2V_T} I'^2 \tag{D.27}$$

Rewriting everything:

$$I'^2 - \frac{2V_T}{R_0 h} I' - \frac{I^2 + I_0^2}{h^2} = 0 \tag{D.28}$$

we can solve algebraically:

$$I' = \frac{V_T}{R_0 h} - \sqrt{\left(\frac{V_T}{R_0 h}\right)^2 + \frac{I^2 + I_0^2}{h^2}} = \frac{V_T}{R_0 h}\left[1 - \sqrt{1 + \left(\frac{R_0}{V_T}\right)^2 (I^2 + I_0^2)}\right] \tag{D.29}$$

The negative sign was selected for the square root because the current I is expected to decrease when x increases (it must be null at the end of the C region). The point is now to integrate:

$$\frac{dI}{\sqrt{1 + \left(\frac{R_0}{V_T}\right)^2 (I^2 + I_0^2)} - 1} = -\frac{V_T}{R_0 h} dx \tag{D.30}$$

We can transform the left side as:

$$\frac{\left[\sqrt{1 + \left(\frac{R_0}{V_T}\right)^2 (I^2 + I_0^2)} + 1\right] dI}{\left(\frac{R_0}{V_T}\right)^2 \left(I^2 + I_0^2\right)} = -\frac{V_T}{R_0 h} dx \tag{D.31}$$

Rearranging:

$$\frac{dI}{I^2 + I_0^2} + \frac{\sqrt{1 + \left(\frac{R_0}{V_T}\right)^2 (I^2 + I_0^2)}}{I^2 + I_0^2} dI = -\frac{R_0}{hV_T} dx \tag{D.32}$$

For the sake of simplifying notations, let us temporarily set:

$$y = I\frac{R_0}{V_T} \quad \text{and} \quad y_0 = I_0\frac{R_0}{V_T} \tag{D.33}$$

so that the last equation becomes

$$\frac{\left[\sqrt{1+y^2+y_0^2}+1\right]dy}{y^2+y_0^2} = -\frac{dx}{h} \tag{D.34}$$

The left side is a differential expression that has a known integral in the following form:

$$\frac{1}{y_0}\arctan\left(\frac{y}{y_0}\right)+\frac{1}{y_0}\arctan\left(\frac{y}{y_0}\frac{1}{\sqrt{1+y^2+y_0^2}}\right)+\ln\left(y+\sqrt{1+y^2+y_0^2}\right) \tag{D.35}$$

If now we consider that in $x = W$ the current I (and then also y) must vanish, we can write the complete solution:

$$\frac{1}{y_0}\arctan\left(\frac{y}{y_0}\right)+\frac{1}{y_0}\arctan\left(\frac{y}{y_0}\frac{1}{\sqrt{1+y^2+y_0^2}}\right)+\ln\left(\frac{y+\sqrt{1+y^2+y_0^2}}{\sqrt{1+y_0^2}}\right) = \frac{W-x}{h} \tag{D.36}$$

This is a complicate function, but is an analytical expression, that is a solution of the given differential equation and fulfills the boundary condition in $x = W$.

The procedure, now, should be to impose that both I and I' have the same values of the corresponding solution for the B region at the boundary $x = W - H$. The two continuity constraints would allow to eliminate two of the remaining undefined constants, one of which is surely I_0 (that means y_0 in the last notation). The other should be the coordinate H of the separation point between region B and C. The result would be an equation linking I_{in} to V_{in}, and then the total equation for $I(V_{in})$.

At the time of closing the thesis, the ultimate analytical steps have been not yet solved.

Anyway, an approximated expression has been tested, based on a heuristic consideration on the current flowing in region C.

At the interface of regions B and C, the voltage V, measured along the horizontal line of resistors, is exactly that limiting voltage V_A, described at the beginning of this Appendix, required to just bring the diode to its threshold:

$$I'(W-H) = -\frac{I_{VS}}{L}\exp\left(\frac{V_{th}}{V_T}\right) \tag{D.37}$$

$$V(W-H) = V_A = V_{th} + R_S I_{th} \tag{D.38}$$

Because the vertical current reduces the horizontal current that, at the last point vanishes, we try to suppose that the current consumed in traveling from $x = W-H$

to $x = W$ (that is, traveling a distance H) decreases linearly from its maximum to 0. The total current spent in this travel will then be

$$I(W-H) = \frac{1}{2}\left\{\frac{I_{VS}}{L}\exp\left(\frac{V_{th}}{V_T}\right)\right\} \tag{D.39}$$

Being the lateral structure symmetric (it does exists on both sides of the ridge), we take twice this value, so that we assume

$$\begin{cases} V(W-H) = V_A = V_{th} + R_S I_{th} \\ \\ I(W-H) = 2\dfrac{1}{2} I_S \dfrac{H}{L}\exp\left(\dfrac{V_A}{V_T}\right) = I_S \dfrac{H}{L}\exp\left(\dfrac{V_{th}+R_S I_{th}}{V_T}\right) \end{cases} \tag{D.40}$$

Now, we can compare this boundary values with the solution for the B region (D.16a) and (D.16b). Calculating this last pair at the boundary $x = W - H$ we get:

$$\begin{cases} V_{in} = V_{th} + R_S I_S \dfrac{H}{h}\exp\left(\dfrac{V_{th}+R_S I_{th}}{V_T}\right)\sinh\left(\dfrac{W-H}{h}\right) + \\ \qquad + R_S I_{th}\cosh\left(\dfrac{W-H}{h}\right) \end{cases} \tag{D.41a}$$

$$\begin{cases} I_{in} = I_S \dfrac{H}{L}\exp\left(\dfrac{V_{th}+R_S I_{th}}{V_T}\right)\cosh\left(\dfrac{W-H}{h}\right) + \\ \qquad + I_{th}\dfrac{h}{L}\cosh\left(\dfrac{W-H}{h}\right) \end{cases} \tag{D.41b}$$

This is a set of two equations that can be solved for V_{in} and I_{in}, resulting in a parametric definition of the $I_{in}(V_{in})$ relationship, and then making possible to plot all current-voltage characteristics.

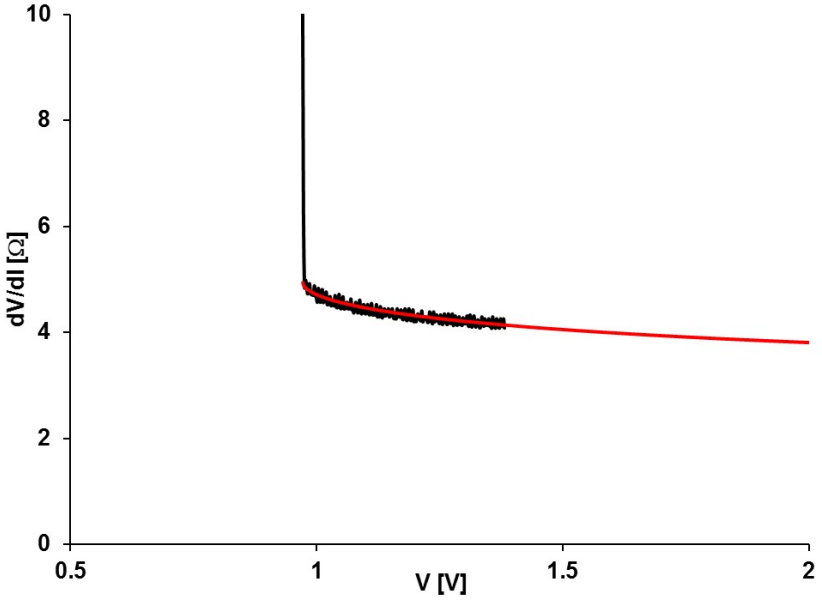

Figure D.2: Calculated and experimental dV/dI curves, according to the distributed model.

Fig.D.2 shows the result of that plot superimposed to the experimental values of a real laser diode. The puzzling point is that, in order to get that nice superposition, the calibration constants, related to the geometry of the real ridge, were quite unrealistic. For this reason the model has not yet been licensed. Anyway, the functional correctness of the prediction is worth of appreciation.

Appendix E

Laser diode technology and investigation techniques

E.1 Introduction

Semiconductor lasers are similar to the solid-state laser ruby laser and helium-neon gas laser. However, laser diodes differ from the other lasers because they are small and easily modulated at high frequency simply by modulating the biasing current. Because of these unique proprieties, the semiconductor laser is one of the most important light source for optical-fiber communication. During the years several structures for lasers have been developed, mostly orientated to improve the confinement of the current inside the active region. In this section it will be presented a summery of laser technology, starting from the simplest vertical structure for laser diodes, describing how the confinement of the current and the light can be achieved, and finally the most important techniques of investigation to address failure analysis will be described at the end of this Appendix.

E.2 Epitaxy and heterostructure

When we consider the vertical stack of epitaxial layers, all laser diodes share the common vertical features along a line that crosses the optically active part of the device: a Double Heterostructure (DH) *pn* junction. The reason for such a structure is that photons are created by electron-hole recombination in direct band-gap semiconductor crystals. In order to have many photons, is then necessary to bring many electrons and many holes to meet in the same place, and to help them to the maximum extent to recombine. The first step, that is to bring electrons and holes to meet, is easily obtained in a forward biased *pn* junction. Anyway, in standard ideal junctions (*pn* homojunctions) electrons and holes run in opposite directions but recombine in separate places: holes in the neutral n region, and electrons in the neutral p region, skipping the whole depletion layer, where jointly their densities p, n and their product pn are maximum. The second step is to insert a thin layer (the active layer) of a different semiconductor material, compatible with the surrounding ones, and with a band gap E_g as smaller as possible than in the rest of the material. The reduced band gap makes the recombination rate higher than in the other material, when the same electron and

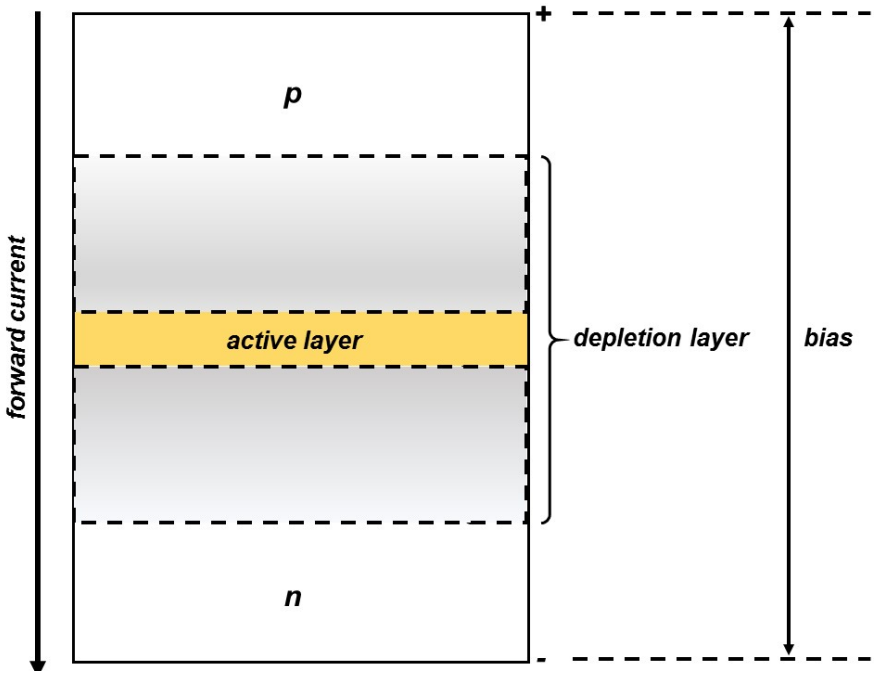

Figure E.1: Common vertical stack of layer of any laser diode

hole densities populate the depletion region. It follows that, different from a standard homojunction diode, strong recombination is forced inside the active layer, despite its total immersion in the middle of the much wider depletion region. The result is that the emitted light spectrum will be completely dominated by the sole characteristics of the active layer. The most significant feature is that the peak energy $h\nu_0$ of the emitted photons will equate, within few percent, the band gap energy E_g of the active material. Epitaxy is, of course, the solution for building such a heterostructure. Some golden rules hold for the epitaxial process for laser diodes (they will be described deeply in par.E.10):

1. All materials must share the same crystal structure (lattice), the same orientation and the same lattice constant. The most part of suitable materials has a zincblende structure, that is an fcc lattice with a binary atom basis.

2. A substrate, some hundreds micrometers thick, must be provided, whose role is to make the structure robust and handling. It must be a stoichiometric material, because of the cost and the technical difficulty to handle non-stoichiometric layers at thicknesses larger than about one micrometer. For vertical diodes, it must be conductive. It is usually n-doped.

3. Three layers must then be epitaxially grown on the substrate: one confining layer (n-type), the active layer (usually undoped) and a second confining layer (p-type). All three can be non stoichiometric (ternary or quaternary compounds) [31].

4. The confining layer must have a band gap as higher as possible than the band gap of the active layer. This ensures both the electron-hole confinement and also the optical confinement of the created photons, building up an efficient optical waveguide.

5. a cap layer is usually grown on the top, to ease the electric ohmic contact of the upper metallization.

6. The band gap of the substrate is of minor importance for edge emitters. For vertical devices (i.e. VCSEL) must have a band gap larger than the active layer, to avoid photon absorption.

Chemistry must also be developed, able to selectively etch even a single layer without affecting the other ones. This in order to ensure patterning during some particular non planar growth (as for buried crescent structures, see later subparagraph E.5.2) or to etch grooves from the top surface to confine current injection on limited areas (see later paragraph E.5). At this point, the common vertical structure of any laser diode appears as in fig.E.2, which updates the previous image fig.E.1.

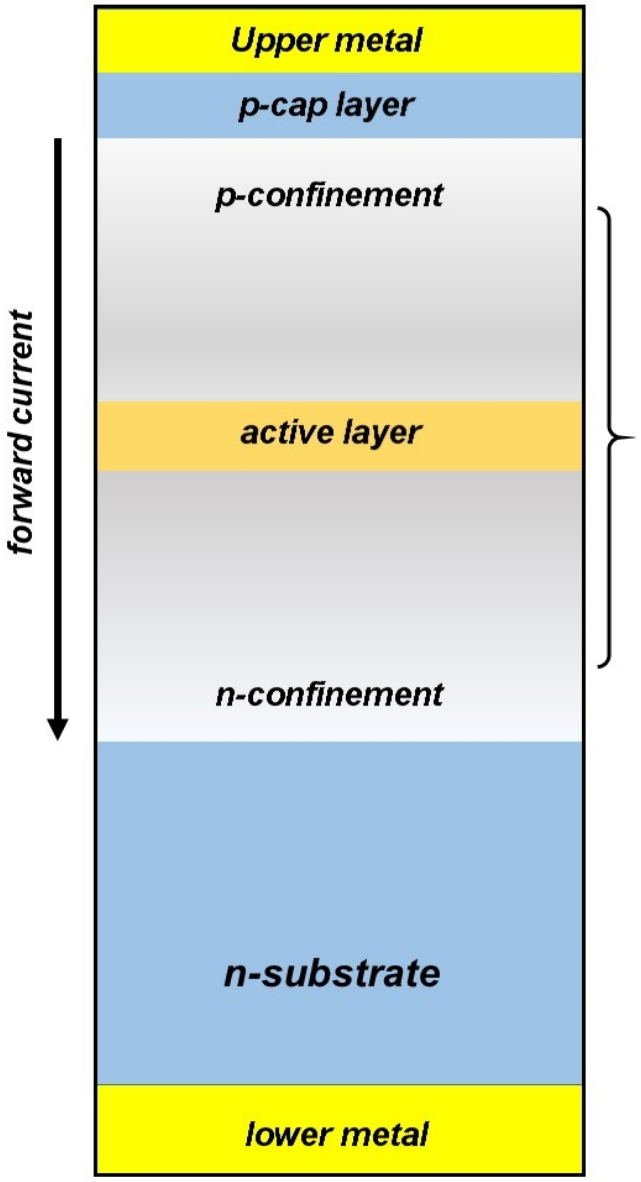

Figure E.2: Update of the common vertical stack of layer of any laser diode with respect to the fig.E.1.

E.3 Lateral confinement

For the same reason that led to require a substrate (the optical active elements: active and confinement layers, are too thin to stand alone), the lateral size of any laser chip is much larger than the strictly needed one for laser operation. The optically active region must then be laterally limited.

Roughly speaking, two main reasons lead to require small vertical and lateral size for the optical cavity of a laser diode:

1. In order to keep the cavity unidimensional the vertical and lateral sizes of the region where photons are produced must be comparable with the wavelength of the emitted light (in order to suppress higher harmonics), that means must lay in the micrometer range. It is not a problem for the thickness, that is so thin to be comparable with the electron wavelength, but is a problem for the lateral extension, that in a normal chip is several tens of a micron or larger.

2. The smaller the volume of the active region, the lower the current required to pump it up to the laser threshold. Many different solutions have been developed during the decades of the laser diode history. Here, based on the [69] and with some integrations, a list of solutions for the edge emitters will be reported.

E.4 Current confinement

One of the most practical ways to get light from a reduced portion of the active region is to feed with current only a portion of the upper surface.

The simplest solution would simply pattern the upper metal in a stripe shape (fig.E.3).

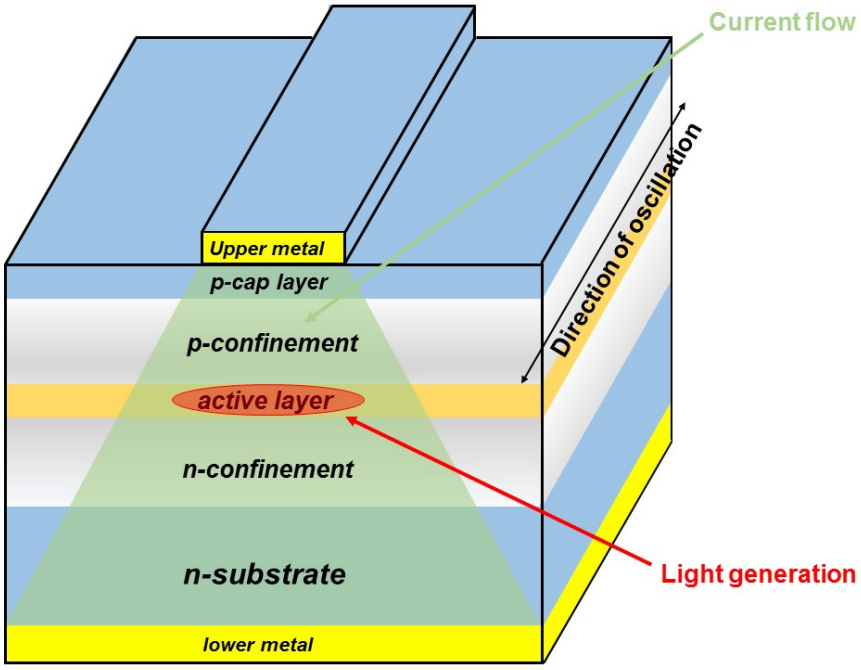

Figure E.3: Vertical structure with upper metal.

This solution unfortunately has many disadvantages:

1. It reduces excessively the top metal surface, and makes impossible wire bonding

2. The exposed remaining part of the cap layer must be protected by a passivation, that should be then patterned to open a window for wire bonding.

E.4.1 Oxide stripe

The closest practical alternative has been a quite popular technology for GaAs based devices, the Oxide Stripe geometry, that it is shown in fig.E.4.

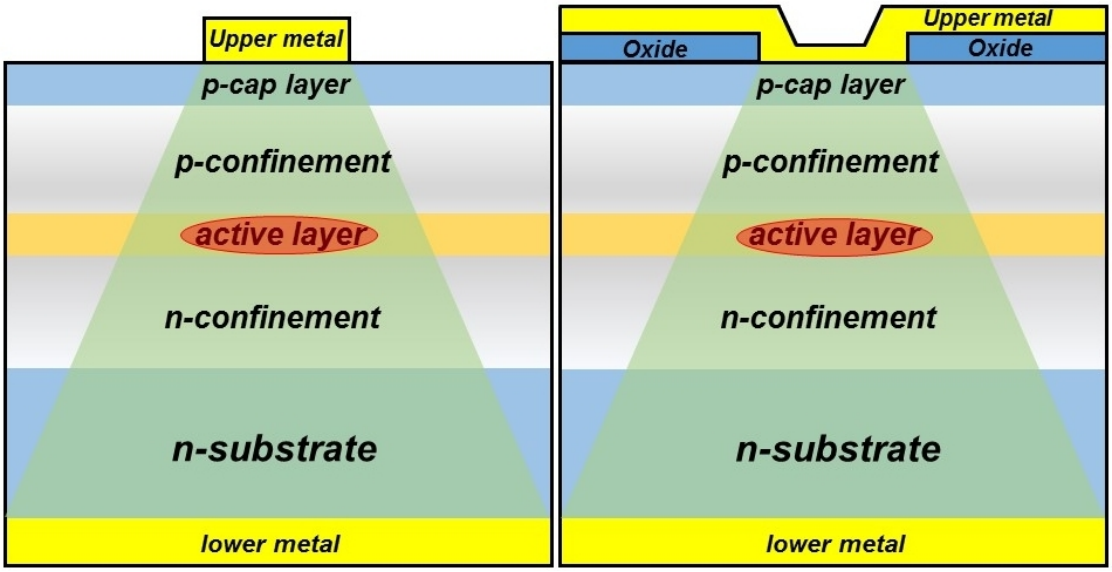

Figure E.4: Oxide stripe geometry.

E.4.2 Ridge structure

The evolution of that solution has been the ridge structure, where the cap layer is first patterned, and then the exposed part of the underlying p-confinement layer is significantly reduced, also by chemical etching.

The result is a sort of funnel that focuses the current onto an even more limited part of the active layer (see fig. E.5). The silicon oxide has been often replaced by silicon nitride.

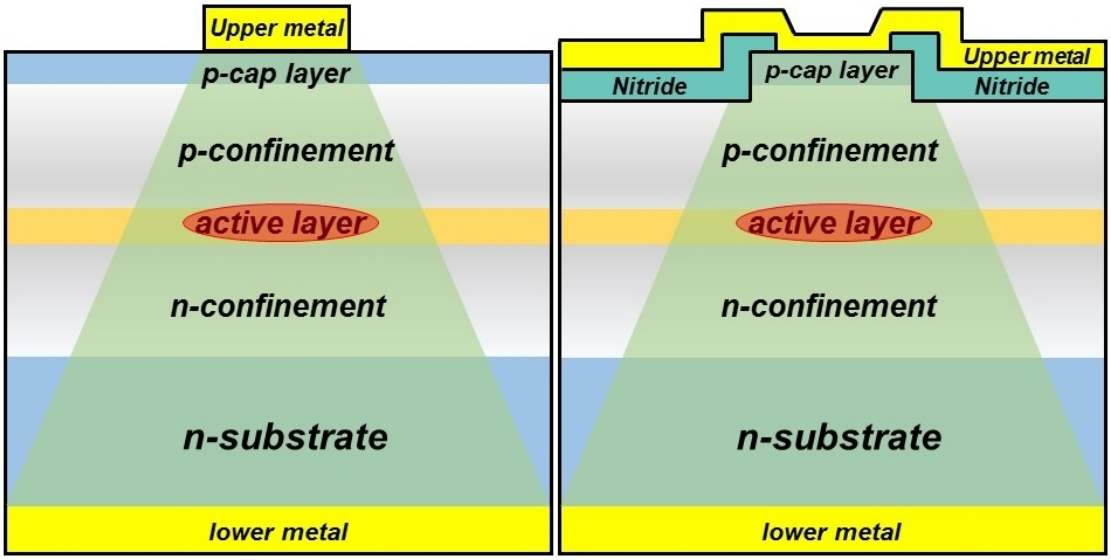

Figure E.5: Ridge structure geometry.

E.4.3 Zn diffused planar

A third way is to replace the p-cap layer with a n-cap layer. This would create a reverse-biased junction that would block any current from flowing into the device. A Zn diffusion, limited to the current injection area, locally destroys the new junction and creates an ohmic path from the upper metal and the p-confinement layer (fig.E.6).

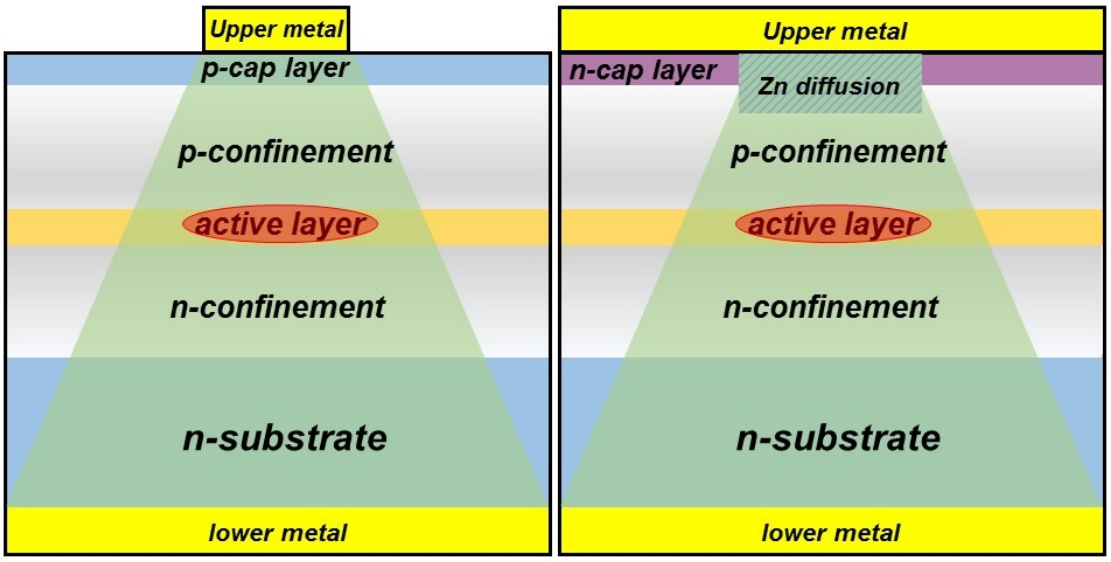

Figure E.6: Zn-diffused planar.

E.5 Light confinement

A second approach is to physically limit the extension of the light producing area.

E.5.1 Proton bombarded

A "brutal" mode is to leave the whole active layer in place, but to destroy its optically efficiency by proton bombardment of the sides of the wanted active area (it is sufficient to shield it during the exposure to protons) (fig.E.7).

This will cause parasitic resistive conduction across the bombarded regions, that acts as a current shunt, parallel to the surviving active diode. The very low impedance of the diode under forward bias will allow its current to rapidly dominate over the shunts.

Moreover, and even more important, the damage of the lattice perfection will enormously enhance, inside the bombarded parts of the active layer, the non radiative recombination. This, in turn, will dramatically reduce the number of photons, and lead the bombarded material to change from gain to absorption for light. This extinguishes the light that attempts to propagate laterally, and suppressed the side modes of the cavity.

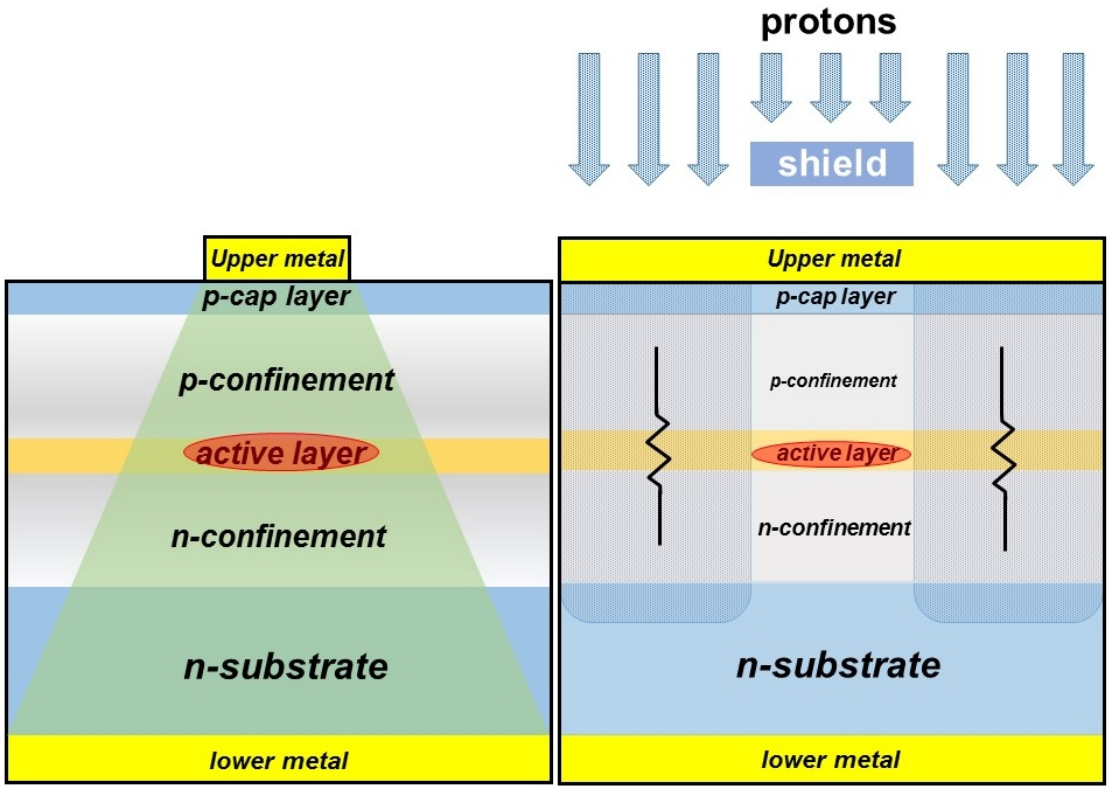

Figure E.7: Proton bombarded.

E.5.2 Buried Heterostructure (BH)

A much more sophisticated solution, usually created in the InP/InGaAsP system, cuts the structure, as for the ridge geometry, but allows the etch to pattern

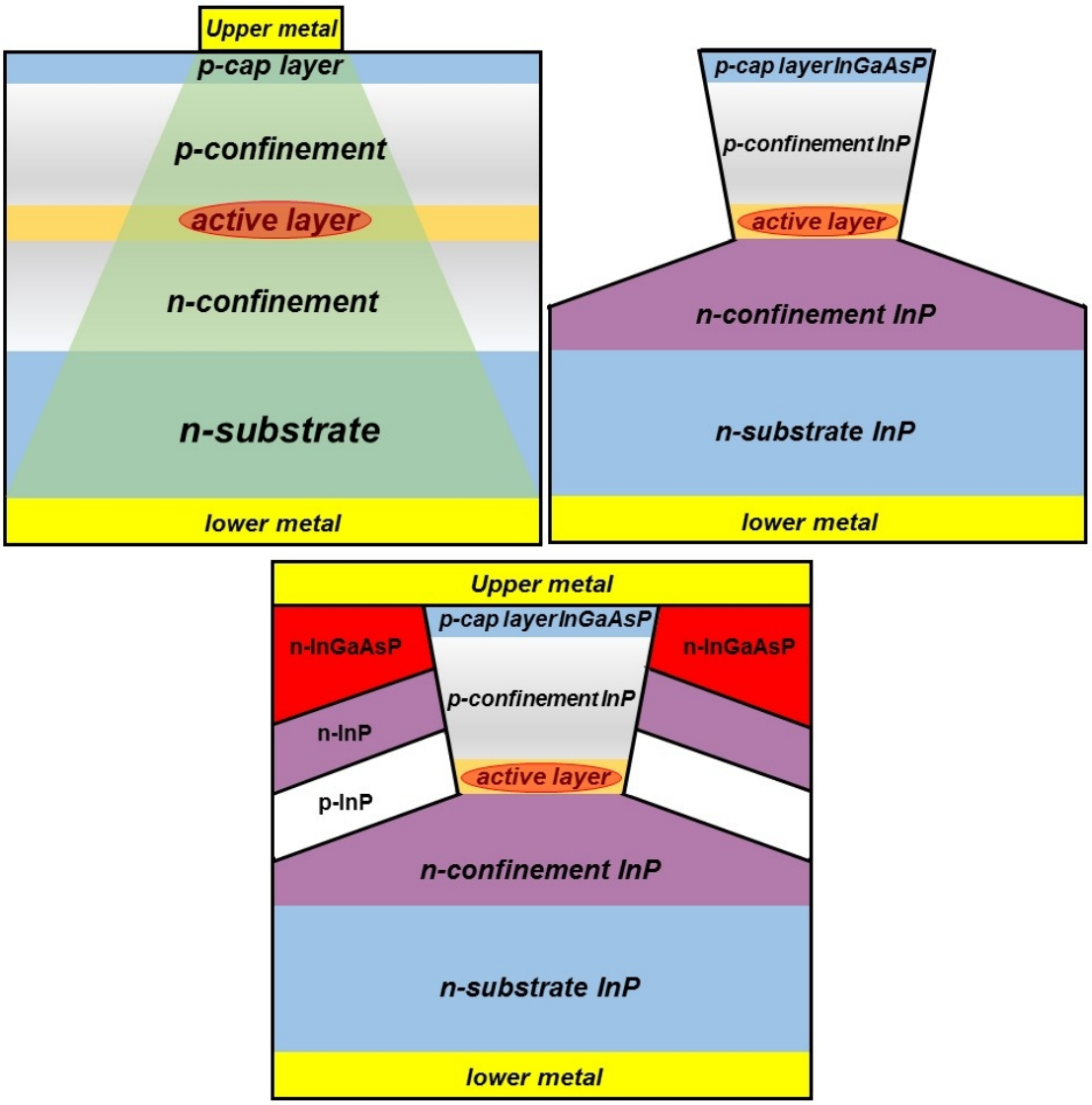

Figure E.8: Technological steps to obtain the Buried Heterostructure structure.

the whole p-cap layer, the whole upper p-confinement layer, the whole active layer and, finally, part of the underlying n-confinement layer.

Such a deep etch will usually require different steps for each layer (here chemistry enters into play at its maximum extent), and many of them employ anisotropic etches (that, acting at different speeds on the different crystal orientations, produce inclined plane surfaces), the steps are shown in fig.E.8.

The last etch, usually isotropic, leaves a curved surface, caused by the central surviving column. At this point a sequence of p-InP, n-InP, n-InGaAsP layers is epitaxially re-grown. The result is a device where side currents still survive, all across pn InP homojunctions (fig.E.9). Here the lower impedance of the central Double Heterostructure p-InP/InGaAsP/n-InP allows the active region to collect more and more current as injection increases.

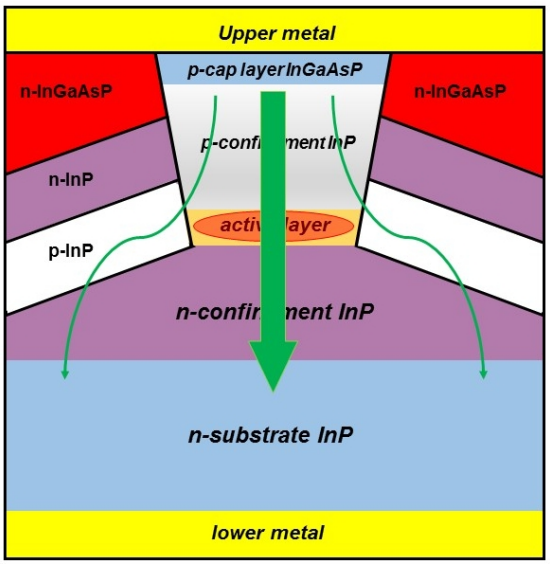

Figure E.9: Buried Heterostructure (BH) structure.

E.5.3 Buried Crescent (BC) or v-grooved substrate BH

Finally, a similar approach, based on a more complex sequence, leads to the Buried Crescent structure, here reported in E.10 from the ref. [69]. From the topological and electrical point of view, it operates as the previous BH structure.

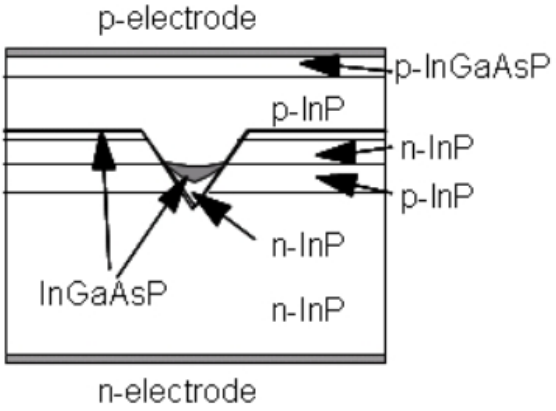

Figure E.10: Buried Crescent (BC) structure.

A mixed use of the various solution can be adopted, as in the following image E.11, where a Buried Crescent structure is coupled with the Ridge technology.

A peculiar feature of the BH solution is that the active region is not only thin but also narrow (and long), completely surrounded, laterally and vertically, by higher bandgap material. This makes the active stripe optically guided also laterally. This means that the active stripe could designed be not straight, forcing the light to follow its shape, as in an optical fiber. This is useful when external cavity configurations are employed (as for some tunable lasers), where the optical resonances internal to the chip must be avoided (while they are requested for internal cavity solution). The image in fig.E.12 shows an optical view from the

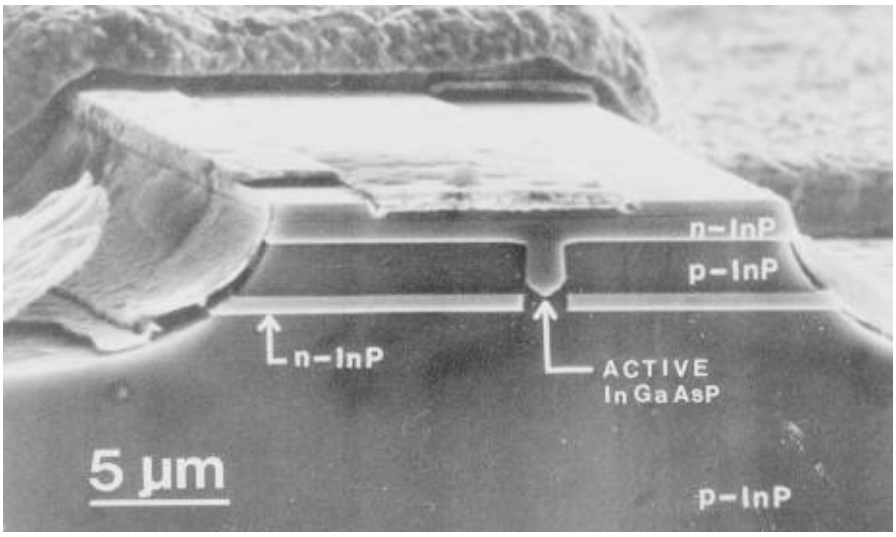

Figure E.11: Mixed solution, in which Buried Crescent structure is coupled with the Ridge technology.

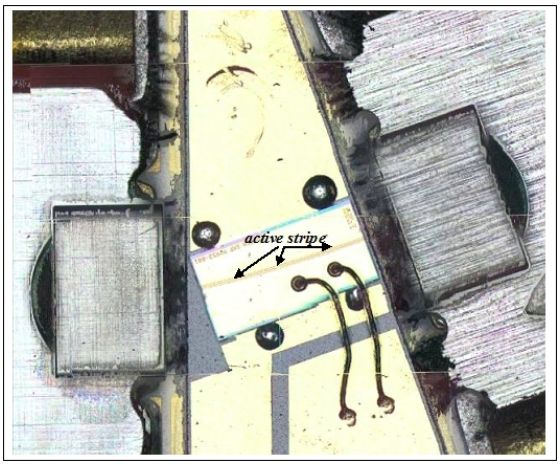

Figure E.12: Optical view from the top of a laser chip.

top of a laser chip, inserted between two external lenses, and the bent thin line visible on the chip individuates the guided active stripe, with a transverse structure probably quite similar to the SEM image reported in fig.E.11.

E.6 Quantum Wells (QW)

The spectrum of a laser diode comes out from the optical frequencies belonging to its spontaneous emission range, that corresponds to the LED regime that holds for current intensities lower than the threshold current I_{th}. This spontaneous emission spectrum, in turn, is quite sensitive to temperature.

This is due to two reasons:

1. Temperature modulates the amplitude of the band gap

2. Temperature affects the density of electrons and holes

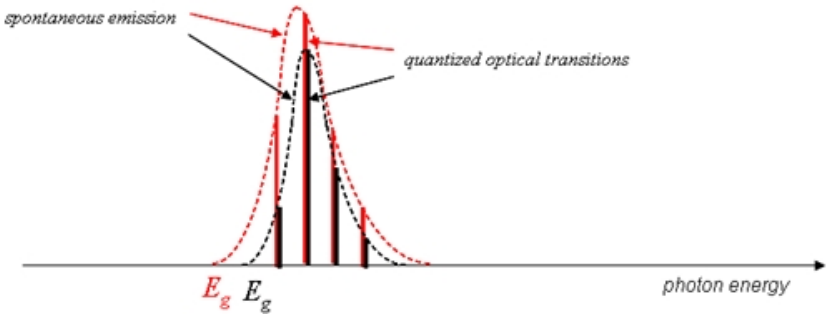

Figure E.13: Comparison between the spectral shapes of the spontaneous emission and the quantized optical transitions.

Both effects contribute to shift the peak and the shape (width) of the spectrum.

But when the thickness of the active layer becomes so small to be comparable with the De Broglie wavelength associated to both Bloch electrons and holes, quantum effects appear, that result in quantization of both electron and hole energy levels inside the active layer.

This reduces the influence of temperature to the only thermal expansion of the thickness of the active layer, that is by far smaller than the previously indicated effects. In this way, wavelength is much more stable with respect to temperature (fig.E.13).

E.6.1 Multiple Quantum Wells (MQW)

One disadvantage of creating an extremely thin active layer is that it reduces the fraction of electron-hole pairs that are forced to recombine inside it.

The problem is solved by creating multiple quantum wells, that is a stack of alternating quantum wells and thin confinement layers (usually undoped).

The stack is still so thin to remain quite well immersed inside the depletion region of the *pn* diode.

Careful design can take full advantage of the resonances that such a periodic structure can activate, and further enhance both recombination efficiency and frequency selection.

E.6.2 Strained Lattice QW

The extremely small thickness of a QW, that corresponds to few crystal planes, allows to create quite artificial situations, where a crystal that should have a smaller lattice constant than the surrounding material (the upper and lower confinement layers) is forced to enlarge its spacing, to fit the dominant periodicity of the more massive parts (fig.E.14).

This solution makes accessible unusual values for optical parameters as quantum efficiency, refractive index (and then optical confinement) etc. It is usually employed in the InGaP/GaAs systems.

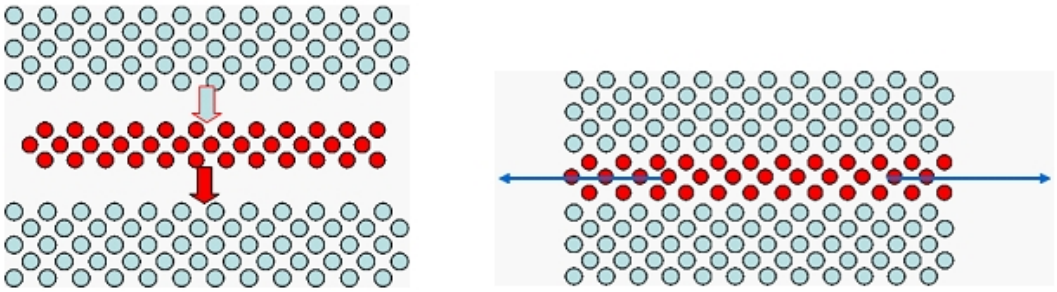

Figure E.14: Effect of the natural and forced spacing

E.7 Distributed Feedback (DFB)

The next paragraph E.8 will deal with the Fabry-Perot cavity, where light reflection inside the chip selects several possible optical frequencies for laser emission from the initial spontaneous spectrum.

In order to select one specific emission line among the many possible ones, one clever solution is to introduce a corrugated heterostructure inside one of the confinement layers.

This structure is made of two layers, both with a bandgap larger than the energy of the photons emitted by the active region, and with different refractive index.

Their interface is shaped (by means of inferential lithography) in a periodic undulation. The effect of such a structure is very well described by the fig.E.15, where it is shown as the optical field due to the photons created inside the thin active layer extends its tails deeply into the confinement (guide) layers. The longitudinal propagation of such an optical field then senses the corrugation (grating).

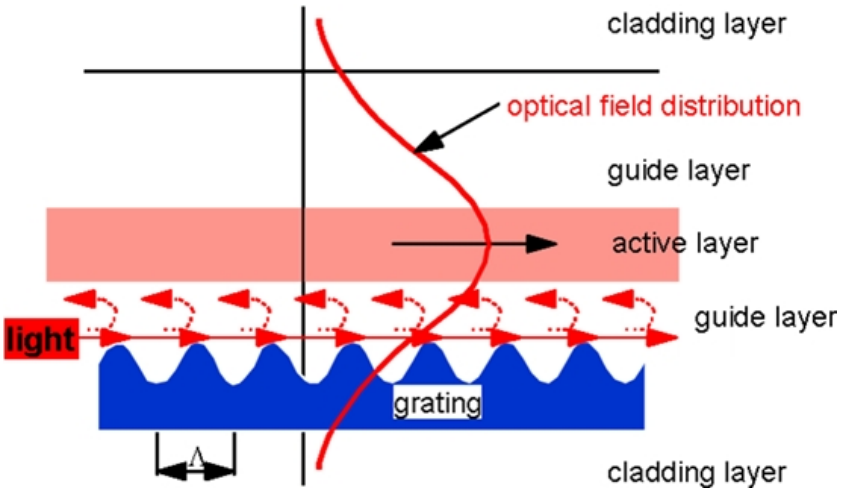

Figure E.15: Effect of DFB structure.

It is a classical result of the wave propagation theory, first introduced by Bragg for x-rays and then by Block for the Schroedinger waves, that a back-reflected wave sets up when the optical propagating wavelength λ is equal to the periodicity a of the grating.

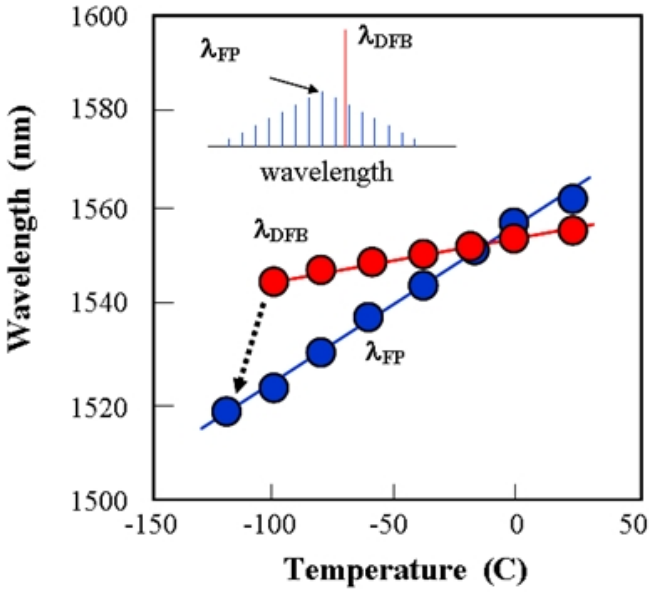

Figure E.16: Comparison of wavelength stability with temperature between the FP and DFB structure.

The complete theorem states that this holds also for

$$\frac{\lambda}{2} = \frac{a}{m} \tag{E.1}$$

where m is an integer. But for laser diodes, the other possible wavelengths lay out of the available spectrum. This structure, not only selects a wavelength, but is also much more stable with respect to temperature, as reported in fig.E.16

E.8 Longitudinal confinement. Fabry-Perot optical cavity

No matter the solution adopted for the lateral confinement, and after having appreciated the common vertical structure for any laser chip, the longitudinal dimension remain to play the role of the one-dimensional optical cavity. Its extension (in the order of many hundreds of a micrometer) is by far larger than the other two dimensions. Its length L plays a fundamental role for the optical modes. Within this cavity light must undergo several reflections before exiting.

The opposite facets of the longitudinal cavity must be planar at an optical level of accuracy. This is easily achieved by cleaving them along the preferential crystal directions (usually [110] planes). The difference in the refractive index between the active material (n) and vacuum (n_0=1) introduces a certain amount of natural reflectivity

$$R_0 = \left(\frac{n-1}{n+1}\right)^2 \tag{E.2}$$

that, on the other side, for standard semiconductor does not exceed the value of 40%. This is not sufficient for laser requirements. A low reflection coefficient

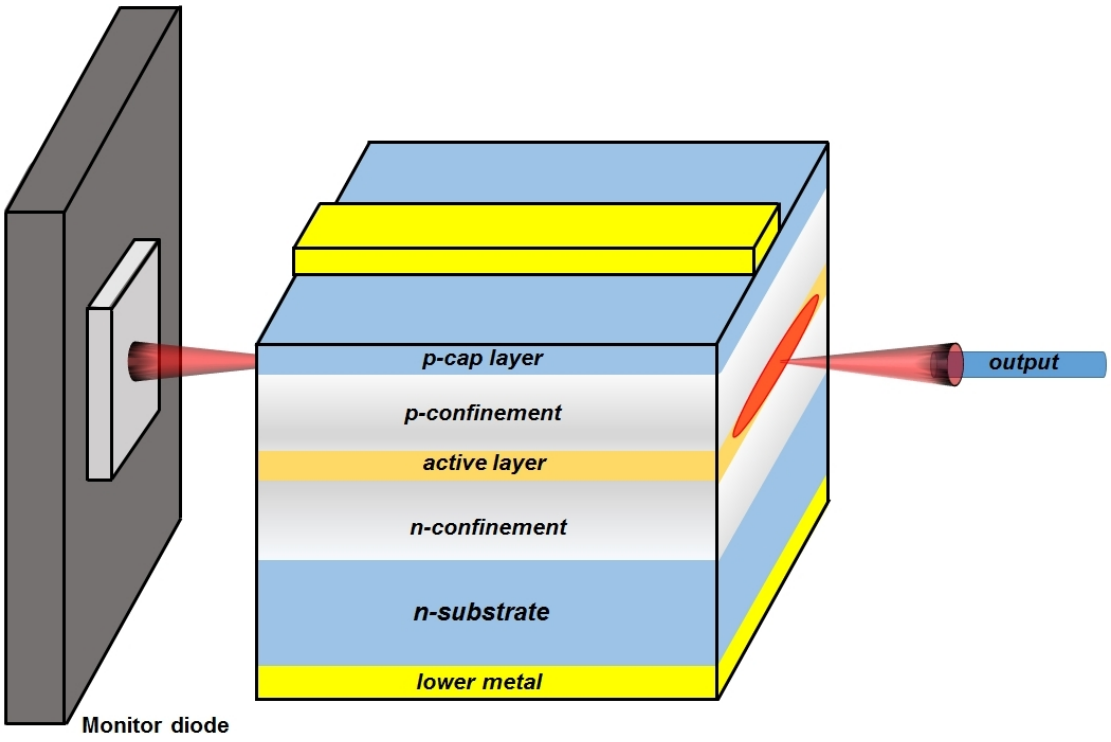

Figure E.17: Fabry-Perot structure.

means high total losses, that, in turn, increases the value of the threshold current. The standard configuration of an edge emitter laser calls for different reflection coefficients.

Light is indeed allowed to exit the cavity from both its opposite sides (fig.E.17). From one of them the output light is collected (or directly by a fiber or by means of an output window, possibly coupled with some focusing elements).

From the other side a minimum optical power is sent to a photodetector (a diode). The role of the monitor diode (conventionally assumed to be on the back of the laser diode, being the output facet on its front) is to supply the direct measurement of the emitted optical power required to provide a feedback for constant-power operation. Its function does not require as many light as the output system, and then the back facet is highly (but not totally) reflecting, while the front facet is mostly reflecting, too, but at a minor extent. For this reason the two facets are often indicated as back and front mirror, respectively.

On a reliability ground, the different reflectivity means that the back mirror is usually hotter than the front mirror. The needed reflectivity is achieved by coating both facets with a carefully designed stack of dielectric layers, differing by refractive index and thickness.

The final configuration shown in fig.E.17, that is the simplest one for a laser chip, is known with the name of Fabry-Perot.

E.9 Vertical Cavity Surface Emitting Laser (VCSEL)

The vertical-cavity surface-emitting laser, or VCSEL, is a type of semiconductor laser diode where the emitted light leaves the device in a direction perpendicular to the chip surface, contrary to conventional edge-emitting semiconductor lasers

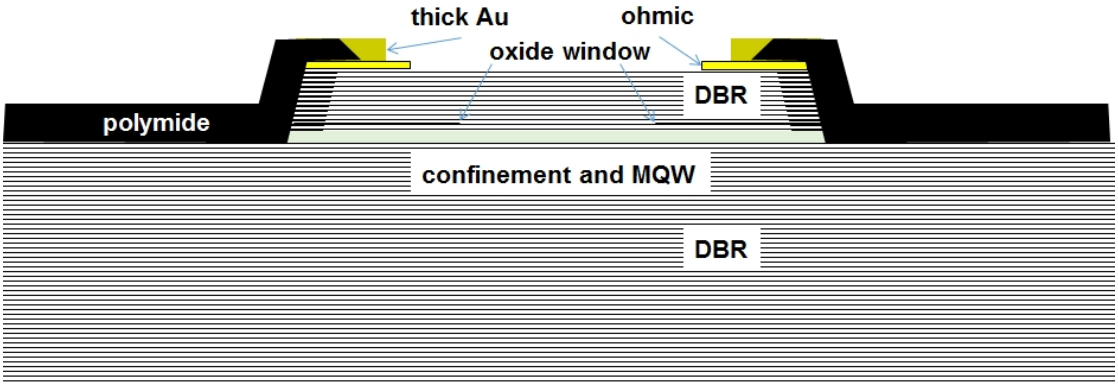

Figure E.18: Base schematic structure of a VCSEL.

(also in-plane lasers) which emit from surfaces formed by cleaving the individual chip out of a wafer. The laser resonator consists of two distributed Bragg reflector (DBR) mirrors parallel to the wafer surface with an active region consisting of one or more quantum wells for the laser light generation in between. The planar DBR-mirrors consist of layers with alternating high and low refractive indices (fig.E.18). In common VCSELs the upper and lower mirrors are doped as p-type and n-type materials, forming a diode junction. In more complex structures, the p-type and n-type regions may be embedded between the mirrors, requiring a more complex semiconductor process to make electrical contact to the active region, but eliminating electrical power loss in the DBR structure.

The vertical-cavity lasers typically consist of a circular dot geometry with lateral dimensions of a few microns. This emitting aperture of a few microns facilitates coupling to optical fiber or other simple optics because it is sufficiently narrow to support only a single lateral mode of the resulting optical waveguide, but sufficiently wide to provide an emerging optical beam with a relatively small refraction angle. However, VCSELs continue to be an important multi-mode fiber optic market in which it is usually desired to use multimoded VCSELs that can fill the modal spectrum of the fibers. Figure E.19 show a SEM image of a typical VCSEl laser.

Figure E.19: Cross-section SEM imiage of a typical VCSEL.

The main methods for current and light confinement in a VCSEL are illustrated

in fig.E.20, which shows the schematic VCSEL cross section for three typer of lateral confinement structures. The first case (a) illustrates a proton-implanted VCSEL that uses the implant together a current confinement aperture. The second example illustrates the dieletrically apertured VCSEL. The aperture is usually formed by an oxidation of AlAs or a high Al content AlGaAs layer very close to the active region (sometimes referred to as"oxide-confined"). The low-index, insulating aperture provides lateral current and optical confinement. As the aperture is close to the active region, the current confinement tends to be quite good.

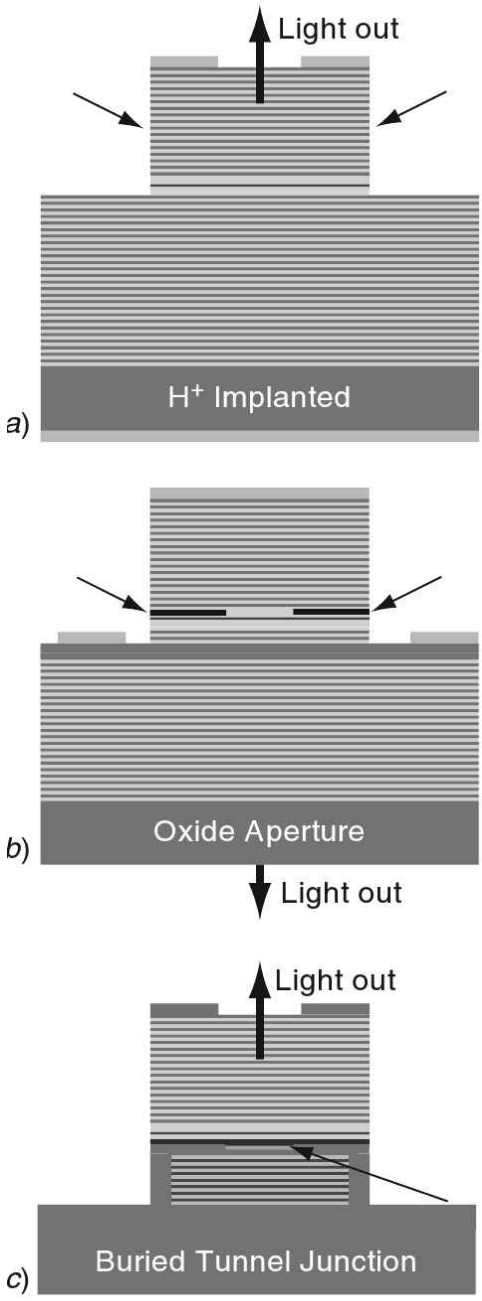

Figure E.20: Schematic of a VCSEL. (a) Proton-implanated, with only current confinement; (b) dieletrically apertured with current confinement; (c) mesa-confined with possible current confinement.

The optical confinement results from the lensing action of the dielectric aperture that refocuses light resonating between the two planar mirror stack. The third VCSEL example (c) also provides good optical and current confinement, but in this case the inclusion of a small thickness semiconductor disk above the active region provides the optical lensing element.

E.10 Epitaxial rules for DH lasers

The successful fabrication of laser diodes relies very heavily on the properties of the materials involved. There is a very limited set of semiconductors that possess all necessary properties to make a good laser. For the desired double heterostructure at least two compatible materials must be found, one fr the cladding layer and another for the active region. The most fundamental requirement for these different materials is that they have the same crystal structure and the same lattice constant, so that single-crystal, defect-free films of one can be epitaxially grown on the other. Defect generally became non-radiative recombination centers, which can steals many of the injected carriers that otherwise would provide gain and luminescence.

It is important to understand how to select materials that meet this fundamental boundary conditions. To this scope it is introduced fig.E.21, that plots the bandgap versus lattice constant for several families of III-V semiconductor. These III-V compounds have emerged as the material of choice for lasers that emit in the 0.7-1.6μm wavelength range.

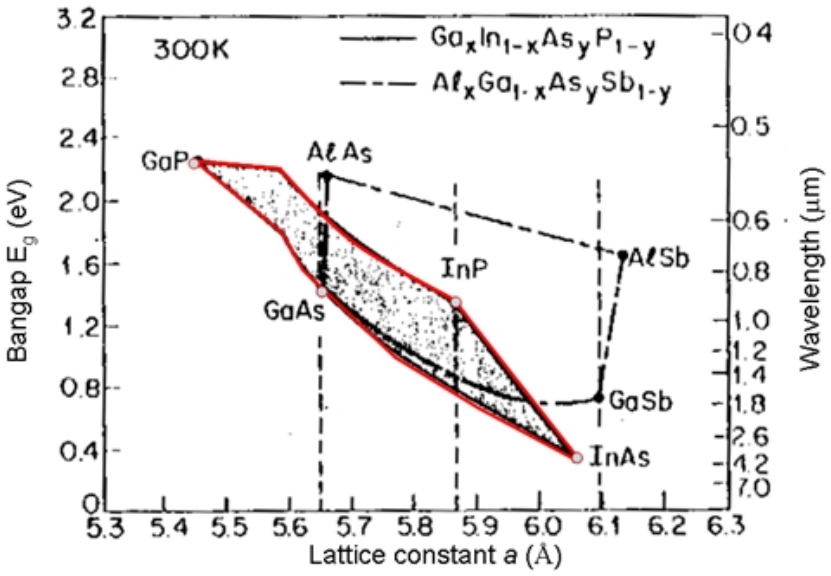

Figure E.21: Energy gap vs. lattice constant of the two quaternary compounds $Ga_xIn_{1-x}As_yP_{1-y}$ and $Al_xGa_{1-x}As_ySb_{1-y}$.

The figure E.21 defines the two quaternary systems and $Ga_xIn_{1-x}As_yP_{1-y}$ and $Al_xGa_{1-x}As_ySb_{1-y}$. For each system, any choice of x and y identify a quaternary compound that crystallizes in the zinc-blende form (face centered cubic, fcc) with

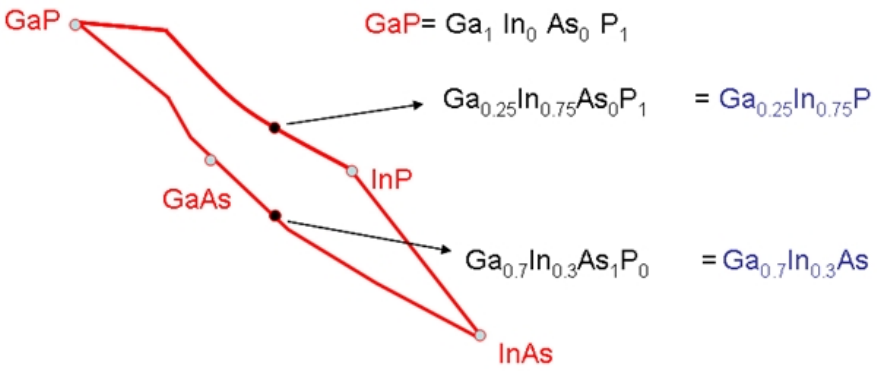

Figure E.22: Energy gap vs. lattice constant: estimation the composition of the binary compound.

binary basis made of the couple AB of different atoms. The index x indicates the fraction of, say Ga and In, that fill the A position, while y does the same for As and P in the B position into the basis of the crystal. Let us consider the first one, highlighted with a red boundary. All possible compounds must lay inside the bounded area, or on its boundary. It locates four stoichiometric compounds (GaP, $AlAs$, $GaAs$, $InAs$) along the boundary. (It should be clear that in this case, for instance, $GaP = Ga_1In_0As_0P_1$). For each compound, the horizontal axis gives the lattice constant a, the left vertical axis the corresponding amplitude of the energy gap Eg and the right vertical axis reads this value in terms of optical emitted wavelengths. Before trying to design a true laser chip, let us try to find the composition (that means the values of x,y) of a generic quaternary compound. First of all, any point on the boundary has a measurable distance from the closest pair of stoichiometric compounds, that always share one or the A or the B atoms.

For instance, in the fig.E.22, two points have been identified on the boundary, and their composition has been calculated by means of simple proportionality: the closest the point to one binary compound, the higher its relative abundance in the ternary. The two points in fig.E.22 have been selected on the same vertical, keeping in mind the next construction o fan epitaxial structure: having the same crystal lattice, they must share the same lattice constant a, in order to allow defect-free epitaxy. At this point, any intermediate point along the vertical line joining the two given points is calculated by the same means (fig.E.23). Now, we are ready to design a laser diode, following the rules given in the main text:

1. Select the emission wavelength on the right vertical axis.
2. Draw an horizontal line passing for that point
3. Search for a possible substrate drawing vertical lines across the binary compound and looking for a cross point with the previous horizontal line that lies inside one of the quaternary systems
4. Select the compound (ternary or quaternary) corresponding to that crossing point. This is the active material.
5. Select on the same vertical line of the crossing point the highest possible point that belongs to the same system. Often it lays on the upper boundary. That is the material for the confinement layers.

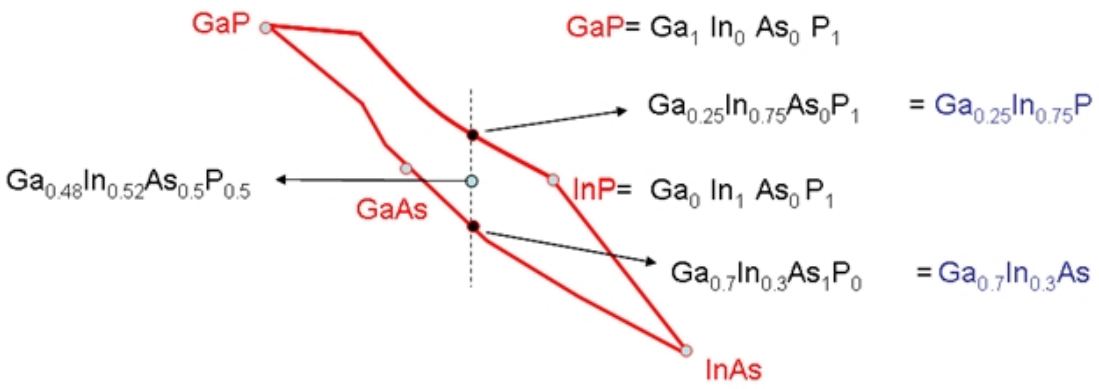

Figure E.23: Energy gap vs. lattice constant: estimation the composition of the quaternary compound.

The following example deals with a 1300 nm laser diode. It is clearly grown on an InP substrate, has a quaternary active region and again InP for the confinement layers.

For a rough estimate of the compositions, we can appreciate that the point where the lower boundary crosses the InP vertical line is a little bit closer to $InAs$ than to $GaAs$, that leads to a ternary $Ga_{0.45}In_{0.55}As$. The active region is at a distance 1/3 from this ternary, whose abundance is then roughly 2/3 with respect to InP at the upper extreme

$$(Ga_{0.45}In_{0.55}As_1P_0)\frac{2}{3} + (Ga_0In_1As_0P_1)\frac{1}{3} = (Ga_{0.3}In_{0.7}As_{0.67}P_{0.33})$$

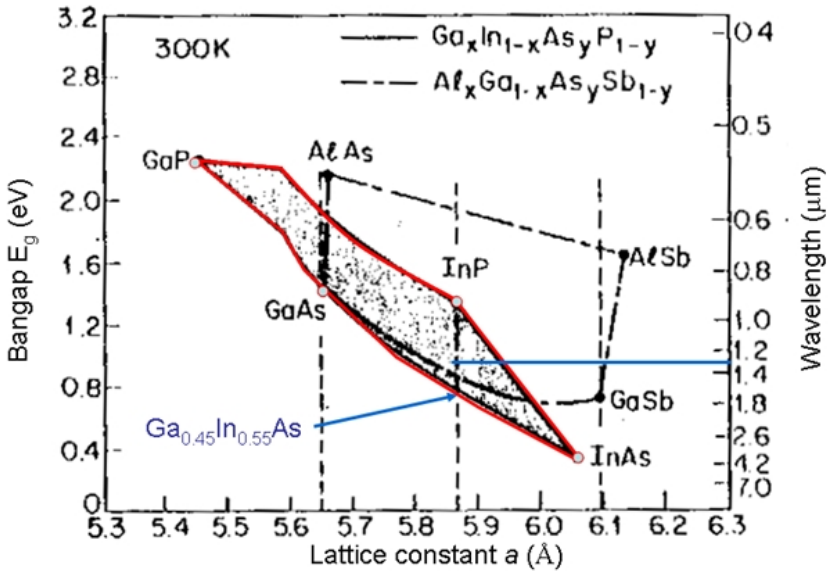

Figure E.24: Energy gap vs. lattice constant: estimation of the composition.

E.11 Fundamental investigation techniques for failure analysis.

Failure analysis is an important tool for improving laser diode design and manufacturing. It provides information necessary for technology advancement and for corrective actions to improve quality and reliability. For this reason, in this last paragraph of appendix E, the most important tools for failure analysis of laser diodes are summarized.

Electron Microscopy is the basis of inspection for semiconductor devices, not only because of the extraordinary detail imaging provided by the most important tools are, of course, the Transmission Electron Microscope(TEM) and the Scanning Electron Microscope (SEM), but also for some extremely peculiar obervation modes possible at the SEM (the Electron Beam INduced Current, EBIC) and for the amazing specimen preparation capabilities of the Focused Ion Beam (FIB). For such reasons, a summary of the microscopic techniques and methods is here given.

E.11.1 Focused Ion Beam (FIB).

The Focused Ion Beam (FIB) instrument is almost identical to a Scanning Electron Microscope (SEM), but uses a beam of ions rather than electrons. The focused ion beam can directly modify or "ill" the specimen surface, via the sputtering process, and this milling can be controlled with nanometer precision. By carefully controlling the energy and intensity of the ion beam, it is possible to perform very precise nano-machining to produce minute components (lamellas) or to investigate in a more precise part of the device. For instance in fig.E.25 is reported an example in which are shown all the needed steps to preparing a lamella from a semiconductor device (in this case it is not a laser diode).

The new lamella is useful for depth investigation of the structure of the devises under test, indeed it can be analyzed with TEM that allows to observe structures on the order of nm. For example in fig.E.26 is reported the lamella of an edge emitter laser with ridge structure, in which it is possible to observe the presence of the MQWs under the ridge, exactly where the active region is located. These would be impossible to observe with SEM.

Otherwise the FIB can be used also to induce piloted modification on the devices. For example consider the experiments in par.2.2 and [36, 49, 50], in which FIB will help in modifying the optical cavity affecting the sole internal losses. During this study, a reference sample DFB laser diode, that emits at 1310nm, was modified, grooving a progressively enlarging trench with FIB, parallel to the ridge and very close to it. The aim of such operation was to perturb the optical propagation without affecting the mirror facets, and possibly keeping any electrical modification negligibly small. The results of this operation had been deeply described in subparagraphs 2.2.1 and 2.2.2.

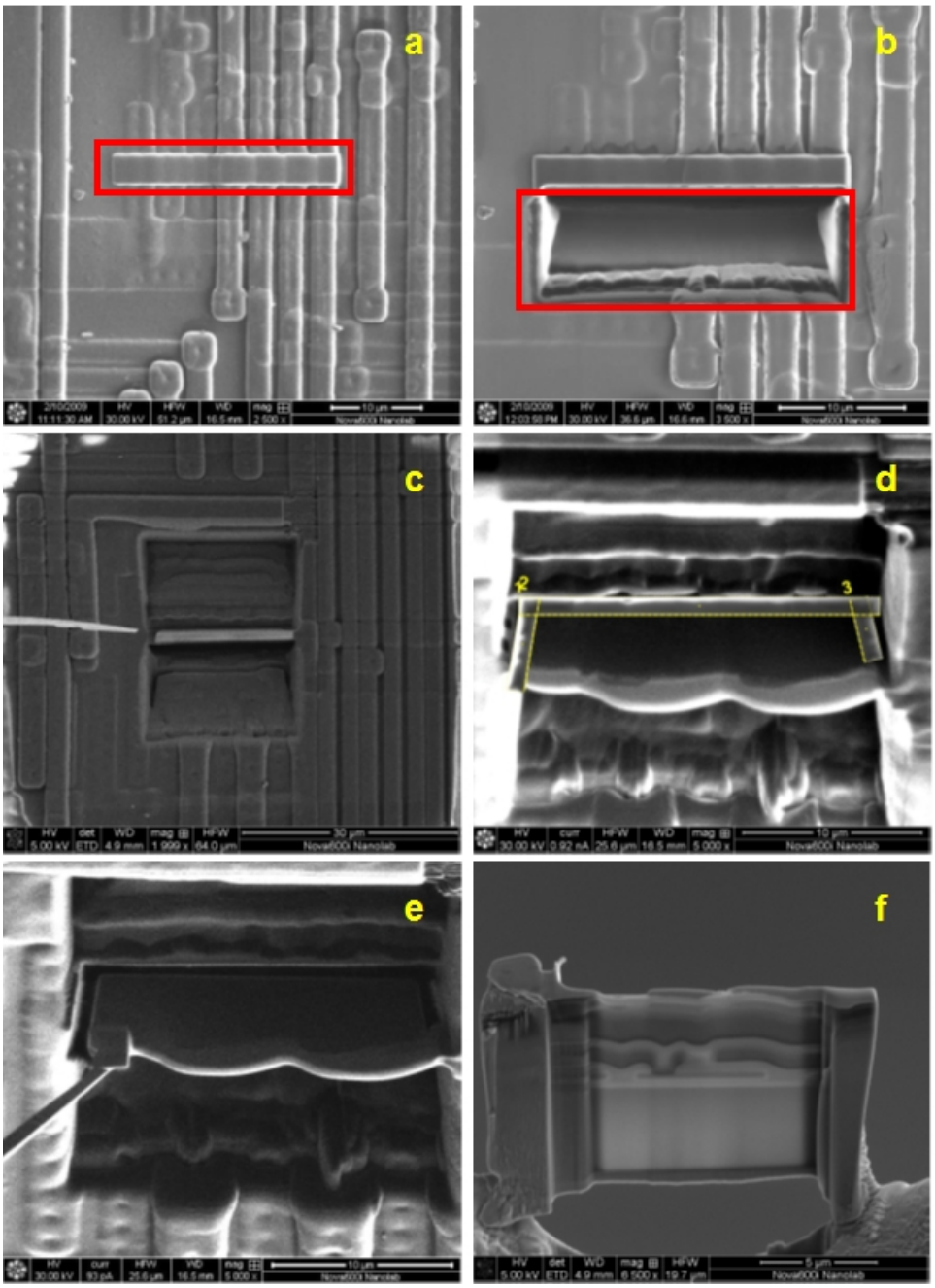

Figure E.25: Steps of FIB erosion to create a lamella: (a) SEM image that shows the protective layer of platinum in the position in which is going to be dig the section. (b) First digging on one side of the platinum layer. (c) Second digging on the other side of the platinum layer. (d) The lamella is going to be detached from the whole device. (e) The lamella has been linked up with the top of the omniprobe and it is ready to leave the rest of the device. (f) The final lamella (after several cleaning steps), ready for further investigation, for example at the Transmission Electron Microscopy (TEM).

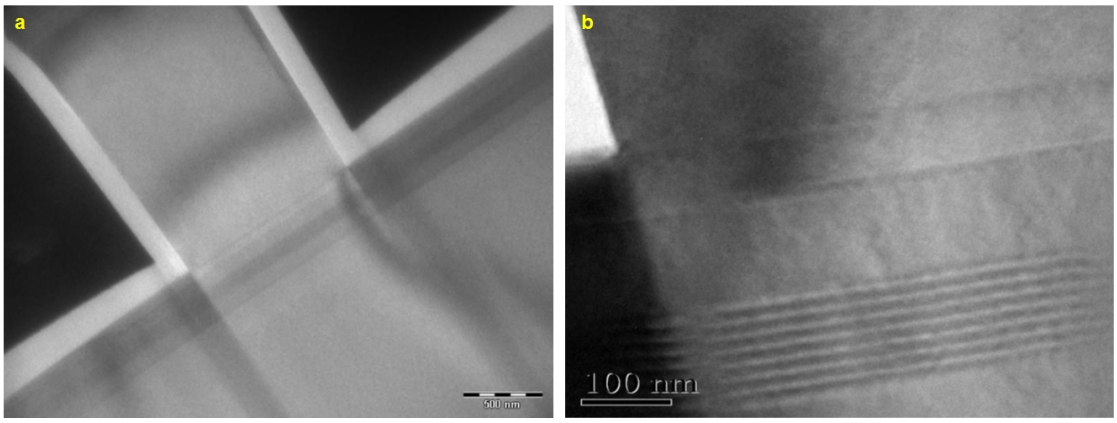

Figure E.26: (a) TEM image of a edge emitter with ridge structure, in which are evident the MQWs. (b) A zoomed image of fig.E.26a.

E.11.2 Electron Beam Induced Current (EBIC)

The role of EBIC in Failure Analysis has been assessed since decades [70, 71], and historically supported the development of the young Silicon technology, supplying a tool for mapping electrically active defects inside the depletion layer of a p–n or a Schottky junction [72–74]. The top achievement in EBIC measurements was given by the theoretical assessment of its physical basis, performed by Donolato in the 1980s of the past century [75].

An elegant Reciprocity Theorem completed the Donolato's job [76,77], allowing to give the EBIC detected defects those active role in junction degradation that could not be recognized, in principle, for those detected by Electroluminescence, the EBIC competitor for direct band-gap materials.

The Electron Beam Induced Current (EBIC) is a signal available at the SEM when one observes a semiconductor device where at least one *pn* or Schottky junction is present, is reached by the electron beam and is electrically connected to a current amplifier.
EBIC has two main applications:
1) To reveal where junctions are
2) To detect electrically active defects (recombination centers) inside the junctions.

An evolution of the EBIC is the XEBIC [78], indeed of the FIB opened the door to precise micro-sectioning, adding the possibility of complementing the standard EBIC top view in fig.E.27 with the cross-sectional EBIC in fig.E.28, shortly: XEBIC. In fig.E.28 the superimposed EBIC and SEM images of the front-facet of a laser diode show the simplest application of XEBIC. The facet coating has first been removed by FIB and EBIC has been then recorded. The relevant information is here the strong confinement of the junction activity under the ridge, despite the junction itself extends also at right and left sides, up to the trenches. This tool has been used in several works made during this three year of the Author's PhD and they are completely reported Chapter 2 and in [35, 49, 50].

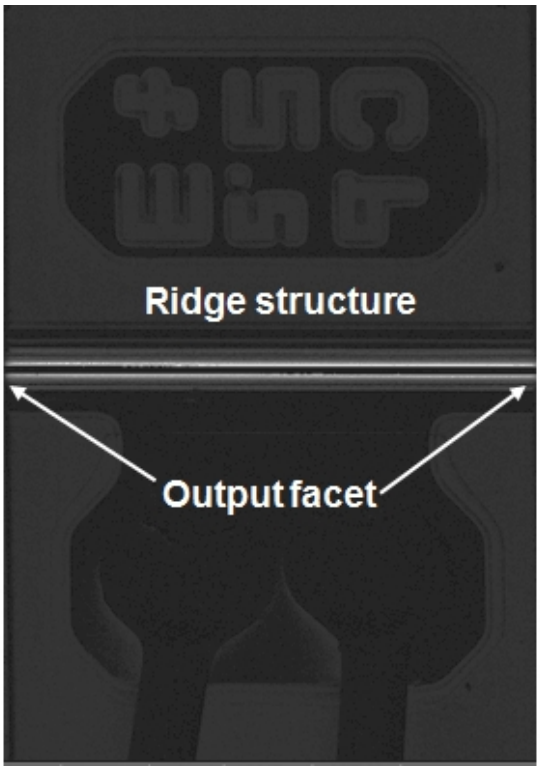

Figure E.27: Standard top view EBIC.

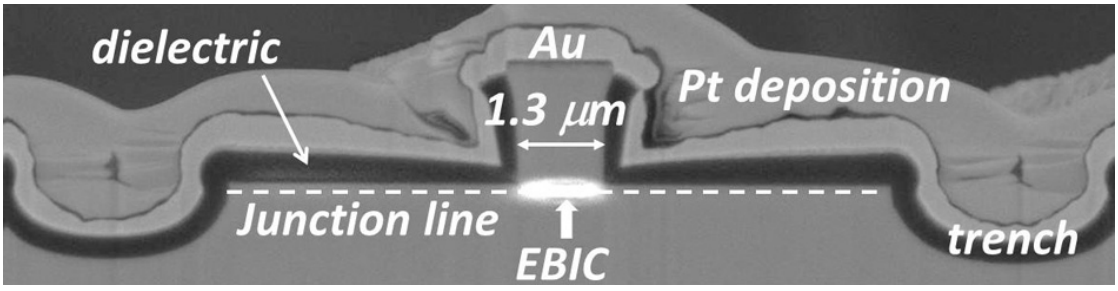

Figure E.28: Cross-sectional EBIC.

Bibliography

[1] M. Vanzi, *"A model for the DC characteristics of a laser diode"*, ICECS2008, La Valletta, Malta, 2008, pp. 874-877

[2] G.Mura, M.Vanzi, *"The interpretation of the DC characteristics of LED and laser diodes to address their failure analysis*", Microelectronics Reliability, vol.50, no.4, pp.471-478, Apr. 2010.

[3] M.Vanzi, G.Mura, G.Martines, *"DC parameters for laser diodes from experimental curves"*, Microelectronics Reliability, vol.51, no. 9-11, pp. 1752–1756, Nov. 2011.

[4] A. Einstein, *"Strahlungs-Emission und - Absorption nach der Quantentheorie [Emission and Absorption of Radiation in Quantum Theory]"*. Verhandl. D. Deutch. Phys. Ges., vol. 18, pp. 318-323, 1916.

[5] A. Einstein, *"Zur Quantentheorie der Strahlung [On the Quantum Theory of Radiation]"*, Phys. ZS., vol. 18, pp. 121-128, 1917.

[6] C.H Townes, J.P Gordon, H.J Zeiger, *"Molecular Microwave Oscillator and New Hyperfine Structure in the Microwave Spectrum of NH3"*, Physical Review, vol. 95, no. 1, pp. 282-284, July 1954.

[7] A.L Schawlow, C.H Townes, *"Infrared and Optical Masers"*, Physical Review, vol. 112, no. 6, pp. 1940-1949, Dec. 1958.

[8] T.H Maiman, *"Stimulated Optical Radiation in Ruby"*, Nature, vol 187, no. 4736, pp. 493-494, Aug. 1960.

[9] H. Statz, G. De Mars, *"Transients and Oscillation Pulses in Masers"*, Quantum Electronics, p.530, 1960.

[10] W.E Lamb, *"Theory of an Optical Maser"*, Phys. Rev, vol. 134, A1429, 1964.

[11] W. Paul, *"Über den Zusammenhang des Abschlusses der Elektronengruppen im Atom mit der Komplexstruktur der Spektren"*, Z. Phys. vol. 31, p.765,1925.

[12] E. Fermi, *"Zur Quantelung des Idealen Einatomigen Gases"*, Z. Phys. vol.36, p.902, 1926.

[13] P.A.M Dirac, *"On the Theory of Quantum Mechanics"*, Proc. Roy. Soc., vol.A112, p.661, 1926.

[14] F. Bloch, *"Über die Quantenmechanik der Elektronen in Kristallgittern"*, Z. Physik, vol. 52, p. 555, 1928.

[15] W. Shockley, *"Electrons and Holes in Semiconductors."*, Princeton, NJ: Van Nostrand, (1950).

[16] H. Statz, C.L. Tang, J.M. Lavine, *"Spectral output of semiconductor lasers"*, J. Appl. Phys.,vol. 35, p.2581, 1964.

[17] G.J. Lasher, *"Analysis of a proposed bistable injection laser"*, Solid State Electronics, vol. 7, p. 707, 1964.

[18] T. Ikegami, Y. Suematsu, *"Resonance-Like Characteristics of the Direct Modulation of a Junction Laser"*, IEEE letters, vol. 55, p. 122, 1967.

[19] T. Ikegami, Y. Suematsu, *"Direct modulation semiconductor junction lasers"*, Electron. Commun. Japan, vol. B51, p. 51, 1968.

[20] T.L Paoli, J.E. Ripper, *"Direct modulation of semiconductor lasers"*, Proc. IEEE , vol. 58, p. 1457, 1970.

[21] M.J Adams, *"Rate equations and transient phenomena in semiconductor lasers"*, Opto-electron., vol. 5, p.201, 1973.

[22] R. Salathé, C. Voumard, H. Weber, *"Rate equation approach for diode lasers"*, Opto-electron. vol. 6, p. 451, 1974.

[23] P.M Bores, M. Danielsen, M.T Vlaardingerbroek, *"Dynamic behaviour of semiconductor laser"*, Electron.Lett., vol. 11, p.206, 1975.

[24] H. Kressel, J.K Butler, *"Semiconductor lasers and heterojunction LEDs"*, Academic Press (1977).

[25] H.C Casey, M.B. Panish, *"Heterostructure lasers"*, Academic Press (1978).

[26] J.H.B Thompson, *"Physics of Semiconductor Laser Devices"*, John Wiley and Sons (1980).

[27] G. Arnold, P. Russer, and K. Petermann, *"Modulation of laser diodes", in Semiconductor devices for optical communication*, Springer Verlag (1982).

[28] C.H Henry, *"Spectral Properties of Semiconductor Lasers", in Semiconductors and Semimetals* ed W.T. Tsang, Academic Press (1985).

[29] K. Lau, A. Yariv, *"High-frequency current modulation of semiconductor lasers", in Semiconductors and Semimetals*, ed. W.T. Tsang, Academic Press (1985).

[30] A. Yariv Optical Electronics, 4th ed., Oxford University Press.(1995)

[31] L.A. Coldren, S.W Corzine, M.L Masanovic, *"Diode Lasers and Photonic Integrated Circuits"*, 2nd ed., John Wiley and Sons (2012)

[32] G.P. Agrawal, N.K. Dutta, *"Long-Wavelength Semiconductor Lasers"*, Van Nostrand Reinhold (1986).

[33] J.T. Verdeyen, *"Laser Electronics*, 3rd ed., Prentice Hall (1995).

[34] L.A. Coldren, S.W Corzine, M.L Masanovic, *"A phenomenological approach to Diode Laser"*, in *Diode Lasers and Photonic Integrated Circuits*, 2nd ed., pp. 45-90, John Wiley and Sons (2012)

[35] G.Mura, M.Vanzi, G.Marcello and R.Cao, *"The role of the optical trans-characteristics in laser diode analysis"*, Microelectronics Reliability, vol. 53, no. 9–11, pp 1538–1542, Nov. 2013.

[36] M. Vanzi, G. Mura, G. Martines and T. Tomasi, *"Optical losses in single-mode laser diodes"*, Microelectronics Reliability, vol. 53, no. 9- 11, pp 1529–1533, Nov. 2013

[37] Hakki BW, Paoli TL., *"Gain spectra in GaAs double heterostructure injection lasers."*, J Appl Phys 1975;46:1299.

[38] Cassidy DT.,*"Technique for measurement of the gain spectra of semiconductor diode lasers."*, J Appl Phys 1984 56,3096-3099

[39] Henry CH, Logan RA, Merritt FR.,*Measurement of gain and absorption spectra in AlGaAs buried heterostructure lasers."*, J Appl Phys 1980;51:3042.

[40] Hofstetter D, Faist J.,*"Measurement of semiconductor laser gain and dispersion curves utilizing fourier transforms of the emission spectra."*, IEEE Photonics Technol Lett 1999;11:1372.

[41] G.Lasher, F.Stern, *"Spontaneus and stimulated recombination in semiconductors"*, Phys. Rev., Vol. 133, n.2, pp.A553-A563, 1964

[42] J.T. Verdeyen, *"Gain coefficient in semiconductors"*, in *Laser Electronics*, 3rd ed., pp.454–459, Prentice Hall (1995).

[43] L.A. Coldren, S.W Corzine, M.L Masanovic, *"Active materials and their characteristics"*, in *Diode Lasers and Photonic Integrated Circuits*, 2nd ed., pp.218-234 ,John Wiley & Sons (2012)

[44] G. E. Shtengel, R. F. Kazarinov, G. L. Belenky, M. S. Hybertsen, D. A. Ackerman, *"Advances in Measurements of Physical Parameters of Semiconductor Lasers"*, Int. J. Hi. Spe. Ele. Syst., 09, pp. 901-940, 1998.

[45] L. F. De Chiaro, *"Damage-induced spectral perturbations in multilongitudinal-mode semiconductor lasers"*, in Journal of Lightwave Technology, vol. 8, no. 11, pp. 1659-1669, Nov 1990.

[46] Y. Barbarin, E. A. J. M. Bente, G. Servanton, L. Mussard, Y. S. Oei, R. Nötzel, and M. K. Smit, *"Gain measurements of Fabry-Perot InP/InGaAsP lasers using an ultrahigh-resolution spectrometer"*, Appl. Opt. 2009, 45:9007-9012.

[47] Ma, M. L., et al., *"Measurement of gain characteristics of semiconductor lasers by amplified spontaneous emissions from dual facets."*, Optics express 21.8 (2013): 10335-10341.

[48] Goldberg Lew et al., *"Spectral characteristics of semiconductor lasers with optical feedback."*,Microwave Theory and Techniques, IEEE Transactions on, 1982, 30(4):401-410.

[49] G.Mura, M.Vanzi, G.Marcello, *"FIB induced electro-optical alterations in a DFB InP laser diode"*, Microelectronics Reliability, vol. 54, no. 9–10, pp 2151–2153, 2014.

[50] G.Marcello, M.Vanzi, G.Mura, *"Experimental gain in single mode laser diodes"*, Proc. ISROS 2014.

[51] B.W. Hakki and T. L. Paoli, *"Cw degradation at 300K of GaAs double-heterostructure junction laser. II. Electronic gain."*, J. Appl. Phys. 1973 44, 4113.

[52] G. P. Agrawal, N. K. Dutta, *"Long-Wavelength Semiconductor Lasers"*, Van Nostrand Reinhold, 1986, pp. 74-146

[53] H. C. Casey, M. B. Panish, *"Heterosctucture Lasers. Part B. Material and Operating Characteristics"*, Academic Press, New York, 1978, pp. 236-240.

[54] T. L. Paoli, P. A. Barnes, *"Saturation of the junction voltage in stripe-geometry (AlGa)As double-heterostructure junction lasers"*, Applied Physics Letters, 28(12), pp. 714-716, 1976.

[55] H. Kogelnik, C. V. Shank, *"Coupled-Wave Theory of Distributed Feedback Lasers"*, J. Appl. Phys., vol. 43, pp. 2327-2335, 1972.

[56] G. P. Agrawal, N. K. Dutta, *"Long-Wavelength Semiconductor Lasers"*, Van Nostrand Reinhold, 1986, pp. 319-384.

[57] Vanzi M., Mura G., Marcello G., & Martines G., *"Clamp voltage and ideality factor in laser diodes."*, Microelectronics Reliability, 55(9), 1736-1740 (2015).

[58] D. Zhu, Jiuru Xu, A. Noemaun, J.K. Kim, E.F. Schubert, M.H. Crawford, D.D. Koleske, *"The origin of the high diode-ideality factors in GaInN/GaN multiple quantum well light-emitting diodes."*, Appl. Phys. Lett. 94 (8) (02/2009).

[59] K. Hennessy, A. Badolato, M.Winger, D. Gerace, M. Atature, S. Gulde, S. Fält, E.L. Hu, A. Imamoglu, *"Quantum nature of a strongly coupled single quantum dot–cavity system."*, Nature 445 (22 February 2007) 896–899.

[60] K. P. Sinha, A. Meulenberg, P. L. Hagelstein, *"Quantum coupling between closely-spaced surfaces via transverse photons."*, http://arxiv.org/ftp/cond-mat/papers/0606/0606184.pdf.

[61] G.Marcello, G.Mura, M. Vanzi, M. Bagatin, S. Gerardin, A. Paccagnella, *"Proton irradiation effects on commercial laser diodes."*,2015 15th European Conference on Radiation and Its Effects on Components and Systems (RADECS), Moscow, 2015, pp. 1-4.

[62] P. Barnes and T. Paoli, *"Derivative measurements of the current-voltage characteristics of double-heterostructure injection lasers"*, in IEEE Journal of Quantum Electronics, vol. 12, no. 10, pp. 633-639, Oct 1976.

[63] P. D. Wright, *"Electrical derivative characteristics of InGaAsP buried heterostructure lasers with a rectifying contact"*, J. Appl. Phys. 61, 1720 (1987).

[64] P. D. Wright, W. B. Joyce and D.C. Craft, *"Electrical derivative characteristics of InGaAsP buried heterostructure lasers"*, J. Appl. Phys. 53, 1364 (1982)

[65] Tomm JW, Ziegler M, Hempel M, Elsaesser T., *"Mechanisms and fast kinetics of the catastrophic optical damage (COD) in GaAs-based diode lasers."* Laser Photonic Rev 2011;5(3):422–41.

[66] Sarlet G, Buus J, Rigole P-J, *"Tunable laser diodes.*, In: Dutta AK, Dutta NK, Fujiwara M, Dutta AK, Dutta NK, Fujiwara M, editors. WDM technologies. Academic Press; 2008.

[67] L.A. Coldren, S.W Corzine, M.L Masanovic, *Diode lasers and photonic integrated circuits"*, 2nd ed. Hoboken, New Jersey: Jhon Wiley & Sons, Inc.; 2012 [chapter 5].

[68] Sze SM, Ng Kwok K., *"Physics of semiconductor devices."*, 3rd ed. J. Wiley; 2007 [chapter 12, §12.4.3].

[69] M.Fukuda, *"Degradation and Radiation Damage in Laser Diodes – the Relationship between Space and Telecom Reliability"*, invited talk at ISROS 2010

[70] Smith C et al., *"Resistive contrast imaging: a new SEM mode for failure analysis."*, IEEE Trans Electron Dev 1986;33(2):282–5.

[71] Soden J, Anderson R. *"IC failure analysis: techniques and tools for quality reliability improvement."*, Microelectron Reliab 1995;35(3):429–53.

[72] Mizuta M et al., *"Electron beam induced current investigation on cw annealed laser silicon."*, Appl. Phys. Lett. 1980;37(2):154–6.

[73] Burton et al., *"Degradation of blue AlGaN/InGaN/GaN LEDs subjected to high current pulses."*, Proc. IRPS 1995:191–9.

[74] Vanzi M et al., *"Electron microscopy of life-tested semiconductor laser diodes."*, Micron. 2000;31:259–67.

[75] Donolato C., *"Evaluation of diffusion lengths and surface recombination velocities from electron beam induced current scans."*, Appl. Phys. Lett. 1983;43(1):120–2.

[76] Donolato C., *"A reciprocity theorem for charge collection.*, Appl. Phys. Lett. 1985; 46(3):270–2.

[77] Donolato C., *"An alternative proof of the generalized reciprocity theorem for charge collection."*, J. Appl. Phys. 1983;66(9):4524–5.

[78] Vanzi et al., *"XEBIC at the dual beam."*, Microelectron Reliab 2013; 53(9–11):1399–402.

[79] Verdeyen JT., *Laser electronics."*, 3rd ed. Prentice Hall; 1995 [chapter 11, §11.4.1].

[80] M. Fukuda, M. Okayasu, J. Temmyo, and J. Nakano, *"Degradation Behavior of 0.98μm strained quantum well InGaAs/AlGaAs lasers under high-power operation"*, IEEE J. Quantum Electronics, vol. 30, pp. 471-476, 1994.

[81] A. Moser, A. Oosenbrug, E. E. Latia, Th. Forster, and M. Gasser, *"High-power operation of strained InGaAs/AIGaAs single quantum well lasers"*, Applied Physics Letters, vol. 59, pp. 2642 - 2644, 1991.

[82] C. H. Henry, P. M. Petroff, R. A. Logan, and F. R. Meritt, *"Catastrophic Damage of $Al_xGa_{1-x}As$ double-heterostructure laser material"*, J. Appl. Phys., vol. 50, pp. 3721–3723, 1979.

[83] O. Ueda, K. Wakao, S. Komiya, A. Yamaguchi, S. Isozumi, and I. Umebu, *"Catastrophic degradation of InGaAsP/InGaP double-heterostructure lasers grown on (001) GaAs substrates by liquid-phase epitaxy"*, J. Appl. Phys., vol. 58, no. 11, pp. 3996–4002, 1985.

[84] W. A. Tiller, *"Theoretical analysis of requirements for crystal growth from solution"*, Journal of Crystal Growth, vol. 2, no. 2, pp. 69–79, 1968.

[85] D. P. Cooper, C. H. Gooch, and R. J. Sherwell, *"Internal self-damage of gallium arsenide lasers"*, IEEE J. Quantum Electron, vol. QE-2, no. 8, pp. 329-330, 1966

[86] D. A. Shaw, P.R. Thornton, *Catastrophic degradation in GaAs laser diodes"*, Solid State Electronics, vol. 13, no. 7, pp. 919-922, July 1970.

[87] H. Kressel, H. Nelson and F. Z. Hawrylo, *"Control of optical losses in p-n junction lasers by use of a heterojunction: theory and experiment"*, J. Appl. Phys., vol. 41, pp. 2019-2031, 1970.

[88] M. Ettenberg, H. S. Sommers, H. Kressel, H. F. Lockwood, *"Control of facet damage in GaAs laser diodes"*, Appl Phys Lett., vol. 18, pp. 571–573, 1971.

[89] B. W. Hakki and F. R. Nash, *"Catastrophic failure in GaAs double heterostructure injection lasers"*, J. Appl. Phys., vol. 45, no. 9, pp. 3907-3912, 1974.

[90] M. Bou Sanayeh, P. Brick, W. Schmid, B. Mayer, M. Muller, M. Reufer, K. Streubel, M. Ziegler, J. W. Tomm, G. Bacher , *"The physics of catastrophic optical damage in high-power AlGaInP laser diodes"*, Proc. SPIE 6997, Semiconductor Lasers and Laser Dynamics III, 699703, May 2008.

[91] M. Hempel et al.,*"Microscopic Origins of Catastrophic Optical Damage in Diode Lasers"*, IEEE Journal of Selected Topics in Quantum Electronics, vol. 19, no. 4, p. 1500508, 2013.

[92] Jens W. Tomm, M. Ziegler, V. Talalaev, C. Matthiesen, T. Elsaesser, M. Bou Sanayeh, P. Brick, M. Reufer, *"New approaches towards the understanding of the catastrophic optical damage process in in-plane diode lasers"*, SPIE 7230, Novel In-Plane Semiconductor Lasers VIII, 72300V, Feb. 2009.

[93] M. Bou Sanayeh, P. Brick, W. Schmid, B. Mayer, M. Müller, M. Reufer, K. Streubel, M. Ziegler, J. W. Tomm, G. Bacher, *The physics of catastrophic optical damage in high-power AlGaInP laser diodes"*, SPIE 6997, Semiconductor Lasers and Laser Dynamics III, 699703, May 2008.

[94] M. Ziegler, V. Talalaev, J. W. Tomm, T. Elsaesser, P. Ressel, B. Sumpf, G. Erbert, *"Surface recombination and facet heating in high-power diode lasers"*, Appl. Phys. Lett., vol. 92, no. 20, p. 203506, 2008.

[95] M. Ziegler, J. W. Tomm, T. Elsaesser, C. Matthiesen, M. Bou Sanayeh, P. Brick, *"Real-time thermal imaging of catastrophic optical damage in red-emitting high-power diode lasers"*, Appl. Phys. Lett., vol. 92, pp. 103514, 2008.

[96] M.Vanzi, M.Giansante, L.Zazzetti, F.Magistrali, D.Sala, G.Salmini and F.Fantini, *"Interpretation of Failure Analysis Results on ESD-Damaged InP Laser Diodes"*, ASM Intl., Proc. ISTFA 91, pp. 305-314, 1991.

[97] J.T.Verdeyen, *"Laser Electronics"*, Third Edition, Prentice Hall series in solid state physical electronics, Ch. 4 and Ch.6

[98] S.Sze, *"Physics of Semiconductor Devices"*, 2nd edition, John Wiley &Sons, 1981, pp 718-719.

[99] A. Bonfiglio, M. B. Casu, M. Vanzi, F. Magistrali, M. Maini, G. Salmini, *"Interpretation of sudden failures in pump laser diodes"*, ASM Intl., Proc. ISTFA 97, pp.189-196.

[100] F. Magistrali, G. Salmini, G.Martines, M.Vanzi. *"A charge Diffusion and Reciprocity Theorems: a direct approach to EBIC of Ridge Laser Diodes"*, ASM Intl., Proc. ISTFA 96, pp. 233–238

[101] ESD-DS5.2-1996, *"Sensitivity Testing, Machine Model."*, ESD Association, Rome, NY.

[102] ESD-STM5.1-1998, *"Sensitivity Testing, Human Body Model (HBM)."*, ESD Association, Rome, NY.

[103] ESD DS5.3.1-1996, *"Device Testing: Charged Device Model."*, ESD Association, Rome, NY.

[104] MIL STD 883.C/3015.7 notice 8", *"Military Standard for Test Methods and Procedures for Microelectronics: ESD Sensitivity Classification."*, 1989

[105] "EIA/JESSD22-A114", 1996

[106] IEC 61000-4-2: Electrostatic Discharge Immunity Tests

[107] Kim T., Kim, T., Kim, S., & Kim, S. B., *"Degradation behavior of 850 nm AlGaAs/GaAs oxide VCSELs suffered from electrostatic discharge."*, ETRI journal 2008, 30(6), 833-843.

[108] Cheng Y. M., Herrick R. W., Petrof P. M., Hibbs-Brenner,M. K., & Morgan R. A., *"Degradation mechanisms of vertical cavity surface emitting lasers."*, In Reliability Physics Symposium, 1996. 34th Annual Proceedings, IEEE International (pp. 211-213). IEEE.

[109] Hawkins B. M., Hawthorne R. A., Guenter, J. K. Tatum, J. A. & Biard J. R., *"Reliability of various size oxide aperture VCSELs."*, In Electronic Components and Technology Conference, 2002. Proceedings. 52nd (pp. 540-550). IEEE.

[110] Kim H. D., Jeong W. G., Shin H. E., Ser J. H., Shin H. K., & Ju Y. G.,*"Reliability in the oxide vertical-cavity surface-emitting lasers exposed to electrostatic discharge."*, Optics express 2006, 14(25), 12432-12438.

[111] Ueda O., & Pearton S. J. (ed.)., *"Materials and reliability handbook for semiconductor optical and electron devices."*, Springer Science & Business Media, 2012, Ch 6.

[112] Voldman S. H., *"ESD physics and devices."*, John Wiley & Sons, 2005.

[113] Mathes D., Guenter J., Hawkins B., Hawthorne B., & Johnson C., *"An atlas of ESD failure signatures in vertical cavity surface emitting lasers."*, In Istfa 2005: Proceedings of the 31st International Symposium for Testing and Failure Analysis (Vol. 1). ASM International, 2005.

[114] M. Vanzi, *"The rules of the Rue Morgue."*, in Proc. ISTFA, Santa Clara, CA, pp. 249–256, 1995.

[115] G.Mura, M.Vanzi, G.Cassanelli, F.Fantini, *"The rules of the Rue Morgue: a decade later"*, Proc. Of Physical and Failure Analysis of Integrated Circuits (IPFA), pp.71-74, 2006

[116] G.Mura and M.Vanzi, *"Failure Analysis of Failure Analyses: The Rules of the Rue Morgue, Ten Years Later"*, IEEE TDMR, Vol.7, I.3 2007

[117] G.Mura and M.Vanzi, *"Faulty Failure Analysis"*, Proc. Of Physical and Failure Analysis of Integrated Circuits (IPFA), pp. 599-602, 2013

[118] G.Mura and M.Vanzi, *"Logics of Failure Analysis: 20 years of Rules of the Rue Morgue."*, Proc. Of Physical and Failure Analysis of Integrated Circuits (IPFA), in press, 2016.

[119] H. Lischka, H. Henschel, O. Kohn, W. Lennartz, and H. Schmidt, *"Radiation effects in light emitting diodes, laser diodes, photodiodes and optocouplers"*, in Proc. RADECS93, pp. 226–231.

[120] C. E. Barnes and J. J. Wczer, *"Radiation Effects in Optoelectronic Devices"*, Sandia Nat. Lab., Rep. SAND-84–0771, 1984.

[121] Carol C. Phifer, *"Effects of Radiation on Laser Diodes"*, Sandia Nat. Lab., Rep. SAND 04-4725, 2004.

[122] L. W. Aukerman, *"Radiation Effects On Semiconductor Optical Devices For Space Communications"*, in Proc. SPIE, Laser and Laser Systems Reliability, 56, 1982.

[123] A. H. Johnston, T. F. Miyahira, and B. G. Rax, *"Proton Damage in Advanced Laser Diodes"*, IEEE Trans. On Nuclear Sci, VOL. 48, NO. 6, 2001.

[124] Y. F. Zhao et al., *"Annealing Effects on Multi-Quantum Well Laser Diodes after Proton Irradiation"*, IEEE Trans. On Nuclear Sci, VOL 45, NO 6, 1998.

[125] A. H. Johnston and T. F. Miyahira, *"Radiation degradation mechanisms in laser diodes"*, IEEE Trans. Nucl. Sci., vol. 51, no. 6, pp.3564–3571, 2004.

[126] Sabrina Bédard and Laurent J. Lewis, *"Diffusion of hydrogen in crystalline silicon"*, Phys. Rev. B 61, 9895 - Published 15 April 2000.

[127] G. Le Galès, S. Joly, G. Marcello, G. Pedroza, A. Morisset, F. Laruelle, L. Bechou, *"Seed laser diodes in pulsed operation: limitations and reliability investigations."*, Proc. SPIE 10098, Physics and Simulation of Optoelectronic Devices XXV, 100980S (February 22, 2017).

[128] G. Le Galès, G. Marcello, S. Joly, G. Pedroza, A. Morriset, F. Laurelle, F. Darracq, L. Bechou, *"1060nm Seed laser diodes: performances and safe operating area."*, 2016 International Symposium on Reliability of Optoelectronics for Systems.

[129] Fukuda M., *"Reliability and degradation of semiconductor Lasers and LEDs"*, Norwood, Artech House, Inc., Norwood, MA, 1991.

[130] Ettenberg, M., Kressel, H., *"The reliability of (AlGa)As CW laser diodes"*, IEEE Journal of Quantum Electronics, 16(2), 186–196, 1980.

[131] Jolly A., Gokhan F. S., Bello R., Dupriez P., *"SBS management in Yb-fiber-amplifiers using multi-mode seeds and pulse-shaping"*, Optics Express 22(17), 20326, 2014.

[132] Scholz F., *"Need for Seed"*, Laser Technik Journal 12(5), 29–32, 2015.

[133] Bettiati M., G. Beuchet, P. Pagnod-Rossiaux, P. Garabedian, J. Perinet, S. Fromy, J. Bertreux, J. Hirtz, F. Laruelle, *"Reliable pulsed-operation of 1064 nm wavelength-stabilized diode lasers at high-average-power: boosting fiber lasers from the seed"*, Proc. SPIE 7580, 758025, 2010.

[134] Mohrdiek S., Troger J., Pliska T., Pfeiffer H.-U., Jaeggi D., Lichtenstein N., *"Performance and reliability of pulsed 1060 nm laser modules"*, Proc. SPIE 6873, 687320, 2008.

[135] Morasse B., Chatigny S., Gagnon É., de Sandro J.-Ph., Desrosiers C, *"Enhanced pulse-shaping capabilities and reduction of non-Linear effects in all-fiber MOPA pulsed system"*, Proc. SPIE 7195, 71951D, 2009.

[136] Riecke S. M., Wenzel H., Schwertfeger S., Lauritsen K., Paschke K., Erdmann R., Erbert G., *"Picosecond Spectral Dynamics of Gain-Switched DFB Lasers"*, IEEE Journal of Quantum Electronics 47(5), 715–722, 2011.